NASA CR-112306

ABLATION AND RADIATION COUPLED VISCOUS HYPERSONIC SHOCK LAYERS

VOLUME I

by
Carl D. Engel

under the directiom of
Richard C. Farmer
and
Ralph W. Pike

Prepared under
Grant NGR 19-001-059

by

Department of Chemical Engineering
Louisiana State University
Baton Rouge, Louisiana 70803

for

Langley Research Center
NATIONAL AERONAUTICS AND SPACE ADMINISTRATION

October 1971

PREFACE

This report gives the results, in detail, for a stagnation-line analysis of the radiative heating of a phenolic-nylon ablator. The analysis includes flowfield coupling with the ablator surface, equilibrium chemistry, a step-function diffusion model and a coupled line and continuum radiation calculation. This report serves as the documentation, i. e. users manual and operating instructions for the computer programs listed in the report. Copies of the decks have been transferred to Mr. James N. Moss, grant monitor, of the Langley Research Center, and can be obtained from him or from the authors.

This report also served as Carl D. Engel's dissertation requirement in obtaining a Doctor of Philosophy degree in chemical engineering.

ACKNOWLEDGMENTS

This research was performed under the direction of Dr. Richard C. Farmer. His encouragement and guidance are gratefully acknowledged.

Appreciation is also expressed to the National Aeronautics and Space Administration's Langley Research Center which sponsored the research and especially to J. Moss and R. Swann, Grant Monitors.

The author would like to acknowledge Ken H. Wilson of Lockheed Palo Alto Research Laboratory for his helpful discussions and computer subroutine to compute radiative energy transport which was used in the present work.

An acknowledgment is extended to the Charles E. Coates Memorial Fund of the L.S.U. Foundation for funds to pay a portion of the typing cost of the dissertation and to the L.S.U. Computer Research Center for the use of their facilities during the course of this research.

Special thanks are given to D. Esch, G. Perez and J. Balhoff, co-workers during this research; Nancy Roques for her programming assistance; Diane Marabella who typed the manuscript; and many friends who contributed to the successful completion of this research.

TABLE OF CONTENTS

APPENDIX

VOLUME II

LIST OF TABLES

LIST OF FIGURES

NOMENCLATURE**

English

$\overline{B}$	Property flux vectory (property x L)/(L^3 x t)$^{\$}$
B_v	Planckian radiation intensity (m/t^2 x no. of particles)
$\mathbb{B}$	Property generation term (property)/(L^3 x t)
b	Generalized property per unit mass term (property/m)
C_{H_C}	Convective heat transfer coefficient
C_{H_R}	Radiative heat transfer coefficient
C_i	Mass fraction (mass of i/unit mass of fluid) $C_i = \frac{\rho_i}{\rho}\frac{Y_i M_i}{M} = \frac{n_i M_i}{\rho}$, $\sum_i C_i = 1$
$\tilde{C}_i$	Elemental mass fraction $\tilde{C}_i = \sum_j e_{ij} C_j$
c	Velocity of light (L/t)
C_p	Specific heat at constant pressure (L^2/t^2 x T)
D_{ij}	Multicomponent diffusion coefficient (L^2/t)
D_i	Effective multicomponent diffusion coefficient (L^2/t)
D_i^T	Thermal diffusion coefficient (m/L x t)
$\mathbb{D}_{ij}$	Binary diffusion coefficient (L^2/t)
E	Stagnation internal energy (mL^2/t^2)
$\mathbb{E}$	Radiative Flux divergence (m/L x t^2)
$\overline{\overline{e}}$	Strain tensor (1/t)
e_{ij}	Mass fraction of element j within compound i
f′	Velocity function, u/u_s
f	Photon distribution function (no. of photons x t)/L^3
G_j	Gibbs free energy (mL^2/t^2 x mole of j)

$\bar{g}_i$ Gravitational force vector acting on a unit mass of species i (L/t^2)

g Enthalpy function, H/H_s

H Total enthalpy, $H = h + \bar{V}^2/2$

h Static enthalpy, $h = Q + P/\rho$ (L^2/t^2), also Planck's constant

h_1, h_2, h_3 Stretching functions in the ξ_1, ξ_2, ξ_3 directions respectively

$\bar{J}_i$ Mass flux vector of species i ($m/L^2 \times t$)

J Radiative emission term defined in Eq. 1.23 ($m/t^2 \times L$)

k' Coefficient of thermal conductivity without diffusion effects ($mL/t^3 \times T$)

k Ordinary coefficient of thermal conductivity ($mL/t^3 \times T$)

k_c Boltzmann's Constant (mL^2/t^2T)

k_b Bulk thermal conductivity ($mL/t^3 \times T$)

$L_{\ell m}$ Generalized transport coefficient (property/L x t x driving force)

M_i Molecular weight of species i (mass of i/mole of i)

m_i Mass of i (m)

N Number density (particles/L^3)

n_i Molal volume (moles of i/L^3)

n_t Molal density (total moles/L^3)

$\bar{n}$ Unit normal vector

P Static pressure ($m/L \times t^2$) or (F/L^2)#

P_r Prandtl number, $C_p\mu/k$

$\bar{\bar{P}}$ Radiative stress tensor ($m/L \times t^2$)

Q Internal energy per unit mass, including chemical energy (L^2/t^2)

$\bar{q}_R$ Radiative heat flux vector defined by Eq. 1.22 (m/t^3) or $(E/L^2 \times t)^{\#}$

q_c Convective energy flux to a surface (m/t^3)

q_R Radiative energy flux to a surface (m/t^3)

$\bar{q}_D$ Diffusional energy flux vector (m/t^3)

R Body nose radius (L)

R_e Reynolds number, $\rho_\infty U_\infty R/\mu_{s,0}$

R_{e_s} Reynolds number, $\rho_{s,0} U_\infty R/\mu_{s,0}$

R_i Mass rate of formation of species i by heterogeneous reactions (m/tL^2)

$\mathfrak{R}$ Universal gas constant ($mL^3/t^2 \times T \times$ no. of moles)

$\tilde{\mathfrak{R}}$ $\mathfrak{R}/M$, mean molecular weight weighted gas constant $(L^2/t^2 \times T)$

r Cylindrical radius defined in Fig. A.3 (L)

S Induction or resistance energy generation term (L^2/t^3)

S_i Total surface generation of species i ($m/t\ L^2$)

T Thermodynamic temperature (T)

t Time (t)

U_∞ Freestream velocity (L/t)

U_ν Spectral radiant energy density ($m/L \times t \times$ no. of particles)

u Component of $\bar{V}$ in the ξ_1 direction (parallel to the body surface) (L/t)

V Volume (L^3)

$\bar{V}$ Velocity vector, $u\bar{i} + v\bar{j} + w\bar{k}$ (L/t)

v Component of $\bar{V}$ in the ξ_2 direction (normal to the body surface) (L/t)

w	Component of $\bar{V}$ in the ξ_3 direction (L/t)
x	Body oriented coordinate corresponding to ξ_1 (L)
y	Body oriented coordinate corresponding to ξ_2 (L)
Y_i	Mole fraction of species i, $Y = n_i/n_t$, $\sum_i Y_i = 1$
z	Body oriented coordinate corresponding to ξ_3 (L)

Greek

α	Sublimation accomodation coefficient
α_v	Volumetric absorption coefficient, effective (L^2 x no. of particles/L^3)
β	Generalized property, (mass, momentum, or energy/L^3)
∇	Del operator (1/L)
δ	Shock detachment distance (L)
$\tilde{\delta}$	Transformed shock detachment distance
E_n	Exponential integral function of order n
ϵ	Difference between the body and shock angle $\epsilon = \theta - \varphi$ (radians)
ϵ_p	Volume of voids per unit volume
ζ	Distance along an arc (L)
η	Dorodnitzyn variable
θ	Body angle (radians)
I_v	Spectral radiation intensity (m/t^2 x no. of particles x no. of steardians)
$\overline{\overline{I}}$	Unit tensor
κ	Absorption coefficient (L^2 x no. of particles/L^3)
$\varkappa$	Local body curvature (1/L)
$\tilde{\varkappa}$	$1 + \varkappa y$

Λ Diffusional or radiative flux divergence (see Eq. 4.1) ($m/L \times t^2$)

λ $(\tilde{\mu} - 2/3\ \mu)$ ($m/L \times t$)

M $\sum_i Y_i M_i$ mean molecular weight of the mixture (m of mixture/ mole of mixture)

μ Ordinary viscosity ($m/L \times t$)

$\tilde{\mu}$ Bulk viscosity ($m/L \times t$)

ν Frequency ($1/t$)

ξ Orthogonal coordinate$^{\zeta}$; nondimensional x-coordinate when not subscripted

ρ Density (m/L^3), $\rho = n_t M$

ρ_i Partial density of species i, $\rho_i = n_i M_i$ (m of i/L^3)

$\bar{\rho}$ Density ratio across shock ρ_∞ / ρ_s

σ Radiative absorption cross section (L^2)

τ_ν Optical depth at frequency ν

$\overline{\overline{\tau}}$ Viscous stress tensor ($m/L \times t^2$)

φ Shock angle (radians)

$\bar{X}_m$ Generalized driving force (driving force/L)

$\bar{\Omega}_1$ Unit vector in the direction of photon propogation

Ω Solid angle (stearadians)

Ω_{ij}^s Collision integral of colliding species i and j

ω_i Generation of species i ($m/L^3 \times t$)

Script letters

f Direction cosine

Subscripts

a	Atmospheric (sea level) quantities
e	Edge conditions
i	Species i
n	Normal component
t	Tangential component or total quantity
w	Wall quantities
o	Stagnation line quantities
1,2,3	Directions corresponding to positive ξ_1, ξ_2, ξ_3 respectively
∞	Freestream conditions
s,δ	Quantities immediately behind the shock

Superscripts

D	Diffusion
g	Gravitational
P	Pressure
A	0 or 1 denoting two-dimensional or axisymetric respectively (an exponent)
T	Thermal
*	Denotes dimensional variables
o	Standard state quantity
-	Evaluated on char side of ablator interface
+	Evaluated on flow field side of ablator interface

** Symbols not listed are defined where used.

$ Abbreviations mean: m, mass; L, length; t, time; T, temperature; F, force; E, energy

The product $h_i \xi_i$ has unit of L.

Note $g_c = (mL/t^2 \times F)$ and $J = (FL/E)$ have been used.

ABSTRACT

The aerothermal environment about a manned planetary return spacecraft was determined at typical atmospheric flight conditions. The thin shock layer equations were developed to theoretically evaluate this environment. The stagnation line equations for the shock layer were solved numerically. All known, significant shock-layer and ablator processes were included in this model. These processes include ablation and radiation coupling within the viscous shock layer, line and continuum radiation for both air and ablation species, local chemical equilibrium throughout the shock layer and quasi-steady ablator behavior. Coupled ablator-shock layer solutions were obtained for a phenolic nylon ablator. A two zone model was used to approximate the elemental species distribution within the shock layer and was found to be a valid approximation. The detailed discussion of the mathematical analysis used and the results obtained provide a sound basis for understanding many of the characteristic processes of hyperbolic entry heating.

Emphasis is given to the description of the most significant mode of surface heating--radiation. A method of selecting the most radiatively important molecular species is developed. Selected molecular species and their transport mechanism were incorporated into a radiation model which also accounts for line and continuum radiation from H, C, O and N atoms.

A parametric study of the stagnation line shock layer was made. The primary emphasis in the parametric study was to quantitatively determine the effects of ablation products and radiative energy transport on surface heating rates. From this information, coupled ablator - shock layer solutions were obtained. In addition, results of the calculations were studied to provide additional understanding of shock layer processes. The radiation - gas dynamic coupling is shown to result in an asymptotic behavior of the shock stand-off distance for shock layer pressures larger than 0.5 atmospheres. Other results indicated that the nondimensional ablation-rate parameter alone is insufficient to correlate the nondimensional radiative heating. The nondimensional radiative heating was found to be a strong function of post shock pressure and free stream velocity in addition to ablation rate. Further, ablation products of phenolic nylon were found to be least effective in absorbing radiant energy in frequency levels below 5.0 ev. The continuum contribution to the surface heating was found to be essentially unchanged by increased ablation rate above 5 percent at a constant pressure and was found to increase as the post shock pressure was increased at a constant ablation rate.

The radiative cooling parameter was found to correlate shock layer radiative heating for no ablation and formed the basis of a simplified calculation which was used to obtain stagnation line heating rates. Sufficient graphical information is given from this

method to permit hand calculations of radiative heating rates for hyperbolic entry conditions. The use of the radiative cooling parameter was successfully extended to calculate heating rate distributions around a bluff vehicle. No corresponding simple correlation for radiative heating with ablation was found.

The effects of stagnation line shock wave bluntness on the surface heating was studied for both the stagnation line and around the body. In order to assess the effects of initial shock curvature, numerical methods for calculating the shock location around the body were investigated and a method is recommended. The results indicate that this initial curvature significantly influences the shock stand-off distance and the surface heating rate.

The unique contributions of this entry analysis are that all major processes have been included in one definitive analysis, that improvements in specific processes have been made where appropriate, and that simplified models for specific processes have been developed and used where they do not compromise the results.

Our knowledge is the amassed
thought and experience of
innumerable minds.
Emerson - Letters and
Social Aims

CHAPTER I

INTRODUCTION

BACKGROUND

Man is basically curious about his surroundings. The Apollo 11 landing of man on the moon in 1969 has in a concrete way increased man's surroundings to include the solar system. This basic curiosity is sufficient itself to assure that there will be manned planetary missions. The main scientific objectives for missions to the planets has been concisely stated by Findlay, 1968 chairman of the Lunar and Planetary Missions Board of NASA, (Ref. 1.1), "To learn more of the origin and history of the solar system and to explore the possibilities that life exist or has existed in other parts of that system". The physical realization of manned planetary exploration will require many technological advances. The goal of the research presented herein is to contribute to the advancement of one technological area which must be developed for a successful manned planetary mission.

Many of the technological developments required for a successful manned planetary mission were discussed and documented at the AIAA meeting on Technology for Manned Planetary Missions held in New Orleans in March 1968. Layton (Ref. 1.2) discussed the limitations of the presently used chemical rockets and the undeveloped potential of nuclear and electric rockets from the perspective of propulsion requirements. Improvements must be made in structural design and

synthesis (Ref. 1.3). Developments in hardware, software, man-machine integration and other sub areas of guidance and control technology are required (Ref. 1.4). The reliability and length of operation of present life support systems must be increased (Ref. 1.5). Advanced communications hardware must be developed to accomodate high data rates transmitted from interplanetary distances (Ref. 1.6). The technologies for man-machine integration and experimental design among others must be developed. Furthermore, planetary entry and landing technology must be improved (Ref. 1.7). The vehicle heating aspect of planetary entry is the technological area of concern of the present research.

The technology which must be developed for a successful manned earth entry from interplanetary travel is dictated by the type of interplanetary trajectory, atmospheric braking trajectory and vehicle shape used. These trajectories determine the type of thermal environment, which in turn, determines the type and amount of heat shielding required to adequately protect the entry vehicles.

Interplanetary trajectories are primarily determined by minimum energy and transit time constraints. For a manned mission to Mars two types of interplanetary trajectories are under consideration. These trajectories consist of either a direct flight to Mars or a Venus swing-by as illustrated in Fig. 1.1 from Ref. 1.8. The swing-by mission has two major advantages. First, additional scientific information could be gained by a manned pass near Venus. Secondly, the entry velocity upon earth arrival is significantly reduced due

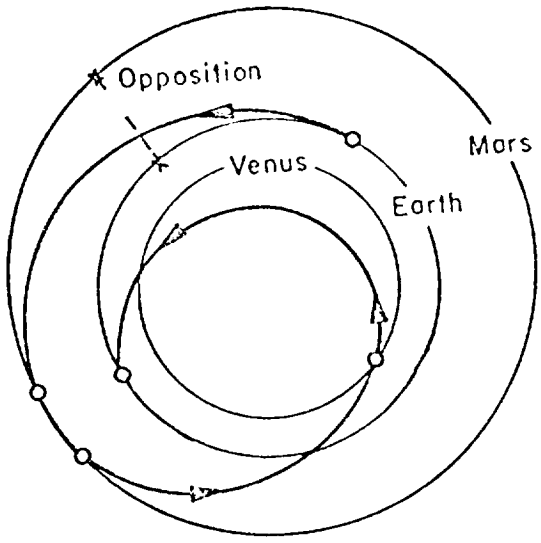

(b) Mars stopover
Inbound Venus swingby

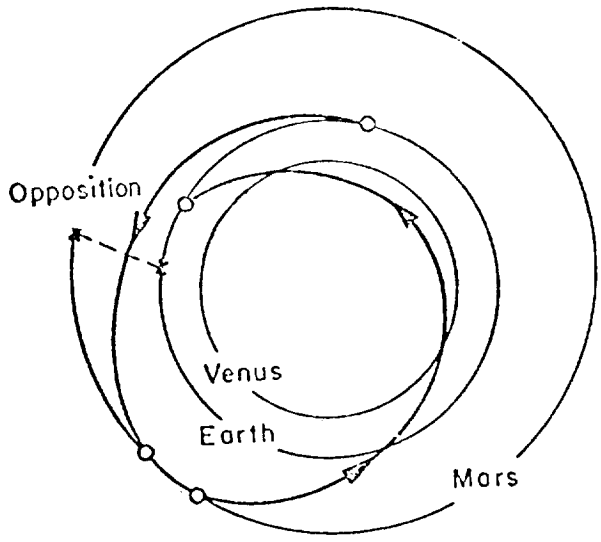

(c) Mars stopover - Direct

Fig. 1.1 Representive Mars Missions (From Ref. 1.8)

to the encounter with the gravitational field of Venus. This is illustrated in Fig. 1.2 from Ref. 1.7 for missions during the 1980 to 1999 period. Earth entry speeds are displayed for both direct and Venus swing-by trajectories. The left edge of each bar in Fig. 1.2 indicates velocities for trajectories optimized assuming Mars atmospheric braking for capture while the right edge indicates velocities for trajectories optimized assuming propulsive braking. The resulting entry velocities for several planetary missions are presented in Fig. 1.3. It is noted from Fig. 1.3 that the earth entry velocity is between 11 and 19 km/sec for essentially all missions considered.

The earth arrival velocity from interplanetary trajectories provides initial conditions for earth atmospheric entry trajectories. These trajectories are limited by heating, aerodynamic and deceleration constraints. Due to human limitations a loading limit of nominally 10 g's (i.e. 10 times the earth gravitational force) is placed on the possible entry trajectories. For a direct entry this trajectory is called the undershoot boundary (Ref. 1.9). The aerodynamics of the entry vehicle, determined primarily by body shape and weight, establishes the size of the usable entry corridor. Furthermore, the body shape has a significant effect on the surface heating. Thus an optimum vehicle shape is a compromise between maximizing manuverability and minimizing the heat input to the vehicle.

The magnitude of the kinetic energy which is dissipated during atmospheric braking is proportional to the velocity squared. Since

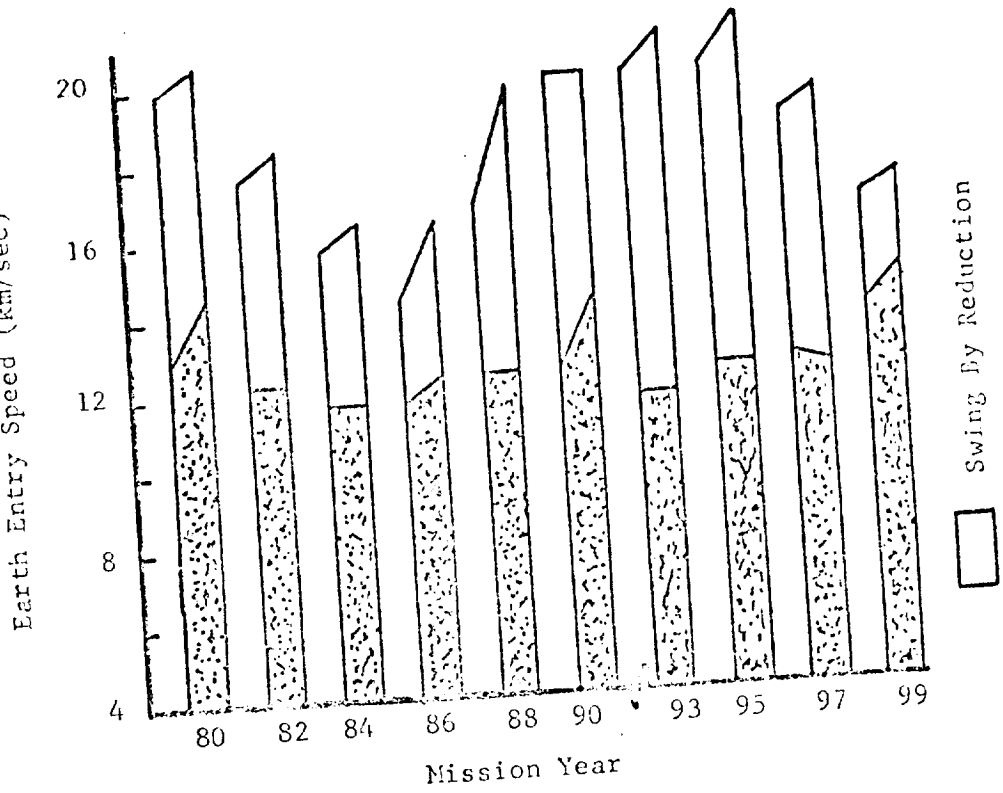

Fig. 1.2 Earth Entry Speeds for Mars Missions (From Ref. 1.7)

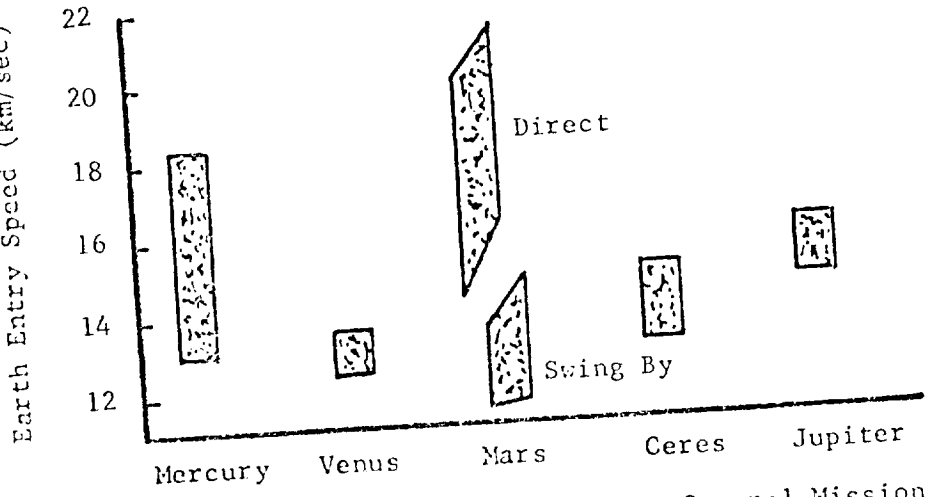

Fig. 1.3 Earth Entry Speeds for Several Mission Objectives (From Ref. 1.7)

the apparent velocity toward the vehicle is also volumetric flow rate per unit area of streamtube toward the vehicle, it follows that the energy flow per unit area, i.e. flux, toward the vehicle is proportional to the velocity cubed. From the typical entry velocities presented in Fig. 1.2 and 1.3 and noting that the Apollo lunar return velocity is approximately 11 km/sec it is evident that the amount of energy and energy flux is substantially higher for planetary return velocities. Such velocities, which are greater than the earth escape velocity, are called hyperbolic since interplanetary trajectory for kinetic energies of this magnitude result in hyperbolic shaped trajectories. The main concern, of course, is to determine the fraction of this kinetic energy which is transferred to the vehicle's surface during atmospheric deceleration.

The present capabilities of experimentally simulating the flight conditions anticipated during hyperbolic entry is illustrated in Fig. 1.4. This figure shows that present facilities are not capable of simultaneously producing both high enthalpy and flow energies. The problem of building a test facility which provides the required energy flux and enthalpy is a major one (Ref. 1.7). Alternately, free-flight model experiments could be performed, but such experiments are very expensive and difficult to scale. Hence, our knowledge would not be rapidly increased even if the high cost were accepted (Ref. 1.10). These are the reasons why there has been and will continue to be a considerable reliance placed upon analytical techniques to predict atmospheric entry heating and the resulting surface material response.

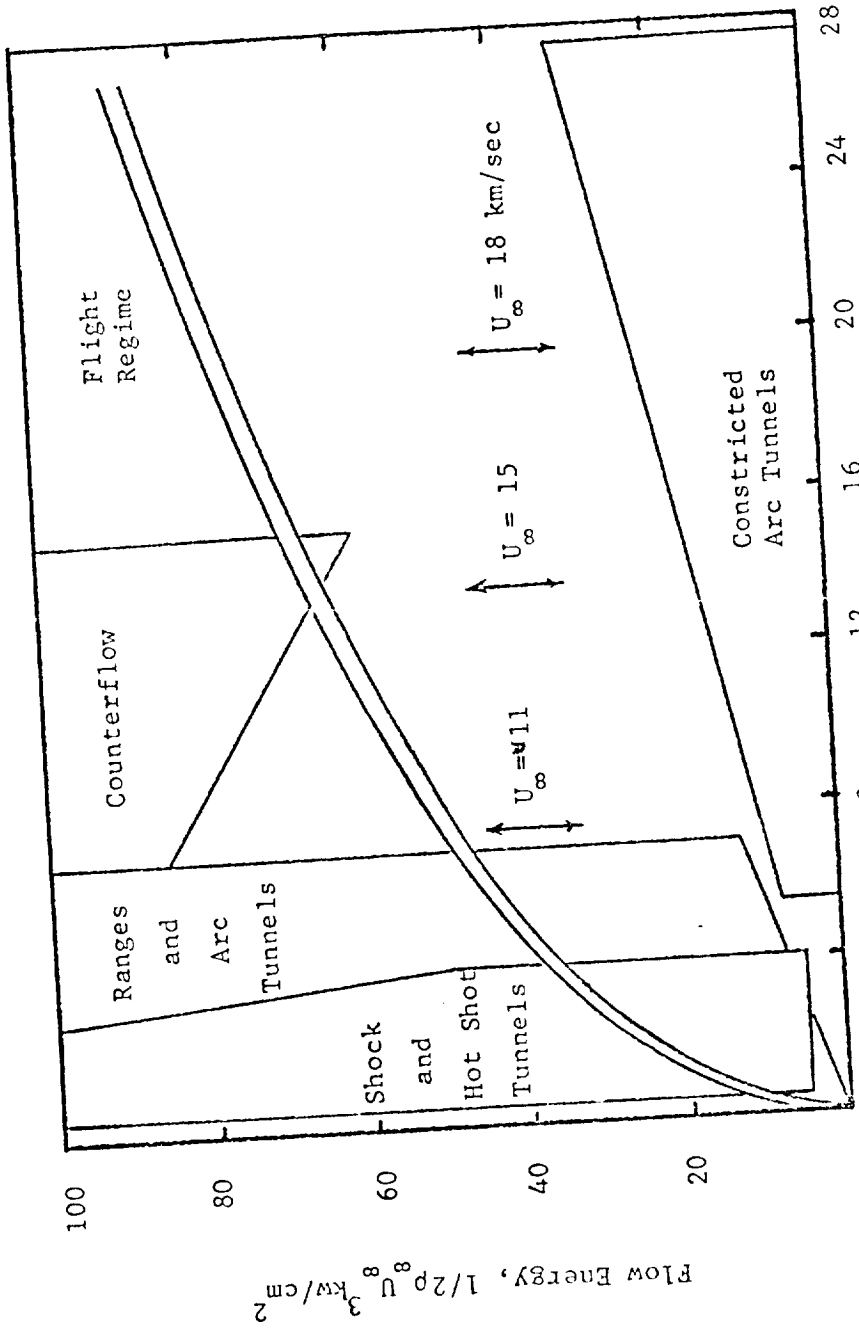

Fig. 1.4 Typical Facility Capabilities for Flow Energy (from Syvertson, Ref. 1.7)

THE VISCOUS HYPERSONIC SHOCK LAYER PROBLEM

In this work the interaction of the stagnation region flow-field and an ablative protection system of vehicles which experience a hyperbolic atmospheric encounter is analyzed. The analysis is aimed at resolving major uncertainties in the current state of knowledge by systematically examining the effects of radiation, viscous coupling and ablator coupling. These effects are measured in terms of the heating rate to the ablator surface.

The processes which govern the heat transfer rate to a blunt vehicle in a hypersonic flow are, for the most part, contained in a layer adjacent to the vehicle. This shock layer formed by a blunt body in a hypersonic stream is shown in Fig. 1.5. The radiating shock layer (white region) is the thinnest in the nose region where the highest heating rates are experienced. For protection from the high heating rates encountered during entry an ablator will be used. An ablator is a surface material which absorbs heating loads by changing phase and mass loss thus reducing the transmission by conduction to the interior of the protected material. In terms of weight efficiency for entry deceleration an ablator protection system requires 10 to 50 times less entry vehicle weight than would be required by either nuclear or chemical propulsive system (Ref. 1.11). Vehicle weight minimization is quite important since one pound of re-entry spacecraft weight requires approximately 300 to 1000 pounds of launch vehicle weight (Ref. 1.11). Many types of ablative materials are available which could be used for vehicle

Fig. 1.5 (Next page this location)
Photograph of a blunt body in a multiple arc jet wind tunnel showing the ionized shock layer about the body. (Mach no. ≈ 7)
Courtesy of: T. A. Barr, Jr., U. S. Army Missile Command, Redstone Arsenal, Alabama, 1969.

Fig. 1.6 (Next page this location)
Photograph of a cross section of a phenolic-nylon ablator. Courtesy of: C. W. Stroud, NASA TN D-4817, 1968.

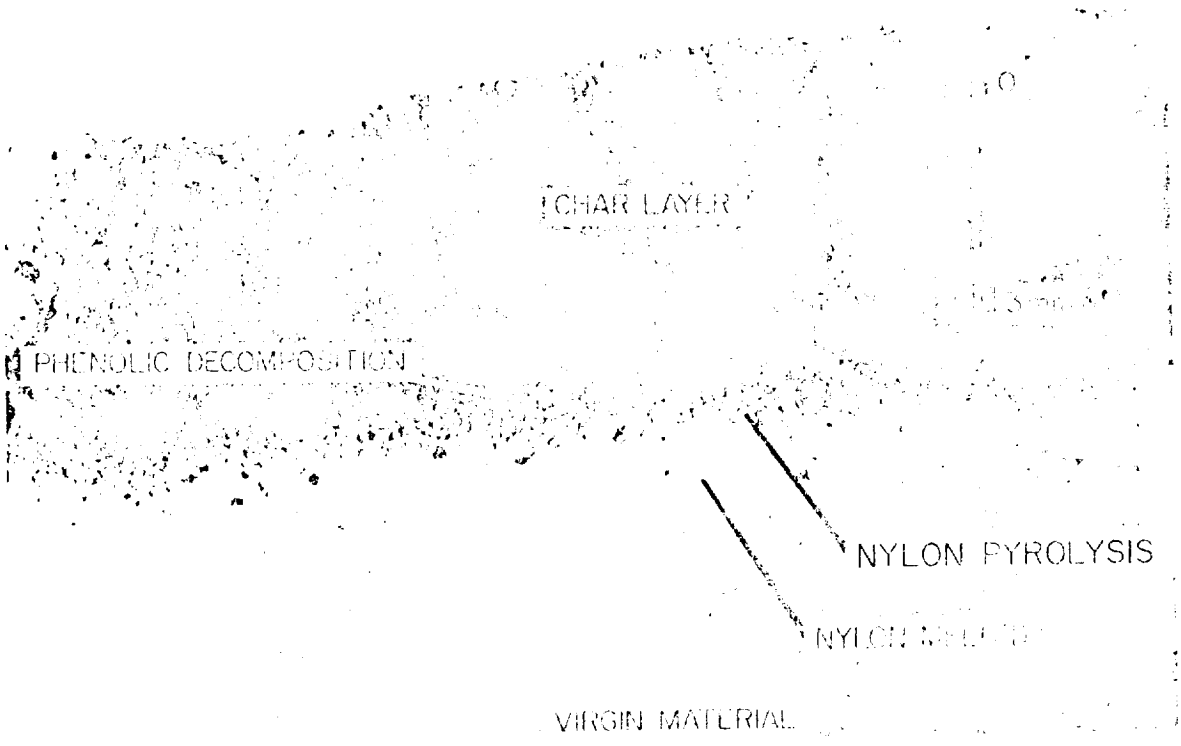
CHAR LAYER
PHENOLIC DECOMPOSITION
NYLON PYROLYSIS
VIRGIN MATERIAL

protection. Typical of the better materials is the charring phenolic-nylon ablator (Ref. 1.12). Fig. 1.6 presents a photograph of a cross-section of a phenolic-nylon ablative composite which has been exposed to a severe heating environment and which decomposed to a char of porous carbon and low molecular weight gases. This type of ablator protects the vehicle not only by subliming the char, but also by acting as a heat sink, by transpiring high energy gases which reduce convective heating, by reradiating from the char surface, by reacting exothermically and by blocking radiation from the shock layer. These ablator processes are intimately coupled with the shock layer processes. Thus to determine the amount and type of ablator to use for entry protection a quantitative understanding of both the shock layer and ablator response is needed.

The major mode of energy transfer to the surface for entry velocities above 11 km/sec is by radiation as illustrated in Figure 1.7. This figure shows that, for typical flight conditions of interest, the convective heat transfer coefficient is essentially independent of velocity whereas the radiative coefficient increases rapidly dwarfing the convective coefficient for the higher velocities. The principle reason for the high radiative transfer is the elevated temperatures experienced in the shock layer (i.e., on the order of 15000^{o}K) for typical flight conditions.

Figure 1.8 presents a schematic of the important regions in a ablation coupled shock layer. The outer region of the shock layer primarily consists of high temperature radiating air which was heated

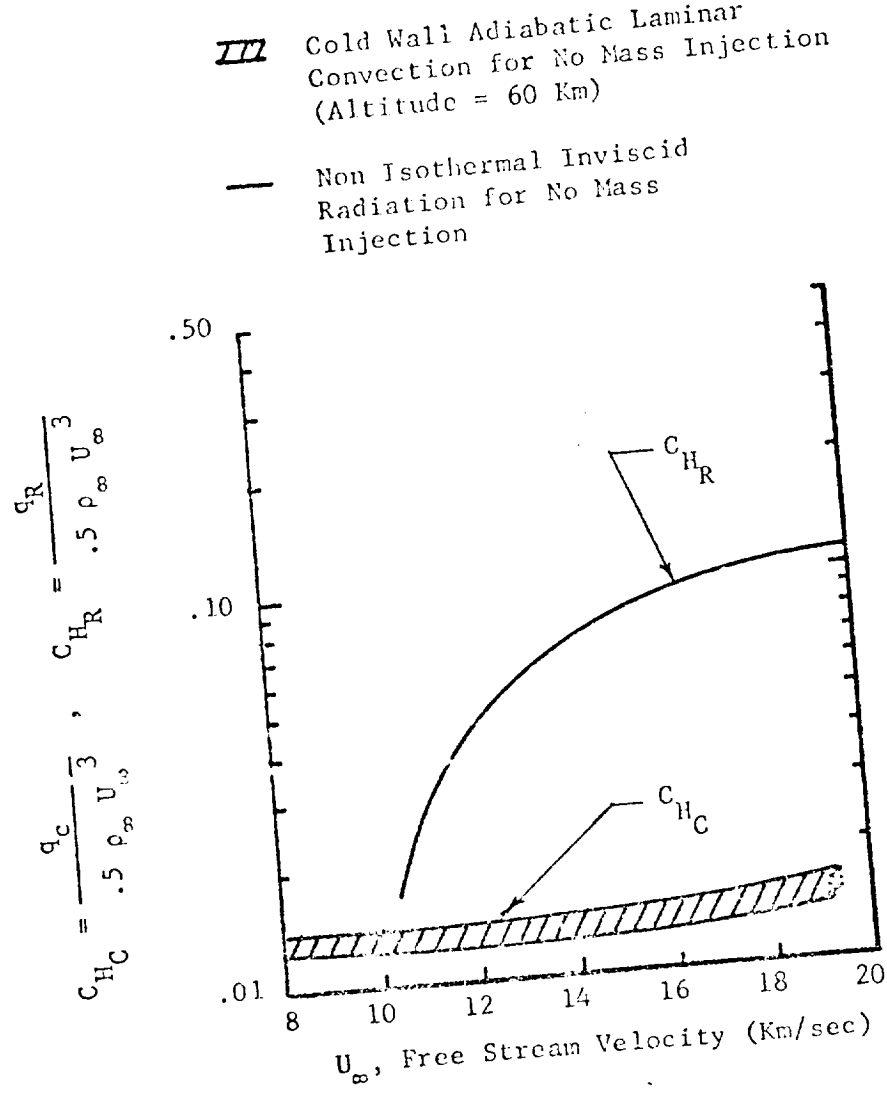

Fig. 1.7 Effect of Free Stream Velocity on Heat Transfer Coefficients, δ = 10 cm, P_δ = 1.0 atm (From Ref. 1.13)

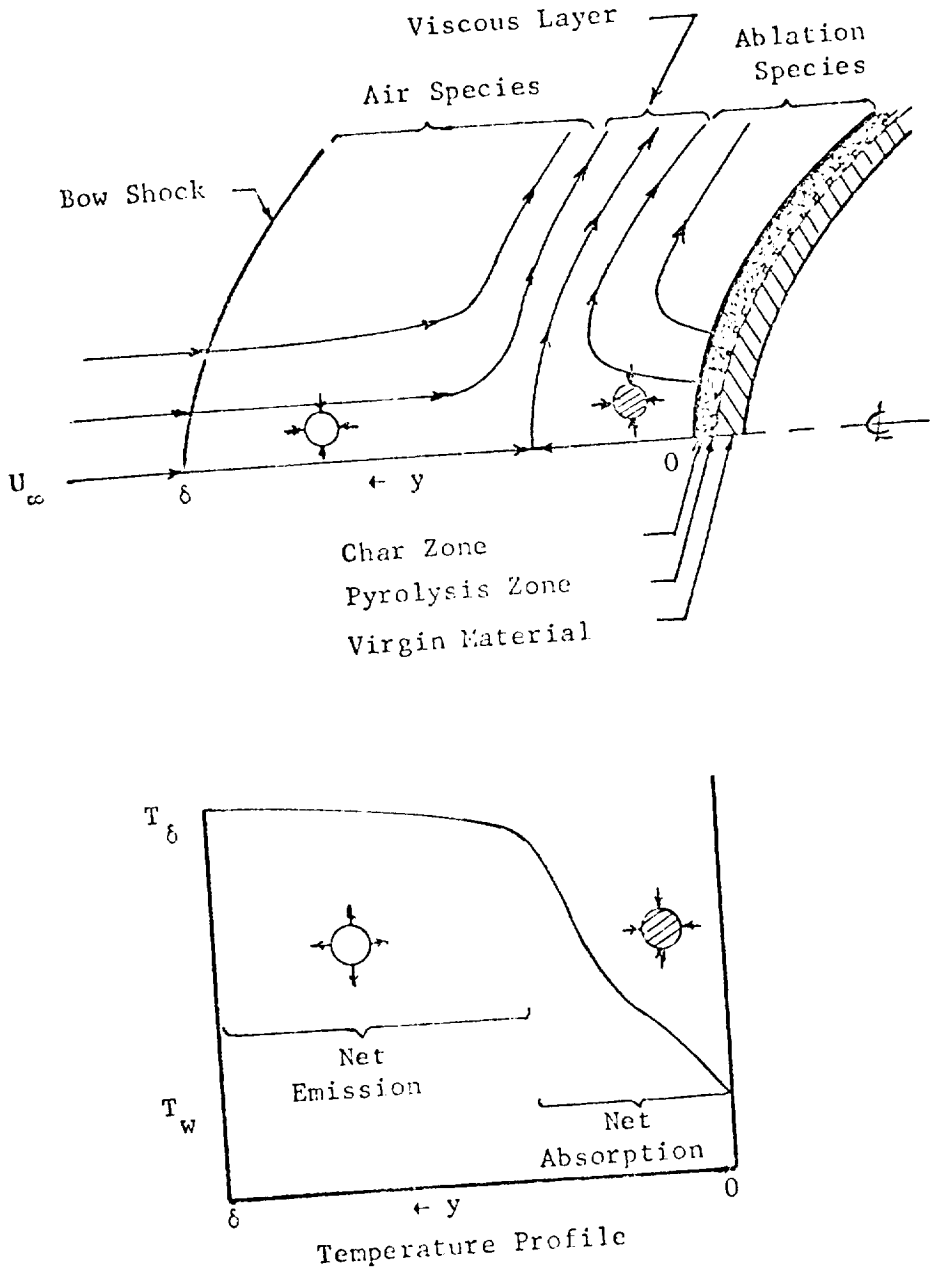

Fig. 1.8 Schematic of Various Regions in An Ablator Coupled Shock Layer

by the preceeding bow shock wave. Some of the radiation is emitted directly away from the body and, if not absorbed is lost through the shock wave. The radiation loss reduces the temperature in the shock layer and thus reduces the radiative flux. This description excludes the consideration of radiation absorption by the free-stream gas called precursor radiation. Further, the radiation emitted from the hot air region is partially absorbed by the cooler air and ablation species and the remainder is absorbed by the ablator surface. Some of this energy to the surface is reradiated into the shock layer and the remainder is absorbed by the ablator surface. For large ablation rates (i.e. 20% of the free-stream flow rate) the region near the body as well as the near shock region is inviscid. The convective heating rate is much smaller than indicated in Fig. 1.7. A viscous region exists between these two inviscid regions in which several important processes occur. In the viscous region energy is transferred by viscous dissipation and gaseous conduction in addition to radiation. Moreover, species concentrations change quite rapidly due to diffusion and the large temperature change in the viscous region. The schematic in Fig. 1.8 is for a case of large ablation rates; however as the ablation rate is lowered the viscous region becomes attached to the surface. In this situation convective heating to the surface becomes a more significant heat transfer mode to the ablator. Furthermore, the effects of air species diffusing to the surface and a consequential inhomogenuous surface reaction become probable. In addition to these processes, it is noted that as a particle flows away from the axis of symmetry (i.e. the

stagnation line) it is accelerated, its temperature is reduced and the pressure decreases. Consequently the heating rate to the surface decreases.

The region near the stagnation line experiences the most severe environment and thus is the most critical region in a design analysis. Fortunately, the conservation laws which describe the stagnation line region are more simple than those which describe the entire shock layer. Therefore, their solution provides a succinct and conservative characterization of the entire shock layer for a given set of flight conditions. Numerous researchers have mathematically modeled the near stagnation region processes in various degrees of completeness during the past ten to fifteen years. Recently three review papers (Ref. 1.7, 1.14, and 1.15) have been published which discuss the profuse amount of work which has been done. Consequently only some of the most current work which is pertinent to this research will be reviewed.

Several recent papers (Ref. 1.15, 1.16, and 1.17) present solutions to the blunt body flow problem which include line and continuum air radiation coupling and assume the entire shock layer is inviscid. Page et. al. (Ref. 1.13) present stagnation point radiative and convective heating rates for various shock layer pressures and thicknesses. The effects of ablation products are not included. Olstad (Ref. 1.16) calculated radiative heating rate distributions using an inverse method (i.e. specifying the shock shape and computing the body shape); this method describes non-stagnation line regions only. The shock layer was assumed to

consist of an inviscid air and inviscid ablation layer, although air properties were used in the ablation layer. The radiation model used included line and continuum mechanisms and was coupled to the flow field solution. Chin (Ref. 1.16) assumed the stagnation line shock layer flow could be divided into a inviscid air and an inviscid ablation layer. Computationally each of these layers were divided into six sublayers. The coupled radiative heating rates were computed with a model which contained line and continuum mechanisms of air and ablation products. A carbon-phenolic ablator was coupled to the flow-field analysis by assuming equilibrium sublimation.

In order to determine the shock layer processes more precisely, many researchers (Ref. 1.18 to 1.24) have included viscous effects in their flow-field models. Wilson (Ref. 1.18) reported stagnation line solutions of fully coupled viscous, radiating shock layers including specified ablation injection. The momentum equation was solved by finite differences using two methods. One method is valid for small mass injection rates whereas the second is valid for large rates. The effect of radiation blocking by carbon-phenolic ablation products was studied. Shock layer elemental compositions were determined using a single species equation for ablation products diffusing into air. The radiation model used contained line and continuum radiative mechanisms for C, H, O and N atoms. A limited number of solutions were presented. Rigdon et. al. (Ref. 1.19) presented several viscous, radiation coupled stagnation line solutions which included cases for specified carbon phenolic ablation rates.

The viscous stagnation line momentum equation was solved using an initial value technique which was started at the stagnation point. The integration was then carried out toward the body and toward the shock. The radiative model used included line and continuum mechanisms of air and ablator species. A species equation was solved using an effective binary diffusion coefficient for diffusion of air into ablation products. The effects of precursor radiation were examined. Smith et. al. (Ref. 1.20) reported solutions for a quasi-steady response of a phenolic-nylon ablator to a flow-field solution which was broken into two regions. The outer air region was analyzed as an inviscid region using a one strip integral method. The inner ablation layer was analyzed using two techniques. For small ablation rates a boundary layer solution was used; whereas for large ablation rates an integral method was used. No radiation coupling between air and ablation layer was considered. The radiation model used included various line and continuum mechanisms for atoms, ions and molecules excluding line mechanisms for C and H atoms. Heating rates for the stagnation point and around the body along a trajectory were presented. Engel and Spradley (Ref. 1.21) presented stagnation point radiative heating rates for a typical hyperbolic entry trajectories using a radiation model which contained only continuum mechanisms of air. The viscous momentum equation was solved using the integral technique of Hoshizaki et. al. (Ref. 1.21) which is limited to low ablation rates. The ablator response and resulting estimated heat shield weights were computed using the calculated cold wall heating rates in an uncoupled manner.

Other viscous analyses which endeavor to define the effects of finite rate chemistry and multicomponent diffusion in the shock layer, have not included radiation (Ref. 1.23 to 1.26). Adams et. al. (Ref. 1.23) present results for chemical nonequilibrium inviscid and laminar viscous flow over spherically blunted cone geometries. The calculations were made for flight velocities and altitudes where radiative transport is negligible. The chemistry was restricted to air species and injected species of argon, helium or carbon dioxide. Multicomponent diffusion was discussed; however no results were presented. For the cases studies the influence of a noncatalytic wall with mass injection significantly reduced the convective heat transfer. Davy et. al. (Ref. 1.24) presented solutions of the multicomponent, reacting, stagnation-point boundary layer with chemical equilibrium. A comparison with binary solutions was given. A nitrogen or air external stream with injection of hydrogen or a mixture of hydrogen and argon were the chemical systems studied. The results presented indicate that the H_2 and H species compositions computed with multicomponent diffusion were the only species that significantly deviated from their binary solution. Liu (Ref. 1.24) studied the finite rate chemistry effects in injecting hydrogen into air at an axisymmetric stagnation point. The hydrogen-air chemistry system was restricted to low stagnation temperatures where ionization does not occur. Liu demonstrated the difficulties associated with the chemistry of these flows but did not propose a general solution. Blottner (Ref. 1.26) investigated a finite-difference method and a nonlinear overrelaxation method for solving

the stagnation line viscous blunt body problem. A seven species air model was used to study nonequilibrium chemistry effects. Results were presented for flight conditions where radiative transfer is not important. Numerical studies indicated that the finite difference procedure converged more rapidly than the nonlinear overrelaxation method.

The studies reviewed represent the best currently available. Unfortunately no single analysis includes all of the important effects of radiation and ablator coupling although many of the analyses adequately account for certain shock layer processes. The inviscid analyses lack the generality of being applicable to small ablation rates. With the exception of Chin (Ref. 1.16) the inviscid analyses have not adequately accounted for ablation product effects in the shock layer. Unfortunately Chin's results do not include all of the important line radiation mechanisms. The viscous analyses, which are by and large the best, are limited by either numerical difficulties or computation time in addition to incomplete radiation, flow-field or ablation models. The main limitations of Wilson's (Ref. 1.18) analysis are the lack of molecular radiation and numerical difficulties with the momentum equation. The analysis of Rigdon et. al. (Ref. 1.19) includes the most detailed radiation model which unfortunately consumes excessive computation time and this analysis has not been used to study ablator coupling. The other viscous analyses reviewed do not include as many important ablator-shock layer processes as the two just discussed. The third group of

papers reviewed did not include radiation transport effects which is the main heating mode being studied. These papers are helpful in deciding how the particular processes examined might be handled numerically and in understanding the role that finite rate chemistry or multicomponent diffusion might play in the shock layer.

In summary, the studies reviewed are inadequate in varying degrees. Further, the analyses which are complete enough to define some shock layer processes have not been used successfully to define many cause and effect relationships. Consequently many questions remain unresolved. The most important of these questions are:

1. Under what conditions, if any, can the shock layer be treated as inviscid?
2. Is molecular radiation important and if so what molecules contribute?
3. How effective is ablation in reducing the heating rate to the surface?
4. What are the ablation rates which correspond to the estimated shock layer heating for various flight conditions?
5. What is the error introduced into analyses by assumptions made in the flow-field model? For example, shock shapes.
6. Can the shock layer heating process be correlated in a simple manner with any shock layer parameters?

In addition to the uncertainties remaining in current heating analyses, there is a significant uncertainty in the basic data used in these analyses. Several major areas where basic data is not precisely known are:

1. Gaseous radiation data
2. Surface emissivities

3. Sublimation temperatures

4. High temperature transport properties

Using the 1968 state of the art as a basis, the estimated heat shield weight would account for 12 to 24 percent of the total vehicle weight for a 50,000 ft/sec entry velocity trajectory (Ref. 1.27). The 12 percent range of uncertainty in the total weight is due directly to uncertainties associated with defining the flow-field and ablator behavior for various vehicle shapes. A detailed study of uncertainties due to incomplete analyses and a discussion of the effects of uncertainties in available data were made in an attempt to reduce them. This document describes this study.

PRESENT RESEARCH OBJECTIVES

The overall objective of this research is to develop the capability to accurately predict the performance of ablative thermal protection systems when exposed to aero-thermal environments such as those encountered by planetary atmospheric probes and return vehicles from interplanetary missions. Emphasis is placed on diminishing some of the uncertainties presently existing in ablative thermal protection design. Specific research objectives are:

1. Investigate the interaction of the stagnation region and around the body flow-field and ablation protection system.

   (a) Develop the governing equations from a general property balance and systematically point out the assumptions made in obtaining the equations to be solved.

(b) Describe mathematically the various levels of approximation which may be introduced into the equations describing the shock layer flow.

2. Calculate the stagnation flow-field with the use of a radiation transport model which does not impair the accuracy of the best available radiation property data. Emphasis is placed on making the resulting program an engineering tool.

   (a) Develop a numerical method to solve the momentum equation which is stable and equally valid for large and small ablation rates.

   (b) Determine a procedure for evaluating the relative contribution of molecular species radiation and include the ones necessary for an accurate radiation calculation.

   (c) Examine numerical simplications for the species equation.

3. Perform parametric studies on entry velocities, altitudes and vehicle shapes, and then determine if a more simple empirical model could be used to represent the results of these detailed calculations.

   (a) Examine the effects of ablation at various rates to determine cause and effect relations.

   (b) Obtain coupled ablator-shock layer solutions for various flight conditions.

   (c) Examine parametrically the effects of stagnation line shock bluntness on surface heating rates.

   (d) Determine the importance of molecular species radiation in effecting the surface heating rate.

In general, the research reported in this dissertation is a study of the uncertainties which exists in entry heating analyses. Furthermore, it is a definitive study of the thermal radiation which occurs during such entries.

CHAPTER I

References

1.1 Findlay, J. W., "The Objectives for Manned Planetary Missions," AIAA Technology for Manned Planetary Missions Meeting, Supplement, March 1968.

1.2 Layton, J. P., "Propulsion Technology for Manned Planetary Missions," AIAA Technology for Manned Planetary Missions Meeting, Supplement, March 1968.

1.3 Harris, L. A., "Structures for Manned Planetary Missions," AIAA Technology for Manned Planetary Missions Meeting, March 1968.

1.4 Duncan, R. C., R. J. Hayes, G. Kootch, "Guidance and Control for Manned Planetary Missions," AIAA Technology for Manned Planetary Missions Meeting, March 1968.

1.5 Mason, J. L., "Life Support for Manned Planetary Missions," AIAA Technology for Manned Planetary Missions Meeting, Supplement, March 1968.

1.6 Noda, M., "Hardware Aspects of Communications, Instrumentation and Data Handling for Manned Planetary Missions," AIAA Technology for Manned Planetary Missions Meeting, March 1968.

1.7 Syvertson, C. A., "Entry and Landing Requirements for Manned Planetary Missions," AIAA Technology for Manned Planetary Missions Meeting, March 1968.

1.8 Deerwester, J. M., "References System Characteristics for Manned Stopover Missions to Mars and Venus," NASA TN D-6226, March 1971.

1.9 Loh, W. H. T., Re-entry and Planetary Entry Physics and Technology, Ch. 1, Springer-Verlag, New York Inc., 1968.

1.10 Allen, H. J., "Hypersonic Aerodynamic Problems of the Future," in The High Temperature Aspects of Hypersonic Flow, ed. by W. C. Nelson (Pergament Press, MacMillian Co., New York, N.Y.), 1964.

1.11 Eggers, A. J. and N. B. Cohen, "Progress and Problems in Atmospheric Entry," Proceedings of the XVIth International Aero. Congress, Gauthier - Villars, Paris, 1965.

1.12 Stroud, C. W., "A Study of the Reaction - Plane Approximation in Ablation Analysis," NASA TN D-4817, Oct. 1968.

1.13 Page, W. A., D. L. Compton, W. J. Borucki, D. L. Ciffone and D. M. Cooper, "Radiative Transport in Inviscid Non-adiabatic Stagnation-Region Shock Layers," AIAA 3rd Thermophysic Conference, paper no 68-784, June 1968.

1.14 Blottner, F. G., "Finite Difference Methods of Solution of Boundary-Layer Equations," AIAA J., Vol. 8, No. 2, Feb. 1970.

1.15 Anderson, J. D. Jr., "An Engineering Survey of Radiating Shock Layers," AIAA J. 7, No. 9, Sept. 1969.

1.16 Olstad, W. B., "Nongray Radiating Flow about Smooth Symmetric Bodies," AIAA J., 9, No. 1, Jan. 1971.

1.17 Chin, J. H., "Radiation Transport for Stagnation Flows Including Effects of Lines and Ablation Layer," AIAA J., 7, No. 7, July 1969.

1.18 Wilson, K. H., "Stagnation Point Analysis of Coupled Viscous-Radiation Flow With Massive Blowing," NASA CR-1548, June 1970.

1.19 Rigdon, W. S., R. S. Dirling Jr., and M. Thomas, "Stagnation Point Heating During Hypervelocity Atmospheric Entry," NASA CR-1462, Feb. 1970.

1.20 Smith, G. L., J. T. Suttles, and E. M. Sullivan, "Viscous Radiating Flow-Field on an Ablating Blunt Body," AIAA Paper No. 70-218, Jan. 1970.

1.21 Engel, C. D. and L. W. Spradley, "Radiation Absorption Effects on Heating Loads Encountered During Hyperbolic Entry," JSR, Vol. 6, No. 6, 1969.

1.22 Hoshizakii, H. and K. H. Wilson, "Convective and Radiative Heat Transfer during Superorbital Entry," AIAA J, 5, No. 1, Jan. 1967.

1.23 Adams, J. G., C. H. Lewis, H. S. Brahensky, et. al, "Nonequilibrium, Mass Transfer, and Viscous Interaction on Spherically Blunted Cones at Hypersonic Conditions," AEDC-TR-69-237, Arnold Engineering Development Center, Jan. 1970.

1.24 Davy, W. C., R. A. Craig, and G. C. Lyle, "An Evaluation of Approximations Used in the Analysis of Chemically Reacting, Stagnation-Point Boundary Layers with Wall Injection," Proc. 1970 Heat Trans. and Fluid Mech. Ins., ed. by Sarpkaya, Stanford University Press, 1970.

1.25 Liu, Tsong-mou, "Hydrogen Injected Into Air at an Axisymmetric Stagnation Point," Ph.D. Dissertation, Univ. of California, San Diego, 1970.

1.26 Blottner, F. G., "Viscous Shock Layer at the Stagnation Point with Nonequilibrium Chemistry," AIAA J., 7, No. 12, Dec. 1969.

1.27 Coleman, W. D., L. F. Hearne, J. M. Lefferdo, and N. S. Vojvadich, "A Study of the Effects of Environmental and Ablator Performance Uncertainties on Heat Shielding Requirements for Blunt and Slender Hyperbolic-Entry Vehicles," AIAA Paper No. 68-154, Jan. 1968.

CHAPTER 2

DEVELOPMENT OF GOVERNING EQUATIONS

As with most physical problems, the flow about a blunt body entering the earth's atmosphere obeys the conservation laws of mass, momentum and energy. The equations representing these laws for a multicomponent, radiating, chemically reacting fluid in an inertial reference system are derived using a general property balance approach in Appendix A. Following the derivation, the conservation equations are written in time independent vector form from which they are written in general orthogonal coordinates. In the third section of Appendix A the conservation equations are written in orthogonal body oriented coordinates for application to the blunt body flow problem. In this chapter these equations are simplified using physical arguments and order of magnitude assessments. Care is taken to indicate the approximations made throughout the development.

THIN VISCOUS SHOCK LAYER EQUATIONS

In order to determine the proper mathematical model to describe the flow-field developed by a blunt body moving at hypersonic velocities, one must assess the behavior of the gas that the vehicle will encounter. Fig. 2.1 based on the work of Ref. 2.1 presents the flight regimes which are encountered by a body during atmospheric entry. The regimes can be grouped into two gasdynamic domains - continuum and noncontinuum. Hayes and Probstein, Ref. 2.2, demonstrate the continuum domain can be divided into five regimes:

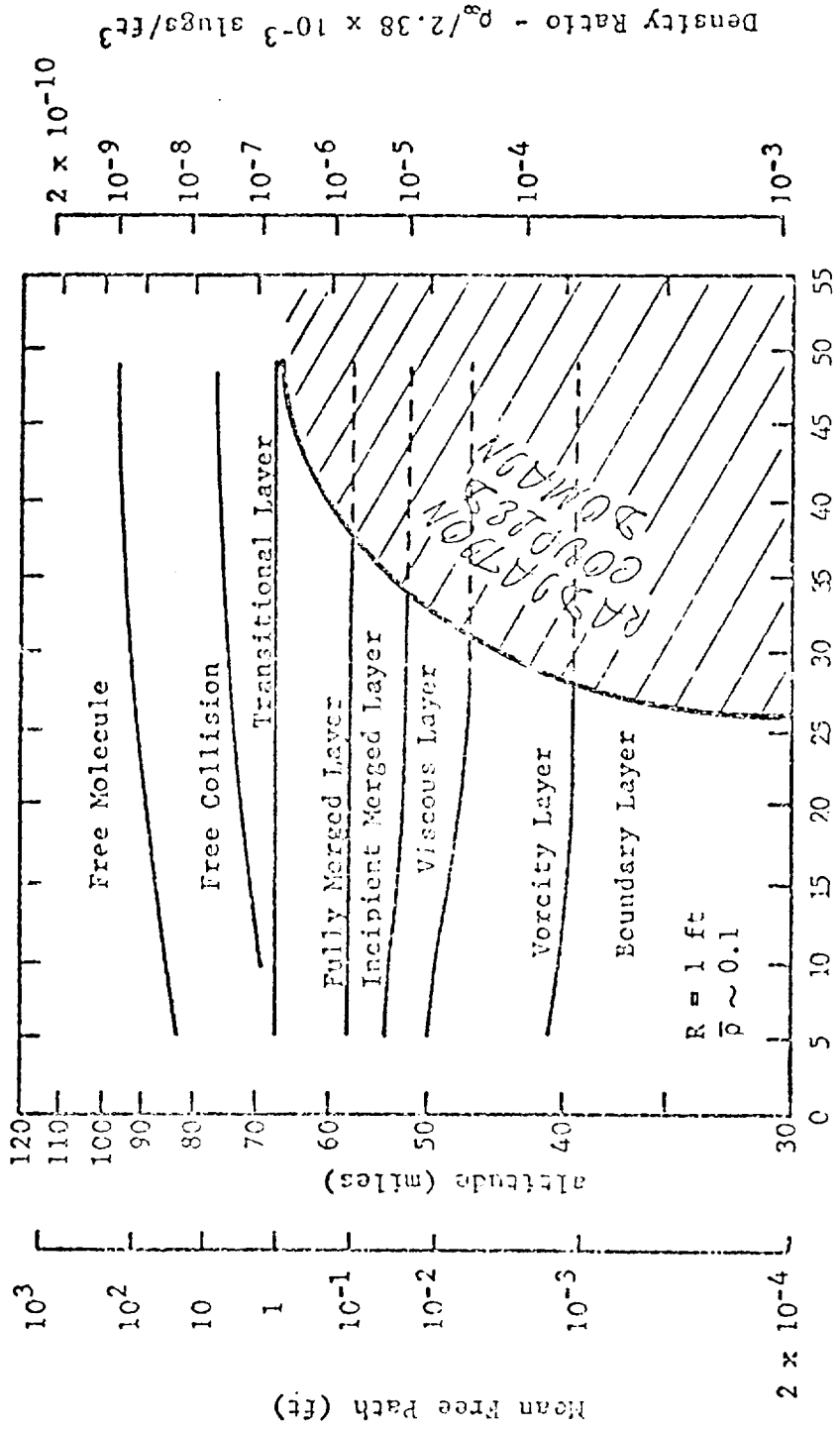

Fig. 2.1 Flight Regimes (Based on Ref. 2.1 and Modified From Ref. 2.27)

(1) classical boundary layer, (2) vorticity interaction, (3) fully viscous, (4) incipient merged layer, and (5) fully merged layer. The behavior of the gas flowing over a body in the five continuum regimes can be described using the equations developed in Appendix A. Let us consider further the characteristics of fluid flow in the five continuum regimes.

1. Boundary layer regime: The classical boundary layer equations are a valid approximation of the viscous effects for high Reynolds numbers corresponding to lower altitudes. Viscous effects dominate near the wall in a region which is small compared to the shock layer thickness. Vorticity generated by shock curvature is therefore negligible thus not affecting the boundary layer flow.
2. Vorticity interaction becomes important at lower Reynolds numbers where shock generated vorticity becomes significant in respect to viscous effects near the body. Here the outer region of the shock layer, usually considered the inviscid layer, becomes coupled through momentum transport to the higher shear region near the body, usually thought of as the boundary layer. The high shear region near the body is also larger than that experienced at higher Reynolds numbers.
3. Viscous layer Regime: Viscous effects from the body interaction are spread throughout the shock layer (i.e., the boundary layer and shock layer thicknesses are of the same order). This occurs at lower Reynolds numbers and

correspondingly higher altitudes than does the vorticity interaction regime. Viscous dissipation at the shock is still small in comparison to dissipation at the body. This condition is true so long as the ratio of the mean free path behind the shock over the shock layer thickness is much smaller than the square root of the density ratio across the shock wave, Ref. 2.2. This implies that the Rankine-Hugoniot shock wave equations are valid for determination of shock layer boundary conditions.

4. Incipient merged layer regime: The incipient merged layer begins when dissipative effects at the shock are significant. The shock wave is thin relative to the shock layer thickness but the Rankine-Hugoniot relations must be modified to account for viscous effects at the shock boundary.

5. Fully merged layer regime: At higher altitudes and low Reynolds numbers a distinct shock does not exist. The free stream mean free path over the major body radius is approximately one or less. The flow behaves continuously from the free stream to the body. Above this altitude range continuum concepts are no longer applicable and the flow goes through a transition to free molecular flow.

The foregoing discussion of the five continuum flow regimes follows in part the reasoning of Hayes and Probstein, Ref. 2.2. This reasoning was based upon the assumption that radiative energy transport and ablative mass injection were negligible. In the present

development these two effects are the primary flow field-body interaction mechanisms which are to be assessed. Fig. 2.1 shows the flight regimes where radiative heating to a one foot spherical body becomes significant. For the most part, significant ablation rates are also encountered in these regimes when using present day charring ablators such as carbon phenolic or phenolic nylon. Therefore, let us make additional observations about the flow characteristics in these continuum flight regimes where the effects of ablation and radiative energy transfer in the shock layer are important. In proceeding, our attention will be restricted to the first three flight regimes, where the heating rates to a vehicle's surface are the most significant.

Significant radiative energy transfer has several important effects on the shock layer behavior. First, radiative transfer couples the energy equation and thus the thermal boundary layer over the entire shock layer. This is apparent by recalling that the flux divergence term in the energy equation is evaluated by an integration over all space in the shock layer. This effect has been demonstrated by several authors including Ref. 2.3 and 2.4. Further, the thermal boundary layer exists from the shock to the body for all three flight regimes in the radiative coupled domain. Secondly, radiative energy transfer produces nonadiabatic or energy loss effects. Principally, radiant energy is lost through the transparent shock wave. Thirdly, the effect of radiative transfer in the shock wave is coupled through the energy equation to the momentum equation. Although this coupling effect is not altogether negligible, it does not change the conclusions

obtained about momentum transfer in the shock layer in the first three flight regimes. Therefore, even though the viscous effects may be approximated through boundary layer concepts with possible modifications of edge conditions in the vorticity layer regime, the energy transport occurs over the entire shock layer. In the viscous layer regime both viscous and energy transport are significant over the entire shock layer.

Appreciable mass injection rates of ablation products results in additional effects on energy and momentum transfer within the shock layer. High mass addition rates tends to enlarge the region of shear dominated flow near the body. Libby, Ref. 2.5 showed experimentally and theoretically that in the boundary layer regime, boundary layer concepts could be applied when mass injection or suction rates were quite large. This study did not include the effects of radiation, but since energy transport does not change the character of momentum transport these conclusions are also valid insofar as momentum transfer is concerned for radiative coupled shock layers. Mass injection has other effects such as reduction of shear at the wall, Ref. 2.4, and reduction of heat transfer at the wall, Ref. 2.4, 2.5 and many others. These effects although of great importance do not change the basic characteristics of momentum or energy transfer in the shock layer.

We may conclude that for flight conditions in the radiative coupled domain where ablation rates are also significant, the character of the momentum transfer is essentially the same as without these

effects. However, the characteristics of energy transfer are significantly different in that the entire shock layer must be considered in all three flight regimes.

With the foregoing statements as background the problem which we wish to solve can be stated. The basic conservation equations stated in Appendix A are appropriate to describe the flow of a continuum reacting and radiating gas mixture over a blunted surface when thermodynamic equilibrium exists. For the present work, we will determine the reduced set of equations which describe the flow in a shock layer over a blunt body when the outer boundary of the shock layer is a shock wave described by the Rankine-Hugoniot equations. Thus the equations governing the flow in the shock layer will be applicable to the three higher Reynolds number regimes both in and out of the radiation coupled domain. The prime concern and motivation for obtaining this set of equations is to describe the heat transfer mechanisms which produce surface heating such that surface heating conditions can be predicted by numerical calculation.

Order of Magnatude Analyses

In order to determine the appropriate set of equations which realistically approximate the flow situation just described, an order of magnitude assessment of the terms in the basic conservative equations is needed. This is properly carried out by first nondimensionalizing the conservation equations. The following nondimensional variables are introduced.

$$\xi = \frac{x^*}{R^*} \qquad y = \frac{y^*}{R^*} \qquad u = \frac{u^*}{U_\infty^*} \qquad v = \frac{v^*}{U_\infty^*}$$

$$\rho = \frac{\rho^*}{\rho_{\infty,0}^*} \qquad \mu = \frac{\mu^*}{\mu_{s,0}^*} \qquad \lambda = \frac{\lambda^*}{\mu_{s,0}^*} \qquad \delta = \frac{\delta^*}{R^*}$$

$$r = \frac{r^*}{R^*} \qquad \kappa = \kappa^* R^* \qquad P = \frac{P^*}{\rho_\infty^*(U_\infty^*)^2} \qquad H = \frac{H^*}{H_s^*}$$

$$h = \frac{h_s^*}{H_s^*} \qquad h = \frac{h^*}{h_s^*} \quad \text{where} \quad H_s^* = \tfrac{1}{2}U_\infty^{*2} \tag{2.1}$$

$$\tilde{\kappa} = 1 + \kappa y \qquad \omega_i = \frac{R^*\omega_i^*}{\rho_\infty^* U_\infty^*} \qquad J_i = \frac{J_i^*}{\rho_\infty^* U_\infty^*} \qquad \Lambda_{R,x} = \frac{\Lambda_{R,x}^*}{\rho_\infty^*(U_\infty^*)^3}$$

$$\Lambda_{R,y} = \frac{\Lambda_{R,y}^*}{\rho_\infty^*(U_\infty^*)^3} \qquad \Lambda_{D,x} = \frac{\Lambda_{D,x}^*}{\rho_\infty^*(U_\infty^*)^3} \qquad \Lambda_{D,y} = \frac{\Lambda_{D,y}^*}{\rho_\infty^*(U_\infty^*)^3}$$

where

$$\Lambda_{R,x}^* = \frac{\partial}{\partial x^*}(r^{*A} q_{R,x}^*) \qquad \Lambda_{R,y}^* = \frac{\partial}{\partial y^*}(r^{*A\tilde{\kappa}} q_{R,y}^*)$$

$$\Lambda_{D,x}^* = \frac{\partial}{\partial x^*}(r^{*A} q_{D,x}^*) \qquad \Lambda_{D,y}^* = \frac{\partial}{\partial y^*}(r^{*A\tilde{\kappa}} q_{D,y}^*)$$

It should be noted that the equations in the Appendix A are in dimensional form. In this chapter a superscript * will denote dimensional variables unless it is explicitly stated otherwise.

The dimensional global continuity equation is:

$$\frac{\partial}{\partial x^*}(r^{*A}\rho^* u^*) + \frac{\partial}{\partial y^*}(\tilde{\kappa} r^{*A}\rho^* v^*) = 0 \tag{2.2}$$

Using the dimensionless variables stated in Eq. 2.1 the above equation may be written as

$$\rho_\infty^* U_\infty^* \frac{R^*}{R^*} \frac{\partial}{\partial \xi}(r^A \rho u) + \rho_\infty^* U_\infty^* \frac{R^*}{R^*} \frac{\partial}{\partial y}(\tilde{\kappa} r^A \rho v) = 0$$

Dividing by $\rho_\infty^* U_\infty^*$ yields the dimensionless form

$$\frac{\partial}{\partial \xi}(r^A \rho u) + \frac{\partial}{\partial y}(\tilde{\kappa} r^A \rho v) = 0 \tag{2.3}$$

From Eq. A.78 the dimensional species continuity equation is:

$$\frac{\partial}{\partial x^*}(r^{*A} \rho^* C_i u^*) + \frac{\partial}{\partial y^*}(\tilde{\kappa} r^{*A} \rho^* C_i v^*) = -\frac{\partial}{\partial x^*}(r^{*A} J^*_{i,x})$$

$$- \frac{\partial}{\partial y^*}(\tilde{\kappa} r^{*A} J^*_{i,y}) + \tilde{\kappa} r^{*A} \omega_i^* \tag{2.4}$$

Introducing dimensionless variables gives

$$\rho_\infty^* U_\infty^* \frac{R^*}{R^*} \left[\frac{\partial}{\partial \xi}(r^A \rho C_i u) + \frac{\partial}{\partial y}(\tilde{\kappa} r^A \rho C_i v) \right]$$

$$= -\rho_\infty^* U_\infty^* \frac{R^*}{R^*} \left[\frac{\partial}{\partial \xi}(r^A J_{i,x}) + \frac{\partial}{\partial y}(\tilde{\kappa} r^A J_{i,y}) \right] +$$

$$\rho_\infty^* U_\infty^* \frac{R^*}{R^*} \tilde{\kappa} r^A \omega_i$$

which yields

$$\frac{\partial}{\partial\xi}(r^{A}\rho C_i u) + \frac{\partial}{\partial y}(\tilde{\kappa} r^{A}\rho C_i v) = -\frac{\partial}{\partial\xi}(r^{A}J_{i,x})$$

$$-\frac{\partial}{\partial y}(\tilde{\kappa} r^{A}J_{i,y}) + \tilde{\kappa} r^{A}\omega_i \qquad (2.5)$$

Units of the terms in Eq. 2.5 are mass of specie i per mass of mixture.

Substituting Eqs. A.86, A.88 and A.89 into Eq. A.84 yields the dimensional x-momentum equation:

$$\rho^{*} r^{*A} u^{*} \frac{\partial u^{*}}{\partial x^{*}} + \rho^{*} \tilde{\kappa} r^{*A} v^{*} \frac{\partial u^{*}}{\partial y^{*}} + \rho^{*} \kappa^{*} r^{*A} u^{*} v^{*}$$

$$+ r^{*A} \frac{\partial P^{*}}{\partial x^{*}} - \frac{\partial}{\partial x^{*}}\left(r^{*A}\left[\frac{\lambda^{*}}{\tilde{\kappa} r^{*A}}\left\{\frac{\partial}{\partial x}(r^{*A}u^{*}) + \frac{\partial}{\partial y^{*}}(\tilde{\kappa} r^{*A}v^{*})\right\}\right.\right.$$

$$\left.\left. + \frac{2\mu^{*}}{\tilde{\kappa}}\left[\frac{\partial u^{*}}{\partial x^{*}} + \kappa^{*} v^{*}\right]\right]\right) - \frac{\partial}{\partial y^{*}}\left(\tilde{\kappa} r^{*A}\mu^{*}\left[\frac{1}{\tilde{\kappa}}\frac{\partial v^{*}}{\partial x^{*}} + \frac{\partial u^{*}}{\partial y^{*}}\right.\right.$$

$$\left.\left. - \frac{\kappa^{*}}{\tilde{\kappa}} u^{*}\right]\right) - \kappa^{*} r^{*A}\mu^{*}\left[\frac{1}{\tilde{\kappa}}\frac{\partial v^{*}}{\partial x^{*}} + \frac{\partial u^{*}}{\partial y^{*}} - \frac{\kappa^{*}}{\tilde{\kappa}} u^{*}\right] \qquad (2.6)$$

$$+ \frac{\lambda^{*}}{\tilde{\kappa} r^{*A}}\left[\frac{\partial}{\partial x^{*}}(r^{*A}u^{*}) + \frac{\partial}{\partial y^{*}}(\tilde{\kappa} r^{*A}v^{*})\right]\left[\frac{\partial r^{*A}}{\partial x^{*}}\right]$$

$$+ \frac{2\mu^{*} u^{*}}{\tilde{\kappa} r^{*A}}\left[\frac{\partial r^{*A-2}}{\partial x^{*}}\right] + 2\mu^{*}\frac{v^{*}}{r^{*A}}\frac{\partial r^{*A}}{\partial x^{*}}\frac{\partial r^{*A}}{\partial y^{*}} = 0$$

Proceeding as before the dimensionless variables are introduced.

$$\rho_\infty^* R^* \frac{U_\infty^{*2}}{R^*} \left[\rho r^A u \frac{\partial u}{\partial \xi} \right] + \rho_\infty^* R^* \frac{U_\infty^{*2}}{R^*} \left[\rho \tilde{\kappa} r^A v \frac{\partial u}{\partial y} \right]$$

$$+ \rho_\infty^* R^* U_\infty^{2*} \frac{1}{R^*} \left[\rho \kappa r^A u v \right] + \frac{R^*}{R^*} \rho_\infty^* U_\infty^{*2} \left[r^A \frac{\partial P}{\partial \xi} \right]$$

$$- R^* \mu_{s,0}^* \frac{R^* U_\infty^*}{R^* R^* R^*} \left[\frac{\partial}{\partial \xi} \left(\frac{\lambda}{\tilde{\kappa}} \left\{ \frac{\partial}{\partial \xi} (r^A u) + \frac{\partial}{\partial y} (\tilde{\kappa} r^A v) \right\} \right) \right]$$

$$- R^* \frac{\mu_{s,0}^* U_\infty^*}{R^* R^*} \left[\frac{\partial}{\partial \xi} \left(\frac{2 r^A \mu}{\tilde{\kappa}} \left\{ \frac{\partial u}{\partial \xi} + \kappa v \right\} \right) \right]$$

$$- \frac{\mu_{s,0}^* R^* U_\infty^*}{R^* R^*} \left[\frac{\partial}{\partial y} \left(\tilde{\kappa} r^A \mu \left\{ \frac{1}{\tilde{\kappa}} \frac{\partial v}{\partial \xi} + \frac{\partial u}{\partial y} \right\} \right) \right]$$

$$+ \frac{R^* \mu_{s,0}^* U_\infty^*}{R^* R^*} \left[\frac{\partial}{\partial y} (\kappa r^A \mu u) \right]$$

$$- \frac{1}{R^*} R^* \mu_{s,0}^* \frac{U_\infty^*}{R^*} \left[\kappa r^A \mu \left(\frac{1}{\tilde{\kappa}} \frac{\partial v}{\partial \xi} + \frac{\partial u}{\partial y} - \frac{\kappa}{\tilde{\kappa}} u \right) \right]$$

$$+ \mu_{s,0}^* \frac{R^* U_\infty^* R^*}{R^* R^* R^*} \left[\frac{\lambda}{\tilde{\kappa} r^A} \left(\frac{\partial}{\partial \xi} (r^A u) + \frac{\partial}{\partial y} (\tilde{\kappa} r^A v) \right) \left(\frac{\partial r^A}{\partial \xi} \right) \right]$$

$$+ \mu_{s,0}^* \frac{U_\infty^* R^* R^*}{R^* R^* R^*} \left[\frac{2 \mu u}{\tilde{\kappa} r^A} \left(\frac{\partial r^A}{\partial \xi} \right)^2 + 2 \mu \frac{v}{r^A} \frac{\partial r^A}{\partial y} \frac{\partial r^A}{\partial \xi} \right] = 0$$

By letting

$$R_e = \frac{\rho_\infty^* U_\infty^* R^*}{\mu_{s,0}^*} \tag{2.7}$$

and cancelling dimensional terms yields the dimensionless ξ-momentum equation.

$$\rho r^{A}_{u} \frac{\partial u}{\partial \xi} + \rho \tilde{\kappa} r^{A}_{v} \frac{\partial u}{\partial y} + \rho \kappa r^{A}_{uv} + r^{A} \frac{\partial P}{\partial \xi}$$

$$- \frac{1}{R_e} \left\{ \frac{\partial}{\partial \xi} \left(\frac{\lambda}{\tilde{\kappa}} \frac{\partial}{\partial \xi} (r^{A}_{u}) + \frac{\lambda}{\tilde{\kappa}} \frac{\partial}{\partial y} (\tilde{\kappa} r^{A}_{v}) \right) \right.$$

$$+ \frac{\partial}{\partial \xi} \left(\frac{2 r^{A}_{\mu}}{\tilde{\kappa}} \left[\frac{\partial u}{\partial \xi} + \kappa v \right] \right)$$

$$+ \frac{\partial}{\partial y} \left(r^{A}_{\mu} \frac{\partial v}{\partial \xi} + \tilde{\kappa} r^{A}_{\mu} \frac{\partial u}{\partial y} - \kappa r^{A}_{\mu u} \right) \qquad (2.8)$$

$$+ \kappa r^{A}_{\mu} \left(\frac{1}{\tilde{\kappa}} \frac{\partial v}{\partial \xi} + \frac{\partial u}{\partial y} - \frac{\kappa}{\tilde{\kappa}} u \right)$$

$$- \frac{\lambda}{\tilde{\kappa} r^{A}} \left(\frac{\partial}{\partial \xi} (r^{A}_{u}) + \frac{\partial}{\partial y} (\tilde{\kappa} r^{A}_{v}) \right) \left(\frac{\partial r^{A}}{\partial \xi} \right)$$

$$\left. - 2 \frac{\mu u}{\tilde{\kappa} r^{A}} \left(\frac{\partial r^{A}}{\partial \xi} \right) - 2\mu \frac{v}{r^{A}} \frac{\partial r^{A}}{\partial \xi} \frac{\partial r^{A}}{\partial y} \right\} = 0$$

The y-momentum equation can be stated in dimensional form from Eqs. A.85 → A.89

$$\rho^{*} r^{*A}_{u^{*}} \frac{\partial v^{*}}{\partial x^{*}} + \rho^{*} r^{*A}_{\tilde{\kappa} v^{*}} \frac{\partial v^{*}}{\partial y^{*}} - \rho^{*} \kappa^{*} r^{*A}_{u^{*}2}$$
$$+ \tilde{\kappa} r^{*A} \frac{\partial P^{*}}{\partial y^{*}} - \frac{\partial}{\partial x^{*}} \left(r^{*A}_{\mu^{*}} \left[\frac{1}{\tilde{\kappa}} \frac{\partial v^{*}}{\partial x^{*}} + \frac{\partial u^{*}}{\partial y^{*}} - \frac{\kappa^{*}}{\tilde{\kappa}} u^{*} \right] \right)$$
$$- \frac{\partial}{\partial y^{*}} \left(\lambda^{*} \frac{\partial}{\partial x^{*}} (r^{*A} u^{*}) + \lambda^{*} \frac{\partial}{\partial y^{*}} (\tilde{\kappa} r^{*A} v^{*}) \right) \qquad (2.9)$$
$$- \frac{\partial}{\partial y^{*}} (2 \tilde{\kappa} r^{*A}_{\mu^{*}} \frac{\partial v^{*}}{\partial y^{*}}) + \lambda^{*} \frac{\kappa^{*}}{\tilde{\kappa}} \left[\frac{\partial}{\partial x^{*}} (r^{*A} u^{*}) + \frac{\partial}{\partial y^{*}} (\tilde{\kappa} r^{*A} v^{*}) \right]$$
$$+ 2\mu^{*} \frac{\kappa^{*} r^{*A}}{\tilde{\kappa}} \left[\frac{\partial u^{*}}{\partial x^{*}} + \kappa^{*} v^{*} \right]$$
$$+ \frac{\lambda^{*}}{r^{*A}} \left[\frac{\partial}{\partial x^{*}} (r^{*A} u^{*}) + \frac{\partial}{\partial y^{*}} (\tilde{\kappa} r^{*A} v^{*}) \right] \left[\frac{\partial r^{*A}}{\partial y^{*}} \right]$$
$$+ 2\mu^{*} \frac{u^{*}}{r^{*A}} \left[\frac{\partial r^{*A}}{\partial y^{*}} \right] \left[\frac{\partial r^{*A}}{\partial x^{*}} \right] + 2\mu^{*} \frac{\tilde{\kappa} v^{*}}{r^{*A}} \left[\frac{\partial r^{*A}}{\partial y^{*}} \right]^{2} = 0$$

Introduction of nondimensional variables into the y-momentum equations follows the same procedure and pattern as in the x-momentum equation. The resulting nondimensional y-momentum equation is:

$$\rho r^{A} u \frac{\partial v}{\partial \xi} + \rho r^{A} \tilde{\kappa} v \frac{\partial v}{\partial y} - \rho \kappa r^{A} u^{2} + \tilde{\kappa} r^{A} \frac{\partial P}{\partial y}$$

$$- \frac{1}{R_e} \left\{ \frac{\partial}{\partial \xi} \left(r^{A} \mu \left[\frac{1}{\tilde{\kappa}} \frac{\partial v}{\partial \xi} + \frac{\partial u}{\partial y} - \frac{\kappa}{\tilde{\kappa}} u \right] \right) \right.$$

$$+ \frac{\partial}{\partial y} \left(\lambda \frac{\partial}{\partial \xi} (r^{A} u) + \lambda \frac{\partial}{\partial y} (\tilde{\kappa} r^{A} v) \right) + \frac{\partial}{\partial y} \left(2 \tilde{\kappa} r^{A} \mu \frac{\partial v}{\partial y} \right)$$

$$- \frac{\lambda \kappa}{\tilde{\kappa}} \left[\frac{\partial}{\partial \xi} (r^{A} u) + \frac{\partial}{\partial y} (\tilde{\kappa} r^{A} v) \right] - 2\mu \frac{\kappa r^{A}}{\tilde{\kappa}} \left[\frac{\partial u}{\partial \xi} + \kappa v \right]$$

$$- \frac{\lambda}{r^{A}} \left[\frac{\partial}{\partial \xi} (r^{A} u) + \frac{\partial}{\partial y} (\tilde{\kappa} r^{A} v) \right] \left[\frac{\partial r^{A}}{\partial y} \right] - 2\mu \frac{u}{r^{A}} \left[\frac{\partial r^{A}}{\partial y} \right]^{2}$$

$$\left. - 2\mu \frac{\tilde{\kappa} v}{r^{A}} \frac{\partial r^{A}}{\partial \xi} \frac{\partial r^{A}}{\partial y} \right\} = 0 \qquad (2.10)$$

Using Eqs. A.90 with A.86, A.87 and A.89 the energy equation can be written in dimensional form:

$$\rho^{*} r^{*A} u^{*} \frac{\partial H^{*}}{\partial x^{*}} + \rho^{*} \tilde{\kappa} r^{*A} v^{*} \frac{\partial H^{*}}{\partial y^{*}} = - \Lambda^{*}_{D,x} - \Lambda^{*}_{D,y} - \Lambda^{*}_{R,x}$$

$$- \Lambda^{*}_{R,y} + \frac{\partial}{\partial x^{*}} \left(\frac{\lambda^{*} u^{*}}{\tilde{\kappa}} \left[\frac{\partial}{\partial x^{*}} (r^{*A} u^{*}) + \frac{\partial}{\partial y^{*}} (\tilde{\kappa} r^{*A} v^{*}) \right] \right.$$

$$+ 2\mu^{*} r^{*A} \frac{u^{*}}{\tilde{\kappa}} \left[\frac{\partial u^{*}}{\partial x^{*}} + \kappa^{*} v^{*} \right] + r^{*A} v^{*} \mu^{*} \left[\frac{1}{\tilde{\kappa}} \frac{\partial v^{*}}{\partial x^{*}} + \frac{\partial u^{*}}{\partial y^{*}} \right.$$

$$\left. \left. - \frac{\kappa^{*} u^{*}}{\tilde{\kappa}} \right] \right) + \frac{\partial}{\partial y^{*}} \left(\tilde{\kappa} r^{*A} \mu^{*} u^{*} \left[\frac{1}{\tilde{\kappa}} \frac{\partial v^{*}}{\partial x^{*}} + \frac{\partial u^{*}}{\partial y^{*}} - \frac{\kappa^{*}}{\tilde{\kappa}} u^{*} \right] \right.$$

$$\left. + \lambda^{*} v^{*} \left[\frac{\partial}{\partial x^{*}} (r^{*A} u^{*}) + \frac{\partial}{\partial y^{*}} (\tilde{\kappa} r^{*A} v^{*}) \right] + 2 \tilde{\kappa} r^{*A} \mu^{*} v^{*} \frac{\partial v^{*}}{\partial y^{*}} \right) \qquad (2.11)$$

where the diffusional and radiative flux divergence terms, Λ^*, are defined in Eq. 2.1. Substitution of the nondimensional ratios from Eq. 2.1 yields

$$\rho_\infty^* \frac{R^*}{R^*} U_\infty^* \frac{U_\infty^{*2}}{2} \left[r^A \rho u \frac{\partial H}{\partial \xi} + \tilde{\kappa} r^A \rho v \frac{\partial H}{\partial y} \right] = - \rho_\infty^* (U_\infty^*)^3 \left[\Lambda_{D,x} + \Lambda_{D,y} + \Lambda_{R,x} + \Lambda_{R,y} \right] + \mu_{s,0}^* \frac{U_\infty^{*2}}{R^*} \frac{R^*}{R^*} \left\{ \frac{\partial}{\partial \xi} \left(\frac{\lambda u}{\tilde{\kappa}} \left[\frac{\partial}{\partial \xi} (r^A u) + \frac{\partial}{\partial y} (\tilde{\kappa} r^A v) \right] + 2\mu r^A \frac{u}{\tilde{\kappa}} \left[\frac{\partial u}{\partial \xi} + \kappa v \right] + r^A \mu v \left[\frac{1}{\tilde{\kappa}} \frac{\partial v}{\partial \xi} + \frac{\partial u}{\partial y} - \frac{\kappa u}{\tilde{\kappa}} \right] \right) + \frac{\partial}{\partial y} \left(\tilde{\kappa} r^A \mu u \left[\frac{1}{\tilde{\kappa}} \frac{\partial v}{\partial \xi} + \frac{\partial u}{\partial y} - \frac{\kappa u}{\tilde{\kappa}} \right] + \lambda v \left[\frac{\partial}{\partial \xi} (r^A u) + \frac{\partial}{\partial y} (\tilde{\kappa} r^A v) \right] + 2 \tilde{\kappa} r^A \mu v \frac{\partial v}{\partial y} \right) \right\}$$

Introducing the Reynolds number the nondimensional energy equation can be written:

$$r^A \rho u \frac{\partial H}{\partial \xi} + \tilde{\kappa} r^A \rho v \frac{\partial H}{\partial y} = - 2 \left[\Lambda_{D,x} + \Lambda_{D,y} + \Lambda_{R,x} + \Lambda_{R,y} \right] + \frac{2}{R_e} \left\{ \frac{\partial}{\partial \xi} \left(\frac{\lambda u}{\tilde{\kappa}} \left[\frac{\partial}{\partial \xi} (r^A u) + \frac{\partial}{\partial y} (\tilde{\kappa} r^A v) \right] + 2 r^A \mu \frac{u}{\tilde{\kappa}} \left[\frac{\partial u}{\partial \xi} + \kappa v \right] + r^A \mu v \left[\frac{1}{\tilde{\kappa}} \frac{\partial v}{\partial \xi} + \frac{\partial u}{\partial y} - \frac{\kappa u}{\tilde{\kappa}} \right] \right) + \frac{\partial}{\partial y} \left(\tilde{\kappa} r^A \mu u \left[\frac{1}{\tilde{\kappa}} \frac{\partial v}{\partial \xi} + \frac{\partial u}{\partial y} - \frac{\kappa u}{\tilde{\kappa}} \right] + \lambda v \left[\frac{\partial}{\partial \xi} (r^A u) + \frac{\partial}{\partial y} (\tilde{\kappa} r^A u) \right] + 2 \tilde{\kappa} r^A \mu v \frac{\partial v}{\partial y} \right) \right\} \tag{2.12}$$

Having stated the nondimensional conservation equations we are confronted with the problem of estimating the relative magnitude of the terms in each equation.

According to the results of Hayes and Probstein, Ref. 2.2, the gas behind a bow shock of a hypervelocity vehicle is a continuum for freestream Reynolds numbers greater than 100 based on principle body radius. Further, the standoff distance nondimensionalized by body radius for flight Reynolds numbers greater than 100 has been shown, Ref. 2.2 and others, to be approximatedly equal to the density ratio across the bow shock. The density ratio for hypersonic Mach numbers is of the order of one tenth and less for dissociating gases. These stated relationships can be expressed as follows:

$$R_e > 100 \ , \qquad \frac{\delta^*}{R^*} \simeq \bar{\rho} \leq .10 \tag{2.13}$$

Since we are concerned with a thin layer with respect to the body radius, Prandtl's concepts for the relative order of magnitude of terms in the conservation equations can be employed. Following the procedure given by Schlichting, Ref. 2.6, the relationships for the relative order of nondimensionalized terms may be written.

$$\begin{array}{llllllll}
u \sim 1 & v \sim \bar{\rho} & \varkappa \sim 1 & \tilde{\varkappa} \sim 1 \\
H \sim 1 & \rho \sim 1 & \mu \sim 1 & C_i \sim 1 \\
\frac{\partial u}{\partial \xi} \sim 1 & \frac{\partial^2 u}{\partial \xi^2} \sim 1 & \frac{\partial v}{\partial \xi} \sim \bar{\rho} & \frac{\partial^2 v}{\partial \xi^2} \sim \bar{\rho} \\
\frac{\partial u}{\partial y} \sim \frac{1}{\bar{\rho}} & \frac{\partial^2 u}{\partial y^2} \sim \frac{1}{\bar{\rho}^2} & \frac{\partial v}{\partial y} \sim 1 & \frac{\partial^2 v}{\partial y^2} \sim \frac{1}{\bar{\rho}} \\
\frac{\partial C_i}{\partial \xi} \sim 1 & \frac{\partial^2 C_i}{\partial \xi^2} \sim 1 & \frac{\partial C_i}{\partial y} \sim \frac{1}{\bar{\rho}} & \frac{\partial^2 C_i}{\partial y^2} \sim \frac{1}{\bar{\rho}^2} \\
J_{i,x} \sim \frac{1}{R_e} \frac{\partial C_i}{\partial \xi} & J_{i,y} \sim \frac{1}{R_e} \frac{\partial C_i}{\partial y} & \frac{\partial r^A}{\partial \xi} \sim 1 & \frac{\partial r^A}{\partial y} \sim \bar{\rho}
\end{array} \tag{2.14}$$

Using the above estimates the relative order of magnitude of the terms in the four conservation equations have been determined.

Global continuity

$$\underset{0[1]}{\frac{\partial}{\partial \xi}\left(r^{A}\rho u\right)} + \underset{0[1]}{\frac{\partial}{\partial y}\left(\underset{\sim}{\kappa} r^{A}\rho v\right)} = 0 \tag{2.15}$$

Species continuity

$$\underset{0[1]}{\frac{\partial}{\partial \xi}\left(r^{A}\rho C_{i} u\right)} + \underset{0[1]}{\frac{\partial}{\partial y}\left(\underset{\sim}{\kappa} r^{A}\rho C_{i} v\right)} = \underset{0\left[\frac{1}{R_e}\right]}{-\frac{\partial}{\partial \xi}\left(r^{A} J_{ix}\right)} - \underset{0\left[\frac{1}{\rho R_e}\right]}{\frac{\partial}{\partial y}\left(\underset{\sim}{\kappa} r^{A} J_{iy}\right)} + \underset{\sim}{\kappa} r^{A}\omega_{i} \tag{2.16}$$

ξ - Momentum

$$\begin{aligned}
&\underset{0[1]}{\rho r^{A} u \frac{\partial u}{\partial \xi}} + \underset{0[1]}{\rho \underset{\sim}{\kappa} r^{A} v \frac{\partial u}{\partial y}} + \underset{0[\bar{\rho}]}{\rho \underset{\sim}{\kappa} r^{A} uv} + \underset{0[1]}{r^{A} \frac{\partial P}{\partial \xi}} \\
&- \frac{1}{R_e}\left\{ \underset{0[1]}{\frac{\partial}{\partial \xi}\left(\frac{\lambda}{\underset{\sim}{\kappa}} \frac{\partial}{\partial \xi}\left(r^{A} u\right)\right)} + \underset{0[\bar{\rho}]}{\frac{\partial}{\partial \xi}\left(\frac{\lambda}{\underset{\sim}{\kappa}} \frac{\partial}{\partial y}\left(\underset{\sim}{\kappa} r^{A} v\right)\right)} \right. \\
&+ \underset{0[1]}{\frac{\partial}{\partial \xi}\left(\frac{2 r^{A} \mu}{\underset{\sim}{\kappa}} \frac{\partial u}{\partial \xi}\right)} + \underset{0[\bar{\rho}]}{\frac{\partial}{\partial \xi}\left(\frac{2 r^{A} \mu \underset{\sim}{\kappa} v}{\underset{\sim}{\kappa}}\right)} + \underset{0[\bar{\rho}]}{\frac{\kappa}{\underset{\sim}{\kappa}} r^{A} \mu \frac{\partial v}{\partial \xi}} \\
&+ \underset{0[\bar{\rho}]}{\frac{\partial}{\partial y}\left(r^{A} \mu \frac{\partial v}{\partial \xi}\right)} + \underset{0\left[\frac{1}{\bar{\rho}^2}\right]}{\frac{\partial}{\partial y}\left(\underset{\sim}{\kappa} r^{A} \mu \frac{\partial u}{\partial y}\right)} - \underset{0\left[\frac{1}{\bar{\rho}}\right]}{\frac{\partial}{\partial y}\left(\kappa r^{A} \mu u\right)} \\
&+ \underset{0\left[\frac{1}{\bar{\rho}}\right]}{\kappa r^{A} \mu \frac{\partial u}{\partial y}} - \underset{0[1]}{\frac{\kappa^2}{\underset{\sim}{\kappa}} r^{A} \mu u} - \underset{0[1]}{\frac{\lambda}{\underset{\sim}{\kappa} r^{A}} \frac{\partial}{\partial \xi}\left(r^{A} u\right)\left(\frac{\partial r^{A}}{\partial \xi}\right)} \\
&\left. - \underset{0[1]}{\frac{\lambda}{\underset{\sim}{\kappa} r^{A}} \frac{\partial}{\partial y}\left(\underset{\sim}{\kappa} r^{A} v\right)\left(\frac{\partial r^{A}}{\partial \xi}\right)} - \underset{0[1]}{2 \frac{\mu u}{\underset{\sim}{\kappa} r^{A}}\left(\frac{\partial r^{A}}{\partial \xi}\right)^{2}} - \underset{0[\bar{\rho}^2]}{\frac{2 u v}{r^{A}} \frac{\partial r^{A}}{\partial \xi} \frac{\partial r^{A}}{\partial y}} \right\} = 0
\end{aligned} \tag{2.17}$$

y - Momentum:

$$
\begin{array}{ccccccc}
O[\bar{\rho}] & & O[\bar{\rho}] & & O[1] & & \\
\rho r^A u \frac{\partial v}{\partial \xi} & + & \rho r^A \tilde{\kappa} v \frac{\partial v}{\partial y} & - & \rho \kappa r^A u^2 & + & \tilde{\kappa} r^A \frac{\partial P}{\partial y} \\
 & & O[\bar{\rho}] & & O\left[\frac{1}{\bar{\rho}}\right] & & O[1]
\end{array}
$$

$$
- \frac{1}{R_e} \left\{ \frac{\partial}{\partial \xi} \left(\frac{r^A \mu}{\tilde{\kappa}} \frac{\partial v}{\partial \xi} \right) + \frac{\partial}{\partial \xi} \left(r^A \mu \frac{\partial u}{\partial y} \right) - \frac{\partial}{\partial \xi} \left(\frac{r^A \mu \kappa u}{\tilde{\kappa}} \right) \right.
$$

$$
O\left[\frac{1}{\bar{\rho}}\right] \qquad O\left[\frac{1}{\bar{\rho}}\right] \qquad O[1]
$$

$$
+ \frac{\partial}{\partial y} \left(\lambda \frac{\partial}{\partial \xi} (r^A u) \right) + \frac{\partial}{\partial y} \left(\lambda \frac{\partial}{\partial y} (\tilde{\kappa} r^A v) \right) - \frac{\lambda \kappa}{\tilde{\kappa}} \frac{\partial}{\partial \xi} (r^A u)
$$

$$
O[1] \qquad O[1] \qquad O[\bar{\rho}]
$$

$$
- \frac{\lambda \kappa}{\tilde{\kappa}} \frac{\partial}{\partial y} (\tilde{\kappa} r^A v) - 2\mu \frac{\kappa r^A}{\tilde{\kappa}} \frac{\partial u}{\partial \xi} - 2\mu \frac{\kappa^2}{\tilde{\kappa}} r^A v
$$

$$
O[\bar{\rho}] \qquad O[\bar{\rho}] \qquad O[\bar{\rho}^2]
$$

$$
- \frac{\lambda}{r^A} \frac{\partial}{\partial \xi} (r^A u) \left(\frac{\partial r^A}{\partial y} \right) - \frac{\lambda}{r^A} \frac{\partial}{\partial y} (\tilde{\kappa} r^A v) \left(\frac{\partial r^A}{\partial y} \right) - 2\mu \frac{u}{r^A} \left(\frac{\partial r^A}{\partial y} \right)^2
$$

$$
O[\bar{\rho}^2] \qquad O\left[\frac{1}{\bar{\rho}}\right]
$$

$$
\left. - 2\mu \frac{\tilde{\kappa} v}{r^A} \frac{\partial r^A}{\partial \xi} \frac{\partial r^A}{\partial y} + \frac{\partial}{\partial y} \left(2 \tilde{\kappa} r^A \mu \frac{\partial v}{\partial y} \right) \right\} = 0 \qquad (2.18)
$$

Energy:

$$
\begin{array}{llll}
O[1] & O[1] & O\left[\frac{1}{R_e}\right] & \left[\frac{1}{\bar{\rho}^2 R_e}\right] \\
r^A \rho u \frac{\partial H}{\partial \xi} + \tilde{\kappa} r^A \rho v \frac{\partial H}{\partial y} = -2\Big[& \Lambda_{D,x} + & \Lambda_{D,y} & \\
O\left[\frac{1}{R_e}\right] & O\left[\frac{1}{\bar{\rho}^2 R_e}\right] & O[1] & \\
+ \Lambda_{R,x} + & \Lambda_{R,y}\Big] + \frac{2}{R_e}\Big\{ & \frac{\partial}{\partial \xi}\left(\frac{\lambda u}{\tilde{\kappa}} \frac{\partial}{\partial \xi}(r^A u)\right) & \\
O[1] & O[1] & & \\
+ \frac{\partial}{\partial \xi}\left(\frac{\lambda u}{\tilde{\kappa}} \frac{\partial}{\partial y}(\tilde{\kappa} r^A v)\right) + & \frac{\partial}{\partial \xi}\left(2 r^A \mu \frac{u}{\tilde{\kappa}} \frac{\partial u}{\partial \xi}\right) & & \\
O[\bar{\rho}] & O[\bar{\rho}^2] & & \\
+ \frac{\partial}{\partial \xi}\left(2 r^A \frac{\kappa}{\tilde{\kappa}} \mu u v\right) + & \frac{\partial}{\partial \xi}\left(r^A \mu \frac{v}{\tilde{\kappa}} \frac{\partial v}{\partial \xi}\right) & & \\
O[1] & O[\bar{\rho}] & O[\bar{\rho}] & \\
+ \frac{\partial}{\partial \xi}\left(r^A \mu v \frac{\partial u}{\partial y}\right) - & \frac{\partial}{\partial \xi}\left(r^A \frac{\kappa}{\tilde{\kappa}} \mu u v\right) + & \frac{\partial}{\partial y}\left(r^A \mu u \frac{\partial v}{\partial \xi}\right) & \\
O\left[\frac{1}{\bar{\rho}^2}\right] & O\left[\frac{1}{\bar{\rho}}\right] & O[1] & \\
+ \frac{\partial}{\partial y}\left(\tilde{\kappa} r \mu u \frac{\partial u}{\partial y}\right) - & \frac{\partial}{\partial y}\left(\kappa r^A \mu u^2\right) + & \frac{\partial}{\partial y}\left(\lambda v \frac{\partial}{\partial \xi}(r^A u)\right) & \\
O[1] & O[1] & & \\
+ \frac{\partial}{\partial y}\left(\lambda v \frac{\partial}{\partial y}(\tilde{\kappa} r^A v)\right) + & \frac{\partial}{\partial y}\left(2\tilde{\kappa} r^A \mu v \frac{\partial v}{\partial y}\right)\Big\} & &
\end{array}
\tag{2.19}
$$

Using the lower limit on Reynolds number we observe

$$\frac{1}{R_e} \approx \bar{\rho}^2 \approx \frac{1}{100}$$

At this lower limit on Reynolds number, let us drop all terms of order $\bar{\rho}^{-2}$ and higher in all equations except the y-momentum equation. In the y-momentum equation terms of order $\bar{\rho}^{-2}$ are retained for a specific reason. Along the stagnation line, $\xi = 0$, the u component of velocity is zero. Thus the y-momentum equation is of one order lower at $\xi = 0$. It is appropriate in this case to consider terms of two orders of magnitude in this equation namely $\bar{\rho}$ and $\bar{\rho}^{-2}$. The resulting conservation equations are presented in Tab. 2.1.

At $\xi = 0$ the y-momentum equation, Eq. 2.23, has terms which are of order $\bar{\rho}$ and $\bar{\rho}^{-2}$. Two terms which can be directly eliminated from this equation when $u = 0$ at $\xi = 0$ are indicated by arrows.

The simplified set of conservation equations, Eqs. 2.15, 2.20 - 2.24 form a set of partial differential equations (neglecting the radiative terms) which are valid for Reynolds numbers greater than 100. It is obvious that the terms which have been dropped due to order of magnitude reasoning become less significant as the Reynolds number is increased. These "thin shock layer" equations are the same as second order boundary layer equations with curvature terms and are valid for continuum flow of the viscous, vorcity, and classical boundary layer regime.

To this point little has been said about the bulk viscosity which appears in the λ term in the momentum and energy equations. This has been done for the sake of generality. However, to interpret the pressure in our equations as the local thermodynamic pressure Stokes' postulate

TABLE 2.1

LISTING OF CONSERVATION EQUATION WITH

ORDER ASSESSMENT RESULTS

Global continuity:

$$\underset{O[1]}{\frac{\partial}{\partial \xi}(r^A \rho u)} + \underset{O[1]}{\frac{\partial}{\partial y}(\tilde{\kappa} r^A \rho v)} = 0 \qquad (2.15)$$

Species continuity:

$$\underset{O[1]}{\frac{\partial}{\partial \xi}(r^A \rho C_i u)} + \underset{O[1]}{\frac{\partial}{\partial y}(\tilde{\kappa} r^A \rho C_i v)} = \underset{O[1]}{- \frac{\partial}{\partial y}(\tilde{\kappa} r^A J_{iy})} + \tilde{\kappa} r^A \omega_i \qquad (2.20)$$

ξ - momentum:

$$\underset{O[1]}{\rho r^A u \frac{\partial u}{\partial \xi}} + \underset{O[1]}{\tilde{\rho} \tilde{\kappa} r^A v \frac{\partial u}{\partial y}} + \underset{O[\bar{\rho}]}{\rho \kappa r^A uv} + \underset{O\left[\frac{1}{\rho^2}\right]}{r^A \frac{\partial P}{\partial \xi}}$$

$$- \underset{O\left[\frac{1}{\rho}\right]}{\frac{1}{R_e}} \left\{ \underset{O\left[\frac{1}{\rho}\right]}{\frac{\partial}{\partial y}\left(\tilde{\kappa} r^A \mu \frac{\partial u}{\partial y}\right)} - \underset{O\left[\frac{1}{\rho}\right]}{\frac{\partial}{\partial y}(\kappa r^A \mu u)} + \underset{O\left[\frac{1}{\rho}\right]}{\kappa r^A \mu \frac{\partial u}{\partial y}} \right\} = 0 \qquad (2.21)$$

TABLE 2.1 (Cont.)

y - momentum: ($0[\bar{\rho}]$ and larger terms)

$$\underset{0[\bar{\rho}]}{\rho r^A u \frac{\partial v}{\partial \xi}} + \underset{0[\bar{\rho}]}{\rho r^A \tilde{\kappa} v \frac{\partial v}{\partial y}} - \underset{0[1]}{\rho \tilde{\kappa} r^A u^2} + \underset{0\left[\frac{1}{\bar{\rho}}\right]}{\tilde{\kappa} r^A \frac{\partial P}{\partial y}}$$

$$- \frac{1}{R_e} \left\{ \underset{0\left[\frac{1}{\bar{\rho}}\right]}{\frac{\partial}{\partial \xi} \left(r^A \mu \frac{\partial u}{\partial y} \right)} + \underset{0\left[\frac{1}{\bar{\rho}}\right]}{\frac{\partial}{\partial y} \left(\lambda \frac{\partial}{\partial \xi} (r^A u) \right)} \right. \tag{2.22}$$

$$\left. + \frac{\partial}{\partial y} \left(\lambda \frac{\partial}{\partial y} (\tilde{\kappa} r^A v) \right) + \frac{\partial}{\partial y} \left(2 \tilde{\kappa} r^A \mu \frac{\partial v}{\partial y} \right) \right\} = 0$$

y - momentum: ($0[\bar{\rho}^2]$ and larger terms)

$$\underset{0[\bar{\rho}]}{\cancel{\rho r^A u \frac{\partial v}{\partial \xi}}^{\to 0}} + \underset{0[\bar{\rho}]}{\rho r^A \tilde{\kappa} v \frac{\partial v}{\partial y}} - \underset{0[1]}{\cancel{\rho \tilde{\kappa} r^A u^2}^{\to 0}} + \underset{0\left[\frac{1}{\bar{\rho}}\right]}{\tilde{\kappa} r^A \frac{\partial P}{\partial y}}$$

$$- \frac{1}{R_e} \left\{ \underset{0\left[\frac{1}{\bar{\rho}}\right]}{\frac{\partial}{\partial \xi} \left(r^A \mu \frac{\partial u}{\partial y} \right)} + \underset{0\left[\frac{1}{\bar{\rho}}\right]}{\frac{\partial}{\partial y} \left(\lambda \frac{\partial}{\partial \xi} (r^A u) \right)} \right.$$

$$\left. + \underset{0[1]}{\frac{\partial}{\partial y} \left(\lambda \frac{\partial}{\partial y} (\tilde{\kappa} r^A v) \right)} + \underset{0[1]}{\frac{\partial}{\partial y} \left(2 \tilde{\kappa} r^A \mu \frac{\partial v}{\partial y} \right)} - \underset{0[1]}{\frac{\partial}{\partial \xi} (r^A \mu_\kappa u)} \right.$$

$$\left. - \underset{0[1]}{\frac{\lambda \kappa}{\tilde{\kappa}} \frac{\partial}{\partial \xi} (r^A u)} - \underset{0[1]}{\frac{\lambda \kappa}{\tilde{\kappa}} \frac{\partial}{\partial y} (\tilde{\kappa} r^A v)} - \underset{0[1]}{2 \mu \frac{\kappa r^A}{\tilde{\kappa}} \frac{\partial u}{\partial \xi}} \right\} = 0 \tag{2.23}$$

TABLE 2.1 (Cont.)

y - momentum: ($0[\bar{\rho}]$ and larger terms)

$$\underset{0[\bar{\rho}]}{\rho r^A u \frac{\partial v}{\partial \xi}} + \underset{0[\bar{\rho}]}{\rho r^A \tilde{\kappa} v \frac{\partial v}{\partial y}} - \underset{0[1]}{\rho \tilde{\kappa} r^A u^2} + \underset{0\left[\frac{1}{\bar{\rho}}\right]}{\tilde{\kappa} r^A \frac{\partial P}{\partial y}}$$

$$- \frac{1}{R_e} \left\{ \underset{0\left[\frac{1}{\bar{\rho}}\right]}{\frac{\partial}{\partial \xi} \left(r^A \mu \frac{\partial u}{\partial y} \right)} + \underset{0\left[\frac{1}{\bar{\rho}}\right]}{\frac{\partial}{\partial y} \left(\lambda \frac{\partial}{\partial \xi} (r^A u) \right)} \right. \tag{2.22}$$

$$\left. + \frac{\partial}{\partial y} \left(\lambda \frac{\partial}{\partial y} (\tilde{\kappa} r^A v) \right) + \frac{\partial}{\partial y} \left(2 \tilde{\kappa} r^A \mu \frac{\partial v}{\partial y} \right) \right\} = 0$$

y - momentum: ($0[\bar{\rho}^2]$ and larger terms)

$$\underset{0[\bar{\rho}]}{\cancel{\rho r^A u \frac{\partial v}{\partial \xi}}^{\to 0}} + \underset{0[\bar{\rho}]}{\rho r^A \tilde{\kappa} v \frac{\partial v}{\partial y}} - \underset{0[1]}{\cancel{\rho \tilde{\kappa} r^A u^2}^{\to 0}} + \underset{0\left[\frac{1}{\bar{\rho}}\right]}{\tilde{\kappa} r^A \frac{\partial P}{\partial y}}$$

$$- \frac{1}{R_e} \left\{ \underset{0\left[\frac{1}{\bar{\rho}}\right]}{\frac{\partial}{\partial \xi} \left(r^A \mu \frac{\partial u}{\partial y} \right)} + \underset{0\left[\frac{1}{\bar{\rho}}\right]}{\frac{\partial}{\partial y} \left(\lambda \frac{\partial}{\partial \xi} (r^A u) \right)} \right.$$

$$\left. + \underset{0[1]}{\frac{\partial}{\partial y} \left(\lambda \frac{\partial}{\partial y} (\tilde{\kappa} r^A v) \right)} + \underset{0[1]}{\frac{\partial}{\partial y} \left(2 \tilde{\kappa} r^A \mu \frac{\partial v}{\partial y} \right)} - \underset{0[1]}{\frac{\partial}{\partial \xi} (r^A \mu \kappa u)} \right. \tag{2.23}$$

$$\left. - \underset{0[1]}{\frac{\lambda \mu}{\tilde{\kappa}} \frac{\partial}{\partial \xi} (r^A u)} - \underset{0[1]}{\frac{\lambda \kappa}{\tilde{\kappa}} \frac{\partial}{\partial y} (\tilde{\kappa} r^A v)} - \underset{0[1]}{2 \mu \frac{\kappa r^A}{\tilde{\kappa}} \frac{\partial u}{\partial \xi}} \right\} = 0$$

TABLE 2.1 (Cont.)

Energy:

$$\underset{O[1]}{r^{A}\rho u\frac{\partial H}{\partial \xi}} + \underset{O[1]}{\tilde{\kappa}\, r^{A}\rho v\frac{\partial H}{\partial y}} = \underset{O[1]}{-2\left(\Lambda_{D,y} + \Lambda_{R,y}\right)} + \underset{O\left[\frac{1}{\rho^{2}}\right]}{\frac{2}{R_e}\left\{\frac{\partial}{\partial y}\left(\tilde{\kappa} r^{A}\mu u\frac{\partial u}{\partial y}\right)\right.} \underset{O\left[\frac{1}{\rho}\right]}{\left. - \frac{\partial}{\partial y}\left(\kappa r^{A}\mu u^{2}\right)\right\}} \qquad (2.24)$$

$$2\mu^* + 3\lambda^* = 0 \tag{2.25}$$

must be accepted. The bulk viscosity $\tilde{\mu}$ is a direct indication of the departure of the mean pressure from the thermodynamic pressure expressed by the equation of state Ref. 2.7. Further, Laitone Ref. 2.7 points out that by accepting Stokes postulate for compressible flows we are at best restricted to monatomic gases. This appears to be a rather stringent assumption until one examines the type of behavior a polyatomic gas must exhibit to significantly deviate from monatomic behavior. To a first approximation the bulk viscosity $\tilde{\mu}$ characterizes the dependence of pressure on the rate of change of density Ref. 2.8. Gases which exhibit showly excited internal degrees of freedom (i.e. rotational or vibrational) in flows which have rapid changes in the state of the fluid, the pressure cannot follow the changes in density and differs from its thermodynamic equilibrium value. Thus, acceptance of Stokes' postulate for bulk viscosity is consistent with our basic assumption of local thermodynamic equilibrium used throughout this development. Henceforth, we will use

$$\lambda^* = -\frac{2}{3}\mu^* \tag{2.26}$$

in our equations. In thin shock layer equations Stokes' relation is needed only for the y-momentum equation. The order analysis has eliminated all terms containing λ in both the x-momentum and energy equation.

Plane Slab Radiation Approximation

In addition to the simplifications from the order of magnitude analysis, further simplification of the radiative flux divergence term in the energy equation is necessary in order to solve the set of integro-partial differential equations in a practical manner. Without additional simplification the conservation equations are elliptic. Two assumptions are made here in order to evaluate the radiative flux divergence term $\Lambda_{R,y}$.

- The shock layer geometry is approximated locally by an infinite plane slab.
- The shock layer is assumed to be locally one-dimensional in that radiative transport characteristics vary only across the infinite plane slab.

It has been shown that this one-dimensional plane slab model can be used in obtaining quantitative valid results, Ref. 2.9. Further, this model identically satisfies the order of magnitude analysis which dropped $\Lambda_{R,x}$. The mathematical development of this model follows that presented by Spradley and Engel, Ref. 2.10, with the exception that boundary conditions are left general following the work of R. and M. Goulard Ref. 2.11.

We note that dimensional equations will be used throughout the rest of this section without the superscript * notation unless the superscript is needed for clarity.

Let us consider the radiative transfer Eq. A.28.

$$\frac{1}{c}\frac{\partial I_\nu}{\partial t} + \bar{\Omega}_1 \cdot \nabla I_\nu = \alpha_\nu (B_\nu - I_\nu)$$

Following the steady state assumption let

$$\frac{1}{c}\frac{\partial I_\nu}{\partial t} = 0$$

Therefore our transfer equation can be written

$$\bar{\Omega}_1 \cdot \nabla I_\nu = -\alpha_\nu (I_\nu - B_\nu) \tag{2.27}$$

By imposing the one-dimensional approximation, the radiative transfer equation for the y-direction may be written

$$((\bar{j} f)) \cdot \left(\bar{j} \frac{dI_\nu}{dy} \right) = f \frac{dI_\nu}{dy} = -\alpha_\nu (I_\nu - B_\nu) \tag{2.28}$$

where $f \equiv \cos \Psi$

For the one-dimensional problem the absorption and emission characteristics vary only in one direction, y. This fact is sufficient information to solve Eq. 2.28 for the specific intensity by integration in y. We will see later that although the specific intensity is evaluated one-dimensionally the radiative flux and flux divergence must be evaluated over all space. Consequently the flux divergence is integrated over an infinite plane slab which has the same intensity variation across the slab at any station down the slab.

In order to clarify the solution of Eq. 2.28, Fig. 2.2 is presented. From Fig. 2.2 we observe

$$dy = \cos \Psi \, ds = f ds \tag{2.29}$$

By defining the optical depth as

$$\tau_v = \int \alpha_v \, dy \tag{2.30}$$

and using Eq. 2.30 the radiative transfer equation can be rewritten

$$-f \frac{dI_v}{d\tau_v} = I_v - B_v \tag{2.31}$$

The radiative transfer Eq. 2.31 can be solved formally by using the variable coefficient method:

$$I_v = C(\tau_v) \exp (\tau_v / f)$$

Substitution of the above relation into Eq. 2.31 and solving for the function $C(\tau_v)$ yields

$$C(\tau_v) = C(\tau_{v1}, \tau_{v2}) + \int B_v \exp (-\tau_v / f) d \frac{\tau_v}{f} \tag{2.32}$$

Thus the general expression for the specific intensity is

$$I_v = C(\tau_{v,1}, \tau_{v,2}) \exp (\tau_v / f) + \exp (\tau_v / f) \int_{\tau_{v,1}}^{\tau_{v,2}} B_v \exp(-\tau_v / f) \frac{d\tau}{f} \tag{2.33}$$

Splitting the integration into two parts and evaluating boundary conditions yields

$$I_v = I_v^+ + I_v^-$$

where

$$I_\nu^+ = +\int_{\tau_{\nu,w}}^{\tau_\nu} B_\nu \exp\left(-(\hat{\tau}_\nu - \tau_\nu)/f\right) \frac{d\hat{\tau}_\nu}{f} + I_\nu^+(\tau_{\nu,w}) \exp\left(-(\tau_{\nu,w} - \tau_\nu)/f\right) \tag{2.34a}$$

$$I_\nu^- = +\int_{\tau_\nu}^{\tau_{\nu,s}} B_\nu \exp\left(-(\hat{\tau}_\nu - \tau_\nu)/f\right) \frac{d\hat{\tau}_\nu}{f} + I_\nu^-(\tau_{\nu,s}) \exp\left(-(\tau_{\nu,s} - \tau_\nu)/f\right) \tag{2.34b}$$

The above equations describe the radiation field in terms of temperature through Planck's function B_ν for a nonscattering gas. The quantities $I_\nu^-(\tau_{\nu,s})$ and $I_\nu^+(\tau_{\nu,w})$ are boundary conditions and the exponentials represent attenuation over optical path length.

Using Eqs. 2.34 for the specific intensity, the radiative flux and flux divergence may be evaluated. Recalling from Appendix A, Eq. A.22, radiative flux term can be expressed as

$$\bar{q}_R(\bar{r}) = \int_0^\infty \int_0^{4\pi} I_\nu \bar{\Omega}_1 \, d\Omega \, d\nu \tag{2.35}$$

For the geometry under consideration the unit vector $\bar{\Omega}_1$ can be replaced by the direction cosine f. From Fig. 2.3 we note that

$$d\Omega = \sin \Psi \, d\Psi \, d\Theta$$

and

$$f = \cos \Psi$$

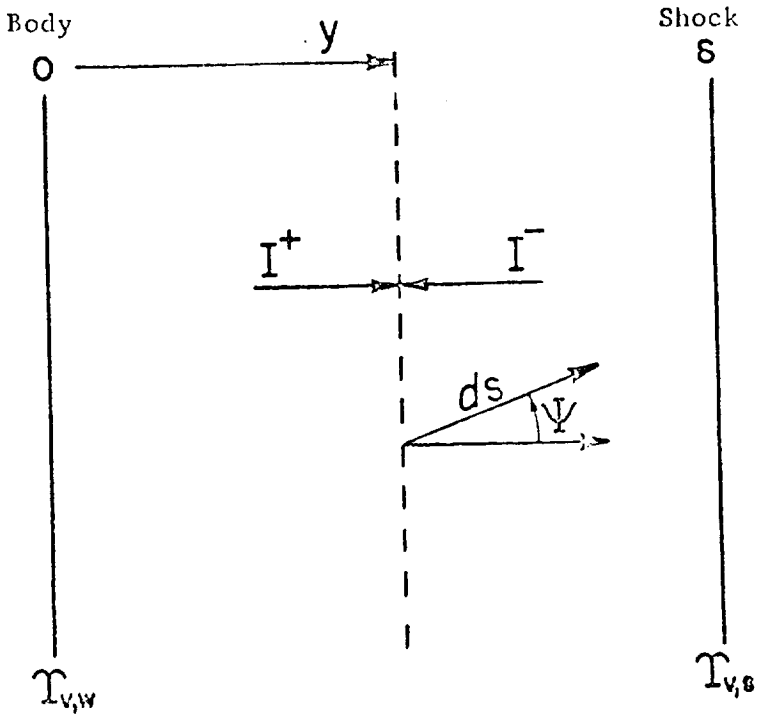

Fig. 2.2 Radiating Slab Nomenclature

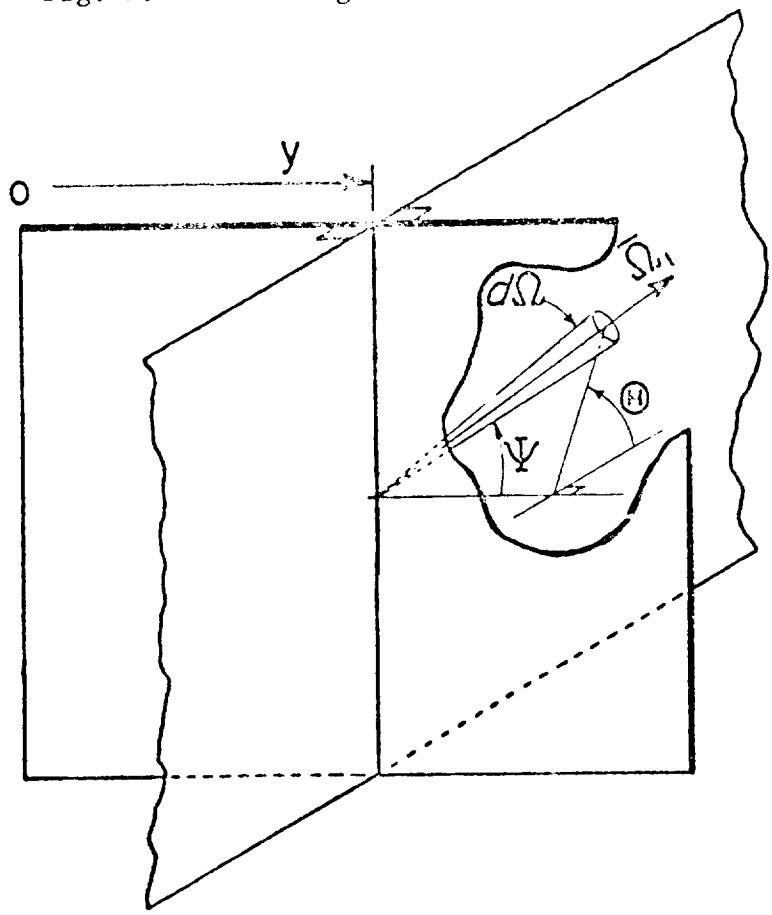

Fig. 2.3 Radiating Slab Geometry

Therefore

$$d\Omega = - df\ d\Theta \tag{2.36}$$

Substitution of Eq. 2.36 into 2.35 yields

$$q_{R,y} = - \int_0^{\infty} \int_{-1}^{1} \int_0^{2\pi} I_\nu d\Theta f \quad df\ d\nu \tag{2.37}$$

Simplifying for the one dimensional case by integration in $d\Theta$ yields

$$q_{R,y} = - 2\pi \int_0^{\infty} \int_{-1}^{1} I_\nu f\ df\ d\nu \tag{2.38}$$

It is convenient to split the integration in Eq. 2.38.

$$q^{+}_{R,y,\nu} = 2\pi \int_0^{1} I_\nu^{+} f df$$

$$q^{-}_{R,y,\nu} = 2\pi \int_0^{-1} I_\nu^{-} f df \tag{2.39}$$

Thus the monocromatic heat flux is the

$$q_{R,y,\nu} = q^{+}_{R,y,\nu} - q^{-}_{R,y,\nu}$$

Substituting Eq. 2.34 into 2.39 yields

$$q^{+}_{R,y,\nu} = - 2\pi \int_{\tau_{\nu,w}}^{\tau_\nu} B_\nu E_2(\hat{\tau}_\nu - \tau_\nu) d\hat{\tau}_\nu + 2q^{+}_{R,\nu}(\tau_{\nu,w}) E_3(\tau_{\nu,w} - \tau_\nu) \tag{2.40a}$$

$$q^{-}_{R,y,\nu} = - 2\pi \int_{\tau_\nu}^{\tau_{\nu,s}} B_\nu E_2(\tau_\nu - \hat{\tau}_\nu) d\hat{\tau}_\nu + 2q^{-}_{R,\nu}(\tau_{\nu,s}) E_3(\tau_{\nu,s} - \tau_\nu) \tag{2.40b}$$

where the direction cosine, f, dependence is expressed in terms of the exponential integral function of order n.

$$E_n = \int_0^1 f^{n-2} \exp(-t/f)df \tag{2.41}$$

Let us examine the radiative flux equation given in the third section of Appendix A.

$$q_{R,y} = \int_{y(\bar{r}_0)}^{y(\bar{r}_1)} \int_0^\infty \alpha_\nu \left(4\pi B_\nu - \int_0^{4\pi} I_\nu(\bar{r})d\Omega\right)d\nu\, dy \tag{2.42}$$

Differentiating with respect to y we obtain

$$\frac{\partial q_{R,y}}{\partial y} = \int_0^\infty \alpha_\nu \left(4\pi B_\nu - \int_0^{4\pi} I_\nu d\Omega\right)d\nu \tag{2.43}$$

which is the radiative flux divergence in the y direction. In our energy equation, Eq. 2.24, we have the term

$$\Lambda_{R,y} = \frac{\partial}{\partial y}(\tilde{\kappa} r^A q_{R,y})$$

Due to the one-dimensional planar slab approximation this term will be represented by

$$\frac{\partial}{\partial y}(\tilde{\kappa} r^A q_{R,y}) \simeq \tilde{\kappa} r^A \frac{\partial q_{R,y}}{\partial y} + q_{R,y} \frac{\partial \tilde{\kappa} r^A}{\partial y} \quad (\approx 0)$$

As a result of this approximation, an evaluation of Eq. 2.43 is sufficient to describe the radiative transfer influence in the energy equation.

In order to evaluate Eq. 2.43, the intensity at a fixed point y and in a direction defined by θ and f is integrated over all solid angles. Substituting for the solid angle, the integration for a

one-dimensional plane slab can be readily carried out.

$$\frac{\partial q_{R,y}}{\partial y} = \int_0^\infty \alpha_\nu \left(2\pi \int_{-1}^{1} I_\nu df - 4\pi B_\nu\right) d\nu \tag{2.44}$$

where the inner integral is

$$\begin{aligned}\int_1^{-1} I_\nu df = &- \int_1^0 \left[\int_{\tau_{\nu,w}}^{\tau_\nu} B_\nu \exp\left(\frac{-(\hat{\tau}_\nu - \tau_\nu)}{f}\right) \frac{d\hat{\tau}}{f} \right] df \\ &+ \int_1^0 I^+(\tau_{\nu,w}) \exp\left(\frac{-(\tau_{\nu,w} - \tau_\nu)}{f}\right) df \\ &- \int_0^1 \left[\int_{\tau_\nu}^{\tau_{\nu,s}} B_\nu \exp\left(\frac{-(\hat{\tau}_\nu\ \tau_\nu)}{f}\right) \frac{d\hat{\tau}_\nu}{f} \right] df \\ &+ \int_0^{-1} I_\nu^-(\tau_{\nu,s}) \exp\left(\frac{-(\tau_{\nu,s} - \tau_\nu)}{f}\right) df\end{aligned} \tag{2.45}$$

Eq. 2.45 can be simplified by interchanging the order of integration as substituting the exponential integral function.

$$\begin{aligned}\int_1^{-1} I_\nu df = &\int_{\tau_{\nu,w}}^{\tau_\nu} B_\nu E_1(\hat{\tau}_\nu - \tau_\nu) d\hat{\tau}_\nu \\ &- I_\nu^+(\tau_{\nu,w}) E_2(\tau_{\nu,w} - \tau_\nu) \\ &+ \int_{\tau_\nu}^{\tau_{\nu,s}} B_\nu E_1(\hat{\tau}_\nu - \tau_\nu) d\hat{\tau} \\ &- I_\nu^-(\tau_{\nu,s}) E_2(\tau_\nu - \tau_{\nu,s})\end{aligned} \tag{2.46}$$

Substituting Eq. 2.46 into 2.44 provides an expression for the radiative flux divergence in a one-dimensional slab.

$$\frac{-\partial q_R}{\partial y} = \int_0^\infty 2\pi\, \alpha_\nu \Big[\int_{\tau_{\nu,w}}^{\tau_\nu} B_\nu E_1(\tau_\nu - \hat{\tau}_\nu) d\hat{\tau}_\nu$$

$$+ I_\nu^+(\tau_{\nu,w}) E_2(\tau_\nu - \tau_{\nu,w}) \qquad (2.47)$$

$$+ \int_{\tau_\nu}^{\tau_{\nu,s}} B_\nu E_1(\hat{\tau}_\nu - \tau_\nu) d\hat{\tau}$$

$$+ I_\nu^-(\tau_{\nu,s}) E_2(\tau_{\nu,s} - \tau_\nu) - 2B_\nu \Big] d\nu$$

where the exponential integral function E_n has the following characteristics:

$$E_n(t) = E_n(-t) \quad \text{for } n = 1, 3, 5, 7, \ldots$$

$$E_n(t) = -E_n(-t) \quad \text{for } n = 2, 4, 6, 8, \ldots \qquad (2.48)$$

Eq. 2.47 is valid for arbitrary boundary conditions with the exception that only one boundary reflection of a photon packet is allowed. In practice, for a shock layer solution, the subscript "w" is interpreted as conditions at the wall or body and "s" as conditions at the shock. Under this interpretation $I^-(\tau_{\nu,s}) = 0$ barring precursor radiation and the optical depth at the wall $\tau_{\nu,w} = 0$. Further, for the case of a perfect absorbing wall $I^+(0) = 0$. These simplifications are the usual ones made in describing radiation transport in a radiating shock layer. Making these simplifications reduces Eq. 2.47 to Eq. B.31 of Ref. 2.10.

In order to numerically compute the flux and flux divergence when considering line radiation it is advantageous to solve the radiative transfer equation in physical space rather than in optical depth space. To this end the following development is given.

The radiative transfer equation is

$$-f\frac{dI_\nu}{dy} = \alpha_\nu(I_\nu - B_\nu) \tag{2.31}$$

The formal solution of Eq. (2.31) follows the same procedure stated before with the exception that f is assumed to be an average value of 1/2 (Ref. 2.12)

$$I_\nu^+ = +\int_0^y \frac{\alpha_\nu B_\nu}{f} e^{-\frac{1}{f}\int_{y'}^{y}\alpha_\nu d\hat{y}}\, d\hat{y}$$

$$I_\nu^- = +\int_y^\delta \frac{\alpha_\nu B_\nu}{f} e^{-\frac{1}{f}\int_{y}^{y'}\alpha_\nu d\hat{y}}\, d\hat{y} \tag{2.49}$$

These two equations are the counter parts of Eqs. 2.34 a and b with the boundary conditions set to zero. From Eq. 2.39 the radiative flux equations may be written

$$q_R^+ = \pi\int_0^\infty I_\nu^+ d\nu$$

$$q_R^- = \pi\int_0^\infty I_\nu^- d\nu \tag{2.50}$$

Finally using Eq. 2.44 the flux divergence equation may be written as

$$\frac{\partial q_{R,y}}{\partial y} = -2\pi\int_0^\infty \alpha_\nu(2B_\nu - I_\nu)d\nu \tag{2.51}$$

The one-dimensional planar slab approximations which result in Eq. 2.51 have important ramifications to our shock layer problem. Radiation calculations can be made using Eq. 2.51 at each ξ location independent of other ξ locations. This makes the thin shock layer equations a set of parabolic partial integro-differential equations which can be solved using marching schemes which are used for solving classical boundary layer equations.

An observation concerning the planar slab approximation is in order at this point. This approximation eliminates all curvature effects from the radiation calculation. A more appropriate approximation for most axisymmetrically blunted vehicles would be a concentric sphere approximation for the boundaries of the shock layer as proposed by Viskanta, Ref. 2.13. For a two-dimensional body the corresponding approximation is quite obviously concentric cylinder boundaries. However, as pointed out by Viskanta, Ref. 2.13, comparatively little attention has been given to radiative transfer in curvilinear systems. The paper by Viskanta analyzed the steady state radiative transfer between two concentric, gray, opaque spheres separated by a gray absorbing and emitting medium which generated heat uniformily. He concluded, for constant absorption coefficients, that curvature effects were evident for concentric sphere radii ratios as high as .99. This corresponds approximately to a shock standoff distance of $\delta/R \approx .01$. Nominal hypersonic standoff distances are $.04 \leq \delta/R \leq .10$. From Viskanta's work we are led to expect that

curvature effects may be significant for both radiative flux and flux divergence in a typical shock layer. The actual magnitude of these effects are difficult to assess because of the constant absorption coefficient assumption and differences in boundary conditions for the problem under consideration. Thus as far as is known an accurate assessment of curvature effects on shock layer radiative transport is absent today. It is felt that using a concentric sphere model is analogus to including both first and second order effects whereas the infinite parallel plate model includes only first order effects. However, for the present we will use the infinite parallel plate model in our development.

Statement of Shock Layer Equations

As a result of the order of magnitude analysis, the bulk viscosity assumption, and the planar radiative transfer model the second order thin shock layer equations may be written in a more usable form. In addition, a relation for the y-component of the heat flux vector from Appendix A was used to yield the second order equations given in Tab. 2.2.

Let us now examine the simplifications which are needed to obtain the first order shock layer equations and classical boundary layer equations from the equations stated above. First let us drop all terms of order $\bar{\rho}$ or smaller. The resulting first order shock layer equations are given in Tab. 2.3. Additional simplifications can be made by assuming the boundary layer thickness to be small in comparison to the local body radius. This implies

TABLE 2.2

SECOND ORDER SHOCK LAYER EQUATIONS

Global continuity:

$$\frac{\partial}{\partial x}\left(r^{A}\rho u\right) + \frac{\partial}{\partial y}\left(\tilde{\kappa} r^{A}\rho v\right) = 0 \tag{2.52}$$

Species continuity:

$$\frac{\partial}{\partial x}\left(r^{A}\rho C_{i} u\right) + \frac{\partial}{\partial y}\left(\tilde{\kappa} r^{A}\rho C_{i} v\right) = -\frac{\partial}{\partial y}\left(\tilde{\kappa} r^{A} J_{i,y}\right) + \tilde{\kappa} r^{A}\omega_{i} \tag{2.53}$$

x - Momentum:

$$\rho r^{A} u \frac{\partial u}{\partial x} + \rho \tilde{\kappa} r^{A} v \frac{\partial u}{\partial y} + \rho \kappa r^{A} uv = -r^{A}\frac{\partial P}{\partial x}$$

$$+ \frac{\partial}{\partial y}\left(\tilde{\kappa} r^{A}\mu \frac{\partial u}{\partial y}\right) - \kappa u \frac{\partial r^{A} u}{\partial v} \tag{2.54}$$

y - Momentum: ($O[\bar{\rho}]$ and larger terms)

$$\rho r^{A} u \frac{\partial v}{\partial x} + \rho \tilde{\kappa} r^{A} v \frac{\partial v}{\partial y} - \rho \kappa r^{A} u^{2} = -\tilde{\kappa} r^{A}\frac{\partial P}{\partial y}$$

$$+ \frac{\partial}{\partial x}\left(r^{A}\mu \frac{\partial u}{\partial y}\right) - \frac{2}{3}\frac{\partial}{\partial y}\left(\mu \frac{\partial r^{A} u}{\partial x}\right) + \frac{4}{3}\frac{\partial}{\partial y}\left(\kappa r^{A}\mu \frac{\partial v}{\partial y}\right) \tag{2.55}$$

$$- \frac{2}{3}\frac{\partial}{\partial y}\left(\kappa r^{A}\mu v + \tilde{\kappa}\mu v \frac{\partial r^{A}}{\partial y}\right)$$

TABLE 2.2 (Cont.)

y - Momentum: (0 $[\bar{\rho}^2]$ and larger terms)

$$\rho r^A u \frac{\partial v}{\partial x} + \rho r^A \underset{\sim}{\kappa} v \frac{\partial v}{\partial y} - \rho \kappa r^A u^2 = - \underset{\sim}{\kappa} r^A \frac{\partial P}{\partial y}$$

$$+ \frac{\partial}{\partial x}\left(r^A \mu \frac{\partial u}{\partial y}\right) - \frac{2}{3}\frac{\partial}{\partial y}\left(\mu \frac{\partial r^A u}{\partial x}\right) + \frac{4}{3}\frac{\partial}{\partial y}\left(\underset{\sim}{\kappa} r^A \mu \frac{\partial v}{\partial y}\right)$$

$$- \frac{2}{3}\frac{\partial}{\partial y}\left(\kappa r^A \mu v\right) - \frac{\partial}{\partial x}\left(r^A \kappa \mu u\right) + \frac{2}{3}\mu \frac{\kappa}{\underset{\sim}{\kappa}} \frac{\partial}{\partial x}\left(r^A u\right) \qquad (2.56)$$

$$+ \frac{2}{3}\mu \frac{\kappa}{\underset{\sim}{\kappa}} \frac{\partial}{\partial y}\left(\underset{\sim}{\kappa} r^A v\right) - 2\mu \frac{\kappa}{\underset{\sim}{\kappa}} r^A \frac{\partial u}{\partial x} - \frac{2}{3}\frac{\partial}{\partial y}\left(\underset{\sim}{\kappa} \mu v \frac{\partial r^A}{\partial y}\right)$$

Energy:

$$r^A \rho u \frac{\partial H}{\partial x} + \underset{\sim}{\kappa} r^A \rho v \frac{\partial H}{\partial y} = \frac{-\partial}{\partial y}\left[\underset{\sim}{\kappa} r^A \left\{-k \frac{\partial T}{\partial y} + \sum_i h_i J_{i,y}\right.\right.$$

$$\left.\left. - \frac{P}{N^2} \sum_i \sum_{j \neq i} \frac{N_i}{m_i} \frac{D_i^T}{\mathbb{D}_{ij}} \left(\frac{J_{j,y}}{\rho_j} - \frac{J_{i,y}}{\rho_i}\right)\right\}\right] - \underset{\sim}{\kappa} r^A \frac{\partial q_{R,y}}{\partial y} \qquad (2.57)$$

$$\frac{\partial}{\partial y}\left(\underset{\sim}{\kappa} r^A \mu u \frac{\partial u}{\partial y}\right) - \frac{\partial}{\partial y}\left(\kappa r^A \mu u^2\right)$$

TABLE 2.3

FIRST ORDER SHOCK LAYER EQUATIONS

(Order determined at $R_e = \rho_\infty U_\infty R/\mu_{\delta,o} = 100$)

Global continuity:

$$\frac{\partial}{\partial x}(\rho r^A u) + \frac{\partial}{\partial y}(\tilde{\kappa} r^A v) = 0 \tag{2.52}$$

Species continuity:

$$\frac{\partial}{\partial x}(r^A \rho C_i u) + \frac{\partial}{\partial y}(\tilde{\kappa} r^A \rho C_i v) = -\frac{\partial}{\partial y}(\tilde{\kappa} r^A J_{i,y}) + \tilde{\kappa} r^A \omega_i \tag{2.53}$$

x - Momentum:

$$\rho r^A u \frac{\partial u}{\partial x} + \rho \tilde{\kappa} r^A v \frac{\partial u}{\partial y} = -r^A \frac{\partial P}{\partial x} + \frac{\partial}{\partial y}\left[\tilde{\kappa} r^A \mu \frac{\partial u}{\partial y}\right] \tag{2.58}$$

y - Momentum:

$$\rho \kappa u^2 = \tilde{\kappa} \frac{\partial P}{\partial y} \tag{2.59}$$

Energy:

$$r^A \rho u \frac{\partial H}{\partial x} + \tilde{\kappa} r^A \rho v \frac{\partial H}{\partial y} = \frac{\partial}{\partial y}\left(\tilde{\kappa} r^A k \frac{\partial T}{\partial y}\right) - \frac{\partial}{\partial y}\left(\tilde{\kappa} r^A \left\{ \sum_i h_i J_{i,y} - \frac{P}{N^2} \sum_i \sum_{j \neq i} \frac{N_i}{m_i} \frac{D_i^T}{\mathbb{D}_{i,j}} \left(\frac{J_{j,y}}{\rho_j} - \frac{J_{i,y}}{\rho_i} \right) \right\} \right) - \tilde{\kappa} r^A \frac{\partial q_{R,y}}{\partial y} + \frac{\partial}{\partial y}\left(\tilde{\kappa} r^A \mu u \frac{\partial u}{\partial y}\right) \tag{2.60}$$

$$\kappa \to 0, \quad \tilde{\kappa} \to 1 \quad \text{and} \quad r^A \to r_w^A \tag{2.61}$$

Using these limits in the first order shock layer equations results in the boundary layer equations given in Tab. 2.4.

Equations 2.62 through 2.66 are essentially the same as the boundary layer (B.L.) equations which are given by Fay and Riddell Ref. 2.14, Dorance Ref. 2.15 and others. The boundary layer equations for a flat plate are obtained by simply noting that r_w^A is not a function of x. We can conclude from the foregoing simplifications of the thin shock layer equations that the classical Prandtl type boundary equations contain only first order terms which exhibit no normal component curvature effects.

Boundary Conditions

Having stated the thin shock layer and boundary layer equations, the appropriate boundary conditions for the two sets of equations can now be discussed. Figure 2.4 presents a sketch of the various regions and boundaries of particular interest in the thin shock layer problem. We note that, in addition to the shock layer region the char layer and decomposition zone (see Fig. 1.6) are important in our problem. These regions are important because the momentum, energy and mass transfer in the char and decomposition regions are intimately coupled to the transfer in the shock layer. Theoretically we could consider all the processes which take place between the shock wave and the virgin plastic of the body and attempt to solve the governing equations for this boundary value problem. However, it is

TABLE 2.4

BOUNDARY LAYER EQUATIONS

Global continuity:

$$\frac{\partial}{\partial x}\left(r_w^A \rho u\right) + r_w^A \frac{\partial}{\partial y}\left(\rho v\right) = 0 \tag{2.62}$$

Species continuity:

$$\frac{1}{r_w^A}\frac{\partial}{\partial x}\left(r_w^A \rho C_i u\right) + \frac{\partial}{\partial y}\left(\rho C_i v\right) = -\frac{\partial}{\partial y}\left(J_{i,y}\right) + \omega_i \tag{2.63}$$

x - Momentum:

$$\rho u \frac{\partial u}{\partial x} + \rho v \frac{\partial u}{\partial y} = -\frac{\partial P}{\partial x} + \frac{\partial}{\partial y}\left(\mu \frac{\partial u}{\partial y}\right) \tag{2.64}$$

y - Momentum:

$$0 = \frac{\partial P}{\partial y} \tag{2.65}$$

Energy:

$$\rho u \frac{\partial H}{\partial x} + \rho v \frac{\partial H}{\partial y} = \frac{\partial}{\partial y}\left(k \frac{\partial T}{\partial y}\right) - \frac{\partial}{\partial y}\left\{ \sum_i h_i J_{i,y} - \frac{P}{N^2} \sum_i \sum_{i \neq j} \frac{N_i}{m_i} \frac{D_i^T}{\mathbb{D}_{ij}} \left(\frac{J_{j,y}}{\rho_j} - \frac{J_{i,y}}{\rho_i} \right) \right\} - \frac{\partial q_{R,y}}{\partial y} + \frac{\partial}{\partial y}\left(\mu u \frac{\partial u}{\partial y}\right) \tag{2.66}$$

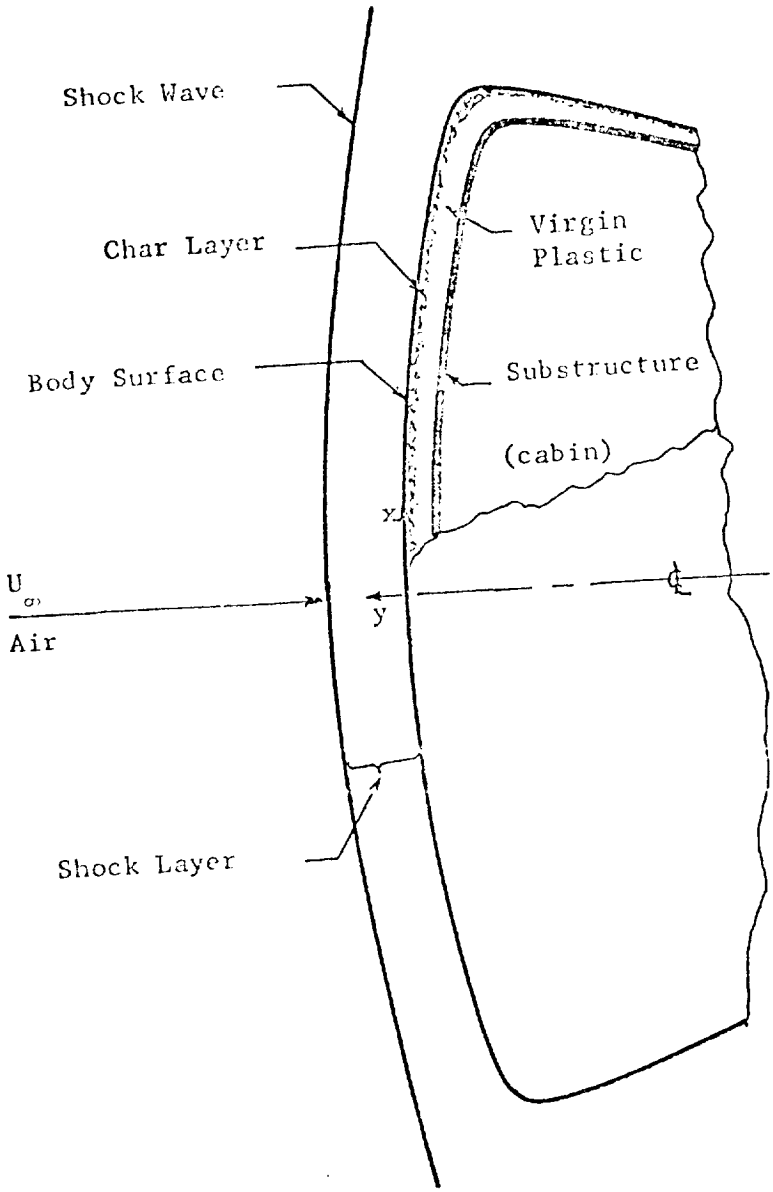

Fig. 2.4 Schematic of Interaction Regions of Shock Heated Air and a Charring Ablator for a Bluff Body

more practical to divide the solution of this general problem into a shock layer and a material response problem and iterate on the boundary conditions at the material surface. Therefore, it is important to realize what information is available from the material response solution which could be used for boundary conditions of the thin shock layer equations. This is accomplished by integrating the conservation equations across the char-gas interface and reducing the spatial increment to zero to yield surface balance equations. With this perspective of the general problem in mind, the nature of the thin shock layer equations and boundary conditions will be discussed.

The parabolic nature of the thin shock layer equations mathematically requires initial conditions as well as boundary conditions in order to obtain a solution. The entry vehicles axis of symmetry is the appropriate location of the starting line for zero angle of attack problems. The determination of conditions along this line, called the stagnation line, is a major and important problem in itself. Consequently, development of the method to obtain these initial conditions (i.e. stagnation line solutions) is delayed until after the boundary conditions are established.

As discussed in the next section, the thin shock equations are a set of parabolic integro-differential equations with initial values given along $x = 0$, the stagnation line. Because the shock wave location is not known before hand, the blunt body problem is mathematically referred to as a free boundary problem. Given initial

conditions along the stagnation line and boundary conditions along the body, the thin shock layer equations can theoretically be solved with a simultaneous development of the shock geometry and corresponding shock boundary conditions. The shock geometry (see Fig. A.3) can be obtained by carrying out the following integration.

$$\delta^* = \int_0^{x^*} (1 + \kappa^* \delta^*) \tan \epsilon dx^* + \delta_o^* \tag{2.67}$$

In practice another technique has been used to determine the shock geometry Ref. 2.3, 2.10 and others. The shock geometry is assumed and specified in terms of $d\epsilon/dx$. Iterations are made around the body until the input and output shock geometry coincide.

If the shock geometry is known, the Rankine-Hugoniot equations can be used to obtain the shock boundary conditions. The development of these equations in curvilinear coordinates follows directly from Ref. 2.10. The dimensional Rankine-Hugonoit equations written in rectangular coordinates are:

Continuity:

$$\rho_\infty^* V_{\infty,n}^* = \rho_s^* V_{s,n}^* \tag{2.68}$$

Momentum:

(normal) $$\rho_\infty^* V_{\infty,n}^{*2} + P_\infty^* = \rho_s^* V_{s,n}^{*2} + P_s^* \tag{2.69}$$

(tangential) $$V_{\infty,t}^* = V_{s,t}^* \tag{2.70}$$

Energy:

$$\tfrac{1}{2} V_{\infty,t}^{*2} + \tfrac{1}{2} V_{\infty,n}^{*2} + h_{\infty}^{*} = \tfrac{1}{2} V_{s,t}^{*2} + \tfrac{1}{2} V_{s,n}^{*2} + h_{s}^{*} \qquad (2.71)$$

Using Fig. 2.5 the above equations can be written in body oriented coordinates. From geometry we have

$$v_s^{*} = V_{s,t}^{*} \sin \epsilon - V_{s,n}^{*} \cos \epsilon \qquad (2.72)$$

$$u_s^{*} = V_{s,t}^{*} \cos \epsilon - V_{s,n}^{*} \sin \epsilon \qquad (2.73)$$

where

$$V_{\infty,n}^{*} = U_{\infty}^{*} \cos \varphi$$

$$V_{s,n}^{*} = \bar{\rho} U_{\infty}^{*} \cos \varphi$$

$$V_{s,t}^{*} = V_{\infty,t}^{*} = U_{\infty}^{*} \sin \varphi$$

Substituting for $V_{\infty,n}^{*}$, $V_{s,n}^{*}$ and $V_{\infty,t}^{*}$ Eqs. 2.72 and 2.73 yield

$$v_s^{*} = U_{\infty}^{*} \sin \varphi \sin \epsilon - \bar{\rho} U_{\infty}^{*} \cos \varphi \cos \epsilon \qquad (2.74)$$

$$u_s^{*} = U_{\infty}^{*} \sin \varphi \cos \epsilon - \bar{\rho} U_{\infty}^{*} \cos \varphi \sin \epsilon \qquad (2.75)$$

The pressure behind the shock can be obtained by using the normal momentum equation and substituting for $V_{\infty,n}^{*}$ and $V_{s,n}^{*}$.

$$\rho_{\infty}^{*}(U_{\infty}^{*} \cos \varphi)^2 + P_{\infty}^{*} = \rho_s^{*}(\bar{\rho} U_{\infty}^{*} \cos \varphi)^2 + P_s^{*} \qquad (2.76)$$

By substituting normal and tangential velocities the energy equation can be written

$$h_s^* = \frac{U_\infty^{*2}}{2} - \tfrac{1}{2}(u_s^{*2} + v_s^{*2}) + h_\infty^* \tag{2.77}$$

The tangential velocity is negligible near the stagnation line and thus reducing 2.77 to

$$h_s^* = \tfrac{1}{2} U_\infty^{*2} (1 - \bar{\rho}^2) \cos^2 \varphi + h_\infty^* \tag{2.78}$$

Nondimensionalizing Eqs. 2.74 through 2.78 and dropping P_∞ and h_∞ which are order $(\bar{\rho}^2)$ yields the following shock boundary conditions.

$$v_s = \sin \varphi \sin \epsilon - \bar{\rho} \cos \varphi \cos \epsilon \tag{2.79}$$

$$u_s = \sin \varphi \cos \epsilon + \bar{\rho} \cos \varphi \sin \epsilon \tag{2.80}$$

$$P_s = (1 - \bar{\rho}) \cos^2 \varphi \tag{2.81}$$

$$h_s = (1 - \bar{\rho}^2) \cos^2 \varphi \tag{2.82}$$

or

$$h_s = 1 - (u_s^2 + v_s^2) \tag{2.83}$$

It is important to realize that the Rankine-Hugoniot relations are valid only if strong precursor radiation effects do not become important. The shock conditions can be more adequately described for the strong precursor radiation problem with modified Rankine-Hugoniot relations presented by Zeldovich and Raezer (Ref. 2.16). However, significant precursor radiation effects are not experienced in air below flight velocities of approximately 60,000 to 65,000 ft./sec. as demonstrated by Lasher and Wilson (Ref. 2.17). Therefore,

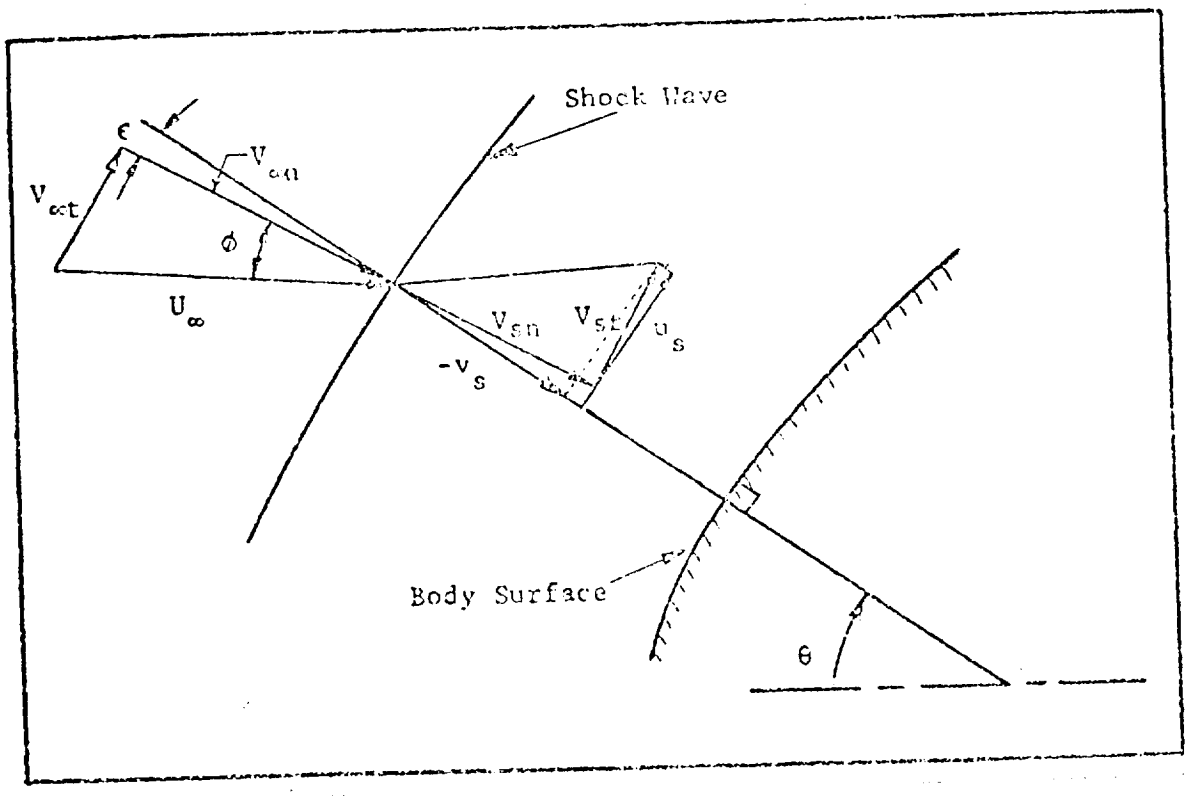

Fig. 2.5 Resolution of Velocity Components in a Body Oriented Coordinate System

the Rankine-Hugoniot relations provide satisfactory boundary conditions for the outer edge of the thin shock layer equations for many problems of current interest in atmospheric entry. Let us now write the shock boundary conditions at $y = \delta$.

$$
\begin{aligned}
u &= u_s \\
v &= v_s \\
P &= P_s \\
h &= h_s \\
C_i &= C_{is}(P_s, h_s) \text{ (Assuming chemical equilibrium)} \\
I_v^-(\tau_{v,s}) &= 0
\end{aligned}
\tag{2.84}
$$

The Rankine-Hugoniot equations provide expressions for u_s, v_s, P_s, and h_s. The equation of state and free stream elemental mass fraction provides the additional information needed to determine the post shock species mass fractions assuming chemical equilibrium. The specific intensity coming through the shock towards the body is specified as zero. We note that in total four boundary conditions are needed for the energy equation because of its integro-differential nature. Thus two boundary conditions, enthalpy and specific intensity, have been specified at the shock.

The corresponding body surface boundary conditions can be written for $y = 0$:

$$
\begin{aligned}
&u = 0 \\
&v = v_w \\
&P = P_w \\
&h = h_w \\
&C_i = C_{i,w} \\
&\begin{cases} I_\nu^{+}(\tau_{\nu,w}) = B_\nu \\ \tau_{\nu,w} = 0 \end{cases}
\end{aligned}
\tag{2.85}
$$

The boundary conditions specified in 2.84 and 2.85 are sufficient to solve the thin shock layer equations. However, substitution of equivalent boundary conditions for some surface conditions is found to be practical. For example the normal velocity at the wall is usually replaced by $(\rho v)_w$. Of greater practical importance is the wall boundary condition on pressure. This pressure is not known a priori. An equivalent boundary condition is then needed. There are at least two suitable boundary conditions which might be used in lieu of pressure. These are the normal pressure gradient at the shock or the normal pressure gradient at the body. The normal pressure gradient at the shock could be specified by evaluating the inviscid y - momentum equation at the shock using the Rankine-Hugoniot equations. The normal pressure gradient at the body could be set equal to zero from boundary layer theory. Each of these conditions would involve some degree of approximation. The effect

of these approximations are not evaluated here. To evaluate the pressure gradient at the shock an approximate form of the continuity equation is needed. Correspondingly the zero normal pressure gradient assumption at the wall neglects the wall velocity head at the body which would push the true stagnation pressure point off the body. An additional complicating factor arises when one observes what boundary condition is needed in the material response analysis. The pressure at the outer wall is usually specified as a boundary condition Ref. 2.18. Ideally one would like to know and specify the pressure boundary condition for both problems. This would eliminate iterating on this variable between the two solutions.

The surface boundary conditions can be derived by integrating the conservation equations across the boundary and taking the limit as the spatial increment approaches zero. This method assures inclusion of all the effects accounted for in the flow-field equations.

A photograph of a section of charring ablator is shown in Fig. 1.5 in which the important zones are indicated. The ablative composite's response during entry may be analyzed in two ways. One is a transient analysis which gives the response of the material as a time function of its heating environment. The other is a quasi-steady analysis which predicts a constant, history independent, rate of decomposition for a given heating environment. Experimental evidence indicates the conditions under which the quasi-steady behavior exist. As the material is heated, the surface is removed

by chemical reactions, sublimation and erosion; as a result, the total thickness of the material decreases as shown by the data in Fig. 2.6. Concurrently decomposition in depth and a char build up occur. When an equilibrium situation exists such that a constant char thickness and a constant surface recession velocity are maintained, a quasi-steady response would physically exist. Additional evidence that a quasi-steady ablator response would occur during hyperbolic entry has been presented by Ref. 2.29. Theoretical calculations using a transient ablator analysis and a quasi-steady analysis were shown to yield essentially identical results over tne peak heating portion of a typical trajectory. This portion of the trajectory is the conditions of current interest.

As indicated in Fig. 2.6 the char depth is of the order 0.3 inches for lunar entry conditions. This thickness should be nearly independent of heating rate and thus applicable to hyperbolic entry conditions. The flow through the char can be considered one dimensional unless the ratio of the char thickness to the local surface curvature is somewhat smaller than .05 (Ref. 2.19). For ratios of the order .05 or greater the flow-field pressure variations may cause multidimensional flow through the char. Since the surface radii under consideration are of the order of 1 to 15 feet, the one dimensional flow approximation should be quite good. Moreover, since the porous char and decomposition zones are quite thin with respect to the body radius, the pressure through the zones can be assumed constant.

The quasi-steady surface balance equations were derived by Esch in Ref. (2.20) using the preceeding assumptions applied to equations

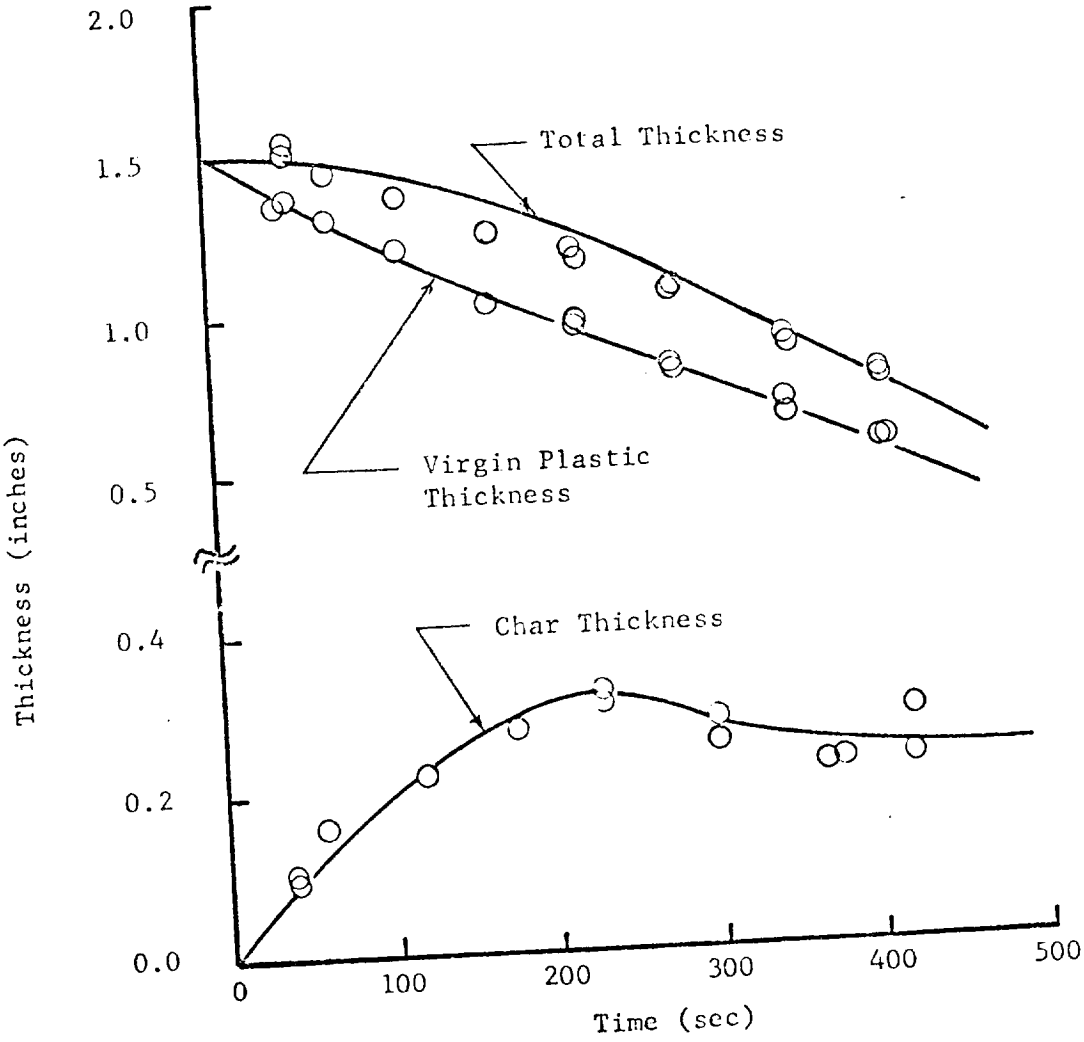

Fig. 2.6 Thickness of the Char and Virgin Plastic as a Function of Time (Ref. 2.28)

2.52 to 2.55 and 2.57. From the development in Ref. (2.20), the species boundary conditions are:

Species boundary conditions:

$$(\rho v C_i)^- + J_i^- + (R_i + S_i)(1 - \epsilon_p) = (\rho v C_i)^+ + J_i^+ \tag{2.86}$$

where R_i = mass rate of formation of species i by heterogeneous reactions

S_i = mass rate of sublimation of species i by homogeneous reactions

ϵ_p = char porosity (volume of voids per unit volume)

and where the superscript - and + means evaluated on the char side and flow-field side of the surface respectively.

The elemental boundary conditions can be obtained by multiplication of Eq. 2.86 by

$$e_{ij} = \frac{A_{ij} m_j}{M_i} \tag{2.87}$$

where

A_{ij} = moles of element j per mole of compound i

m_j = atomic weight of element j

M_i = molecular weight of compound i

and summing over all compounds i.

$$(\rho v)^- \sum_{i=1}^{n} e_{ij} C_i^- + \sum_{i=1}^{n} e_{ij} J_i^- + \sum_{i}^{n} e_{ij}(R_i+S_i)(1-\epsilon_p) = (\rho v)^+ \sum_{i=1}^{n} e_{ij} J_i^+ + \sum_{i=1}^{n} e_{ij} J_i^+ \tag{2.88}$$

The above equation can be expressed in terms of the elemental mass fractions, $\tilde{C}_j$, and the elemental mass fluxes, $\tilde{J}_j$.

Elemental species boundary condition:

$$(\rho v \tilde{C}_j)^- + \tilde{J}_j^- = (\rho v \tilde{C}_j)^+ + \tilde{J}_j^+ \tag{2.89}$$

The momentum boundary condition was obtained using the y - momentum equation of order ρ^{-2}.

Momentum boundary condition:

$$P^+ = P^- - (\rho v + \frac{4}{3}\kappa\, \mu_{ave})(v^+ - v^-) + \frac{4}{3}\left(\mu \frac{dv}{dy}\right)^+ - \frac{4}{3}\left(\mu \frac{dv}{dy}\right)^- \tag{2.90}$$

The surface energy balance equation was derived noting that no significant radiative transfer occurs within the char.

Energy boundary condition:

$$(1+\kappa)k \left.\frac{dT}{dy}\right|^- = \rho v \sum h_i (C_i^+ - C_i^-) + (1+\kappa)\Big[\sum h_i J_i^+ - \frac{P}{\rho N^2} \sum_i^n \sum_{j\neq i} \frac{N_i}{m_i} \frac{D_i^T}{\mathbb{D}_{ij}} \left(\frac{J_j}{C_j} - \frac{J_i}{C_i}\right)^+ \Big] + (1+\kappa) k_b \left.\frac{dT}{dy}\right|^- + q_R^+ \tag{2.91}$$

The radiation term, q_R^+, is the sum of the radiation flux to the surface from the flow-field minus the reradiated energy flux.

These surface boundary conditions express the coupling relationships which exist between the flow-field and the ablator. If diffusion is significant near the surface, the species balance is a boundary condition of the third kind. The momentum balance indicates a complicated coupling of the surface pressure to both the internal and external normal velocity profile if terms of order ρ^{-2} are retained. The energy balance is a boundary condition of the second kind in temperature with additional convective, mass and thermal diffusion, species and radiation coupling. The complexity of these boundary conditions suggest simplifications must be made, where possible, to arrive at a tractable set to be used. A simplified set of boundary conditions is selected in the next section.

Typical boundary conditions for the boundary layer equations can now be discussed in terms of the ones used for the shock layer equations. Outer boundary conditions along a line between the shock and the body known as the boundary layer edge are used rather than the Rankine-Hugoniot equations. These edge conditions are usually obtained using some inviscid layer analysis which is bounded by a shock and a streamline. The method of characteristics is used for the supersonic portion of the flow and typically a Belostserkovskii strip integral technique is used for the near stagnation subsonic flow (Ref. 2.2). These methods provide the following boundary layer edge conditions

$$
\begin{aligned}
&u = u_e \\
&v = v_e = 0 \\
&P = P_e \\
&h = h_e \text{ or } g = g_e = 1 \\
&C_i = C_{ie}(P_e, h_e) \quad \text{(assuming chemical equilibrium)} \\
&I_v^-(\tau_{v,e}) \quad \text{(usually not used)}
\end{aligned}
\tag{2.92}
$$

The boundary layer wall boundary conditions that are usually employed can be written:

$$
\begin{aligned}
&u = u_w = 0 \\
&\rho v = (\rho v)_w \\
&P = P_w = P_e \\
&h = h_w \text{ or } g = g_w \\
&C_i = C_{iw} \\
&I_w^+(\tau_{v_i w}) = B_v \quad \text{(usually not used)}
\end{aligned}
\tag{2.93}
$$

If the spectral intensity is eliminated from the previous two sets of boundary conditions they are equivalent to those presented in Chapter 1 of Ref. 2.15. One can observe that the problem of iterating on pressure between a boundary layer solution and material response solution is eliminated. However, this problem is left unresolved in that the correct edge pressure can be obtained accurately only through an iteration procedure between the inviscid

flow analysis and the boundary layer analysis. It is also significant to point out that, although usually not attempted, it is computationally rather difficult to handle boundary layer and inviscid flows which are coupled by radiative transfer. In addition to the geometrical integration problems the boundary condition on specific intensity or radiative flux is not a single value but a frequency dependent function which must be matched at the boundary layer edge.

Stagnation Line Equations

To this point we have not discussed how initial values for the thin shock layer equations may be determined. This problem is of near equal importance to the entire shock layer problem and will be discussed in the remainder of this section. To obtain initial values for the shock layer solution, a reduced set of the thin shock layer equations must be solved at $x = 0$ along y, the stagnation line (see Fig. 2.4). The solution of this of equations is of major importance because (1) the highest heating rates and pressures on a body are experienced at the stagnation point (2) any distributional shock layer solution because of its parabolic nature is only as valid as its initial values and (3) the thin shock layer equations along characteristics $x = \text{constant}$ reduce to ordinary differential equations like at the stagnation line. Thus by developing a stagnation line solution an important problem is solved and a great deal of the work is completed which is applicable to the total shock layer problem. This is primarily why the stagnation line problem has received a great deal of attention in the past decade.

The solution to the stagnation line (S L) problem by direct methods has been approached in two ways. The work of Ho and Probstein (Ref. 2.22) typifies the stagnation region solutions which use expansions of the dependent variables in x to obtain the stagnation and near stagnation line equations. The work of Hoshizaki and Wilson (Ref. 2.3) typifies the stagnation line solutions which determine the stagnation line equations by formally taking the limit of the terms in the shock layer equations at x = 0 using symmetry conditions. The latter method is used in this development.

From this point on in the development, attention will be restricted to axisymmetric bodies for which the exponent A = 1 (i.e. $r^A = r$). With this restriction noted, let us first examine the global continuity equation in expanded dimensional form.

$$\frac{\partial}{\partial x}(\rho u) + \frac{\partial}{\partial y}(\tilde{\kappa}\rho v) + \frac{\rho u}{r}\frac{\partial r}{\partial x} + \tilde{\kappa}\frac{\rho v}{r}\frac{\partial r}{\partial y} = 0 \tag{2.94}$$

As $x \to 0$ the following limit is approached

$$\lim_{x\to 0}\frac{1}{r}\frac{\partial r}{\partial x} = 0 \quad \text{and} \quad \lim_{x\to 0}\frac{u}{r}\frac{\partial r}{\partial x} = \frac{\partial u}{\partial x} \tag{2.95}$$

assuming a spherically shaped body at x = 0. Also, note that

$$\frac{1}{r}\frac{\partial r}{\partial y} = \left[\frac{\sin\theta}{(1/\kappa + y)\sin\theta}\right] = \frac{\kappa}{1+\kappa y} = \frac{\kappa}{\tilde{\kappa}} \tag{2.96}$$

Using these conditions the global continuity equation can be rewritten.

Global continuity (S L)

$$2\frac{\partial}{\partial x}(\rho u) + \frac{\partial}{\partial y}(\tilde{\kappa}\rho v) + \kappa\rho v = 0 \tag{2.97}$$

The species continuity equation can be rewritten by subtracting the global continuity Eq. 2.52 from the left hand side of Eq. 2.53.

$$r^A \rho u \frac{\partial C_i}{\partial x} + r^A \tilde{\kappa}\rho v \frac{\partial C_i}{\partial y} = -\frac{\partial}{\partial y}(\tilde{\kappa} r^A J_{i,y}) + \tilde{\kappa} r^A \omega_i \tag{2.98}$$

Noting that at x = 0, u = 0 and using Eq. 2.96 in Eq. 2.98 yields

Species continuity: (S L)

$$\tilde{\kappa}\rho v \frac{\partial C_i}{\partial y} = -\frac{\partial}{\partial y}(\tilde{\kappa} J_{i,y}) - \kappa J_{i,y} + \tilde{\kappa}\omega_i \tag{2.99}$$

or by noting $\frac{\partial \tilde{\kappa}}{\partial y} = \kappa$

$$\rho v \frac{\partial C_i}{\partial y} = -\frac{\partial}{\partial y}(J_{i,y}) - \frac{2\kappa}{\tilde{\kappa}} J_{i,y} + \omega_i \tag{2.100}$$

Now consider the x - momentum Eq. 2.54

$$r^A \rho u \frac{\partial u}{\partial x} + \tilde{\kappa} r^A \rho v \frac{\partial u}{\partial y} + \kappa r^A \rho u v = -r^A \frac{\partial P}{\partial x}$$

$$+ \frac{\partial}{\partial y}(\tilde{\kappa} r^A \mu \frac{\partial u}{\partial y}) - \kappa u \frac{\partial}{\partial y}(r^A \mu)$$

By evaluating the above equation at x = 0, relatively little information is obtained. Along the stagnation line u = 0 for all y; therefore

$$\left(\frac{\partial u}{\partial y}\right)_{x=0} = 0 \tag{2.101}$$

Using this information in Eq. 2.54 yields

$$\left(\frac{\partial P}{\partial x} \right)_{x=0} = 0 \tag{2.102}$$

which agrees identically with the Rankine-Hugoniot equations for a symmetrical shock (i.e. $\varphi = 0$ at $x = 0$). The reduction of Eq. 2.54 to 2.102 along the stagnation line yields the expected physical interpretation that no momentum is transferred in the x-direction at the stagnation line. Since this trivial form of the momentum equation is not useful, the rate of change of momentum in the x - direction is used. Therefore let us differentiate the x - momentum equation with respect to x and determine its limiting form along the stagnation line.

$$\begin{aligned} & r^A \rho u \frac{\partial^2 u}{\partial x^2} + \frac{\partial}{\partial x} (r^A \rho u) \frac{\partial u}{\partial x} + \frac{\partial}{\partial x} (\tilde{\kappa} r^A \rho v) \frac{\partial u}{\partial y} \\ & + \tilde{\kappa} r^A \rho v \frac{\partial^2 u}{\partial x \partial y} + \kappa r^A \rho v \frac{\partial u}{\partial x} + u \frac{\partial}{\partial x} (\kappa r^A \rho v) = \\ & - r^A \frac{\partial^2 P}{\partial x^2} - \frac{\partial P}{\partial x} \frac{\partial r^A}{\partial x} + \frac{\partial}{\partial y} \left(\frac{\partial}{\partial x} (\tilde{\kappa} r^A \mu) \frac{\partial u}{\partial y} + \tilde{\kappa} r^A \mu \frac{\partial^2 u}{\partial x \partial y} \right) \\ & - \frac{\partial}{\partial x} (\kappa u) \frac{\partial}{\partial y} (r^A \mu) - \kappa u \frac{\partial^2}{\partial x \partial y} (r^A \mu) \end{aligned} \tag{2.103}$$

After some manipulation and substitution for limit quantities Eq. 2.103 reduces to

$$\frac{\partial}{\partial y}\left(\tilde{\varkappa}\mu\,\frac{\partial}{\partial y}\left(\frac{\partial u}{\partial x}\right)\right)+\left[\varkappa\mu-\tilde{\varkappa}\rho v\right]\frac{\partial}{\partial y}\left(\frac{\partial u}{\partial x}\right)$$

$$-\varkappa\left[\rho v+\mu\,\underset{\sim}{\varkappa}+\tfrac{1}{2}\frac{\partial\mu}{\partial y}\right]\left(\frac{\partial u}{\partial x}\right)-\rho\left(\frac{\partial u}{\partial x}\right)^{2}-\frac{\partial^{2}P}{\partial x^{2}}=0 \tag{2.104}$$

For substitution into Eq. 2.104 the stagnation line global continuity Eq. 2.97 may be rewritten.

$$2\frac{\partial u}{\partial x}=-\left[\frac{1}{\rho}\frac{\partial}{\partial y}\left(\tilde{\varkappa}\rho v\right)+\varkappa v\right] \tag{2.105}$$

or

$$2\frac{\partial u}{\partial x}=-\left[\frac{1}{\rho}\frac{\partial}{\partial y}\left(\rho v\right)+2\,\varkappa v\right] \tag{2.106}$$

Combining Eqs. 2.104 and 2.105 yields

x - Momentum: (S L)

$$\frac{\partial}{\partial y}\left(\mu\frac{\partial}{\partial y}\left(\frac{1}{2\rho}\frac{\partial}{\partial y}\left(\tilde{\varkappa}\rho v\right)+\frac{\varkappa v}{2}\right)\right)+\left[\varkappa u-\tilde{\varkappa}\rho v\right]\frac{\partial}{\partial y}\left(\frac{1}{2\rho}\frac{\partial}{\partial y}\left(\tilde{\varkappa}\rho v\right)\right.$$

$$\left.+\frac{\varkappa v}{2}\right)-\varkappa\left[\rho v+\mu\,\underset{\sim}{\varkappa}+\tfrac{1}{2}\frac{\partial\mu}{\partial y}\right]\left(\frac{1}{2\rho}\frac{\partial}{\partial y}\left(\tilde{\varkappa}\rho v\right)+\frac{\varkappa v}{2}\right) \tag{2.107}$$

$$+\rho\left(\frac{1}{2\rho}\frac{\partial}{\partial y}\left(\tilde{\varkappa}\rho v\right)+\frac{\varkappa v}{2}\right)^{2}+\left(\frac{\partial^{2}P}{\partial x^{2}}\right)_{x=0}=0$$

This is a third order inhomogenous ordinary differential equation where the rate of change of the pressure gradient in the x - direction is an undetermined function of y.

The y - momentum equation can be evaluated directly by substitution of the stagnation line limit quantities. The stagnation line normal momentum equation to order $\bar{\rho}^{2}$ is

y - Momentum: (S L)

$$\tilde{\rho}\kappa v \frac{\partial v}{\partial y} = - \tilde{\kappa} \frac{\partial P}{\partial y} - \mu \frac{\partial}{\partial y} \left[\frac{1}{2\rho} \frac{\partial}{\partial y} (\rho v) + \kappa v \right]$$

$$+ \frac{2}{3} \frac{\partial}{\partial y} \left[\frac{\mu}{2\rho} \frac{\partial}{\partial y} (\rho v) + \mu \kappa v \right] + \frac{2}{3} \frac{\kappa}{\tilde{\kappa}} \mu \left[\frac{1}{2\rho} \frac{\partial}{\partial y} (\rho v) + \kappa v \right] \qquad (2.108)$$

$$+ \frac{4}{3} \kappa \mu \frac{\partial v}{\partial y} + \frac{4}{3} \tilde{\kappa} \frac{\partial}{\partial y} (\mu \frac{\partial v}{\partial y}) - \frac{4}{3} \kappa v \frac{\partial \mu}{\mu y} - \frac{4}{3} \frac{\kappa^2}{\tilde{\kappa}} \mu v$$

$$+ \left\{ \left[\frac{4}{3} \mu \frac{\kappa}{\tilde{\kappa}} + \mu \kappa \right] \left[\frac{1}{2\rho} \frac{\partial}{\partial y} (\rho v) + \kappa v \right] + \frac{4}{3} \mu \frac{\kappa^2}{\tilde{\kappa}} v + \frac{2}{3} \mu \kappa \frac{\partial v}{\partial y} \right\}$$

where the terms in the brackets $\{\ \}$ are the terms of order $\bar{\rho}^2$. By dropping these terms only terms of order $\bar{\rho}$ remain. Since some of the terms of order $\bar{\rho}$ have been expanded in Eq. 2.108 a few of the terms will combine.

y - Momentum: (S L)

$$\tilde{\rho}\kappa v \frac{\partial v}{\partial y} = - \tilde{\kappa} \frac{\partial P}{\partial y} - \mu \frac{\partial}{\partial y} \left(\frac{1}{2\rho} \frac{\partial}{\partial y} (\rho v) + \kappa v \right)$$

$$+ \frac{2}{3} \frac{\partial}{\partial y} \left(\frac{\mu}{2\rho} \frac{\partial}{\partial y} (\rho v) + \mu \kappa v \right) + \mu \kappa \left(\frac{2}{\tilde{\kappa}} + 1 \right) \left(\frac{1}{2\rho} \frac{\partial}{\partial y} (\rho v) \right. \qquad (2.109)$$

$$\left. + \kappa v \right) + 2 \kappa \mu \frac{\partial v}{\partial y} + \frac{4}{3} \tilde{\kappa} \frac{\partial}{\partial y} (\mu \frac{\partial v}{\partial y}) - \frac{4}{3} \kappa v \frac{\partial \mu}{\partial y}$$

It is obvious that either with or without the second order terms the y - momentum equation is a second order, inhomogenous, ordinary differential equation with variable coefficients. Given a solution to the energy equation (i.e. an enthalpy or temperature profile) in

principle the x - and y - momentum equations could be solved for the normal velocity and the normal pressure gradient if the rate of change of the pressure gradient in the x - direction as a function of y is given. This pressure term, $(\partial^2 P/\partial x^2)$, is usually assumed since it is a result of the elliptic nature of the problem.

The energy Eq. 2.57 can be reduced to the stagnation line energy equation by inspection.

$$\tilde{\kappa}\rho v \frac{\partial H}{\partial y} = -\left(1 + \frac{\kappa}{\tilde{\kappa}}\right) \frac{\partial}{\partial y}\left[-\tilde{\kappa} k \frac{\partial T}{\partial y} + \tilde{\kappa} \sum_i h_i J_{i,y}\right. \tag{2.110}$$

$$\left. - \frac{\tilde{\kappa} P}{N^2} \sum \left[\sum \frac{N_i}{m_i} \frac{D_i^T}{\mathbb{D}_{ij}} \left(\frac{J_{j,y}}{\rho_j} - \frac{J_{i,y}}{\rho_i} \right) \right] \right] - \tilde{\kappa} \frac{\partial q_{R,y}}{\partial y}$$

This is a second order, ordinary integrodifferential equation. It is interesting to note that the limiting process has eliminated the viscous dissipation terms.

The stagnation line conservation equation, obtained from the thin shock layer equations, are a set of four ordinary differential equations in five unknowns, (i.e. ρ, v, H, P and C_i). In addition to the conservation equations, the thermal and caloric equation of state is available to provide another independent equation. The global continuity equation was used to eliminate the tangential velocity gradient in the momentum equations and therefore is not needed in a solution of the stagnation line equations. It can be used post priori to provide initial conditions for the thin shock layer equations. For a shock layer solution the rate of change of the pressure gradient in the tangential direction must be specified

TABLE 2.5

STAGNATION LINE BOUNDARY LAYER EQUATIONS

Global continuity:

$$2\frac{\partial u}{\partial x} = -\frac{1}{\rho}\frac{\partial}{\partial y}(\rho v) \tag{2.111}$$

Species continuity:

$$\rho v \frac{\partial C_i}{\partial y} = -\frac{\partial}{\partial y}(J_{i,y}) + \omega_i \tag{2.112}$$

x - Momentum:

$$\frac{\partial}{\partial y}\left[\mu\frac{\partial}{\partial y}\left(\frac{1}{\rho}\frac{\partial}{\partial y}(\rho v)\right)\right] - \rho v\frac{\partial}{\partial y}\left(\frac{1}{\rho}\frac{\partial}{\partial y}(\rho v)\right) + \frac{\rho}{2}\left(\frac{1}{\rho}\frac{\partial}{\partial y}(\rho v)\right)^2 + 2\left(\frac{\partial^2 P}{\partial x^2}\right)_{x=0} = 0 \tag{2.113}$$

y - Momentum:

$$\frac{\partial P}{\partial y} = 0 \tag{2.114}$$

Energy:

$$\rho v\frac{\partial H}{\partial y} = -\frac{\partial}{\partial y}\left[-k\frac{\partial T}{\partial y} + \sum_i h_i J_{i,y} - \frac{P}{N^2}\sum\sum\frac{N_i D_i^T}{m_i \mathbb{D}_{ij}}\left(\frac{J_{j,y}}{\rho_j} - \frac{J_{i,y}}{\rho_i}\right)\right] - \frac{\partial q_{R,y}}{\partial y} \tag{2.115}$$

as a function of the normal direction. Comment on how this might be specified is reserved until we have considered the reduction of the boundary layer equations to stagnation line equations.

Dropping normal curvature effects and retaining only first order terms Eqs. 2.97, 2.99, 2.107, 2.109 and 2.110 reduce to the stagnation line boundary layer equations. These equations are presented in Tab. 2.5

Since $\frac{\partial P}{\partial y} = 0$ and $\frac{\partial P}{\partial x} = 0$ for all y at x = 0, $\frac{d^2P}{dx^2}$ is a constant and may be evaluated at any y station. If the boundary layer equations are evaluated over the whole shock layer as done at the stagnation line by Dirling, Rigdon and Thomas Ref. 2.23 we may use the Rankine-Hugoniot relations to determine this constant.

From Eq. 2.81 the dimensional pressure behind the shock can be expressed as

$$P_s = (1 - \bar{\rho}) \cos^2 \varphi \, \rho_\infty U_\infty^2 \tag{2.116}$$

differentiating we get

$$\frac{\partial^2 P_s}{\partial x^2} = -2(1 - \bar{\rho})\left(\frac{\partial \varphi}{\partial x}^2\right)\left[\cos^2\varphi - \sin^2\varphi\right] \rho_\infty U_\infty^2 \tag{2.117}$$

at x = 0, φ = 0 by symmetry. Therefore

$$\left(\frac{\partial^2 P_s}{\partial x^2}\right)_{x=0} = -2(1 - \bar{\rho}) \left(\frac{\partial \varphi}{\partial x}\right)^2_{x=0} \rho_\infty U_\infty^2 \tag{2.118}$$

In order to get the boundary layer momentum equation into a more common form let us express the rate of change of the pressure gradient

in terms of the velocity gradient behind the shock. From Eq. 2.75, the dimensional tangential velocity behind the shock is

$$u_s = \left[\sin \varphi \cos \epsilon + \bar{\rho} \cos \varphi \sin \epsilon \right] U_\infty$$

from which we can obtain

$$\left(\frac{\partial u_s}{\partial x}\right)_{x=0} = \left[\frac{\partial \varphi}{\partial x} + \bar{\rho} \frac{\partial \epsilon}{\partial x} \right]_{x=0} U_\infty \tag{2.119}$$

The rate of change of the pressure gradient, Eq. 2.118, can be rewritten in terms of the velocity gradient.

$$\left(\frac{\partial^2 P_s}{\partial x^2}\right)_{x=0} = -2\rho_\infty (1 - \bar{\rho}) \left[\left(\frac{\partial u_s}{\partial x}\right)_{x=0} - U_\infty \bar{\rho} \left(\frac{\partial \epsilon}{\partial x}\right)_{x=0} \right]^2 \tag{2.120}$$

If the shock is assumed to be concentric to the body at x = 0 then

$$\left(\frac{\partial \epsilon}{\partial x}\right)_{x=0} = 0 \rightarrow \left(\frac{\partial \varphi}{\partial x}\right)_{x=0} = 1 \tag{2.121}$$

This gives a Newtonian velocity gradient used in many boundary layer analysis. Instead of applying this condition behind the shock most analyses apply this condition at the edge of the boundary layer which is at some intermediate station between the shock and body. Using the concentric assumption Eq. 2.113 may be written

x - Momentum: (B L, S L)

$$\frac{\partial}{\partial y} \left[\mu \frac{\partial}{\partial y} \left(\frac{1}{\rho} \frac{\partial}{\partial y} (\rho v)\right) \right] - \rho v \frac{\partial}{\partial y} \left(\frac{1}{\rho} \frac{\partial}{\partial y} (\rho v)\right) + \frac{\rho}{2} \left(\frac{1}{\rho} \frac{\partial}{\partial y} (\rho v)\right)^2 - 4\rho_\infty (1 - \bar{\rho}) \left(\frac{\partial u_s}{\partial x}\right)^2_{x=0} = 0 \tag{2.122}$$

It has been demonstrated that the thin shock layer and boundary layer equations can be reduced to ordinary differential equations along the stagnation line without resorting to similarity transformations. By doing so one important difference in the resulting two sets has become apparent. The stagnation line boundary layer equations are completely specified by boundary conditions at the surface and outer edge. However, an unknown function of y remains in the thin shock layer equations which cannot be determined, without approximation, by outer and inner boundary conditions. The undetermined function as stated previously is

$$\left(\frac{\partial^2 P}{\partial x^2} \right)_{x=0} = F(y) \tag{2.123}$$

This function like the rate of change of the shock angle is, by physical interpretation, determined by the flow downstream. The downstream flow is to be calculated by specifying these stagnation line conditions such that initial conditions may be determined. The problem is complicated further by the fact that there is no apparent theoretically based means of iterating on this function such that it could be assumed and corrected until some satisfactory convergence is obtained. The derivation of the stagnation line boundary layer equations demonstrates that to a first approximation the function F(y) is a constant which can be evaluated at the shock by specifying the shock geometry. For usual boundary layer problems the edge tangential velocity gradient is specified rather than the rate of change of the pressure gradient at the boundary layer edge. The

velocity gradient has been correlated as a function of flight conditions and body shape for many cases to be used in blunt body boundary layer solutions in order to specify this unknown downstream influence *a priori*.

In shock layer solutions the shock wave has been considered concentric by Refs. 2.3, 2.4, 2.9, 2.10, 2.17, 2.21, 2.22, 2.23 and many others. Furthermore, most of these analyses set the function, Eq. 2.123 equal to a constant. The full extent of influence of these assumptions has not been determined for radiation and ablation coupled flows although some radiative coupled results are presented in Ref. 2.24. This is the point where engineering judgement and or experimental results must be used in order to make the mathematical model useful.

To recapitulate the developments made in this section, it is noted that an appropriate order of magnitude assessment of terms in the conservation equations was made. The radiative transfer equation was developed using a planar slab approximation. Using developed and stated expressions for the flux divergence, bulk viscosity and conductive flux the thin shock layer equations were stated retaining second order terms and first order terms with curvature effects. The first order shock layer equations without curvature effects were found to be the boundary layer equations. Shock and surface boundary conditions were developed. Subsequently, the stagnation line equations were developed and discussed. This total development provides the required information to determining the appropriate equations to select for use in the present problem.

APPLICATION TO PLANETARY RETURN ENTRY

The selection of the proper equations which provide a reasonable description of the processes in the shock layer is quite important. The detailed development of the shock layer, radiative transfer, and surface balance equations in the previous section provides a proper basis from which a selection can be made.

In order to make a logical selection, a set of conditions or objectives must be defined. Based on the current state of the art and anticipated improvements the following set of conditions were arrived at for a criterion to use in selecting the equations to be solved.

Criteria for Selection

1. The equation must yield an accurate description of the mass, momentum, and energy transfer within the shock layer for the body size and flight conditions of interest.
2. The equations must be valid for large and small mass injection rates from the surface.
3. The equations must be coupled property to the surface boundary conditions.
4. Sufficient detail must be maintained in the equations in order to accurately access the effects of diffusion and finite rate chemistry.
5. The computer solution of these equations should be an engineering tool to predict surface heating rates and provide the means to determine ablator behavior.

Based on the objective stated above the first order shock layer equations without curvature effects through the shock layer were selected to be solved. The reasoning leading to this choice follows:

Second order terms in the conservation equations were dropped for the folowing reasons. (1) They do not significantly alter shock layer processes. (2) There are inherent approximations in the theoretical models and experimental data used to predict radiation, thermodynamic, and transport properties. Thus there is no need for more detail in the flow field equations than in the properties used in its calculation. (3) At high Reynold's numbers, typical of Earth entry from Mars, most second order terms become less significant than at the Reynold's number used for the order analysis. (4) Along the stagnation line mathematical rigor required $dP/dy = 0$ in order to uncouple the solution of the x - momentum equation from downstream effects. Stating $dP/dy = 0$ on the stagnation line necessitates dropping second order terms from the y - momentum equation. (5) The addition of second order terms would not present numerical difficulties. However, they would add numerical computation time thus detracting from the objective of an engineering tool.

Curvature effects through the shock layer were not included in the shock layer equations because for the large Reynold's numbers and body radii of interest the shock layer is thin thus making the curvature effects second order. Likewise, the thermal diffusion term of the conductive heat flux vector was dropped because of its second order nature.

It has been argued that for the large Reynold's numbers of interest viscous effects could be neglected. However, in order to assess finite rate chemistry and diffusion effects and in order to properly couple the flow field and the ablator through surfaces balances the controlling viscous terms must be retained.

The selected shock layer equations which are applicable for large as well as small mass injection rates are presented in Tab. 2.6. These equations are the boundary layer equations with the exception of the inviscid y - momentum equation. The Reynolds number limit of validity of these equations is shown in Fig. 2.7 along with the stagnation line post shock conditions for a typical hyperbolic entry trajectory. For the 10-g undershoot trajectory of Ref. 2.26 the maximum heating occurs near the point where the trajectory levels out. Thus the equations are valid in the range of interest. Conditions below flight velocities of 36,000 ft/sec are not considered in Fig. 2.7 and, in general, throughout the remainder of this work since the Apollo flight data is available for these lower flight velocities.

The stagnation line equations which result from Eqs. 2.124 to 2.128 for an axisymmetric body are:

Global continuity:

$$2\left(\frac{\partial u}{\partial x}\right)_{x=0} = -\frac{1}{\rho}\frac{\partial}{\partial y}(\rho v) \tag{2.129}$$

TABLE 2.6

BLUFF BODY FIRST ORDER SHOCK LAYER EQUATIONS

Global continuity:

$$\frac{\partial}{\partial x}\left(r_w^A \rho u\right) + r_w^A \frac{\partial}{\partial y}\left(\rho v\right) = 0 \tag{2.124}$$

Species Continuity:

$$\frac{1}{r_w^A}\frac{\partial}{\partial x}\left(r_w^A \rho C_i u\right) + \frac{\partial}{\partial y}\left(\rho v C_i\right) = -\frac{\partial}{\partial y}\left(J_{i,y}\right) + \omega_i \tag{2.125}$$

x - Momentum:

$$\rho u \frac{\partial u}{\partial x} + \rho v \frac{\partial u}{\partial y} = -\frac{\partial P}{\partial x} + \frac{\partial}{\partial y}\left(\mu \frac{\partial u}{\partial y}\right) \tag{2.126}$$

y - Momentum:

$$\kappa\, \rho u^2 = \frac{\partial P}{\partial y} \tag{2.127}$$

Energy:

$$\rho u \frac{\partial H}{\partial x} + \rho v \frac{\partial H}{\partial y} = \frac{\partial}{\partial y}\left(k \frac{\partial T}{\partial y}\right) - \frac{\partial}{\partial y}\left\{\Sigma\, h_i\, J_i\right\} - \frac{\partial q_R}{\partial y} + \frac{\partial}{\partial y}\left(\mu\, u \frac{\partial u}{\partial y}\right) \tag{2.128}$$

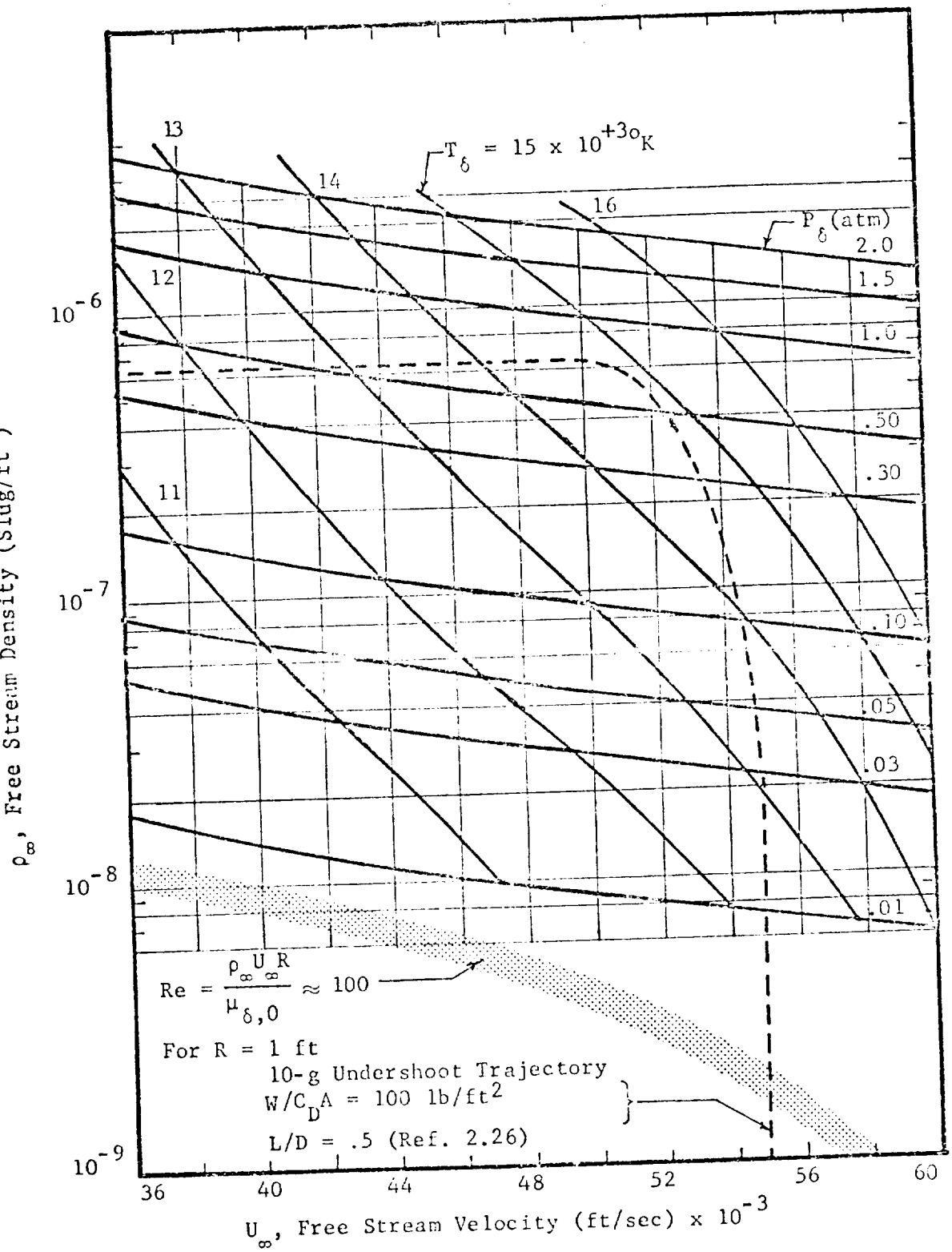

Fig. 2.7 Post Shock Thermodynamic States for Hyperbolic Entry Velocities

Species continuity:

$$\rho v \frac{dC_i}{dy} = - \frac{d}{dy} (J_{i,y}) + \omega_i \tag{2.130}$$

x - momentum:

$$\frac{\partial}{\partial y} \left[\mu \frac{\partial}{\partial y} \left(\frac{1}{\rho} \frac{\partial}{\partial y} (\rho v) \right) \right] - \rho v \frac{\partial}{\partial y} \left(\frac{1}{\rho} \frac{\partial}{\partial y} (\rho v) \right) + \frac{\rho}{2} \left(\frac{1}{\rho} \frac{\partial (\rho v)}{\partial y} \right)^2 + 2 \left(\frac{\partial^2 P}{\partial x^2} \right)_{x=0} = 0 \tag{2.131}$$

y - momentum:

$$\frac{\partial P}{\partial y} = 0 \tag{2.132}$$

Energy:

$$\rho u \frac{dH}{dy} = - \frac{d}{dy} \left(k \frac{dT}{dy} + \sum h_i J_{i,y} \right) - \frac{dq_R}{dy} \tag{2.133}$$

In order to make the surface boundary conditions compatible with the flow-field equations the boundary conditions must be simplified using the same criterion. The appropriate surface boundary conditions are:

Species boundary condition:

$$(\rho v C_i)^- + (R_i + S_i)(1 - \epsilon_p) = (\rho v C_i)^+ + J_i^+ \tag{2.134}$$

Elemental boundary conditions:

$$(\rho v \tilde{C}_j)^- = (\rho v \tilde{C}_j)^+ + \tilde{J}_j^+ \tag{2.135}$$

Momentum boundary condition:

$$P^+ = P^- \tag{2.136}$$

Energy boundary condition:

$$k \left.\frac{dT}{dy}\right|^+ = \rho v \sum h_i (C_i^+ - C_i^-) + \sum h_i J_i^+ + k_b \left.\frac{dT}{dy}\right|^- + q_R^+ \tag{2.137}$$

The species and elemental conservation equations are slightly more tractable than those presented previously since the internal diffusion effects have been dropped. Dropping second order terms significantly simplified the momentum and energy equation. The major complications remaining in these boundary conditions are the effects of external diffusion and surface reactions.

In general Eqs. 2.129 to 2.132 must be used for proper ablator-flow-field coupling if the flexibility of arbitrary ablation rates is maintained in the analyses. However, for the cases in which the ablation rate is large (i.e. at least $(\rho v)_w/(\rho_\infty U_\infty) = .05$) further simplifications can be made. If the ablation rate is large the convective terms at the surface are much larger than the diffusive terms, and consequently the diffusive terms may be dropped. Furthermore, in the absence of diffusion or surface erosion, the only surface reaction of significance is that of sublimation. In this situation the sublimation process can be computed in the

ablator analyses and the effect accounted for in the $(\rho v C_i)^-$ term. With these qualifications a simplified set of surface balance equation can be written.

Species boundary condition:

$$(\rho v C_i)^- = (\rho v C_i)^+ \tag{2.138}$$

Elemental boundary condition:

$$(\rho v \tilde{C}_j)^- = (\rho v \tilde{C}_j)^+ \tag{2.139}$$

Global mass balance:

$$(\rho v)^- = (\rho v)^+ \tag{2.140}$$

Momentum boundary condition:

$$P^- = P^+ \tag{2.141}$$

Energy boundary condition:

$$k_b \left.\frac{dT}{dy}\right|^- = k \left.\frac{dT}{dy}\right|^+ - q_R^+ \tag{2.142}$$

These equations shown, for large ablation rates, the only complicated coupling between the flow-field and the ablator is in the energy boundary condition.

The shock boundary conditions derived in the previous section are unaltered by the qualifications made in this section.

TRANSFORMED STAGNATION LINE EQUATIONS

In this section the stagnation line, bluff body first order shock layer equations are nondimensionalized and transformed into a form suitable for numerical solution. The difference between the nondimensionalization in this section and that of the first section of this chapter is in the use of the post shock density rather than the free stream density. As a result a different Reynold's number appears in the momentum equation than appeared previously. This development begins with the dimensional equations selected in the previous section.

Using the following nondimensional quantities, which are also used for the energy and elemental species equations,

$$u = \frac{u^*}{U_\infty^*} \qquad v = \frac{v^*}{U_\infty^*} \qquad p = \frac{p^*}{\rho_{s,o}^* U_\infty^{*2}} \qquad \rho = \frac{\rho^*}{\rho_{s,o}^*}$$

$$\xi = \frac{x^*}{R^*} \qquad y = \frac{y^*}{R^*} \qquad \mu = \frac{\mu^*}{\mu_{s,o}^*} \qquad T = \frac{T^*}{T_{s,o}^*} \tag{2.143}$$

$$h = \frac{h^*}{\frac{1}{2}U_\infty^{*2}} \qquad C_p = \frac{C_p^* T_{s,o}^*}{\frac{1}{2} U_\infty^{*2}} \qquad k = \frac{k^* T_{s,o}^*}{R^* \rho_{s,o}^* U_\infty^{*3}}$$

$$J_i = \frac{J_i^*}{\rho_{s,o}^* U_\infty^*} \qquad \mathbb{E} = \frac{\mathbb{E}^* R^*}{\rho_{s,o}^* U_\infty^{*3}} \text{ where } \mathbb{E}^* = \frac{dq_R^*}{dy^*} \qquad Re_s = \frac{\rho_{s,o}^* U_\infty^* R^*}{\mu_{s,o}^*}$$

the continuity and momentum Eqs. 2.129 and 2.130 can be rewritten in nondimensional form as:

Continuity:

$$2 \frac{\partial u}{\partial \xi} = - \frac{1}{\rho} \frac{\partial}{\partial y} (\rho v) \tag{2.144}$$

Momentum:

$$\frac{1}{Re_s}\frac{\partial}{\partial y}\left(\mu\frac{\partial}{\partial y}\left(\frac{\partial u}{\partial \xi}\right)\right) - \rho v\frac{\partial}{\partial y}\left(\frac{\partial u}{\partial \xi}\right) - \rho\left(\frac{\partial u}{\partial \xi}\right)^2 - \left(\frac{\partial^2 P}{\partial \xi^2}\right) = 0 \qquad (2.145)$$

As developed in the first section of this chapter, the second derivative of pressure term in the momentum equation can be evaluated at the shock using the Rankine-Hugoniot equations if $\frac{\partial P}{\partial y}$ is assumed zero. This pressure term is

$$\frac{\partial^2 P}{\partial \xi^2} = -2\bar{\rho}(1-\bar{\rho})\left(\frac{\partial \varphi}{\partial \xi}\right)^2 \qquad (2.146)$$

for a concentric shock $\frac{\partial \varphi}{\partial \xi} = 1$. The concentric shock assumption is usually rather good for hypersonic flow, however in this analysis $\frac{\partial \varphi}{\partial \xi}$ will be treated as a paramter and thus will be left general. Substituting this term into the momentum equation yields

$$\frac{1}{Re_s}\frac{\partial}{\partial y}\left(\mu\frac{\partial}{\partial y}\left(\frac{\partial u}{\partial \xi}\right)\right) - \rho v\frac{\partial}{\partial y}\left(\frac{\partial u}{\partial \xi}\right) - \rho\left(\frac{\partial u}{\partial \xi}\right) + 2\bar{\rho}(1-\bar{\rho})\left(\frac{\partial \varphi}{\partial \xi}\right)^2 = 0 \qquad (2.147)$$

To obtain a more classical form of the momentum equation a velocity function is defined

$$f' = \frac{\partial u}{\partial \xi} \Big/ \frac{\partial u_{s,o}}{\partial \xi} = \lim_{\xi \to 0}\frac{u}{u_s} = \text{a function of } y \qquad (2.148)$$

where $\frac{\partial u_{s,o}}{\partial \xi} = \frac{\partial \varphi}{\partial \xi} + \bar{\rho}\frac{\partial \varepsilon}{\partial \xi}$ from the Rankine-Hugoniot equations. Substituting into the momentum equation yields

$$\frac{1}{Re_s}\frac{\partial}{\partial y}\left(\mu\frac{\partial f'}{\partial y}\right) - \rho v\frac{\partial f'}{\partial y} - \rho\left(\frac{\partial u_{s,o}}{\partial \xi}\right)(f')^2 + \frac{2\bar{\rho}(1-\bar{\rho})}{(\partial u_{s,o}/\partial\xi)}\left(\frac{\partial \varphi}{\partial \xi}\right)^2 = 0 \tag{2.149}$$

Thes equations can now be transformed using the Dorodnitsyn transformation

$$\eta = \frac{\int_0^y \rho\, dy}{\int_0^\delta \rho\, dy} = \frac{\int_0^y \rho\, dy}{\tilde{\delta}} \qquad \frac{d}{dy} = \frac{\rho}{\tilde{\delta}}\frac{d}{d\eta} \tag{2.150}$$

Transforming Eqs. (2.144), (2.148) with (2.150) yields

Continuity:

$$2\frac{\partial u}{\partial \xi} = \frac{-1}{\tilde{\delta}}\frac{\partial}{\partial \eta}(\rho v) \tag{2.151}$$

Velocity function:

$$f' = \frac{\frac{\partial u}{\partial \xi}}{\frac{\partial u_{s,o}}{\partial \xi}} = \frac{\frac{-1}{2\tilde{\delta}}\frac{\partial(\rho v)}{\partial \eta}}{\left(\frac{\partial u_{s,o}}{\partial \xi}\right)} = \frac{\partial f}{\partial \eta} \tag{2.152}$$

Momentum:

$$\frac{d}{d\eta}\left(\rho\mu\frac{df'}{d\eta}\right) - \rho v Re_s\tilde{\delta}\frac{df'}{d\eta} + \frac{Re_s\tilde{\delta}}{\rho(\partial u_{s,o}/\partial\xi)}\left[2\bar{\rho}(1-\bar{\rho})\left(\frac{\partial\varphi}{\partial\xi}\right)^2 - \rho\left(\frac{\partial u_{s,o}}{\partial\xi}f'\right)^2\right] = 0 \tag{2.153}$$

Integrating Eq. (2.152) yields

$$\rho v = - 2 \left(\frac{\partial u_{s,o}}{\partial \xi}\right) \tilde{\delta} f \tag{2.154}$$

Equation (2.144) can be used to eliminate ρv in the momentum equation. This yields a third order nonlinear ordinary differential equation

Momentum:

$$\left(\rho \mu f''\right)' + \left[2 \mathrm{Re}_s \tilde{\delta}^2 \left(\frac{\partial u_{s,o}}{\partial \xi}\right)\right] f f'' + \frac{\mathrm{Re}_s \tilde{\delta}^2}{(\partial u_{s,o}/\partial \xi)} \left[\frac{2\bar{\rho}(1 - \bar{\rho})}{\rho} \left(\frac{\partial \varphi}{\partial \xi}\right)^2 - \left(\frac{\partial u_{s,o}}{\partial \xi}\right)^2 (f')^2\right] = 0 \tag{2.155}$$

The boundary conditions for this equation are

$$\eta = 1, \quad f' = 1$$

$$\eta = 0, \quad f' = 0 \tag{2.156}$$

$$\eta = 0, \quad f = f_w = \frac{-(\rho v)_w}{2 \tilde{\delta} (\partial u_{s,o}/\partial \xi)}$$

In addition, Eq. (2.14) has a boundary condition imposed on it to determine the transformed standoff distance, $\tilde{\delta}$.

$$\eta = 1, \quad f = f_s = \frac{-(\rho v)_s}{2 \tilde{\delta} (\partial u_{s,o}/\partial \xi)} \tag{2.157}$$

The momentum equation can be reduced to a first and a second order equation by defining

$$\zeta = \frac{f'}{\tilde{\delta}} \tag{2.158}$$

and substituting into Eq. (2.155)

$$(\rho\mu)\,\zeta'' + \left[2\,Re_s\,\tilde{\delta}^2\left(\frac{\partial u_{s,o}}{\partial \xi}\right)f + (\rho\mu)'\right]\zeta' - Re_s\tilde{\delta}^3\left(\frac{\partial u_{s,o}}{\partial \xi}\right)\zeta^2 = -\frac{2Re_s\,\tilde{\delta}\,\bar{\rho}\,(1-\bar{\rho})}{\rho(\partial u_{s,o}/\partial \xi)}\left(\frac{\partial \varphi}{\partial \xi}\right)^2 \tag{2.159}$$

The resulting boundary conditions for Eq. (2.159) are:

$$\eta = 0 \qquad \zeta = 0 \tag{2.160}$$

$$\eta = 1 \qquad \zeta = 1/\tilde{\delta}$$

The energy equation is transformed in a manner similar to the momentum equation. First, however, the equation is written in terms of temperature as the dependent variable. It is anticipated that using temperature rather than enthalpy as the dependent variable will save computer time since both in thermodynamic equilibrium and chemical kinetic subroutines temperature is used as the independent variable. Thus the use of temperature will eliminate an iteration loop between the energy solution and the property subroutines.

The dimensional stagnation line energy equation is (noting the superscript * is omitted for simplicity).

$$\rho v \frac{dH}{dy} = -\frac{d}{dy}\left[-k\frac{dT}{dy} + \Sigma\, h_i\, J_i\right] - \frac{dq_R}{dy} \tag{2.161}$$

Consider the term on the left hand side of the above equation

$$\rho v \frac{dH}{dy} = \rho v \frac{d}{dy}\left(h + \frac{u^2 + v^2}{2}\right)$$

Noting that

$$h = \Sigma\, C_i\, h_i$$

$$\frac{dh}{dy} = \Sigma\, h_i \frac{dC_i}{dy} + \Sigma\, C_i \frac{dh_i}{dT}\frac{dT}{dy}$$

$$= \Sigma\, h_i \frac{dC_i}{dy} + \frac{dT}{dy}\,\Sigma\, C_i\, C_{pi} \qquad (2.162)$$

$$= \Sigma\, h_i \frac{dC_i}{dy} + C_p \frac{dT}{dy}$$

Thus

$$\rho v \frac{dH}{dy} = \rho v \left[\Sigma\, h_i \frac{dC_i}{dy} + C_p \frac{dT}{dy} + \frac{d(v^2/2)}{dy}\right] \qquad (2.163)$$

by substitution of Eq. (2.162) and observing that $u = 0$ at $x = 0$.

Substituting Eq. (2.163) into (2.161) yields

$$\frac{d}{dy}\left(k \frac{dT}{dy}\right) - \rho v C_p \frac{dT}{dy} = \rho v\, \Sigma\, h_i \frac{dC_i}{dy} + \rho v^2 \frac{dv}{dy} \qquad (2.164)$$

$$+ \frac{d}{dy}\left[\Sigma\, h_i J_i\right] + \frac{dq_R}{dy}$$

Additional manipulation of two terms is necessary.

$$\rho v\, \Sigma\, h_i \frac{dC_i}{dy} = \rho v\, \Sigma\, h_i \left(\frac{\partial C_i}{\partial T}\right)\frac{dT}{dy} \qquad \text{where} \quad \frac{\partial \tilde{C}_i}{\partial y} = \frac{\partial P}{\partial y} = 0$$

$$\frac{d}{dy}\left[\Sigma\, h_i J_i\right] = \frac{d}{dy}\left[\Sigma\, h_i\left(-\rho D_i \frac{dC_i}{dy}\right)\right]$$

$$= -\frac{d}{dy}\left[\Sigma\, h_i \rho D_i \frac{\partial C_i}{\partial T}\frac{dT}{dy}\right]$$

Notice the term $\left(\frac{\partial C_i}{\partial T}\right)$ can only be evaluated for flows in local chemical equilibrium. Since some calculations using this assumption will be presented, further discussion is necessary. Substituting the above relations into Eq. (2.164) and rearranging yields

$$\frac{d}{dy}\left[\left(k + \sum h_i \rho D_i \frac{\partial C_i}{\partial T}\right)\frac{dT}{dy}\right] - \rho v\left(C_p + \sum h_i \frac{\partial C_i}{\partial T}\right)\frac{dT}{dy} = \rho v^2 \frac{dv}{dy} + \frac{dq_R}{dy} \tag{2.165}$$

The terms in the ( ) brackets above are from left to right the frozen plus reacting thermal conductivity, k_T, and the frozen plus reacting heat capacity, C_{p_T}, respectively. Using these definitions the stagnation line energy equation can be written as

$$\frac{d}{dy}\left(k_T \frac{dT}{dy}\right) - \rho v C_{p_T}\frac{dT}{dy} = \rho v^2 \frac{dv}{dy} + \frac{dq_R}{dy} \tag{2.166}$$

Nondimensionalization of Eq. (2.166) by the convension stated in (2.143) results in

$$\frac{d}{dy}\left(k_T \frac{dT}{dy}\right) - \tfrac{1}{2}\rho v C_{p_T}\frac{dT}{dy} = \rho v^2 \frac{dv}{dy} + \mathbb{E} \tag{2.167}$$

Eq. (2.167) can now be transformed using the Dorodnitzn transformation (2.150) to give:

$$\frac{d}{d\eta}\left(\rho\, k_T \frac{dT}{d\eta}\right) - \frac{\tilde{\delta}}{2}\rho v\, C_{p_T}\frac{dT}{d\eta} = \tilde{\delta}\,\rho v^2 \frac{dv}{d\eta} + \frac{\tilde{\delta}^2}{\rho}\,\mathbb{E} \tag{2.168}$$

or

$$\frac{d^2T}{d\eta^2} - \frac{\tilde{\delta}}{2\rho k_T}\left(\rho v C_{P_T} - \frac{2d(\rho k_T)}{\tilde{\delta}\, d\eta}\right)\frac{dT}{d\eta} \tag{2.169}$$

$$= \frac{\tilde{\delta}}{k_T} v^2 \frac{dv}{d\eta} + \frac{\tilde{\delta}^2}{\rho^2 k_T} \mathbb{E}$$

This later form is second order and linear in temperature.

The species equation nondimensionalized using the convension stated in (2.143) retains the same form as Eq. (2.130)

$$\rho v \frac{dC_i}{dy} = - \frac{dJ_i}{dy} + \omega_i \tag{2.170}$$

Transforming using Eq. (2.150) yields

$$\rho v \frac{dC_i}{d\eta} = - \frac{dJ_j}{d\eta} + \frac{\tilde{\delta}}{\rho} \omega_i \tag{2.171}$$

For studies of binary diffusion and chemical equilibrium, Eq. (2.171) can be reduced to the elemental conservation equation using the following relations

$$\tilde{C}_j = \sum_{i=1}^{n} \frac{A_{ij} m_j C_i}{M_i} = \text{mass fraction of element j} \tag{2.172}$$

$$\tilde{J}_j = \sum_{i=1}^{n} \frac{A_{ij} m_j J_i}{M_i} = \text{mass flux of element j} \tag{2.173}$$

which yield

$$\rho v \frac{d\tilde{C}_j}{d\eta} = \frac{d\tilde{J}_j}{d\eta} \tag{2.174}$$

The generation term does not appear in Eq. (2.174) since the net generation of elements is zero.

The thin shock layer equations developed in this section along with the corresponding boundary conditions are the primary set of equations which are solved in this work. Chapter 4 presents the numerical methods used in the solution of these stagnation line equations and results are presented in Chapter 5.

TRANSFORMED AROUND THE BODY EQUATIONS

In order to complete the formulation of equations describing the hypersonic blunt body problem, the around the body equations are manipulated into a form suitable for numerical solution. This is accomplished by nondimensionalization and transformation of the thin shock equations (2.124) to (2.128). A von Mises transformation is used since it yields a set of equations amenable to forward integration and finite rate chemistry can be included using local one-dimensional chemistry along streamlines.

The shock layer equations (2.124) to (2.128) are rewritten here with some changes noted. The global continuity and two momentum equations are unchanged. The global continuity is removed from the species equation. The energy equation is written with temperature as the principle dependent variable. Furthermore, the resulting form of the energy equation was obtained by subtracting the momentum equation, substituting the right hand side of the species equation for the left hand side and assuming binary diffusion. The resulting set of dimensional axisymmetric shock layer equations are:

Global continuity:

$$\frac{\partial}{\partial x}(\rho u r_w) + r_w \frac{\partial}{\partial y}(\rho v) \tag{2.124}$$

Species continuity:

$$\rho u \frac{\partial C_i}{\partial x} + \rho v \frac{\partial C_i}{\partial y} = \frac{\partial}{\partial y}\left(\frac{\mu}{S_{C_i}} \frac{\partial C_i}{\partial y}\right) + \omega_i \tag{2.175}$$

x - momentum:

$$\rho u \frac{\partial u}{\partial x} + \rho v \frac{\partial u}{\partial y} = - \frac{\partial P}{\partial x} + \frac{\partial}{\partial y} \left(\mu \frac{\partial u}{\partial y} \right) \tag{2.126}$$

y - momentum:

$$\varkappa \rho u^2 = \frac{\partial P}{\partial y} \tag{2.127}$$

Energy:

$$\rho u C_p \frac{\partial T}{\partial x} + \rho v C_p \frac{\partial T}{\partial y} = - \Sigma h_i \omega_i + u \frac{\partial P}{\partial x} \tag{2.176}$$

$$+ \frac{\partial}{\partial y} \left(k \frac{\partial T}{\partial y} \right) - \frac{\partial q_R}{\partial y} + \mu \left(\frac{\partial u}{\partial y} \right)^2 + \left(\sum \frac{C_{p_i} \mu}{S_{C_i}} \frac{\partial C_i}{\partial y} \right) \frac{\partial T}{\partial y}$$

It should be noted that the heat capacity (C_p) and thermal conductivity (k) in the equation above consist of only the "frozen" parts. This is unlike the final form of the energy equation derived in the previous section for the stagnation line.

The shock layer equations can be nondimensionalized using the same set of nondimensionalizing quantities used for the stagnation line equations (Eq. 2.143) with the addition of

$$\omega_i = \frac{R^* \omega_i^*}{\rho_{s,o}^* U_\infty^*}$$

With these quantities the preceding equations may be written as:

Global continuity:

$$\frac{\partial (\rho u r_w)}{\partial \xi} + r_w \frac{\partial (\rho v)}{\partial y} = 0 \tag{2.177}$$

Species continuity:

$$\rho u \frac{\partial C_i}{\partial \xi} + \rho v \frac{\partial C_i}{\partial y} = \frac{1}{Re_s} \frac{\partial}{\partial y} \left(\frac{\mu}{S_{C_i}} \frac{\partial C_i}{\partial y} \right) + \omega_i \tag{2.178}$$

x - momentum:

$$\rho u \frac{\partial u}{\partial \xi} + \rho v \frac{\partial u}{\partial y} = - \frac{\partial P}{\partial \xi} + \frac{1}{Re_s} \frac{\partial}{\partial y} \left(\mu \frac{\partial u}{\partial y} \right) \tag{2.179}$$

y - momentum:

$$\varkappa \rho u^2 = \frac{\partial P}{\partial y} \tag{2.180}$$

Energy:

$$\rho u C_p \frac{\partial T}{\partial \xi} + \rho u C_p \frac{\partial T}{\partial y} = - \Sigma h_i \omega_i + u \frac{\partial P}{\partial \xi}$$

$$+ 2 \frac{\partial}{\partial y} \left(k \frac{\partial T}{\partial y} \right) - 2 \mathbb{E} + \frac{2\mu}{Re_s} \left(\frac{\partial u}{\partial y} \right)^2 \tag{2.181}$$

$$+ \frac{\mu}{Re_s} \left(\sum \frac{C_{p_i}}{S_{C_i}} \frac{\partial C_i}{\partial y} \right) \frac{\partial T}{\partial y}$$

The transformation of the independent variables of the above equations from ξ and y to ξ and Ψ respectively is accomplished as follows. Let

$$\Psi \left(\frac{\partial \Psi}{\partial y} \right)_\xi = \rho u r_w \tag{2.182}$$

$$\Psi \left(\frac{\partial \Psi}{\partial \xi} \right)_y = - \rho v r_w \tag{2.183}$$

Consequently any dependent variable F can be written as

$$F = F(\xi, \Psi)$$

$$\left(\frac{\partial F}{\partial \xi}\right) = \left(\frac{\partial F}{\partial \xi}\right)_{\Psi} \cancel{\left(\frac{\partial \xi}{\partial \xi}\right)_{y}}^{1} + \left(\frac{\partial F}{\partial \Psi}\right)_{\xi} \left(\frac{\partial \Psi}{\partial \xi}\right)_{y} \tag{2.184}$$

Substituting Eq. 2.183 into 2.184 yields

$$\left(\frac{\partial F}{\partial x}\right)_{y} = \left(\frac{\partial F}{\partial \xi}\right)_{\Psi} - \frac{\rho v r_w}{\Psi} \left(\frac{\partial F}{\partial \Psi}\right)_{\xi} \tag{2.185}$$

Correspondingly

$$\left(\frac{\partial F}{\partial y}\right)_{\xi} = \left(\frac{\partial F}{\partial \xi}\right)_{\Psi} \cancel{\left(\frac{\partial \xi}{\partial y}\right)_{\xi}}^{0} + \left(\frac{\partial F}{\partial \Psi}\right)_{\xi} \left(\frac{\partial \Psi}{\partial y}\right)_{\xi} \tag{2.186}$$

from which, by using Eq. (2.182), one obtains

$$\left(\frac{\partial F}{\partial y}\right)_{\xi} = \frac{\rho u r_w}{\Psi} \left(\frac{\partial F}{\partial \Psi}\right)_{\Psi} \tag{2.187}$$

The nondimensional shock layer equations after undergoing transformation with Eqs. 2.182, 2.183, 2.185 and 2.187 are:

Global continuity:

$$\frac{\partial}{\partial \xi}\left(\Psi \frac{\partial \Psi}{\partial y}\right) + \frac{\partial}{\partial y}\left(-\Psi \frac{\partial \Psi}{\partial \xi}\right) = 0 \tag{2.188}$$

$$0 \equiv 0$$

Species continuity:

$$\frac{\partial C_i}{\partial \xi} = \frac{1}{Re_s \Psi} \frac{\partial}{\partial \Psi}\left(\frac{a}{S_{C_i}} \frac{\partial C_i}{\partial \Psi}\right) + \frac{\omega_i}{\rho u} \tag{2.189}$$

x - momentum:

$$\frac{\partial u}{\partial \xi} = -\frac{1}{\rho u}\frac{\partial P}{\partial \xi} + \frac{vr_w}{u\Psi}\frac{\partial P}{\partial \Psi} + \frac{1}{Re_s \Psi}\frac{\partial}{\partial \Psi}\left(a\frac{\partial u}{\partial \Psi}\right) \tag{2.190}$$

y - momentum:

$$\frac{\partial P}{\partial \Psi} = \frac{\rho u \Psi}{r_w} \tag{2.191}$$

Energy:

$$C_p \frac{\partial T}{\partial \xi} = \frac{1}{\rho}\frac{\partial P}{\partial \xi} - \frac{vr_w}{\Psi}\frac{\partial P}{\partial \Psi} + \frac{2}{\Psi}\frac{\partial}{2\Psi}\left(\frac{C_p a}{P_r}\frac{\partial T}{\partial \Psi}\right)$$

$$- \frac{1}{\rho u}\left(\Sigma h_i \omega_i + 2\ \mathbb{E}\right) \tag{2.192}$$

$$+ \frac{2a}{Re_s \Psi}\left[\left(\frac{\partial u}{\partial \Psi}\right)^2 + \tfrac{1}{2}\left(\sum \frac{C_{p_i}}{S_{C_i}}\frac{\partial C_i}{\partial \Psi}\right)\frac{dT}{d\Psi}\right]$$

where

$$a = \frac{\mu \rho u r_w^2}{\Psi} \tag{2.193}$$

With the exception of the pressure variation and radiative flux divergence term, the preceding equations are in identical form to those successfully used to describe shear layer and combustion chamber flows with finite rate chemistry (Ref. 2.27)

In addition to transformation of the shock layer equations, the necessary transformed boundary conditions are:

$$1.\quad \left(\frac{\partial \Psi}{\partial y}\right)_{y=0} = 0 \qquad \text{from } y = 0,\ u = 0$$

$$2.\quad \left(\frac{\partial \Psi}{\partial \xi}\right)_{y=0} = \frac{\rho_w v_w r_w}{\Psi_w} \qquad \text{from } y = 0,\ v = v_w,\ \rho = \rho_w$$

$$3.\quad \left(\frac{\partial \Psi}{\partial y}\right)_{y=\delta} = \frac{\rho_\delta u_\delta r_w}{\Psi_\delta} \qquad \text{from } y = \delta,\ u = u_\delta$$

$$4.\quad \left(\frac{\partial \Psi}{\partial \xi}\right)_{y=\delta} = -\frac{\rho_\delta v_\delta r_w}{\Psi_\delta} \qquad \text{from } y = \delta,\ v = v_\delta,\ \rho = \rho_\delta$$

$$5.\quad \left(\frac{\partial P}{\partial \Psi}\right)_{y=0} = 0 \qquad \text{from } y = 0,\ u = 0 \qquad (2.194)$$

$$6.\quad T = T_w \qquad \text{at } y = 0$$

$$7.\quad T = T_\delta \qquad \text{at } y = \delta$$

$$8.\quad C_i = (C_i)_w \qquad \text{at } y = 0$$

$$9.\quad C_i = (C_i)_\delta \qquad \text{at } y = \delta$$

The thermal and caloric equations of state are also required to complete the set of equations and boundary conditions.

CHAPTER 2

References

2.1 Probstein, R. F. "Shock Wave and Flow Field Development in Hypersonic Reentry," Am. Rocket Soc. Jour., 31, 184-94 (Feb. 1961).

2.2 Hayes, W. D. and R. F. Probstein. Hypersonic Flow Theory 2nd Ed, Ch. 5, Academic Press, New York (1966).

2.3 Hoshizaki, H. and K. H. Wilson. "Convective and Radiation Heat Transfer During Superorbital Entry," AIAA Jour., 5(1), 25(Jan. 1967).

2.4 Spradley, L. W. and C. D. Engel, "The Effects of Shock Layer Radiation and Viscous Coupling on the Total Heating Rate to a Reacting Body," NASA CR-61224 (April, 1968).

2.5 Libby, P. A. "The Homogeneous Boundary Layer at an Axisymmetric Stag-Point with Large Rates of Injection," Jour. of Aerospace Sci., p. 48 (Jan. 1962).

2.6 Schlichting, H. Boundary Layer Theory 4th Ed., McGraw-Hill Co., Inc. New York (1960).

2.7 Laitone, E. V. "On Equations of Motion for a Compressible Viscous Gas", Jour. of Aeronautical Sciences, p. 846, (Sept. 1956).

2.8 Zeldovich, Ya. B. and Yu. P. Raizer. Physics of Shock Waves and High Temperature Hydrodynamic Phenomena, Ch. 2, Academic Press, N. Y. (1966).

2.9 Hoshizaki, H. and L. E. Lasher. "Convective and Radiative Heat Transfer to an Ablating Body," AIAA Thermophysics Specialist Conference, Paper No. 67-327 (April 1967).

2.10 Spradley, L. W. and C. D. Engel. "Formulation of a Method for Predicting Coupled Convective and Radiative Heat Transfer About a Blunt Body," NASA CR-61200 (April 1968).

2.11 Goulard, R. and M. "One-Dimensional Energy Transfer in Radiant Media," J. Heat Mass Transfer, Vol. 1, p. 81 (1960).

2.12 Wilson, K. H. "Stagnation Point Analysis of Coupled Viscous-Radiating Flow with Massive Blowing," NASA CR-1548 June 1970.

2.13 Viskanta, R. "Radiative Transfer Between Two Concentric Gray Spheres Separated by Radiating Gas," In Advanced Heat Transfer, Ed. B. T. Chao, (1969).

2.14 Fay, J. A. and F. R. Riddell, "Theory of Stagnation Point Heat Transfer in Dissociated Air," J. Aero./Space Sci., 25(2), 73-85 (1968).

2.15 Dorrance, W. H. Viscous Hypersonic Flow, Ch. 2, McGraw-Hill Co., Inc., New York (1962).

2.16 Zeldovich, Ya. B. and Yu. P. Raizer. Physics of Shock Waves and High Temperature Hydrodynamic Phenomena, Ch. 7, Academic Press, N. Y. (1962).

2.17 Lasher, L. E. and K. H. Wilson. "Effect of Shock Percursor Heating on Radiative Flux to Blunt Bodies," NASA CR-1265 (Dec 1968).

2.18 April G. A. Evaluation of the Energy Transfer in the Char Zone During Ablation, Ph.D. Dissertation, Louisiana State University, Baton Rouge, Louisiana (1969).

2.19 del Casal, E. P. "The Effects of Multidimensional Flow Through Porous Matrices in Mass Transfer Cooling," AIAA Paper No. 69-149, Jan. 1969.

2.20 Engel, C. D., D. D. Esch, R. C. Farmer, and R. W. Pike. "Formulation, Derivation and Development of the Analysis of the Interaction of Ablating Protection Systems and Stagnation Region Heating," NASA CR-66931, Jan. 1970.

2.21 Hoshizaki, H. and K. H. Wilson. "The Viscous, Radiating Shock About a Blunt Body," AIAA Jour., 3, 1614 (Sept. 1965).

2.22 Ho, H. T. and R. F. Probstein. "The Compressible Viscous Shock Layer in Rarefied Hypersonic Flow" in Rarefied Gas Dynamics, Ed. L. Talbot, Academic Press, N. S. (1961).

2.23 Rigdon, W. S., R. B. Dirling, and M. Thomas. "Radiation and Convective Heating During Atmospheric Entry," NASA CR-1170 (Sept. 1968).

2.24 Spradley, L. S. and C. D. Engel. "A Study of the Accuracy of the Radiation-Coupled Shock Layer Program Including an Analysis of Error Sources," LMSC/HREC D 148807, Lockheed Missiles and Space Company, Huntsville, Ala. (April 1969).

2.25 Edelman, R. and J. Hoffman. "Viscous Hypersonic Flow in the Vicinity of the Stagnation Point of Axisymmetric Blunt Bodies - Calculations and Results for Equilibrium Air," General Applied Science Laboratories, TR no. 498, May 1965.

2.26 Korkan, K. D. and G. M. Hanley. "Apollo Command Module Aerothermodynamics Characteristics at Hyperbolic Earth Entry Velocities," J. Spacecraft Roc., Vol. 3, No. 8, Aug. 1966, p 1274-1281.

2.27 Edelman, R. K. and D. Fortune. "Mixing and Combustion in the Exhaust Plumes of Rocket Engines Burning RP1 and Liquid Oxygen," TR-631 General Applied Science Laboratories, Inc., Nov. 1966.

2.28 Peters, R. W. and K. L. Wadlin. "The Effects of Resin Composition and Fillers on the Performance of a Molded Charring Ablator," NASA TND-2024, Dec. 1963.

2.29 Smith, G. L., J. T. Suttles, and E. M. Sullivan, "Viscous Radiating Flow-Field on an Ablating Blunt Body," AIAA Paper No. 70-218, Jan. 1970.

CHAPTER 3

GAS AND ABLATOR PROPERTIES

In order to implement a solution to the shock layer equations radiative, thermodynamic, transport and ablator properties are required. The reliability of these properties naturally influences the reliability of the flow-field solution. This chapter presents a discussion of the properties used in this work with special attention given to radiative properties. A method of determining radiatively important species and species mechanisms is presented and applied to molecular species. Chemical equilibrium, thermodynamic, and transport properties of air and ablator species are discussed. Further, quasi-steady ablator response properties for phenolic nylon are presented and discussed.

RADIATIVE PROPERTIES

Flight conditions, atmospheric compositions and ablator compositions are the three important constraints which should be considered in determining what radiative properties are required. The flight conditions of interest yield shock layer conditions in the ranges (see Fig. 2.7)

$$3000 \lesssim T \lesssim 17000^{\circ}K$$

$$.001 \lesssim P \lesssim 2 \text{ atm.}$$

Gases in these thermodynamic ranges are classified as low temperature plasmas. The gas is not highly ionized as in a full plasma state.

In a low temperature plasma, molecules, atoms and ions may play an important role in radiative energy transport and therefore the contribution and mechanism of these three types of species must be assessed. The atmospheric and ablator compositions define which specific species are present and the relative amounts of each present. Within this context a selection of the radiative properties used in this analysis is made.

Bound-bound transitions: Line radiation results from electronic transitions between the discrete or bound energy levels in atoms or molecules. For atoms the concern is with transitions between states of differing principle quantum numbers within a given ionic state of the atomic species. These transitions are characterized by spectral line series which are limited by the ionization threshold of the next ionic state (Ref. 3.1). The importance of a particular transition is measured by its absorption cross section (Ref. 3.2)

$$\sigma^{b-b}_{\nu_{nn'}} = \frac{\gamma}{mc}\left[\frac{1}{(\nu-\nu_o)^2+\gamma^2}\right] f_{nn'}\,(1-e^{-h\nu_o/kT}) \qquad (3.1)$$

which is a function of the f-number, $f_{nn'}$, and the line half-width γ in addition to frequency and temperature. The f-number is the transition probability and can represent a single line, multiplet or a collection of line transitions having the same lower state.

For molecules, the concern is with transitions between different electronic states of a given molecular species. The electronic transitions are modified by vibrational and rotational effects which produce groups of bands called band systems which are composed of

discrete line transitions (Ref. 3.1). The importance of a band system can be assessed in terms of the spectral cross section for the band. The absorption cross section can be written (Ref. 3.3).

$$\sigma_{\omega}^{b-b} = \pi^{\frac{1}{2}} r_o f (\Delta\omega_T)^{-1} \exp [- (\omega-\omega_o)^2/(\Delta\omega_T)^2] \qquad (3.2)$$

where

$r_o = e^2/mc \cong 2.8 \times 10^{-13}$ cm

f = band system f-number

$\Delta\omega_T = \Delta\omega_o[\tanh (\theta_o/2T)]^{\frac{1}{2}}$

$\Delta\omega_o$ = spectral half width at $T = 0^oK$

$\theta_o = hc\ \omega_e''/k$

ω_e'' = effective vibrational frequency of the lower electronic state

ω_o = origin frequency or absorption maximum center of the system

This relation applies to both diatomic and polyatomic molecules as reported by Ref. 3.3. The important point here is to note that a bands effectiveness in contributing to radiative transport is measured in terms of an absorption cross section which is directly proportional to the band f-number.

Bound-free transitions: Transfer between ionic states for both atomic and molecular species result in continuum

radiation. For a bound-free process, either the initial or final state includes a free electron. The absorption of radiation from a discrete atomic state produced by a photon having enough energy to extend above the ionization threshold results in the process of photoionization.

$$A + h\nu \rightarrow A^{+} + e^{-} \tag{3.3}$$

The reverse process, recombination, occurs when an ion and an electron recombine yielding an emission of a photon

$$A^{+} + e^{-} \rightarrow A + h\nu \tag{3.4}$$

Since the upper state for both processes is continuous, being defined by the kinetic energy of the ion and electron, the radiation absorbed or emitted in the respective processes is continuous. The absorption cross section for atomic species can be expressed as (Ref. 3.4)

for $h\nu < h\nu_T$

$$\sigma_\nu^{b\text{-}f} = 0$$

for $h\nu \geq h\nu_T$

$$\sigma_\nu^{f\text{-}b} = \sigma_\nu^{b\text{-}f} = \sigma_o \sum_{\ell'=\ell+1} C_{\ell\ell'}(L') \frac{G^2_{\ell\ell'}(\nu)\cos^2[\varphi(\ell,\ell',\nu,\epsilon)+\delta_{\ell'}(L',\epsilon)]}{[\gamma_{\ell\ell'}(\epsilon) - 1]\left[1 + \epsilon\nu^2\right]} \tag{3.5}$$

where

$$\sigma_o = \frac{8.55 \times 10^{-19}}{\zeta(\bar{n})}\left[\left(\frac{\bar{n}}{Z+1}\right)\right]^2 \ (cm^2)$$

$\bar{n}$ = effective quantum no. = $[(Z + 1)][R_\infty/\chi_i^{Z})]^{\frac{1}{2}}$

χ_i = ionization energy of i-th state

Z = charge on the residual ion

$C^{-}_{\ell\ell'}(L')$, $G_{\ell\ell'}$, φ are functions of the species and transition

$\delta_{\ell'}$ = phase shift

ν_T = threshold frequency

The bound-free transitions of molecules are not, in general, significant enough to consider for this problem.

Free-free transitions: Transitions between two free energy levels in which free electrons are present in both the initial and final state result in continuum radiation. The emission process is commonly known as Bremestrahlung and takes place in the Coulomb field of an ion (Ref. 3.1) as

$$A^+ + e^- \rightarrow A^+ + e^- + h\nu \tag{3.6}$$

or in the field of a neutral atom as

$$A + e^- \rightarrow A + e^- + h\nu \tag{3.7}$$

The free-free absorption process for an atom takes place according to the relation

$$A + e^- + h\nu \rightarrow A + e^- \tag{3.8}$$

The continuum radiation from these processes may be considered classically to occur as a result of atoms or ions deflecting incident electrons and giving them an acceleration resulting in a photon absorption or emission. The free-free cross section can be expressed as (Ref. 3.4)

$$\sigma_{\nu}^{f\text{-}f} = 1.26 \times 10^{-9} (Z+1)^2 T \frac{Q^{Z+1}}{Q^Z} e^{-\chi^Z/kT} \frac{\bar{g}}{(h\nu)^3} \ (cm^2) \qquad (3.9)$$

where

Z = charge on the residual ion

χ = ionization energy

Q = partition function of the residual ion

$\bar{g}$ = Gaunt factor (a non-hydrogenic correction factor) averged for a shell

For free-free process as with the bound-bound and bound-free the absorption cross-section can be used as a measure of the effectiveness of a particular radiative transfer mode of a species. Furthermore, for bound-bound transitions the absorption cross section is written in terms of the f number.

Many techniques have been used to obtain radiation data (Ref. 3.5) and the final form of the data may be found in forms ranging from intensity measurements of individual lines to total intensities measured from entire gas mixtures at various temperatures and pressures. Accordingly the theories which are used for predictive methods of radiant heating vary in corresponding detail. As

indicated in the previous discussion this work uses absorption cross sections as a basis for a radiative model. Therefore the present discussion is centered around the measurement of the required cross sections and the information needed to use models for computing cross sections.

Quantitative spectroscopic studies which yield absolute intensities and line half-width are required to determine f-numbers, cross-sections or absorption coefficients (Ref. 3.5 and 3.6). Measurements of spectral line profiles of individual lines may be made in the microwave region however integrated band intensities are sufficient for molecules. Additional data such as dissociation energies, ionization energies and line frequency centers along with a quantum mechanical model for the species under consideration is needed to compute the cross section. Intensity measurements are usually carried out in isothermal experimental arrangements. For example low temperature measurements can be carried out in constant volume cells attached to spectrometers (Ref. 3.5). For high temperature studies of continuum radiation shock wave induced plasmas and electrical discharges have been used to achieve the required thermodynamic state (Ref. 3.6).

The purpose here is not to describe equipment. The interested reader is referred to references 3.5, 3.6 and 3.7 and their respective references.

The selection of the species and their transport processes to include in the shock layer radiation calculation is based on the

maximum relative contribution to the absorption coefficient. The species considered are determined by the elemental composition of the atmosphere (air) and the elemental composition of the ablator (phenolic-nylon). Given these elemental constraints and the temperature and pressure ranges under consideration, thermodynamic constraints determine the magnitude of species molar compositions. The selection is divided into two groups (monotomic and polyatomic species).

For monotomic species (atoms and atomic ions) a good deal of work has been done. It has been shown that atomic H, C, O and N line and continuum mechanisms are the major contributors to radiative energy transport in the shock layer (Ref. 3.2, 3.4, and 3.8). Furthermore, the effects of ionic species H^+, C^+, O^+, and N^+ and higher ionizations have been shown to be negligible (Ref. 3.2) for temperatures below 20,000°K. The radiation model of Wilson's (Ref. 3.2) includes line and continuum mechanisms of the four atomic species and neglects the ionic species. For this reasons and because adding molecular species to his model was fairly simple, it was selected as the basis of the present analysis.

Agreement does not exist on which molecular species and respective mechanisms significantly contribute to the radiation transport in an ablation coupled shock layer. The goal here is to suggest a means of selecting the species and mechanisms which could be significant in the shock layer radiative transport process.

Ablator and air molecular species which exist in thermodynamic equilibrium in significant quantities are presented in the folowing section. Restricting consideration to these species, it is noted that the frequency dependent absorption coefficient is directly proportional to the species number density times the species absorption cross-section, see Eq. B.14. Table 3.1 presents, for the molecular species, a list of estimated maximum molar compositions, maximum cross-sections and reported transition probabilities (f-number). This information is needed in order to estimate the relative effectiveness of a species and mechanism as a radiator. It should be noted that the table is not complete. Some information either was not found or does not exist; while other information was reported as being of questionable accuracy. Further, some molecular mechanisms were not listed since their cross sections or f-numbers were negligibly small in comparison with the ones listed in Tab. 3.1.

The effectiveness of a particular mechanism of a species is principly dependent upon its absorption cross section, σ_ν, number density and frequency range in which the absorption cross-section is the same order of magnitude as the maximum cross-section. Other factors which determine the significance of a mechanism of a species are the temperature level and the physical distance in the shock layer in which the species exist. Most molecules will exist in a near constant temperature layer near the body for large mass injection. Therefore evaluation of cross-section at and slightly above the sublimation temperature of carbon is realistic. Further,

TABLE 3.1

MOLECULAR SPECIES CONSIDERED

Species	Maximum mole fraction 100% phenolic-nylon, p=1 atm	Process or spectroscopic transition	Maximum cross-section (cm^2)	f-number	Ref. 3.	Comments
O_2	negligible (air-.20)	Schumann-Runge Photodissociation Photoionization	2×10^{-18}	.17	10,14,3 8 8	Retained omitted omitted
N_2	.011 (AIR - .80)	Birge-Hopfield 1st - positive 2nd - positive photoionization	1.1×10^{-17}	.0014→.0028 .04	10,12 3,15 3,15 8	Retained negligible (omitted) omitted omitted
CN	.027	Red Violet $D^2\pi - A^2\pi$ $D^2\pi - X^2\Sigma^+$ photoionization	$1. \times 10^{-19}$ 3×10^{-19} 4×10^{-20} 5×10^{-18}	.0022 .027 .005 .005	3,9,11 9,13 3,9 3,9	negligible (omitted) omitted negligible (omitted) negligible (omitted) omitted
CO	.147	Asundi 4th - positive 3rd - positive photoionization	$1. \times 10^{-22}$ 9×10^{-18}	.020 .017→.15 .030	9,11 3,9,11,14 14 8	negligible (omitted) retained omitted negligible (omitted)

TABLE 3.1 (Cont. 1)

MOLECULAR SPECIES CONSIDERED

Species	Maximum mole fraction 100% phenolic-nylon, P=1 atm	Process or spectroscopic transition	Maximum cross-section (cm^2)	f-number	Ref. 3.	Comments
C_2	.053	Swan	3×10^{-17}	.005→.029	3,9	omitted
		Deslandres-Dazambya	5×10^{-19}	.005	3,9	negligible (omitted)
		Fox-Herzberg	4×10^{-18}	.05→.13	3,9	retained
		Mulliken	3×10^{-17}	.10	3,9	retained
		Freymark	6×10^{-18}	.10→.20	3,9	retained
		photoionization			8	negligible (omitted)
C_3	.023	$\tilde{A}'\pi_u - X'\Sigma_g^+$	8.5×10^{-17}	.13	3	retained
CH	.002	$B^2\Sigma^- - X^2\pi$		.0049→.012	3,15	negligible (omitted)
		$A^2\Delta - X^2\pi$		.005→.027	3,15	negligible (omitted)
		$C^2\Sigma^+ = X^2\pi_r$		0.10	3	negligible (omitted)
C_4H	.057				none found	omitted
C_3H	.077				none found	omitted

TABLE 3.1 (Cont. 2)

MOLECULAR SPECIES CONSIDERED

Species	Maximum mole fraction 100% phenolic-nylon, P=1 atm	Process or spectroscopic transition	Maximum cross-section (cm^2)	f-number	Ref. 3.	Comments
C_2H_2	.067	$\tilde{A}'A - \tilde{X}'\Sigma_g^+$	3.2×10^{-21}	.0001	3	negligible (omitted)
		$B'(?) - X'\Sigma_g^+$	1.6×10^{-18}	.005	3	retained
		$C'\pi - \tilde{X}'\Sigma_g^+$	3.2×10^{-17}	.050	3	retained
NCN	.026	$\tilde{A}'A'' - \tilde{X}'\Sigma^+$	1.6×10^{-19}	.001	3	negligible (omitted)
		$\tilde{B}'A'' - \tilde{X}'\Sigma^+$	1.6×10^{-19}	.001	3	negligible (omitted)
		$\tilde{C}'A' - \tilde{X}'\Sigma^+$	1.6×10^{-19}	.001	3	negligible (omitted)
C_2H	.108	$\tilde{A}^2\Sigma^+ - \tilde{X}^2\pi$	3.0×10^{-18}	.01	3	negligible (omitted)
		$\tilde{B}^2A' - \tilde{X}^2\pi$	1.1×10^{-18}	.01	3	negligible (omitted)
		$\tilde{C}^2\pi - \tilde{X}^2\pi$	1.6×10^{-17}	.10	3	retained
		$\tilde{D}^2A'' - \tilde{A}^2\Sigma^+$	1.7×10^{-18}	.01	3	negligible (omitted)
		$\tilde{E}^2\Sigma^+ - \tilde{A}^2\Sigma^+$	1.3×10^{-17}	.10	3	retained
H_2	.278	Werner	3×10^{-17}	.40	8,9	retained
		H-H continuum	5×10^{-22}		9	negligible (omitted)
		photoionization	7×10^{-18}		8,9	negligible (omitted

irrespective of the physical dimensions considered if the relative effectiveness of a mechanism of a species is negligible considering the absorption cross-section, number density and frequency range that mechanism will not participate in the radiative exchange. Consequently a measure of the relative effectiveness of mechanisms of species in this work is defined as

$$\mathcal{E}_j^i = (\sigma_j^i)_{max} (Y_j)_{max} (\Delta h\nu)_j^i \quad (ev\ cm^2) \tag{3.10}$$

where

$(\sigma_j^i)_{max}$ = maximum cross section of mechanism i of species j

$(Y_j)_{max}$ = maximum possible mole fraction of species j in the shock layer

$(\Delta h\nu)_j^i$ = spectral interval over which σ_j^i is greater than $.1\ (\sigma_j^i)_{max}$.

In the above definition mole fraction which is directly proportional to number density was used rather than number density. The radiative "effectiveness factor" defined above was computed for the species and their respective mechanism listed in Tab. 3.1. Figure 3.1 presents a ranking of the larger effectiveness factors which vary over a range of four orders of magnitude.

Based on the effectiveness factors in Fig. 3.1 a selection was made of which molecular species and respective mechanisms to include in the radiation calculation. The selection is indicated under the

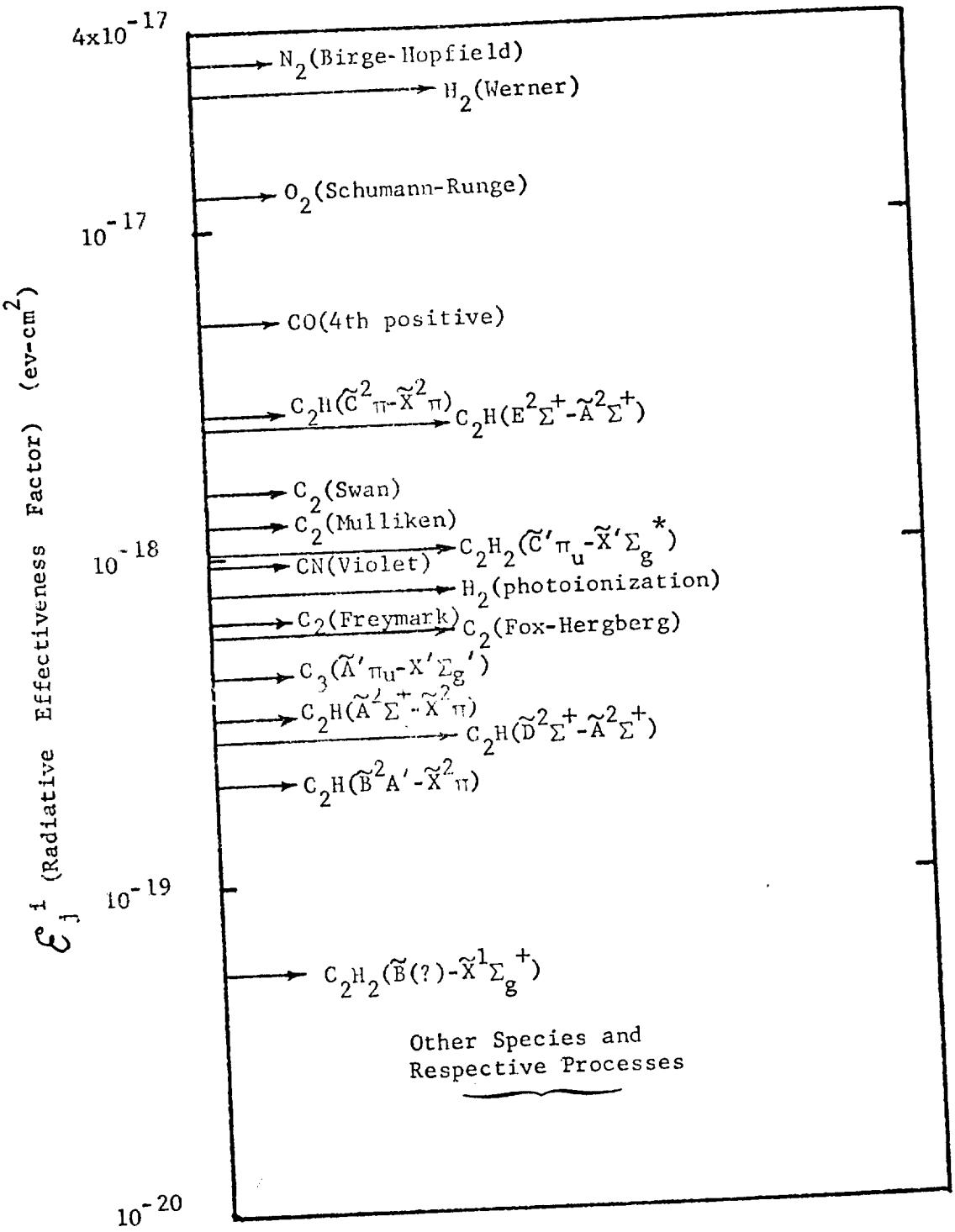

Fig. 3.1 A Comparative Ranking of Molecular Radiative Effectiveness Factors

comments of Tab. 3.1. Based on this selection the mechanisms - H_2(Werner), $C_2H(\tilde{C}^2\Pi \rightarrow \tilde{X}^2\Pi)$ and $C_2H(E^2\Sigma^+ - \tilde{A}^2\Sigma^+)$ - were added to the radiation model of Wilson's. The band average cross sections for all the species mechanisms along with the details of the radiation model used in this work is presented in Appendix B. The radiation model in computer program form is discussed and listed in Appendix C. In this program called LRAD 3 twelve species are considered

H		O_2	CO
C	Line and Continuum	N_2	C_3
O		C_2	C_2H
N		H_2	
e^-			

Continuum

where the molecules listed are the ones selected above. Computationally the frequency range $0 < h\nu \leq 20.$ (ev) is broken into twelve continuum bands with nine line groups used located at nine line centers. The boundary conditions on intensity entering the shock layer from the free stream and from the body are assumed zero. Thus it is assumed that no radiation enters the shock layer althrough radiant energy may leave through either surface. This is the assumption made in state of the art analyses (Refs. 3.10, 3.19, 3.22, 3.27, 3.31 and others). The only questionable part of this assumption appears to be in assuming the reradiation from the surface does not effect the shock layer. This is theoretically

correct for an optically thin shock layer. The results presented in Chapter 5 show that the magnitude of the reradiation flux is small in comparison to the other radiative flux in the shock layer. Further, the shock layer is observed to be optically thin in the lower frequency range where the surface radiation is emitted. Consequently the assumption appears valid. The magnitude of the energy loss from the surface is significant with respect to the energy absorbed and thus is accounted for in the surface balance equations presented in the third section of this chapter.

One additional comment is pertinent regarding the selection of radiative properties. It has been assumed in the foregoing discussion that the ablator surface temperature is at the equilibrium sublimation temperature of the char and the ablator responds in a quasi-steady manner. If however the surface temperature is significantly below the char sublimation temperature, which is the case in the early portion of a re-entry trajectory, higher molecular weight species will be introduced into the shock layer. The radiative properties of such species should be considered. However, by and large the radiative characteristics of polyatomic hydrocarbons are unknown. In addition, if the surface does not sublime completely but rather mechanically erodes, which some experimental evidence indicates can and does occur (Ref. 3.16 and 3.17), then the radiative properties of solid carbon (soot) should be included in the radiative and thermodynamic calculations. The radiative importance of this process is indicated by the absorption cross-

section of soot (10^{-12} cm^2 for a 250 Å particle as computed using data of Ref. 3.18) which is a factor of approximately 10^5 larger than any gas phase species. Chemical equilibrium thermodynamics analyses do not predict the presence of solid carbon at temperatures above the char sublimation temperature. Furthermore, mechanisms which result in solid carbon in the flow-field are not well understood and consequently have not been modeled. Thus, for this work solid carbon was neglected although if it exists in significant quantities it might well have a pronounced effect on the radiative heating.

In addition to the detailed radiation model and associated properties just discussed, a simplified radiation model based on the emission properties of air was used. This model developed by Ref. (3.19) is a correlation of the radiative flux divergence of air presented by Ref. (3.20). The curve fit equations for the radiative flux divergence are listed below.

$$T_t = 1000.\ \log_{10} P + 13800.$$

If $T < T_t$, then

$$\log_{10} \mathbb{E} = .0005\ T + 1.15\ \log_{10} P - 3.15 \qquad (3.17)$$

If $T \geq T_t$, then

$$\log_{10} \mathbb{E} = 1.875\ \log_{10} P + 3.903$$

In the preceeding equations T is temperature in ^{o}K, P is pressure in atm, and $\mathbb{E}$ is the continuum flux divergence in watts/cm^3. This radiation model will be henceforth called the emission model. It provides a computationally fast means of estimating the flux divergence in radiative coupled problems; although, as noted in Ref. (3.19), the emission model tends to overpredict the flux divergence obtained from more detailed models.

The species radiative properties discussed along with the radiation model presented in Appendix B and the emission model are used in a numerical solution of the thin shock layer equations. The primary result from such a solution using either of the radiation models is the surface heating rate. An additional method was used in the present work to compute surface radiative heating rates. This method is based on a correlation of a radiative cooling parameter presented by Ref. (3.21) which is based on the work of Page et. al. (Ref. 3.22). The radiative cooling parameter accounts for the radiative energy losses from an inviscid shock layer as predicted by the numerical calculations of Ref. 3.22. The cooling paramter, Γ, is defined as

$$\Gamma = \frac{2(q_R)_{isothermal}}{\frac{1}{2}\rho_\infty U_\infty^3} \tag{3.12}$$

The surface radiative flux is determined from the relation

$$q_R = (0.2 - 0.295 \log_{10}\Gamma)(q_R)_{isothermal} \quad \text{for } .04 < \Gamma < 1.0 \tag{3.13}$$

where the isothermal radiative flux must be determined from an

independent calculation. In the present work the isothermal flux is determined using the line and continuum radiation model presented in Appendicies B and C. This correlation for radiative heating is used in a computer program called RADCOR developed as part of the present work. Additional details concerning the use of the correlation along with the RADCOR Program are presented in Appendix E. Results and comparisons with more complete analysis are given in Chapter 5.

To recapatulate, the molecular and atomic mechanisms which produce line and continuum radiation have been discussed in relation to the current problem. A method for selecting the mechanisms which significantly contribute to the radiative energy transfer has been developed. This method based on a radiative effectiveness factor was applied in selecting molecular mechanisms. The equations for an emission model of air was stated. Equations for the radiative cooling parameter were stated. These equations were used in the RADCOR computer program for simplified heating rate calculations.

THERMODYNAMIC PROPERTIES

Two sets of thermodynamic properties and computational methods were used in the present work. One method is limited to the species of air whereas the second is applicable to arbitrary gas mixtures. The method which is limited to air species was used, because of the computational speed, in solving the Rankine-Hugoniot equations and in computing thermodynamic properties of shock layer gases where no ablation products exist. The general method was

used to compute thermodynamic properties of air-ablation and ablation product gas mixtures.

Equilibrium thermodynamic properties of air which includes its major components (O_2, N_2, O, N, O^+, N^+, E^-) were obtained in closed form from a set of approximate partition functions using the method of Hansen's (Ref. 3.23). The partition functions and thermodynamic relations for an ideal gas were programmed (Ref. 3.24) such that the total enthalpy, entropy, speed of sound, average molecular weight, heat capacity and species concentrations can be found for a given temperature and pressure. The following section discusses the transport properties which were also computed using Hansen's method. The computational scheme for both the thermodynamic and transport properties of air is embodied in subroutine GAS which is listed in Appendix D. Figure 3.2 presents a comparison of species number densities computed using this method with number densities from two different free energy minimization methods. This agreement is typical and lends validity to the use of the species number densities as well as the overall thermodynamic properties obtained from the approximate partition functions of Reference 3.23.

Thermodynamic properties for arbitrary gas mixtures were computed using a free energy minimization program, CHEMEQ, developed by Ref. (3.26) which is a modification of a program reported by Ref. (3.25). Curve-fits of thermodynamic data for individual species are required as the basic information for a calculation. The forms of the curve-fit for the standard state properties are listed in

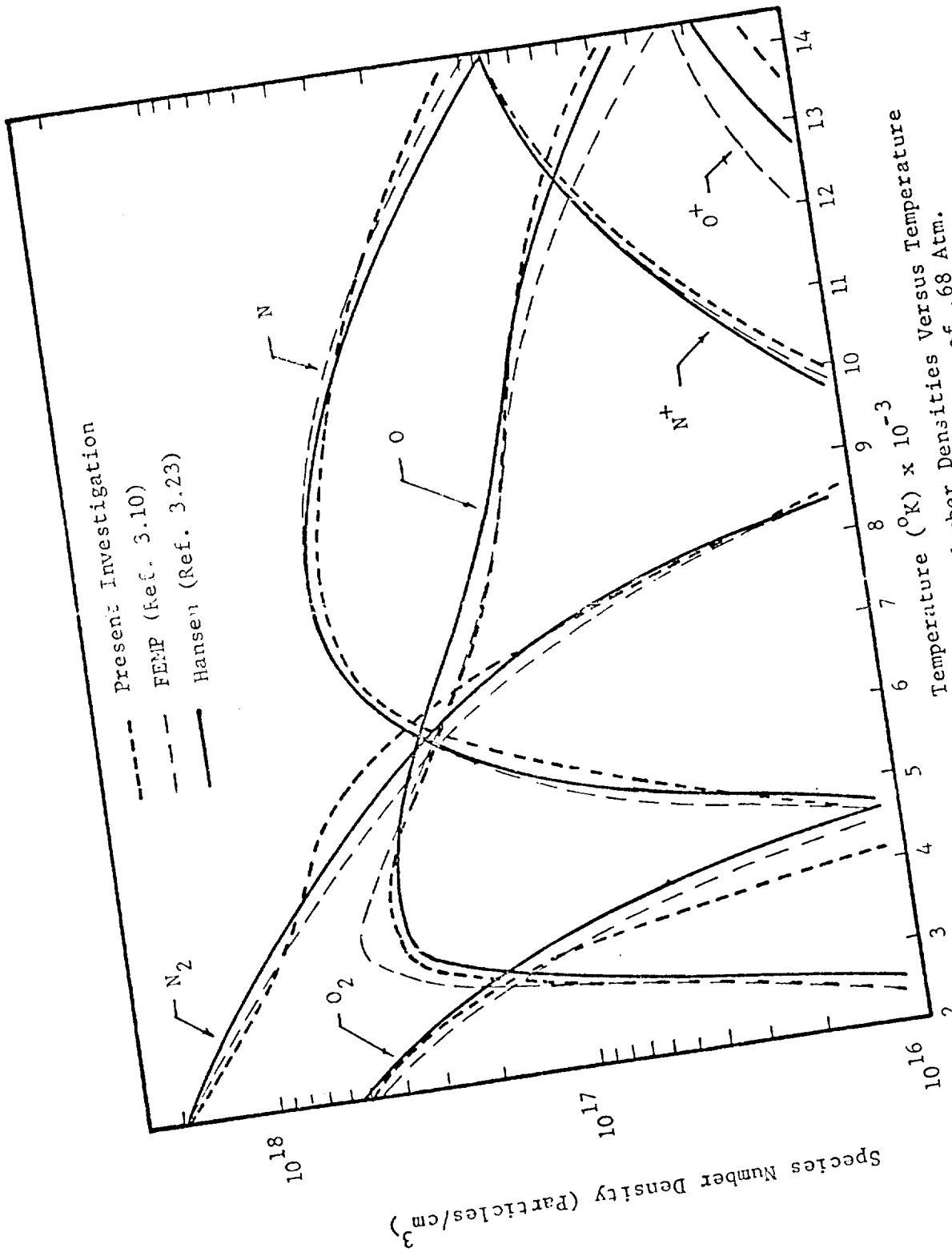

Fig. 3.2 Comparison of Species Number Densities Versus Temperature From Different Methods for a Pressure of .68 Atm.

Tab. 3.2. From the pure component properties which are represented by the curve-fit equations the mixture thermodynamic properties are computed by minimizing the free energy of the system.

The selection of the species to include in the shock layer calculations was based on the ablator composition, the shock layer temperture, and the pressure ranges of interest. Air and the phenolic ablator selected for study contains the four elements, H, C, O, and N. The temperature range considered was from the sublimation temperature of the ablator up to approximately 17000°K and the pressure range considered was from .001 to 2.0 atmospheres. Twenty species were found to have a significant concentration in temperature range of interest at 1.0 atmosphere pressure. This was taken as representative in the pressure range. These species are listed in Tab. 3.3. from Ref. 3.32 along with their respective heats of formations where the reference elements are H_2, N_2, O_2, solid carbon and e^-.

The curve-fit constants obtained from Ref. 3.32 for these twenty species are listed in the block data package of VISRAD 3 presented in Appendix D. Two sets of curve-fits are used for the two temperture ranges 1000°K to 6000°K to 17000°K. Details of the Fortran nomenclature for the curve-fit equations are given in Appendix D.

TABLE 3.2

A SUMMARY POLYNOMIAL EQUATIONS FOR STANDARD

THERMODYNAMIC PROPERTIES

Specific Heat

$$\frac{C_p^{\circ}}{R} = A_1 + A_2T + A_3T^2 + A_4T^3 + A_5T^4$$

Enthalpy

$$\frac{H_T^{\circ}}{RT} = A_1 + \frac{A_2}{2}T + \frac{A_3}{3}T^2 + \frac{A_4}{4}T^3 + \frac{A_5}{5}T^4 + \frac{A_6}{T}$$

Entropy

$$\frac{S_T^{\circ}}{R} = A_1 \ln T + A_2T + \frac{A_3}{2}T^2 + \frac{A_4}{3}T^3 + \frac{A_5}{4}T^4 + A_7$$

Free Energy

$$\frac{F_T^{\circ}}{RT} = A_1(1-\ln T) - \frac{A_2}{2}T - \frac{A_3}{6}T^2 - \frac{A_4}{12}T^3 - \frac{A_5}{20}T^4 + \frac{A_6}{T} - A_7$$

TABLE 3.3

COMPONENTS AND HEATS OF FORMATION

Component	$(\Delta H^{o}_{f})_{298.16}$ (k/cal/gmole)	$(\Delta H_{f}^{o})_{o}$ kcal/gmole
N	112.951	112.507
O	59.544	58.972
C(gas)	171.301	169.990
N^{+}	449.709	447.564
O^{+}	374.867	372.942
C^{+}	432.357	429.537
H	52.098	51.620
C_2	197.0259	195.000
C_3	189.6115	188.000
C_2H	117.6448	116.700
C_2H_2	53.8670	54.300
CO	-26.4179	-27.202
CN	109.7865	109.000
HCN	31.1895	31.281
C_4H	——	154.000
C_3H	——	127.100
O_2	0.0	0.0
N_2	0.0	0.0
H_2	0.0	0.0

TRANSPORT PROPERTIES

The transport properties used in the present work are those of Hansen (Ref. 3.23) for air. As pointed out by Hansen the knowledge of transport properties of air at high temperatures is in an elementary state as compared to the knowledge of the thermodynamic properties. The basic information needed for calculation of transport properties from kinetic theory is the species interaction potential such that the collision integral may be computed. At high temperatures the atom-atom, atom-ion and atom-molecule potentials are required but are not known well enough for accurate transport calculations. The problem is further compounded when ablation products are introduced into the gas mixture. Thus as an engineering approximation, the closed form expressions for transport coefficients (i.e. thermal conductivity and viscosity) for air were used over the entire shock layer.

The calculation of transport properties by the Hansen method is based on simple kinetic theory of hard spheres. The viscosity is calculated by a simple summation formula (Eq. 66 of Ref. 3.23) which is a function of species density, mean velocity and mean free path. These variables are then related to the temperature, pressure and air species composition of the mixture. The thermal conductivity is calculated as the sum of two effects. The first effect accounts for the energy transfer by molecular collision which is processed for ordinary thermal conductivity. The second effect accounts for energy transfer by diffusion of species which are involved in

equilibrium reactions at each point in the flow-field. The first effect is expressed as a function of species density, mean velocity, mean freepath, molecular weight and heat capacity. The second is written in as a function of the temperature, species diffusion coefficients, concentration and stoichiometric coefficient as well as the equilibrium constant. These two effects are the frozen and reacting parts respectively of the thermal conductivity discussed in Chapter 2 (Eq. 2.169) when developing the temperature form of the energy equation.

Using air transport properties is justified not only because significant uncertainty is present in the basic data, but, more importantly, the resulting heating rate from a shock layer solution is essentially uneffected by the difference in air and air-ablation product transport properties. Rigdon et. al. (Ref. 3.27) showed for a typical flight condition a 1.5% change in radiating heating rate as a result of the difference in air and air-ablation product transport properties. More recently Esch (Ref. 3.26) has further substantuated the negligible effect of different transport properties on radiative heating. Specific calculations substantiating this assumption will be given in Chapter 5.

ABLATOR RESPONSE PROPERTIES

The present work uses a quasi-steady ablator analysis of a phenolic-nylon composite ablator. Furthermore, the surface temperature is selected to be the sublimation temperature of the char. These restrictions imply appreciable ablation rates (at least 5% of the

free-stream mass flux); the surface balance equations (2.138 to 2.142) are appropriate to describe such flow-field ablator interaction. Results presented in Chapter 5 will show post priori that this is a valid approximation for most flight conditions of interest.

Since the elemental species, total mass flow rate and pressure are identical across the interface for quasi-steady response with appreciable ablation rates, only the energy boundary conditions is considered here.

$$k_b \frac{dT^-}{dy} = k_T \frac{dT^+}{dy} - q_R^+ \tag{2.142}$$

The left hand side of the above equation represents the heat flux into the body. The quasi-steady model of the ablator can be used to relate this influx of energy to the heat absorbed and convected away. This relation is

$$k_b \frac{dT^-}{dy} = (\rho v)^- \Delta H_{ab} \tag{3.14}$$

Combining Equations (3.14) and (2.142) yields

$$(\rho v)^- \Delta H_{ab} = k_T \frac{dT^+}{dy} - q_R^+ \tag{3.15}$$

or

$$(\rho v)^- \Delta H_{ab} = q_T - \epsilon\sigma T^4 \tag{3.16}$$

where q_T is the total heat flux (convective plus radiative to the surface from the flow-field and ΔH_{ab} is the heat of ablation.

The phenolic-nylon composite considered in this work is

described by Pike et. al. in Ref. 3.28. This composite has a mass elemental composition of 73.03% carbon, 7.29% hydrogen, 4.96% nitrogen and 14.72% oxygen.

The heat of ablation of phenolic-nylon was computed by Balhoff (Ref. 3.29) using a chemical equilibrium program developed by (Ref. 3.26) which accounts for solids as well as gas components. The heat of ablation which includes the heat of pyrolysis (300. BTU/lb_m) is presented in Fig. 3.3 along with the computed sublimation temperature. The computed sublimation temperature and heat of ablation data were least squares fit as a function of pressure for computation work. The equations from the curve fitting process are

$$T_{sub} = 3450.4 + 187.0 \log_{10}P + 9.715 (\log_{10}P)^2 \qquad (3.17)$$

$$\Delta H_{ab} = 9179.7 - 114.81 \log_{10}P + 329.64 (\log_{10}P)^2 \qquad (3.18)$$

Using Eqs. 3.17 and 3.18, the surface balance equation (3.16) was solved for various pressure levels providing the results shown in Fig. 3.4. The results indicate that the ablation rate is a weak function of pressure and a weaker function of the sublimation temperature for a given flow-field heating rate and constant surface emissivity. A conservative value of emissivity is .6; such as that reported by Pope (Ref. 3.30) for phenolic-nylon char. The average value reported in Ref. 3.30 was .67, this is in contrast to an average value of .95 for the data reported earlier by

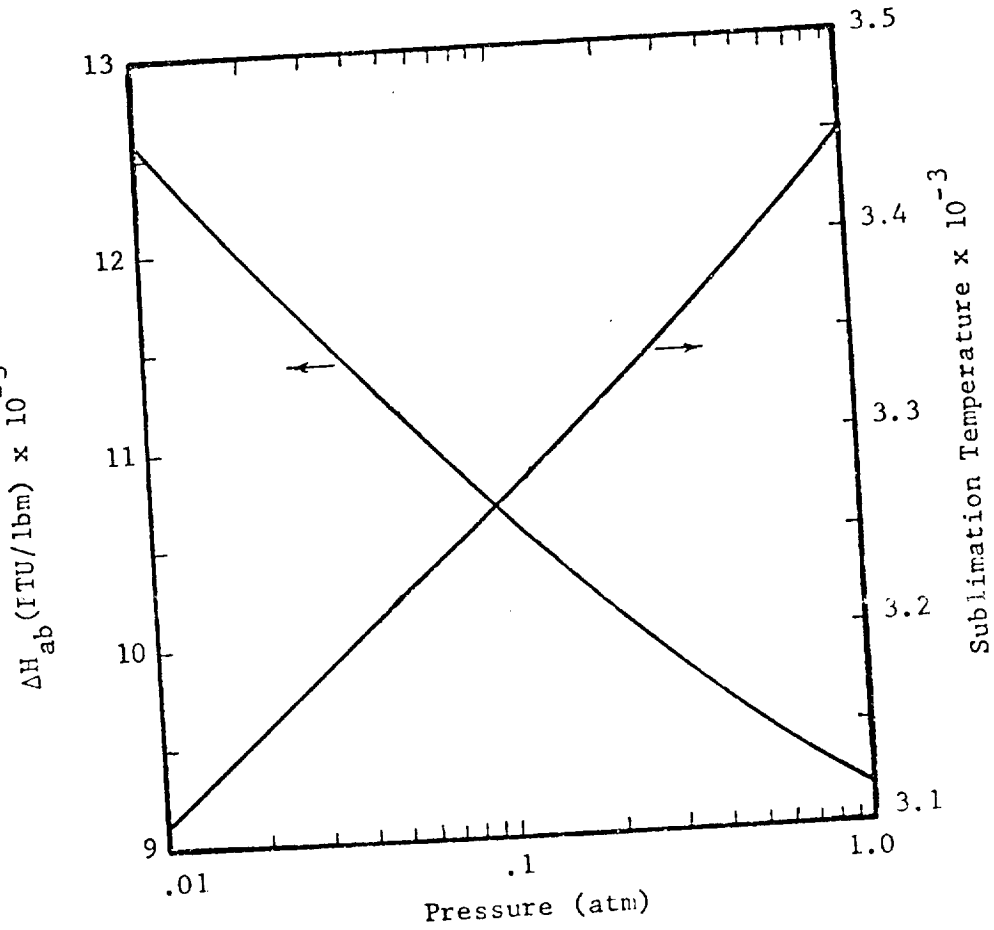

Fig. 3.3 Phenolic Nylon Heat of Ablation and Sublimation Temperature as a Function of Pressure.

Wilson (Ref. 3.31). In order to determine the effects of uncertanties in the surface emissivity on the ablation rate parametric calculations were made for two values of pressure using two values of emissivity, namely: 1.0 and 0.4. The results are shown in Fig. 3.5 and indicate an uncertainty of .056 lb_m/ft^2 sec for 1.0 atmospheres and .031 lb_m/ft^2 sec at 0.1 atmospheres. These values are independent of heating rate; however the percentage uncertainty increases with decreasing heating rate.

The results presented in Fig. 3.4 are used in Chapter 5 to obtain coupled flow-field and ablator solutions.

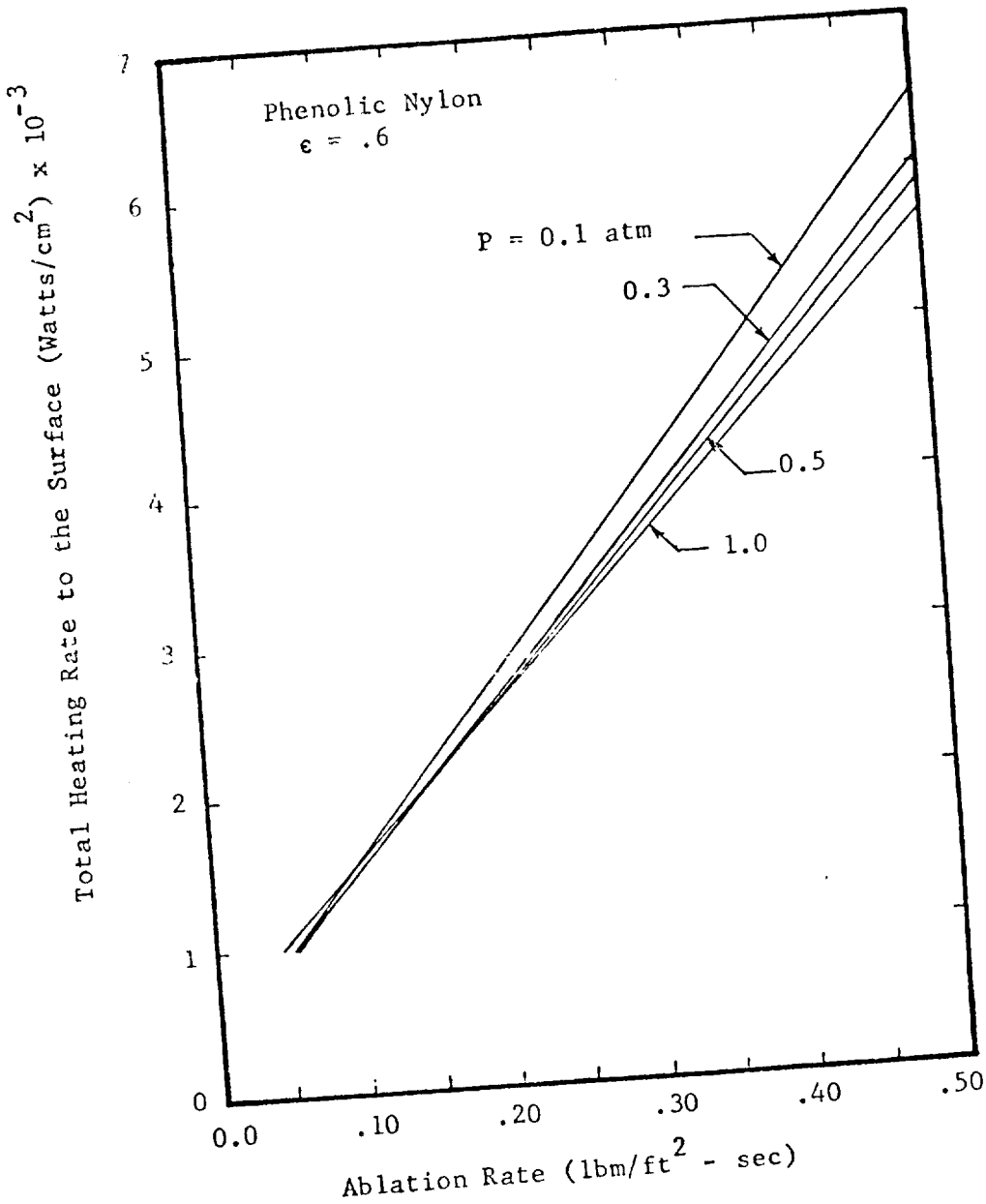

Fig. 3.4 Phenolic Nylon Ablation Rates as a Function of Total Surface Heating for Various Pressure Levels

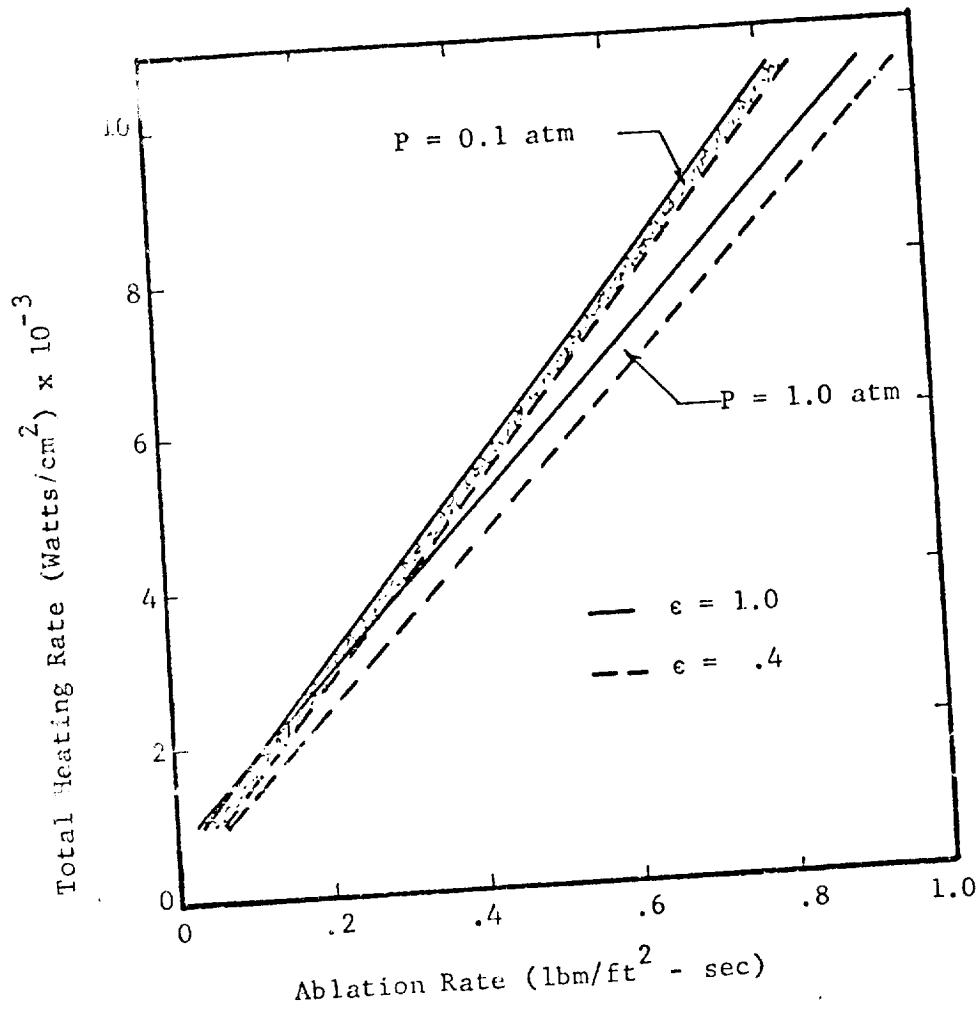

Fig. 3.5 The Effect of Uncertainties in Ablator Surface Emissivity on the Ablation Rate

CHAPTER 3

References

3.1 Marr, Geoffrey, Plasma Spectroscopy, Elsevier Pub. Co., 1968.

3.2 Wilson, K. H., "Stagnation Point Analyses of Coupled Viscous-Radiating Flow with Massive Blowing," NASA CR-1548, June 1970.

3.3 Main, Roger P. and Ernest Bauer, "Equilibrium Opacities and Emissivities of Hydrocarbon-Air Mixtures at High Temperatures," J. Quant. Spectrosc. Radiat. Transfer, Vol. 7, pp. 527-557, 1967.

3.4 Wilson, K. and W. E. Nicolet, "Spectral Absorption Coefficients of Carbon, Nitrogen and Oxygen Atoms," J. Quant. Spectrosc. Radiat. Transfer, Vol. 7, pp 891-941, 1967.

3.5 Penner, S. S., Quantitative Molecular Spectroscopy and Gas Emissivities, Adeleson-Wesley Pub. Co., 1959.

3.6 Cairns, R.B. and J. A. R. Samson, "Studies of Photoionization by Atomic Hydrogen, Oxygen, and Nitrogen," NASA CR-998, March 1968.

3.7 Penner, S. S. and D. B. Olfe, Radiation and Reentry, Academic Press, 1968.

3.8 Nicolet, W. E., "Advanced Methods for Calculating Radiation Transport in Ablation-Product Contaiminated Boundary Layers," NASA CR-1656, Sept. 1970.

3.9 Hoshizaki, H. and L. E. Lasher, "Convective and Radiative Heat Transfer to an Ablating Body," LMSC Report No. 4-06-66-12, Lockheed Missiles and Space Co., July 1966.

3.10 Hoshizaki, H. and K. H. Wilson, "Convective and Radiative Heat Transfer During Superorbital Entry," LMSC Report No. 4-43-65-5, Lockheed Missiles and Space Co., June 1966.

3.11 Myer, H. G., J. T. Ohrenberger and T. R. Thompson, "Emission and Absorption of Radiant Energy in a Model Planetary Atmosphere," AIAA Journal, Vol. 3, No. 12, Dec. 1965.

3.12 Allen, R. A., A. Textoris and J. Wilson, "Measurements of the Free-Bound and Free-Free Continuous of Nitrogen and Oxygen and Air," J. Quant. Spectrosc. Radiat. Transfer, Vol. 5, pp. 95-108, 1965.

3.13 Thomas, G. M. and W. A. Menard, "Experimental Measurements of Nonequilibrium and Equilibrium Radiation from Planetary Atmospheres," AIAA Journal, Vol. 4, No. 2, Feb. 1966.

3.14 Arnold, J. O., V. H. Reis and H. T. Woodward, "Studies of Shock Layer Radiation of Bodies Entering Planetary Atmospheres," AIAA Journal, Vol. 3, No. 11, Nov. 1965.

3.15 Golden, S. A., "Approximate Absorption Coefficients of Electronic Transitions in Diatomic Molecules," J. Quant. Spectrosc. Radiat. Transfer, Vol. 7, pp. 225-250, 1967.

3.16 Sutton, K., "An Experimental Study of a Carbon-Phenolic Ablation Material," NASA TN D-5930, Sept. 1970.

3.17 Page, W. A., "A Survey of Thermal Radiation Studies of Ablating Bodies in the Ballistic Range," NASA TN D-3741, Feb. 1967.

3.18 "Study of the Spectral Emissivity of Carbon Particles Produced by a Rocket Motor," Final Report GD/C-DBE66-006, General Dynamics Corp., May 1966.

3.19 Engel, C. D. and L. W. Spradley, "Radiation Absorption Effects on Heating Loads Encountered During Hyperbolic Entry," J. Spacecraft Roc., Vol. 6, No. 6, 1969, pp. 764-765.

3.20 Yos, J. M., "Transport Properties of Nitrogen, Hydrogen, Oxygen and Air to 30000°K, RAD-TM-63-7, March, 1963, Avco Corp.

3.21 Livingston, F. and J. Williard, "Planetary Entry Body Heating Rate Measurements in Air and Venus Atmospheric Gas up to T = 15000°K," AIAA J. Vol. 9, No. 3, March 1971.

3.22 Page, W. G., D. L. Compton, W. J. Borucki, and D. L. Cliffone, "Radiative Transport in Inviscid Nonadiabatic Stagnation-Region Shock Layers," AIAA Paper No. 68-784, June 1968.

3.23 Hansen, C. F. "Approximations for the Thermodynamic Properties of High Temperature Air," NASA TR R-50, 1959.

3.24 Spradley, L. W. and C. D. Engel, "A Computer Program for Predicting Coupled Convective and Radiative Heat Transfer to a Blunt Body During Superorbital Reentry," LMSC/HREC A791350, Lockheed Missiles & Space Co., Huntsville, Ala., May 1968.

3.25 Stroud, C. W. and K. L. Brinkley, "Chemical Equilibrium of Ablation Materials Including Condensed Species," NASA TN D-5391, August 1969.

3.26 Esch, D. D., Stagnation Region Heating of a Phenolic-Nylon Ablator During Return From Planetary Missions, Ph.D. [illegible] State University, Baton Rouge, La., Aug. [illegible]

3.27 Rigdon, W. S., R. B. Dirling, Jr. and M. Thomas. "Stagnation Point Heat Transfer During Hypervelocity Atmospheric Entry," NASA CR-1462, Feb. 1970.

3.28 Pike, R. W., G. A. April, E. G. del Valle and S. Hacker, "On Methods of Determining Composition of Pyrolysis Products from Ablative Composites," JSR, Vol. 7, 1250-1253 (1970)

3.29 Balholf, J. F., Research Associate, Louisiana State University, Private Communication.

3.30 Pope, R. B., "Measurements of the Total Surface Emittance of Charring Ablators," AIAA J. Vol. 5, 2285-2287 (1967)

3.31 Wilson, R. G., "Hemispherical Emittance of Ablation Chars, Carbon, and Zirconia to 3700°K," NASA TN D-2704, 1965.

3.32 Esch, D. D., A. Siripong, R. W. Pike, "Thermodynamics Properties in Polynomial Form for Carbon, Hydrogen and Oxygen Systems From 300 to 15000°K," NASA RFL TR-70-3, Ch.E. Dept., Louisiana State University, Nov. 1970.

CHAPTER 4

NUMERICAL PROCEDURES

FINITE DIFFERENCE EQUATIONS

The stagnation line continuity, momentum and energy equations selected in Chapter 2 are solved by finite differences using a computer program called VISRAD 3 deveoped as part of this work. This chapter describes the techniques used in VISRAD 3 to obtain numerical solutions.

The implicit finite difference method developed herein has been presented in part by Adams et. al. (Ref. 4.1), Blottner (Ref. 4.2 and 4.3), Davis (Ref. 4.4), Edelman and Hoffman (Ref. 4.5 and 4.6), and Fay and Kay (Ref. 4.7). The stagnation line ordinary differential equations are quasilinearized. Derivatives are replaced by three point finite differences. An implicit set of algebraic equations of the tridiagonal form result from the previous steps for each second order equation. This set can be rapidly solved using an algorithm for tridiagonal matrices. Thus this method is globally implicit in the shock layer coordinate.

In Chapter 2 the continuity and momentum equations were transformed and split into the following first and second order ordinary differential equations.

$$\zeta = \frac{f'}{\tilde{\delta}} \tag{2.158}$$

and

$$(\rho\mu)\,\zeta'' + \left[2\,Re_s\,\tilde{\delta}^2\left(\frac{\partial u_{s,o}}{\partial \xi}\right)f + (\rho\mu)'\right]\zeta' - Re_s\,\tilde{\delta}^3\left(\frac{\partial u_{s,o}}{\partial \xi}\right)\zeta^2 \qquad (2.159)$$

$$= -\frac{2Re_s \cdots}{\rho(\partial u_{s,o}/\partial \xi)}\left(\frac{\partial}{\partial \xi}\right)$$

The boundary conditions for Eq. (2.159) are:

$$\eta = 0 \qquad \zeta = 0 \qquad (2.160)$$

$$\eta = 1 \qquad \zeta = 1/\tilde{\delta}$$

The momentum equation, Eq. 2.159, is second order and nonlinear. In order to solve this equation it is desirable to obtain a linear second order equation of the form

$$\frac{d^2w}{d\eta^2} + a_1\frac{dw}{d\eta} + a_2 w = a_3 \qquad (4.1)$$

Equation (4.1) is the linear form used by Blottner (Ref. 4.2 and 4.3), Davis (Ref. 4.4), Edelman and Hoffman (Refs. 4.5 and 4.6), and Fay and Kaye (Ref. 4.7) and others to solve some or all of the conservation equations with differing degrees of completeness. The nonlinear term in Eq. (2.159) can be quasilinearized in the manner of Lee (Ref. 4.8).

$$\left(\zeta^2\right)^{k+1} = \left(\zeta^2\right)^k + 2\,\zeta^k\left(\zeta^{k+1} - \zeta^k\right) \qquad (4.2)$$

where k is the iteration number. Substituting Eq. (4.2) into (2.159) yields a linear equation of the form of Eq. (4.1).

$$\zeta'' + \left[\frac{2Re_s \tilde{\delta}^2}{\rho\mu}\left(\frac{\partial u_{s,o}}{\partial \xi}\right) f^k + \frac{(\rho\mu)'}{\rho\mu}\right]\zeta' - \frac{2Re_s \tilde{\delta}^3}{\rho\mu}\left(\frac{\partial u_{s,o}}{\partial \xi}\right)\zeta^{(k)}\zeta \tag{4.3}$$

$$= -2\,Re_s \tilde{\delta}\left[\frac{\bar{\rho}(1-\bar{\rho})}{\rho^2\mu(\partial u_{s,o}/\partial \xi)}\left(\frac{\partial \varphi}{\partial \xi}\right)^2 + \frac{\tilde{\delta}^2}{2\rho\mu}\left(\frac{\partial u_{s,o}}{\partial \xi}\right)\zeta^{2(k)}\right]$$

In Eq. (4.3) the superscript k denotes, computed from the k-th iteration, and the superscript k+1 for the current iteration has been dropped.

The three point, variable step size finite differences stated by Davis (Ref. 4.4) and given below were used in Eq. (4.3),

$$\left(\frac{dw}{d\eta}\right)_n = \frac{\Delta\eta_{n-1}}{\Delta\eta_n(\Delta\eta_n + \Delta\eta_{n-1})} w_{n+1} + \frac{\Delta\eta_n - \Delta\eta_{n-1}}{\Delta\eta_n \Delta\eta_{n-1}} w_n - \frac{\Delta\eta_n}{\Delta\eta_{n-1}(\Delta\eta_n + \Delta\eta_{n-1})} w_{n-1} \tag{4.4a}$$

$$\left(\frac{d^2w}{d\eta^2}\right)_n = \frac{2}{\Delta\eta_n(\Delta\eta_n + \Delta\eta_{n-1})} w_{n+1} - \frac{2}{\Delta\eta_n \Delta\eta_{n-1}} w_n + \frac{2}{\Delta\eta_{n-1}(\Delta\eta_n + \Delta\eta_{n-1})} w_{n-1} \tag{4.4b}$$

Using the above relations for the difference equations, Eq. 2.23 can be written as

$$\left[\frac{2 - a_1 \Delta \eta_n}{\Delta \eta_{n-1} (\Delta \eta_n + \Delta \eta_{n-1})}\right]\zeta_{n-1} + \left[\frac{a_1(\Delta \eta_n - \Delta \eta_{n-1}) - 2}{\Delta \eta_n \Delta \eta_{n-1}} + a_2\right]\zeta_n$$

$$+ \left[\frac{2 + a_1 \Delta \eta_{n-1}}{\Delta \eta_n (\Delta \eta_n + \Delta \eta_{n-1})}\right]\zeta_{n+1} = a_3 \tag{4.5}$$

Equation (4.5) is of the form

$$A\ \zeta_{n-1} + B\ \zeta_n + C\ \zeta_{n+1} = D \tag{4.6}$$

which yields a tridiagonal matrix in the vector equation to be solved. Equation (4.6) can be written in the following matrix form:

$$\begin{bmatrix} B_1 & C_1 & & & \\ A_2 & B_2 & C_2 & & \\ & A_3 & B_3 & C_3 & \\ & & & A_n & B_n \end{bmatrix} \cdot \begin{bmatrix} \zeta_1 \\ \zeta_2 \\ \zeta_3 \\ \zeta_n \end{bmatrix} = \begin{bmatrix} D_1 - A_1 \zeta_0 \\ D_2 \\ D_3 \\ D_n - C_n \zeta_{n+1} \end{bmatrix} \tag{4.7}$$

Equation (4.7) was solved using the tridiagonal inversion algorithm program given by Conte (Ref. 4.9). This algorithm gives a rapid and accurate solution of the tridiagonal system. No significant improvement in accuracy has been noted in the use of double precision in calculating variables in this subroutine.

The first order equation (2.158) which accompanies Eq. (2.159) was integrated

$$f = \tilde{\delta} \int_0^{\eta} \zeta \, d\eta + f_w \tag{4.8}$$

where

$$f_w = \frac{-(\rho v)_w}{2\tilde{\delta}\,(\partial u_{s,o}/\partial \xi)} \tag{4.9}$$

using a simple trapezoidal scheme.

The transformed standoff distance, $\tilde{\delta}$, was computed by using the boundary condition

$$\eta = 1, \qquad f = f_s = \frac{-(\rho v)_s}{2\tilde{\delta}\,(\partial u_{s,o}/\partial \xi)} \tag{4.10}$$

and Eq. (4.8) in the following relation

$$\tilde{\delta} = \frac{f_s - f_w}{\int_0^1 \zeta d\eta} \tag{4.11}$$

This computed value was then compared to the assumed $\tilde{\delta}$ for convergence. If necessary a new $\tilde{\delta}$ is assumed and the entire set of equations is solved again.

Finally the actual standoff distance is computed using

$$\delta = \tilde{\delta} \int_0^1 \rho \, d\, \eta \tag{4.12}$$

with a simple trapezoidal scheme.

The transformed energy equation developed in Chapter 2

$$\frac{d^2T}{d\eta^2} - \frac{\tilde{\delta}}{2\rho k_T}\left(\rho v C_{P_T} - \frac{d(\rho k_T)}{d\eta}\right)\frac{dT}{d\eta} = \frac{\tilde{\delta}}{k_T} v^2 \frac{dv}{d\eta} + \frac{\tilde{\delta}^2}{\rho^2 k_T} \mathbb{E} \tag{2.169}$$

is linear in temperature and thus quasilinearization of terms is

not needed. In order to use the above equation in the form of Eq. [illegible] must be a known function of η. Numerically this is accomplished by determining the flux divergence profile from the previous iteration and this profile is then used in the solution of the energy equation. Additional information concerning the iteration technique is given later in this chapter in the discussion related to Fig. 4.8.

The boundary conditions for the preceeding equation are:

$$\eta = 0, \qquad T = T_w$$
$$\eta = 1, \qquad T = T_s \tag{4.13}$$

where T_w is determined by the ablator response (for ablation coupled analysis $T_w = T_{sublimation}$ is chosen) and T_s is determined by the solution of the Rankine-Hugoneot equations.

Following the development of the momentum equation, finite differences (4.4) can be substituted into Eq. (2.169) for all derivatives. This yields

$$\left[\frac{2 - \Delta\eta_n a_1}{\Delta\eta_{n-1}(\Delta\eta_n + \Delta\eta_{n-1})}\right] T_{n-1} + \left[\frac{a_1(\Delta\eta_n - \Delta\eta_{n-1}) - 2}{\Delta\eta_n \Delta\eta_{n-1}}\right] T_n$$
$$+ \left[\frac{2 + \Delta\eta_{n-1} a_1}{\Delta\eta_n(\Delta\eta_n + \Delta\eta_{n-1})}\right] T_{n+1} = a_3 \tag{4.14}$$

where

$$a_1 = \frac{-\tilde{\delta}}{2\rho k_T}\left[\rho v C_{P_T} - \frac{d(\rho k_T)}{d\eta}\right]$$

$$a_3 = \frac{\tilde{\delta}}{k_T} v^2 \frac{dv}{d\eta} + \frac{\tilde{\delta}^2}{\rho^2 k_T} \quad \text{E} \qquad (4.15)$$

Equations (4.14) and (4.15) yield a tridiagonal matrix like Eq. (4.7) which is solved using the algorithm described for the momentum equation.

In the present analysis a simplified species equation solution was used. It was assumed that the elemental composition was constant and equal to the ablator elemental composition from the ablator surface to the stagnation point (i.e. v=0). Likewise from the stagnation point to the shock the elemental composition of air was assumed. Results using this approach are in very close agreement with results containing solutions of the elemental species equation as demonstrated in Chapter 5. If the elemental species equation was to be solved numerically, the same procedure discussed for the other equations can be used.

In order to take advantage of the variable step size finite differences a set of criteria was developed to determine the step size used in various regions of the shock layer. The nondimensional temperature was used as the variable to specify the step size pattern since in general it exhibits regions of more rapid change as a function of η than the velocity function. Numerical experimentation resulted in the following sufficient conditions:

1. $.005 < \Delta T < .05$ (The nondimensional temperature change across a step can not be less than .005 unless condition 2 applies or greater than .05.

2. $\Delta\eta \leq .04$ (The step-size is never greater than .04; no lower limit is set.)

The upper limit on step-size is used to maintain accuracy in the momentum equation integration. The η step-size is updated between momentum and energy solutions as the temperature profile moves towards convergence.

The numerical methods discussed were implemented in the VISRAD 3 computer program which is documented in Appendix D. This appendix also contains additional information on the iteration procedures used in the solution of the stagnation line equations.

SOLUTION BEHAVIOR

The results in this section are presented to demonstrate the validity of the momentum and energy equation selected to illustrate the wide range of applicability of the numerical methods used and to exhibit the manner in which convergence is achieved under different situations.

Figure 4.1 presents the results of four different methods used to solve the shock layer momentum and continuity equations. All four methods agree reasonably well for this case in which there is no mass injection and no radiation coupling. The present method and the Adams-Moulton predictor corrector method used by Howe and

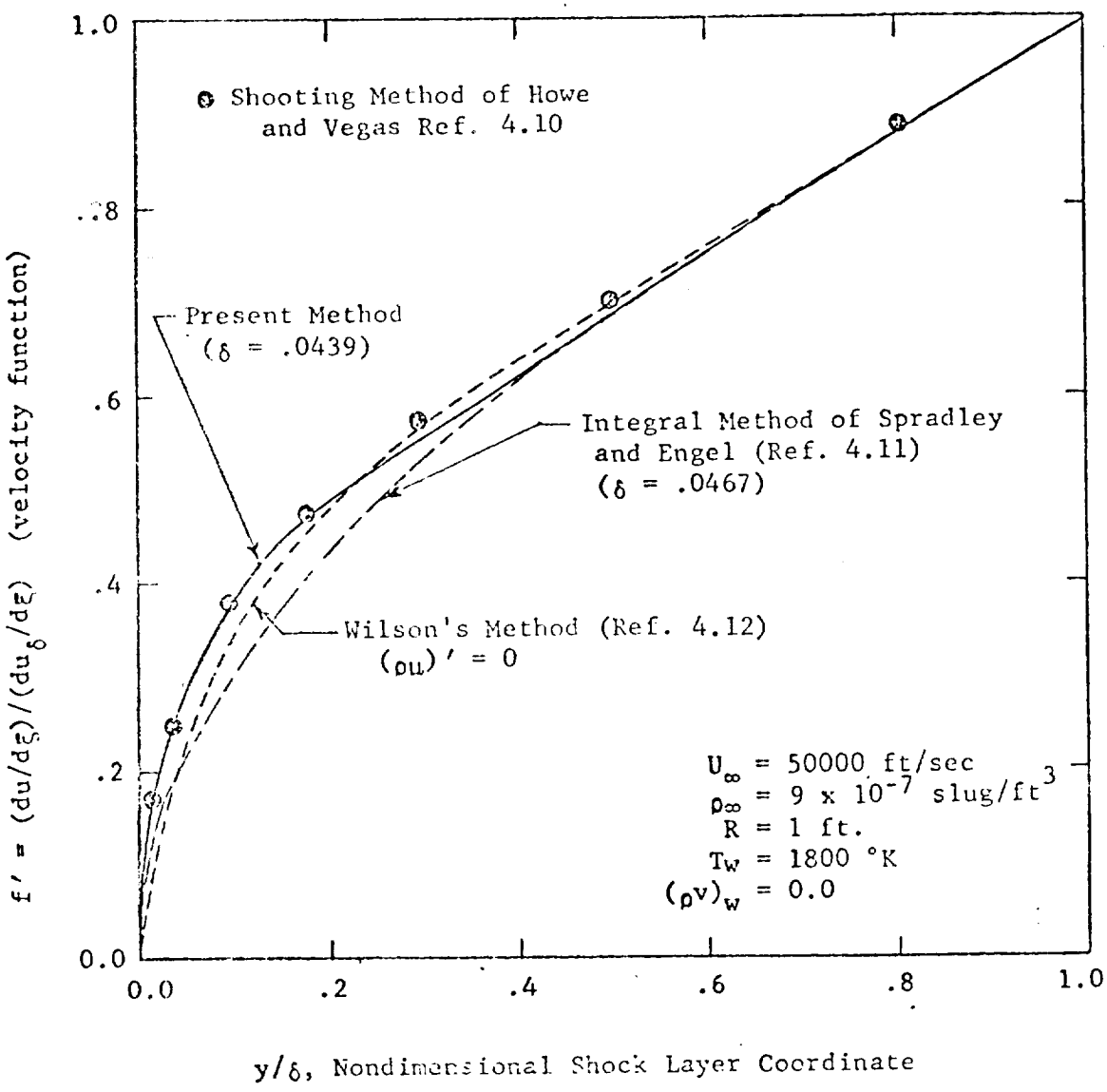

Fig. 4.1 Comparison of Stagnation Line Momentum Equation Solutions for the Case of No Radiation Coupling.

Vegas (Ref. 4.10) agree quite well. Both of these methods as well as the integral method of Spradley and Engel (Ref. 4.11) include [illegible] method reported by Wilson (Ref. 4.12) does not include this effect and it is probable that this effect accounts for the lower values of the velocity predicted by Wilson's method. The deviation of Spradley and Engel's integral solution from the present finite difference method may be accounted for by two effects. First, and foremost is that integral solution is limited by the degree of the polynomial selected in its implementation. Secondly, second order effects are included in the momentum equation solved using the integral approximation. A comparison of computed stand-off distances between the present implicit method and the integral method for the case shown in Fig. 4.1 indicates agreement within 6%.

Figure 4.2 presents a comparison of velocity profiles with variable and zero $d(\rho\mu)d\eta$ for zero and 20 percent mass injection (i.e. $(\rho v)_w/(\rho v)_\delta = 0$ and .2)*. The results indicate that for no mass injection, as anticipated by Wilson (Ref. 4.12), neglecting this effect significantly changes the velocity profile near the wall. Further, the results indicate that for cases when the boundary layer is blown from the wall by large ablation rates the effect of this term is not as significant in determining the velocity profile.

---

* Note the negative sign of $(\rho v)_w/(\rho v)_\delta$ has been dropped.

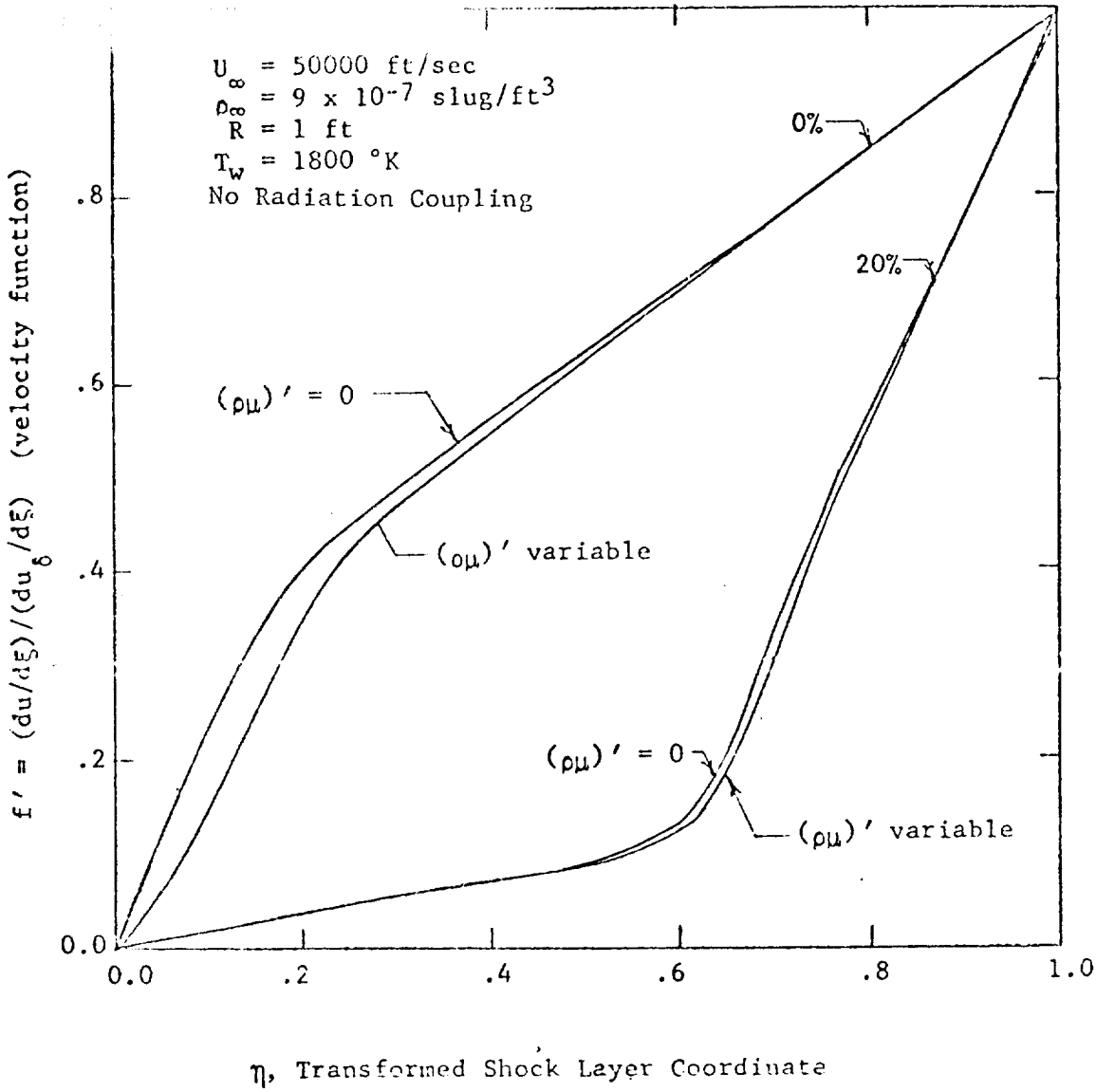

Fig. 4.2 Comparison of the Effects of $(\rho\mu)'$ on the Momentum Equation for 0 and 20 Percent Mass Injection

Figure 4.3 presents a comparison of temperature profiles computed with the present implicit method and with the quadrature relaxation technique of Specchley and Engel (Ref. 4.11). The agreement is quite good. Both solutions use Hansen's thermodynamic and transport properties. Thus the only factors contributing to the differences in the temperature profiles are the numerical techniques used, the effects of second order terms in the equations solved by the relaxation technique and the difference in the velocity profiles shown in Fig. 4.1.

Figure 4.4 presents results of the present method for the momentum equation coupled to the energy equation with emission radiation for various mass injection rates. The velocity profiles exhibit changes due to mass injection and radiation coupling that are expected and reasonable. Furthermore, no numerical problems were experienced in obtaining the momentum solutions. This is in contrast with unstable characteristics reported for the momentum equation by Howe and Vegas (Ref. 4.10) for their $f_w = -.7$, and the need by Wilson (Ref. 4.12) to go to an alternate method for large blowing rates. The present method has been used with no difficulties to solve the momentum equation for a mass injection rate of $(\rho^* v^*)_w / (\rho^* v^*)_\delta = (\rho v)_w = .50$ which corresponds to Howe and Vegas' $f_w = -11.5$.

Numerically, the velocity function f' has been found to converge quadradically in a quasilinearization sense as shown in Fig. 4.5. However, the iteration on $\tilde{\delta}$, see Fig. 4.6, required a damping factor to insure convergence. Likewise, for some cases, the temperature

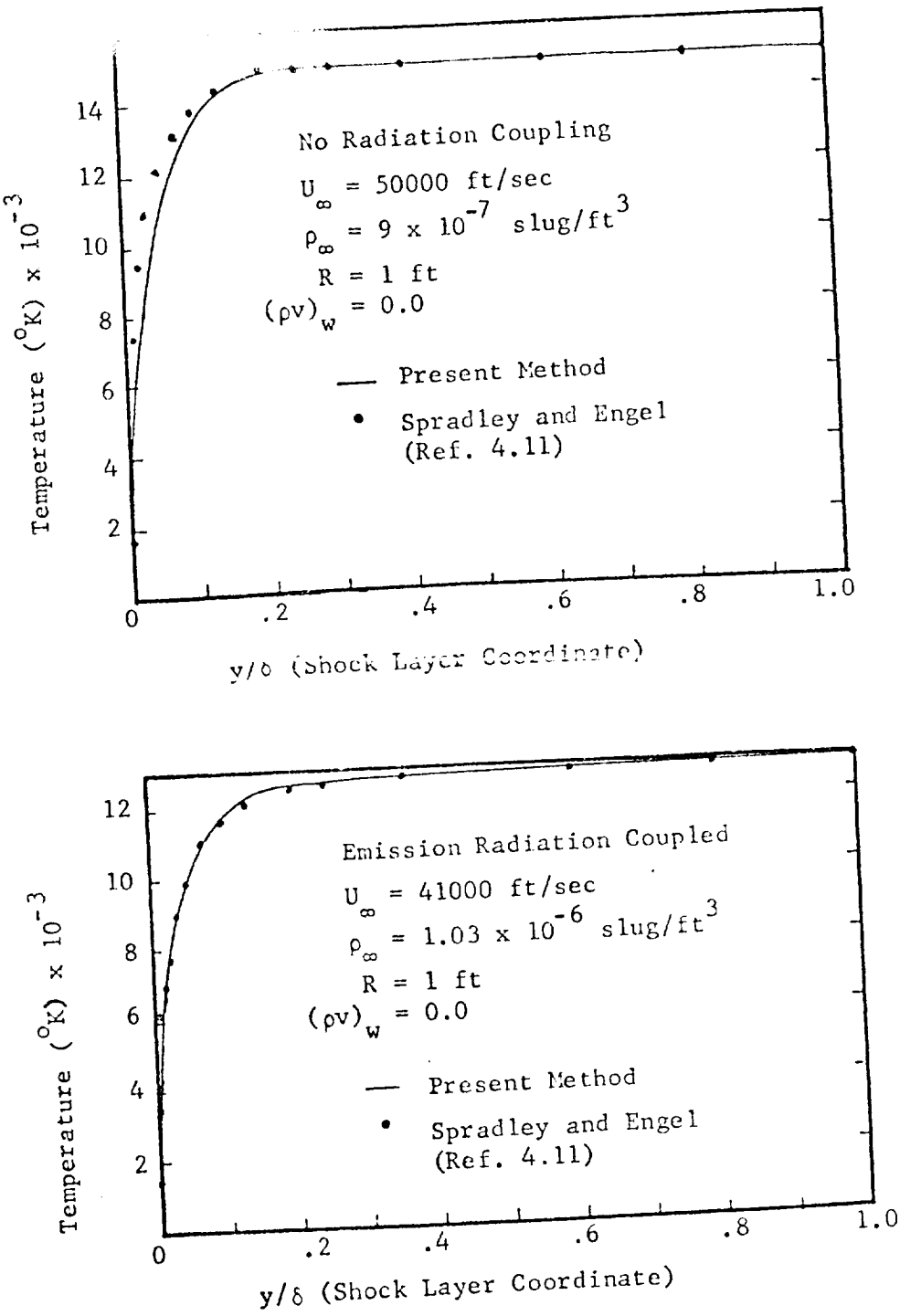

Fig. 4.3 Comparison of Temperature Profiles

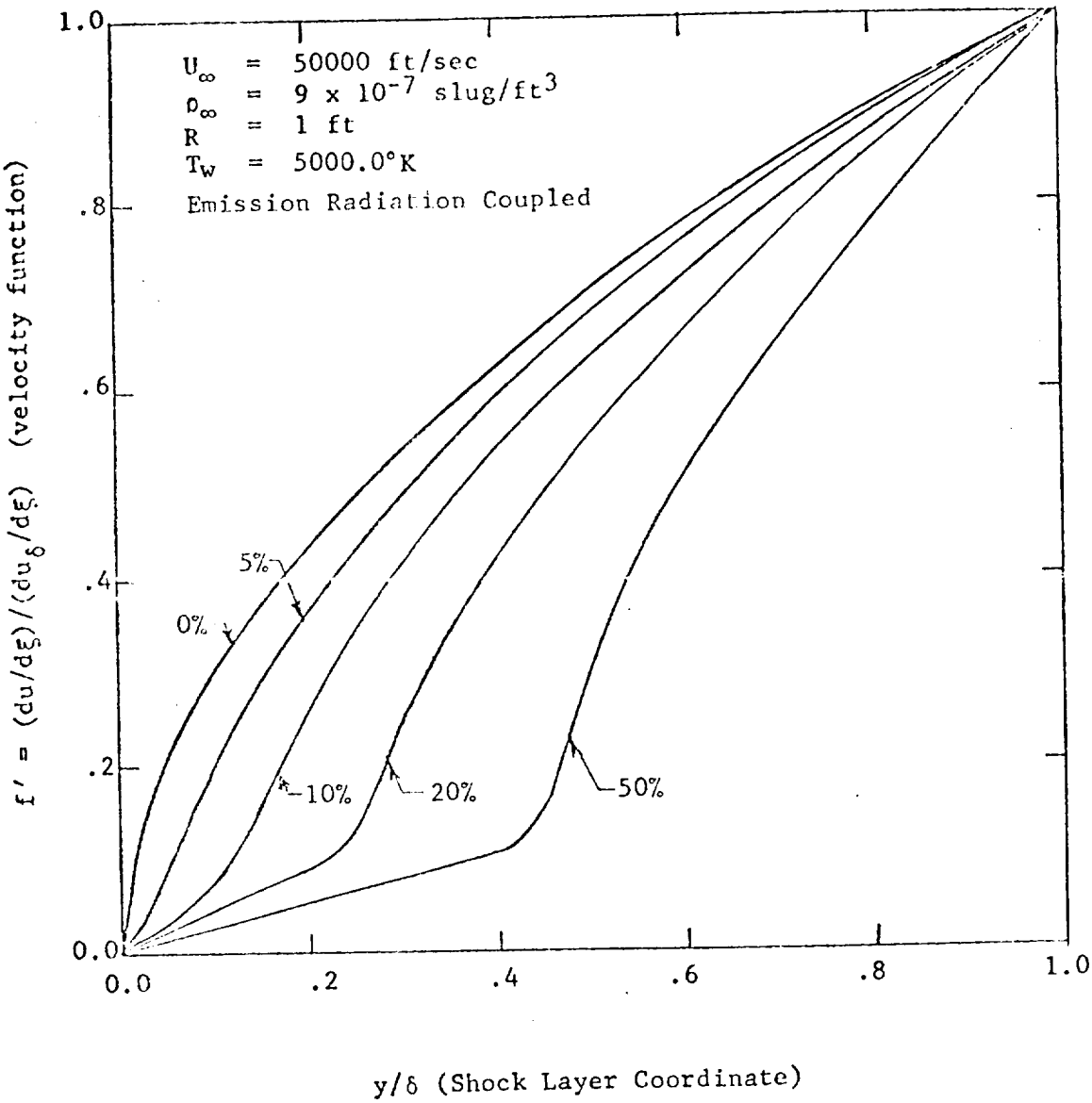

Fig. 4.4 Velocity Function Profiles for Mass Injection Rates from 0. to 50. Percent

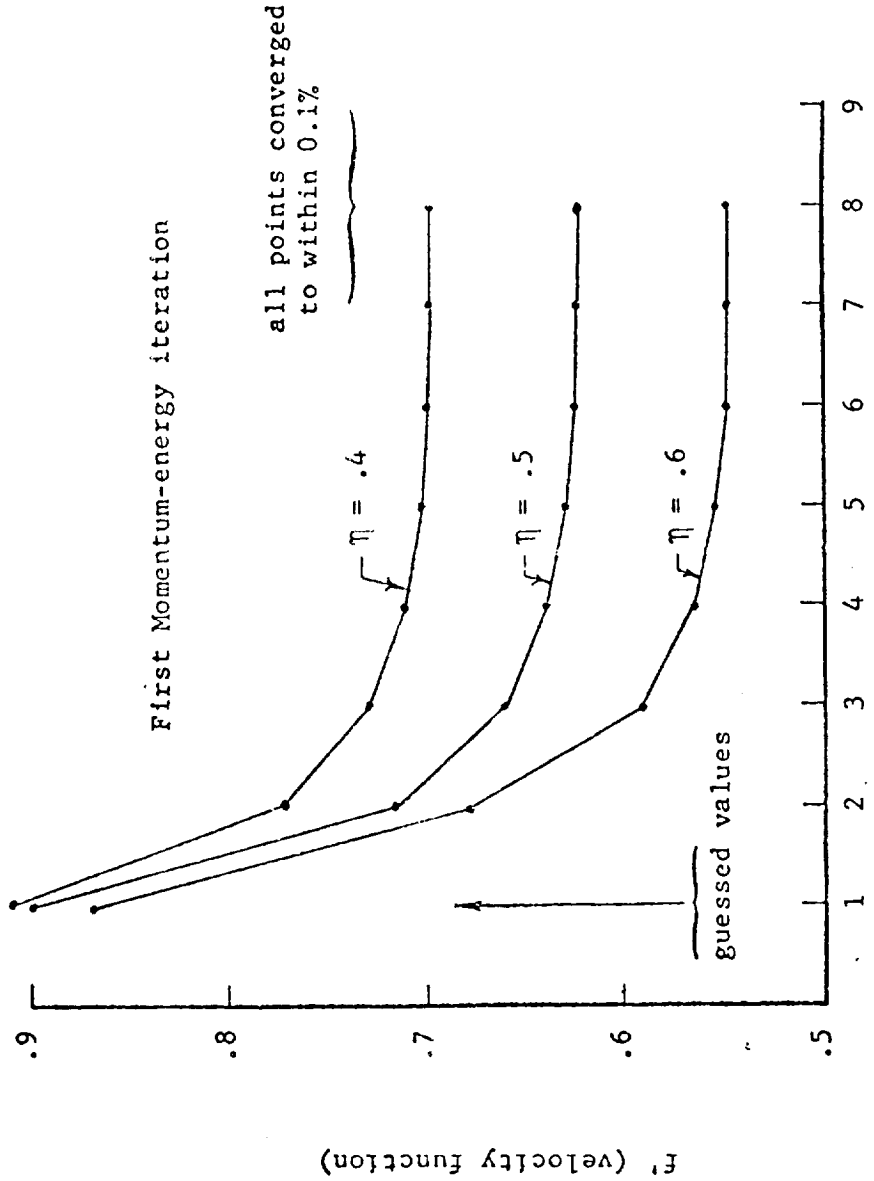

Fig. 4.5 Velocity Function Convergence Behavior

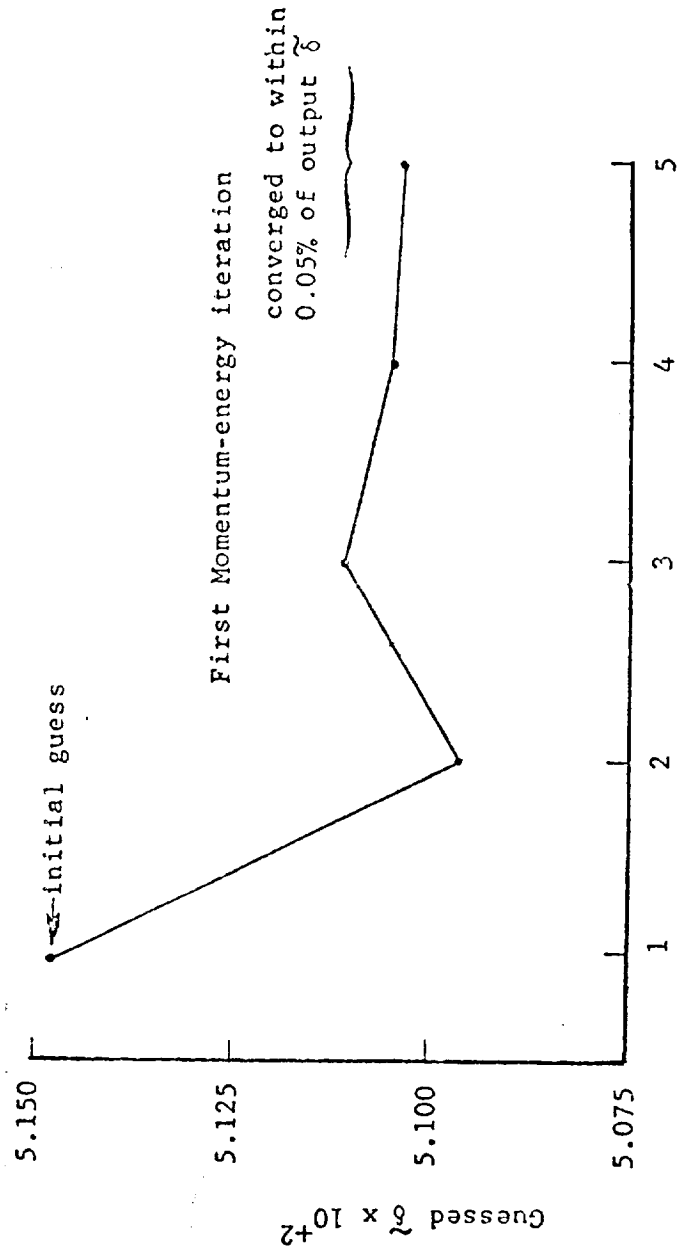

Fig. 4.6 $\tilde{\delta}$ Convergence Behavior

profile is weighed with the previous guess for a new guessed profile. The use of a maximum of 60 points in the flow field have been found adequate for the finite difference solutions of both the momentum and energy equations. Radiative uncoupled solutions converge when each point of the input and output profiles is within one percent. Convergence on $\tilde{\delta}$ was also set at one percent. However, the addition of radiative coupling requires more stringent tolerances to insure convergence to a unique solution. Figures 4.7 and 4.8 present some results of the effect of emission radiative coupling on the temperature profile for different convergence criteria. The temperature profile was selected to study emission radiative coupling effects on convergence since temperature is the most sensitive variable to both the radiative flux term and to the convergence tolerances.

Figure 4.7 presents temperature profiles for no mass injection that result from different convergence criteria. It was found that this case requires more stringent convergence tolerances than most mass injection cases. This case was studied in detail to determine the least stringent tolerances needed to insure convergence to the correct answer. There are three convergent tolerances of direct importance - the tolerances on each point in the temperature and velocity function profile and the tolerance on the $\tilde{\delta}$ change due to a change in the temperature profile. The tolerances are denoted as the energy tolerance, E; momentum tolerance, M; and the energy-momentum coupling tolerance on $\tilde{\delta}$ change in Fig. 4.7 and 4.8 Several

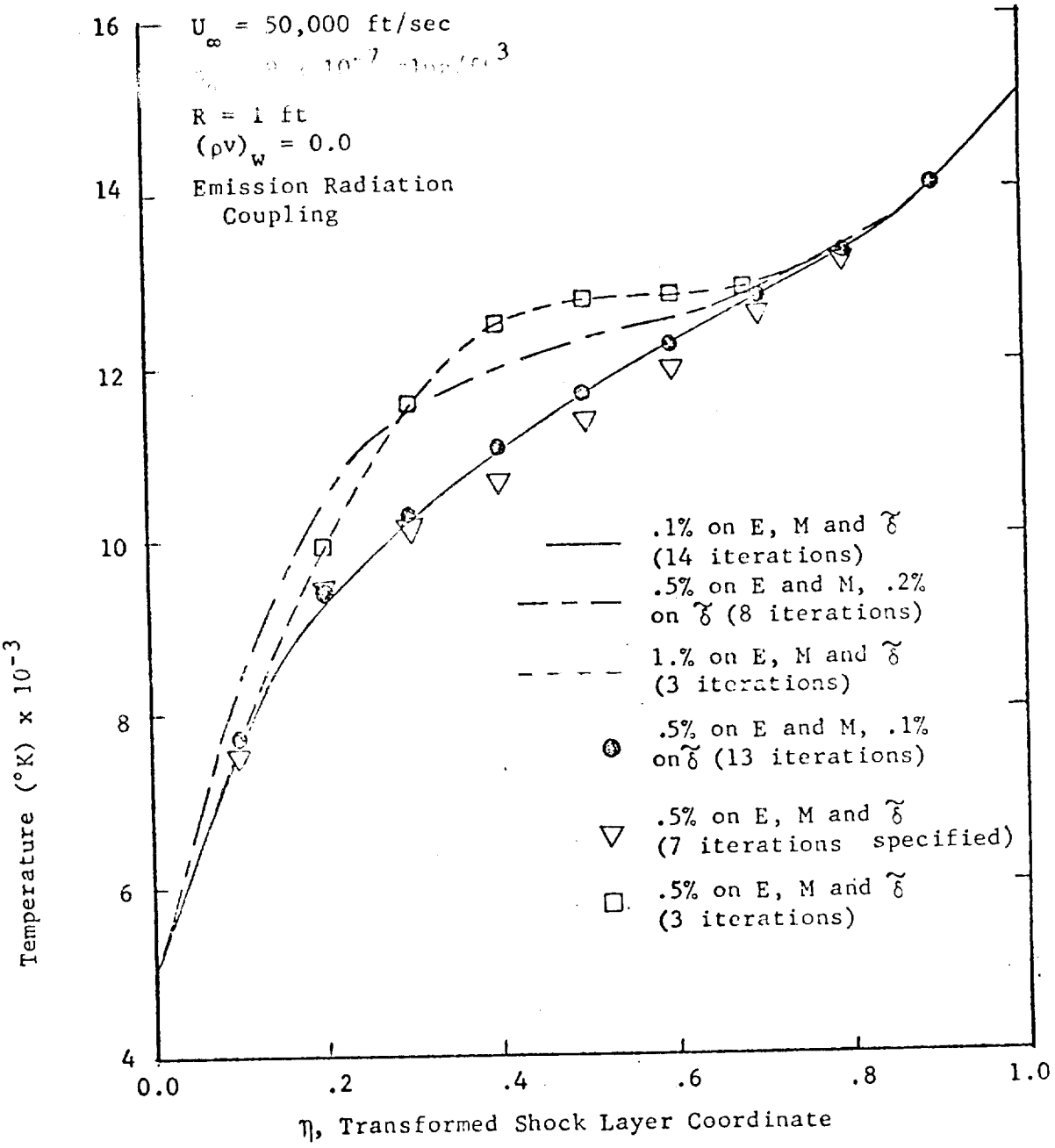

Fig. 4.7 Temperature Profiles for No Mass Injection Resulting from Different Convergence Criterion

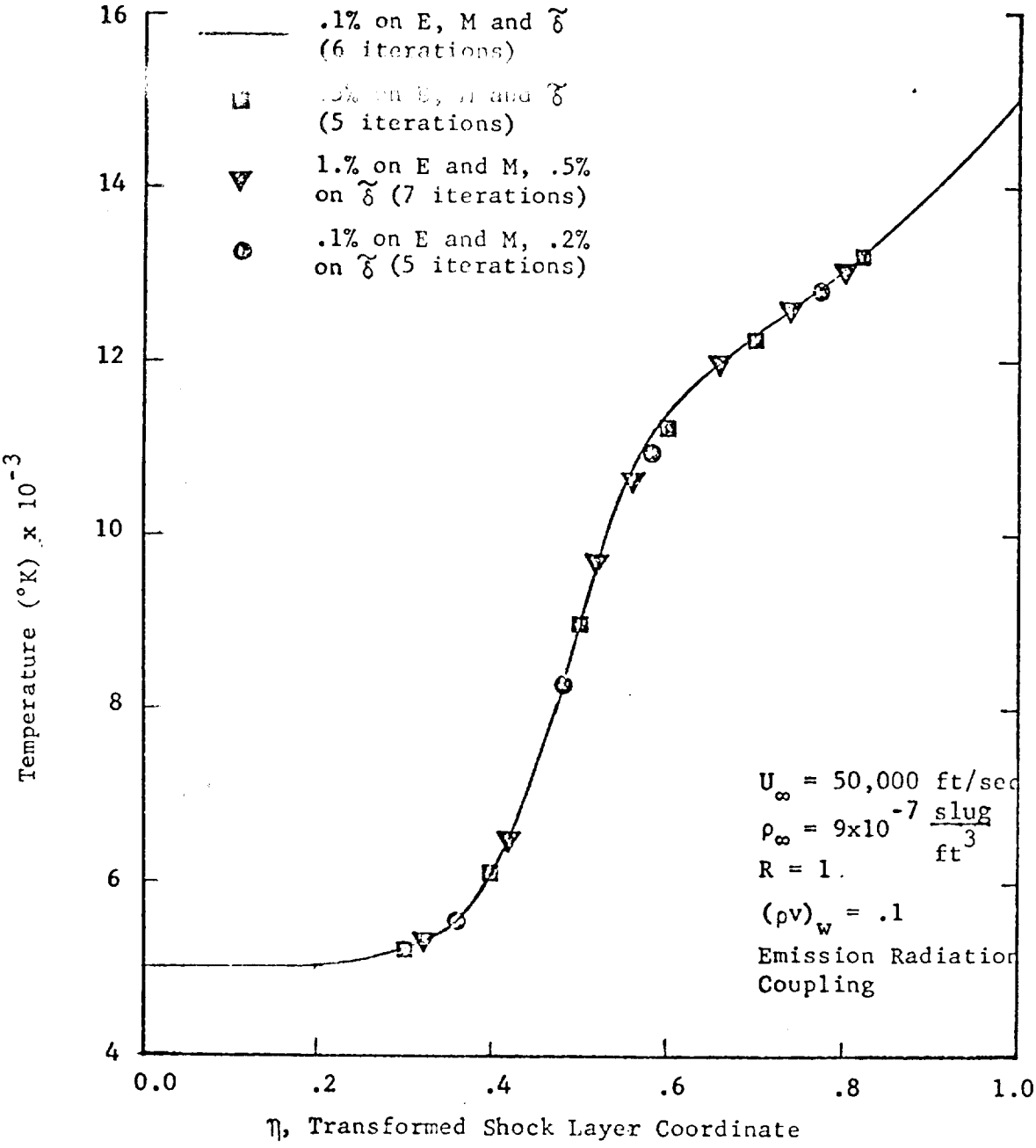

Fig. 4.8 Temperature Profiles for 10% Mass Injection Resulting from Different Convergence Criterion

conclusions can be obtained by close observation of Fig. 4.7. First, neither 1.0% or 0.5% tolerances on E, M and $\tilde{\delta}$ are sufficient to insure convergence to the unique solution obtained using 0.1% for all three tolerances and also obtained using 0.1% on E and M and 0.05% on $\tilde{\delta}$. Secondly, it is noted that only 3 iterations between the momentum and energy equation were required using the 1.0% or .5% tolerances on E, M and $\tilde{\delta}$. Thus the radiative flux divergence term had been calculated only 3 times. It was natural to question whether the integral nature of the energy equation was satisfied with this number of iterations. This leads to the third conclusion. Six or seven energy-momentum iterations appear necessary to insure that the coupling between the radiative flux divergence and the remaining portion of the energy equation is correctly computed. This is demonstrated in Fig. 4.7 by the case where .5% tolerances on E, M and $\tilde{\delta}$ was used again but in addition it was required that the program make 7 energy-momentum iterations. The agreement of the temperature profile for this case and the unique solution is much better than when only 3 iterations were used. Fourth, the energy-momentum coupling was found to be adaquately satisfied when the computed temperature profile did not change $\tilde{\delta}$ more than 0.1%. This is demonstrated by two cases. One case was run with 0.5% on E and M and 0.2% on $\tilde{\delta}$. These tolerances yield a solution significantly different from the unique solution. The solution satisfied the tolerances in 8 energy-momentum iterations. Thus the radiative flux divergence coupling in the energy equation was apparently

satisfied. However, the momentum-energy coupling was not satisfied. Another case was run with 0.5% tolerances on E and M and with 0.1% tolerance on [illegible] profile is in quite good agreement with the unique solution indicating that these tolerances are sufficient to insure proper convergence. Thus, from these numerical experiments one concludes that 0.5% tolerances on E and M, 0.1% tolerance on $\tilde{\delta}$ is required in order to insure proper convergence. Further, a minimum of six or seven energy-momentum iterations appear required.

The results presented in Fig. 4.8 indicate that even though the above convergence tolerances are required for some shock layer solutions, others may not require such stringent tolerances. For the problem stated in Fig. 4.8 all the tolerances employed yielded essentially the same results. It should be noted however that all the cases were required to iterate between the energy and momentum equations at least 5 times thus satisfying the radiative flux divergence and energy equation coupling. Other conditions not studied here or in Chapter 5 might require different criteria.

The establishment of the necessary and sufficient conditions to assure convergence to a unique solution discussed above was carried out using the emission radiation model. These criteria were found to be quite satisfactory for calculation which included line and continuum radiation coupling. However for some flight conditions difficulties were experienced in converging to the required criterion.

The principle cause of convergence difficulties is the very strong non-linear coupling between the temperature and radiative [illegible] ficulties were experienced for cases of no mass injection but convergence became more difficult with increasing pressure for mass injection cases. The extent of radiation coupling is, of course, increased rapidly by increased shock layer pressure. At pressures near one atmosphere the temperature profile exhibits large oscillations over the entire flow-field and instabilities principally near the stagnation point if the profile is not constrained in some manner. This behavior is similar to the behavior discussed by Anfimov and Shari (Ref. 4.13) for the same flight conditions. Several methods were tried to assure and to speed convergence. A combination of methods was necessary to achieve satisfactory convergence-performance. This combination of methods will be discussed first followed by the reasoning leading to the use of the individual parts.

The convergence logic of the VISRAD 3 computer program is presented in Fig. 4.9 in block diagram form. The oval ended blocks in this figure denote operations associated with convergence. The first three of four parts of the convergence scheme are simple weighting factors. The $\tilde{\delta}$, flux divergence profile at each point and temperature profile at each point is weighted with their respective computed values of the previous iteration to provide a guess for the current iteration. These three variables generally exhibit oscillatory behavior if unweighed, thus the weighing procedure tends to

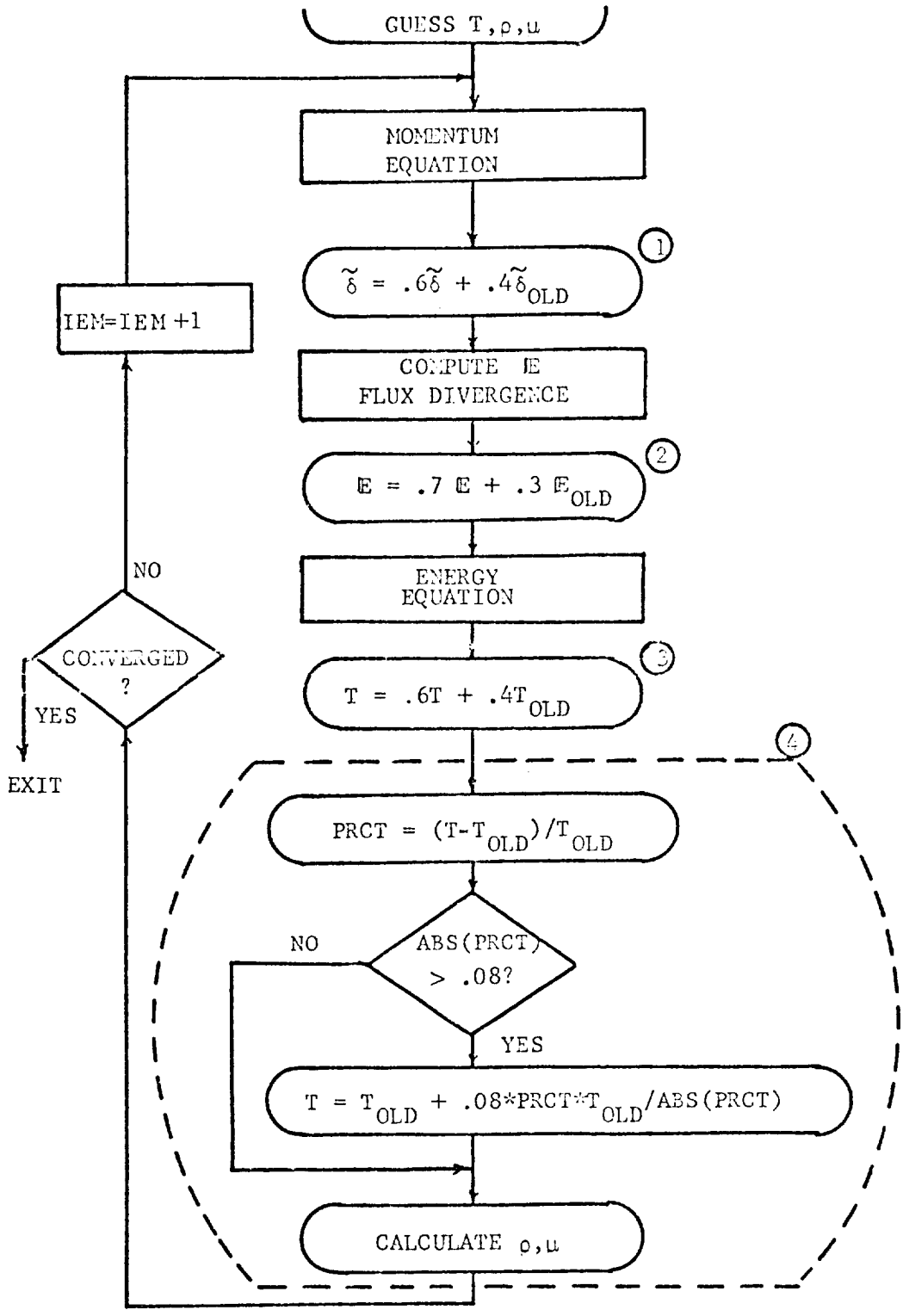

Fig. 4.9 Convergence Logic of VISRAD 3 Computer Program

dampen the oscillations. The fourth part of the convergence scheme is a constraint on the guess of temperature profile. The guess is kept within 8 percent of the temperature profile from the previous iteration. Furthermore, the guessed temperature profile is used to compute updated density and viscosity profiles to be used in the next momentum solution. This procedure works satisfactorily if the initial guess provided to start the program is close to the final result. This can be achieved by running cases at constant $(\rho v)_w$ starting with a low pressure (i.e., 0.1 atm.) and using the converged results as a guess for the next pressure level.

The first part of the convergence scheme weighs the new and old values of $\tilde{\delta}$ in an attempt to reduce the momentum energy coupling between iterations. The effect of this weighing was found to be only slightly influential but beneficial in convergence. The second part of the convergence scheme weighs the new and old radiative flux divergence at each point in the flow-field. This has the result of dampening the oscillations in the flux divergence profile with the main effect being in the stagnation point region where the flux divergence changes sign. The third part of the convergence scheme weighs the new and old temperature at each point in the flow-field. This was done in order to dampen the oscillation in the temperature profile, improve the properties for the next momentum solution and to improve the flux divergence for the next energy solution. This part of the convergence scheme is the principle contributer in obtaining a converged solution. The specific

weighing values for the preceding variables were determined by numerical experimentation and appear to be satisfactory; however, due to the nonlinear coupling involved and the change in coupling for different flight conditions the weighing factors are a compromise.

A converged solution was obtained using the first three parts of the convergence scheme. The behavior from iteration to iteration of $\tilde{\delta}$, stagnation point temperature and radiative flux divergence are shown in Figs. 4.10b, 4.10a and 4.11 respectively. The stagnation point values of temperature and flux divergence were chosen for presentation since they are generally the last value to converge in the profile. Both $\tilde{\delta}$ and temperature exhibit large oscillations during the first five iterations. Corresponding to the large temperature oscillations, Fig. 4.11 shows a much larger change in the flux divergence. Even though convergence was achieved for this low pressure the results indicated that the temperature had to be constrained to achieve convergence for higher values of pressure. This realization lead to the constraining procedure of part four of the convergence scheme. By not allowing the guessed temperature to deviate from the previous profile at each η location by more than a fixed percentage the large oscillations were reduced. Fig. 4.12 shows a typical convergence procedure for a pressure of 0.5 atm. using a maximum percentage change of 4.0%. The temperature profiles in Fig. 4.12 are for intermediate iterations and the converged profile is not shown (it is reported in Chapter 5), however, the progress toward convergence is shown. The eleventh and twelvth

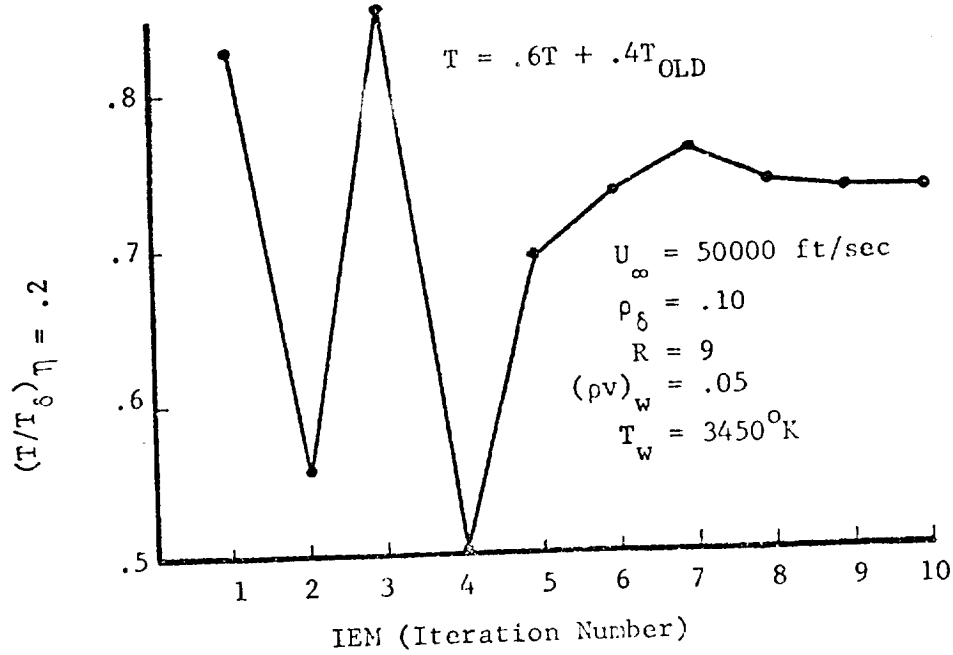

Fig. 4.10a Temperature Convergence Behavior

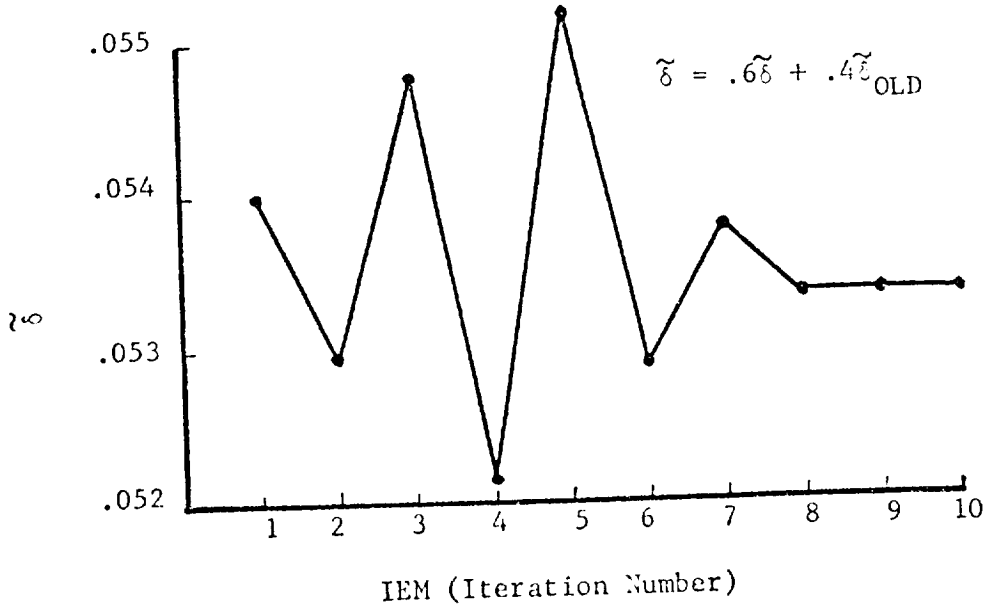

Fig. 4.10b Energy Coupled $\tilde{\delta}$ Convergence Behavior

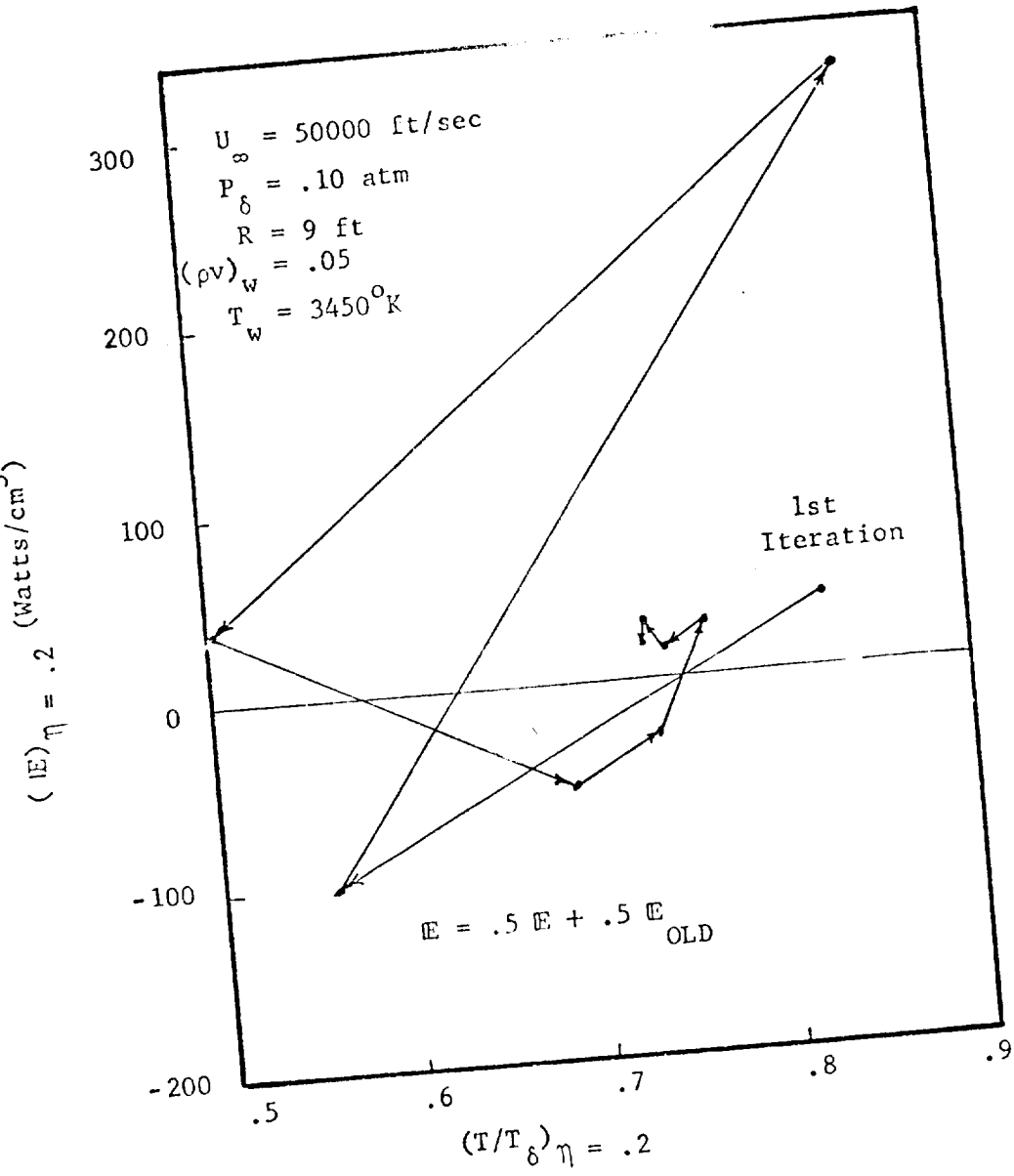

Fig. 4.11 Flux Divergence Convergence Behavior

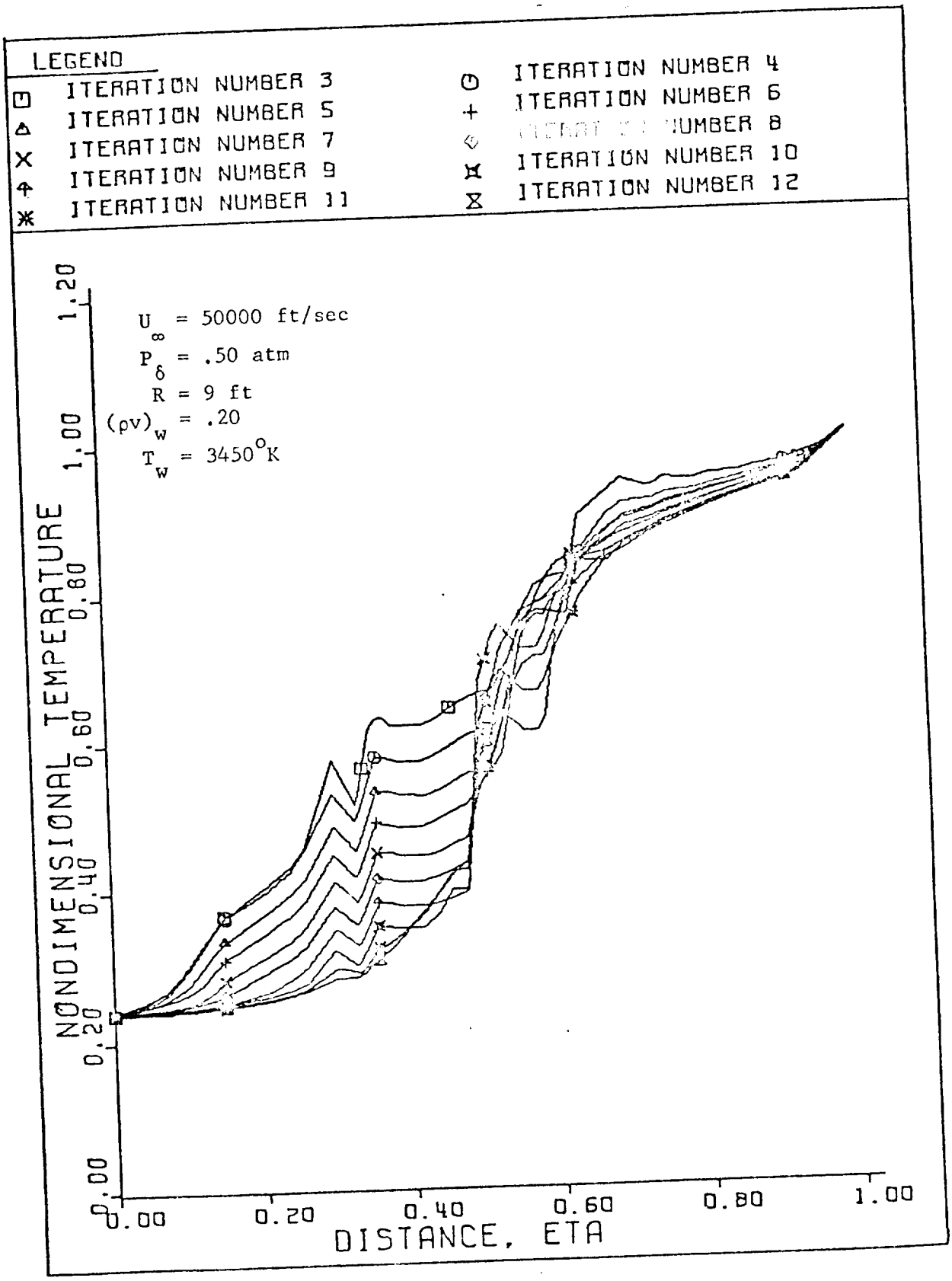

Fig. 4.12 Temperature Profile Convergence Behavior

iterations are near convergence in the near wall and near shock region. The dip in the temperature profiles near the stagnation point is characteristically the last irregularity to disappear before convergence. The results shown in Fig. 4.12 indicate that perhaps the 4.0 percent change constraint was somewhat smaller than required. Subsequent calculations indicated a value of 8.0% is sufficient and provides a good compromise between stability and time required for computation.

From the results presented in Figs. 4.1 and 4.3 it can be concluded that apparently the second order effects do not significantly contribute to the description of the flow-field characteristics and therefore are justifiably neglected. Furthermore, the present method agrees with other described methods for the case where these methods are applicable. The numerical solution of the momentum equation is quite rapid and exhibits no numerical difficulties. Numerical difficulties were experienced in the solution of the energy equation for mass injection cases where the radiative flux divergence profile changes from a large negative to large positive number in the stagnation point region. The convergence scheme presented in Fig. 4.9 is shown to satisfactorily overcome these difficulties.

CHAPTER 4

References

4.1 Adams, J. C., C. H. Lewis, H. S. Brahinsky, et. al. "Effects of Chemical Nonequilibrium, Mass Transfer, and Viscous Interaction on Spherically Blunted Cones at Hypersonic Conditions," AEDC-TR-69-237, January 1970.

4.2 Blottner, F.G. "Nonequilibrium Laminar Boundary-Layer Flow of Ionized Air," AIAA Journal, Vol. 2, No. 11, November 1964.

4.3 Blottner, F. G. "Viscous Shock Layer at the Stagnation Point with Nonequilibrium Air Chemistry," AIAA Journal, Vol. 7, No. 12, December 1969.

4.4 Davis, R. T. "Numerical Solution of the Hypersonic Viscous Shock-Layer Equations," AIAA Journal, Vol. 8, No. 5, May 1970.

4.5 Edelman, R. and J. Hoffman. "Viscous Hypersonic Flow in the Vicinity of the Stagnation Point of Axisymmetric Blunt Bodies - Calculation and Results for Equilibrium Air," Ge. Appl. Sci. Lab., Inc., Tech. Report No. 498, May 10, 1965.

4.6 Edelman, R. and J. Hoffman. "Viscous Hypersonic Flow in the Vicinity of the Stagnation Point for Blunt Axisymmetric Bodies - Numerical Analysis and Computer Programs," Gen. Appl. Sci. Lab., Inc., Tech. Report No. 498, May 10, 1965.

4.7 Fay, James A. and Harvey Kaye. "A Finite-Difference Solution of Similar Nonequilibrium Boundary Layers," AIAA Journal, Vol. 5, No. 11, November 1967.

4.8 Lee, E. Stanley. Quasilinearization and Invariant Imbedding, Academic Press, New York, 1968.

4.9 Conte, S. D. Elementary Numerical Analysis, McGraw-Hill Book Co., New York, 1965.

4.10 Howe, John T. and John R. Vegas, "Solutions of the Ionized Radiating Shock Layer, Including Reabsorption and Foreign Species Effects & Stagnation Region Heat Transfer," NASA TR R-159, 1963.

4.11 Spradley, L. W. and C. D. Engel, "Formulation of a Method for Predicting Coupled Convective and Radiative Heat Transfer about a Blunt Body," NASA CR 61200, April 1968, (also LMSC/HREC A784881 November 1967).

4.12 Wilson, K. H., "Stagnation Point Analysis of Coupled Viscous-Radiating Flow with Massive Blowing," NASA CR-1548, June 1970.

4.13 Anifimov, N. A., and V. I. Shari, "Solution of the System of Motion Equations of a Selectively Radiating Gas in the Shock Layer," Izv. AN SSSR, Mekh. Zhidk. i Gaza, No. 3, p. 18-25, 1968 (N68-34111, 1968).

CHAPTER 5

STAGNATION LINE RESULTS

Two of the basic objectives of this research, as stated in Chapter 1, were to develop a computer program solution for the stagnation line flow field equations and to perform parametric studies for hyperbolic entry conditions. The results presented herein illustrates that these two objectives have been realized.

Two computer programs have been developed which provide two levels of detail in defining stagnation line characteristics. A coupled set of first order stagnation line equations are solved numerically by implicit finite differences in the program called VISRAD 3 which provides the most complete analysis. The equations and numerical procedures used are given in Chapter 4. A second program called RADCOR was used to compute radiative heating rates for no ablation using the radiative cooling parameter correlation discussed in Chapter 3 (Eq. 3.12 and 3.13).

The two computer programs have been used to perform parametric studies and the results of these studies are presented herein. The parametric studies were conducted for continuum flight conditions corresponding to hyperbolic earth entry velocities. These conditions produce radiative heating rates which are much larger than convective heating (Fig. 1.7). Flight velocities below 36000 ft/sec were not considered since the Apollo flight data and other re-entry data are available and define the heating and material response behavior for these less severe conditions. The conditions considered are:

Free stream velocity: 36000 to 58000 ft/sec

Post shock pressure: .01 to 2.0 atm.

Fig. 2.7 illustrates that these conditions are in the range of applicability of the shock layer equations and are appropriate for hyperbolic entry trajectories which lie in the domain of interest. In addition to flight conditions, additional parameters must be specified to obtain a shock layer solution at one point in a trajectory. The basic specifying variables are:

Variables		Specified by
U_∞ or T_δ; ρ_∞ or P_δ	Free-stream or Post shock conditions	Trajectory
R	- Body Radius	Vehicle Shape
$(d\epsilon/d\xi)_{\xi=0}$	- Initial shock curvature	Assumed (zero for a concentric shock)
$(\rho v)_w$	- Mass injection rate	Ablator Response Parameters
T_w	- Surface Temperature	
$\tilde{C}_{iw}$	- Elemental mass fraction at the wall	

Throughout the results presented the wall temperature and elemental species composition at the wall have been specified as:

T_w = 3450°K (sublimation temperature of phenolic nylon at P = 1.0 atm)

$\tilde{C}_{iw}$ = .7303 carbon, .0729 hydrogen, .0496 nitrogen, .1472 oxygen — 40% nylon, 60% phenolic resin — quasi-steady state ablation assumed

The primary emphasis in the parametric studies was to quantitatively determine the effects of ablation products and radiative energy transport on surface heating rates. From this information coupled ablator-shock layer solutions were obtained. In addition, results of the calculations were studied to provide additional understanding of shock layer processes such that the importance of the various transport and coupling processes could be assessed.

In describing radiation, ablation and other effects the word "coupled" has been extensively used in this chapter. It might be well to reflect on its connotation as used here before proceeding. Mathematically, the stagnation line equations are solved as a set of ordinary differential equations in one dependent variable each. Each of the equations contains variable coefficients and terms which are functions of and/or include the dependent variables from the other equations. Thus the equations are coupled in that a solution to the set of equations can not be obtained unless iterations between equations on the dependent variables are made to satisfy the set simultaneously. The extent of coupling may be described by a brief discussion of weak coupling. If one equation is weakly coupled to another equation large variations in the dependent variable of one equation produces only small variations in the dependent variable of the weakly coupled equation. The integrodifferential nature of the energy equation produces another type of coupling. The integro term in the energy equation has been treated as a separate equation with respect to the remainder of the energy equation.

Iterations are performed to satisfy both parts simultaneously. The integro term is the radiative flux divergence which is quite obviously dependent on temperature and is thus coupled to the differential portion of the energy equation. The phrase "ablator-shock layer coupling" has a slightly different connotation. It is used to describe the ablator and shock layer conditions which yield a compatable set of surface boundary conditions.

The first four sections of this chapter present parametric studies of the stagnation line flow-field obtained using the VISRAD 3 program. Some results from the RADCOR program are also presented for comparative purposes. In addition to the parametric studies the fifth section of this chapter presents heating rates obtained from a radiative cooling parameter correlation used in the RADCOR computer program. The main results in this section are a set of graphs for heating rates which were obtained using the RADCOR computer program. These graphs permit hand calculations of hyperbolic entry radiative heating rates for no ablation. A method is suggested for estimating the effect of ablation on heating rates. The ablation adjusted rates could then be used to obtain quasi-steady state ablation rates.

EFFECTS OF RADIATION COUPLING ON THE SHOCK STAND-OFF DISTANCE

The shock wave location is a boundary condition for the thin shock layer equations. Mathematically this boundary condition is known as a free boundary and is determined by the solution of the equations in the bounded region. For the problem under investigation, the shock stand-off distance is determined by the radiation-gas dynamic coupling which occurs in the shock layer.

The purpose of this section is to present results which demonstrate the radiation-gas dynamic coupling effects on the stand-off distance. These results were obtained using the NSRAD 3 and RADCOR computer programs which are discussed in Appendix D and E respectively. A systematic study is presented for the stand-off distance for flight velocities between 36000 and 58000 ft./sec. assuming $T_w = 3450^{\circ}K$, $(\rho v)_w = 0.0$ and a concentric shock. The influence of the concentric shock assumption is assessed at a typical flight condition. In addition, the location of the stagnation point for mass injection cases is examined for a number of flight conditions.

Stagnation line solutions were obtained for free-stream velocities between 36000 and 58000 ft./sec. at post shock pressure levels of $P_\delta = 1.0, .50, .10$ and $.01$ atmospheres using the line and continuum radiation model. The nondimensional stand-off distances resulting from these calculations are shown in Fig. 5.1 as a function of density ratio across the shock. Along with the computed results are plots of two commonly used correlation equations which were developed to predict nonradiatively coupled stand-off distances. It is noted that the correlation of Inouye (Ref. 5.1) predicts larger stand-off distances than any obtained by the present method; however, the correlation presented in Ref. 5.2 agrees to within 3% with the four points for 36000 ft./sec. computed with the present flow-field solution. It will be shown that the effects of radiation coupling is small for this flight velocity (Fig. 5.19 shows the maximum effect). Thus the correlation from Ref. 5.2 provides a quite reasonable estimate of the nonradiatively coupled stand-off distance.

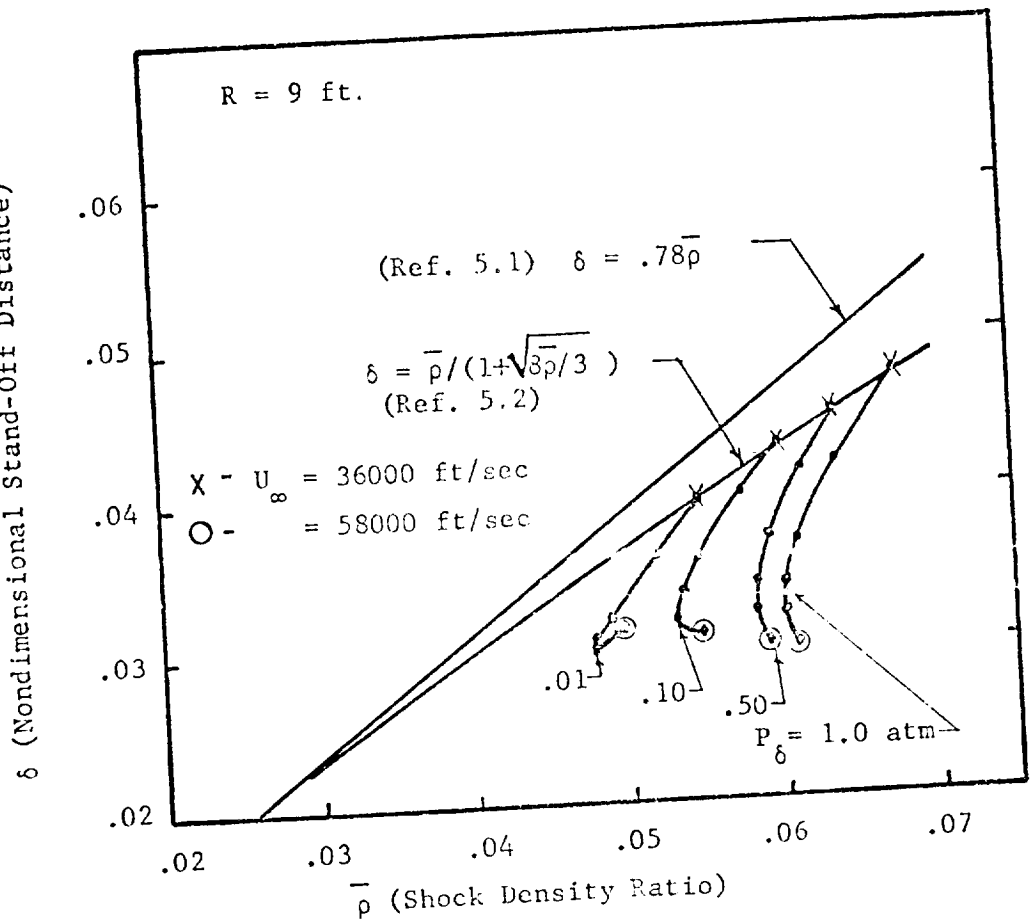

Fig. 5.1 Radiative Coupled Shock Stand-off Distances for Various Post Shock Pressure Levels

The present results shown in Fig. 5.1 indicate some additional interesting processes. Most obviously, the stand-off distance is a strong function of the post shock pressure. The constant pressure lines show a double value for δ at constant $\bar{\rho}$. This effect, which occurs at the higher velocities, is a natural result of air thermodynamics being used to solve the Rankine-Hugoniot equations. As discussed in Chapter 3 the Rankine-Hugoniot equations are solved using the air model of Hansen (Ref. 5.17) which assumes an ideal dissociating and ionizing gas. It is also noted that the turn in the constant pressure line gets sharper with decreasing pressure until the stand-off distance becomes double valued for the pressure $P_\delta = .01$ atm.

A measure of the radiative-gas dynamic coupling effects on the stand-off distance can be shown by observing the actual stand-off distance, δ, divided by the radiationless stand-off distance, Δ. The nondimensional radiationless stand-off distance, Δ, selected for the present work is represented by the equation

$$\Delta = \bar{\rho}/(1 + \sqrt{8\bar{\rho}/3}) \tag{5.1}$$

obtained from Ref. 5.2 This equation was used since it appears to be compatible with the flow-field predictions for small radiation coupling as shown in Fig. 5.1 and the use of Eq. 5.1 makes the information to be presented more accessible to other investigators than radiationless flow-field results. Accordingly the deviation from the radiationless shock layer distance is expressed as

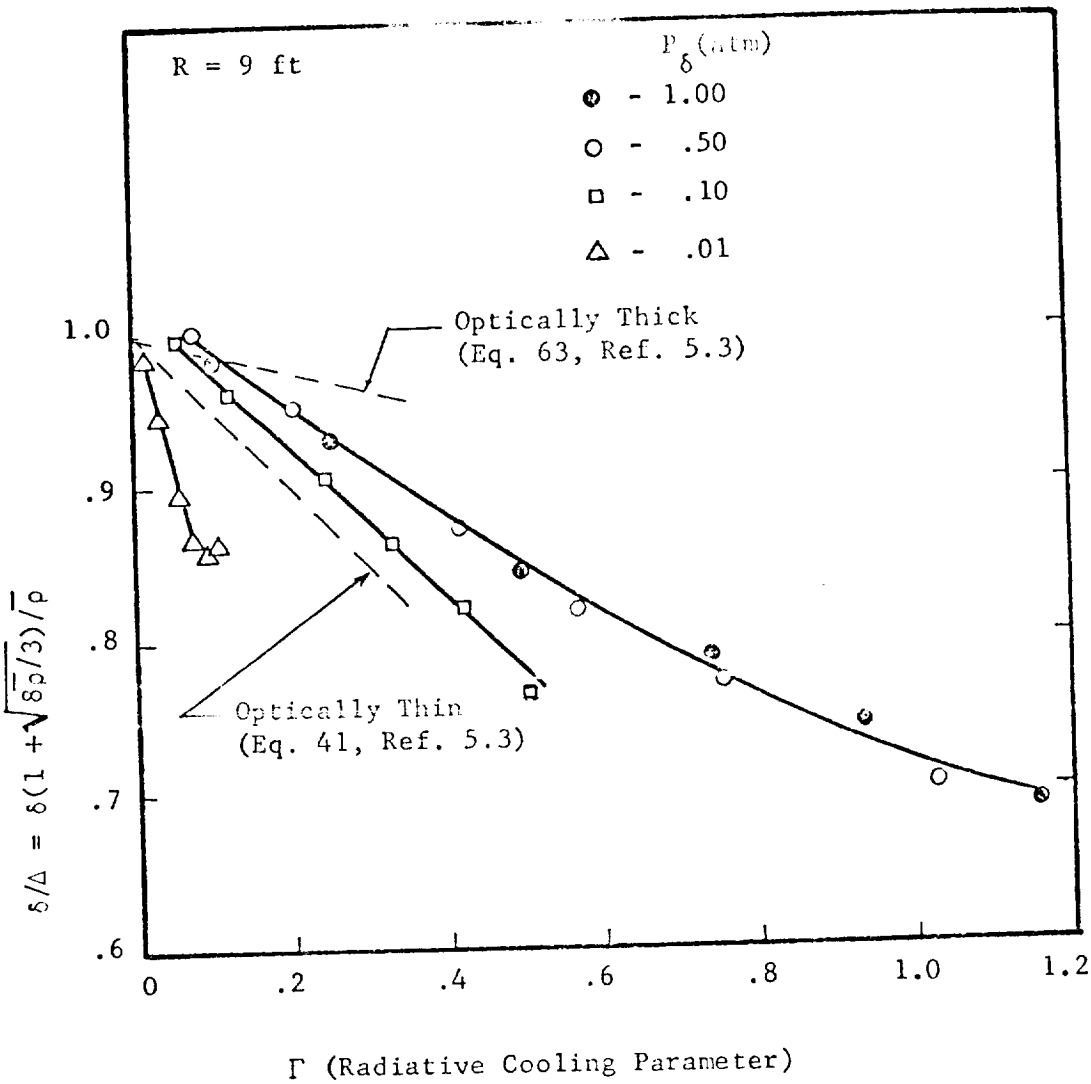

Fig. 5.2 Radiative Cooling Effects on the Stand-off Distance for Constant Post Shock Pressure Flight

$$\delta/\Delta = \delta(1 + \sqrt{8\bar{\rho}/3})/\bar{\rho} \tag{5.2}$$

Figure 5.2 shows the effects of [illegible] on the stand-off distance as a function of the radiative cooling parameter, Γ. The cooling parameter was computed using the same line and continuum radiation model used in the flow-field solution and is based on the radiationless stand-off distance, Δ. The results indicates that the ratio δ/Δ varies linearly with Γ for small values of Γ. It is noted that there is an apparent translation at $\delta/\Delta = 1.0$ for different pressure levels. This is attributed to the representation of Δ with Eq. 5.2 rather than using the actual radiationless stand-off distance.

A comparison of the present results with previous estimates of Goulard (Ref. 5.3) shown in Fig. 5.2 provides additional insight into the radiation coupling effects. Goulard formulated the stagnation line problem with a simple inviscid flow field model and a gray gas radiation model. The effects of radiation - gas dynamic coupling on the stand-off distance were studied using a perturbation scheme for small values of Γ. Results were obtained for optically thin and thick limits. The optically thick result, Eq. 63 of Ref. 5.1,

$$\delta/\Delta = 1 - \tfrac{1}{2}\,\Gamma\, E_2\left(\frac{\eta_\Delta}{2}\right) \tag{5.3}$$

is in terms of a parameter, $\eta_\Delta = \rho_\delta K_\delta \Delta$. This parameter is the product of the post shock density, frequency averaged mass absorption coefficient and Δ. The optically thin results were identical to the preceding expression with the exception that the exponential

integral, E_2, was equal to one. For the optically thick limit, Goulard found a minimum value of δ/Δ for horizontal flight and this minimum corresponded to a value of $\frac{1}{\Delta}$ [illegible] and the optically thin results are shown in Fig. 5.2 The optically thin limit predicts a larger reduction of the stand-off distance than that observed for P_δ = .01 atm; and this result is in agreement with Goulard's assessment that his optically thin relationship would overestimate the cooling effect. It should be emphasized also that Goulard's analysis is valid only for $\Gamma \ll 1$. The optically thick line tends to underpredict the radiative cooling effects for small values of Γ. It is interesting to note, however, that the trends shown by the simplified model are in agreement with the present results. That is the increase in optical thickness corresponding to increasing post shock pressure tends to decrease the radiative cooling effect of reducing the shock stand-off distance.

The functional relationship of the radiative heat transfer coefficient and δ/Δ is shown in Fig. 5.3 for the same conditions as those in Fig. 5.2. These results indicate the nonlinear relationship between the stand-off distance and the radiative heating. This is in contrast to adiabatic inviscid analyses which show a direct proportionality relation.

The results presented in Fig. 5.2 and 5.3 are for constant post shock pressures which is approximately horizontal flight (see Fig. 2.7). The results presented in Figs. 5.4 and 5.5 are for vertical flight for a fixed set of velocities. The optically thin and thick estimates

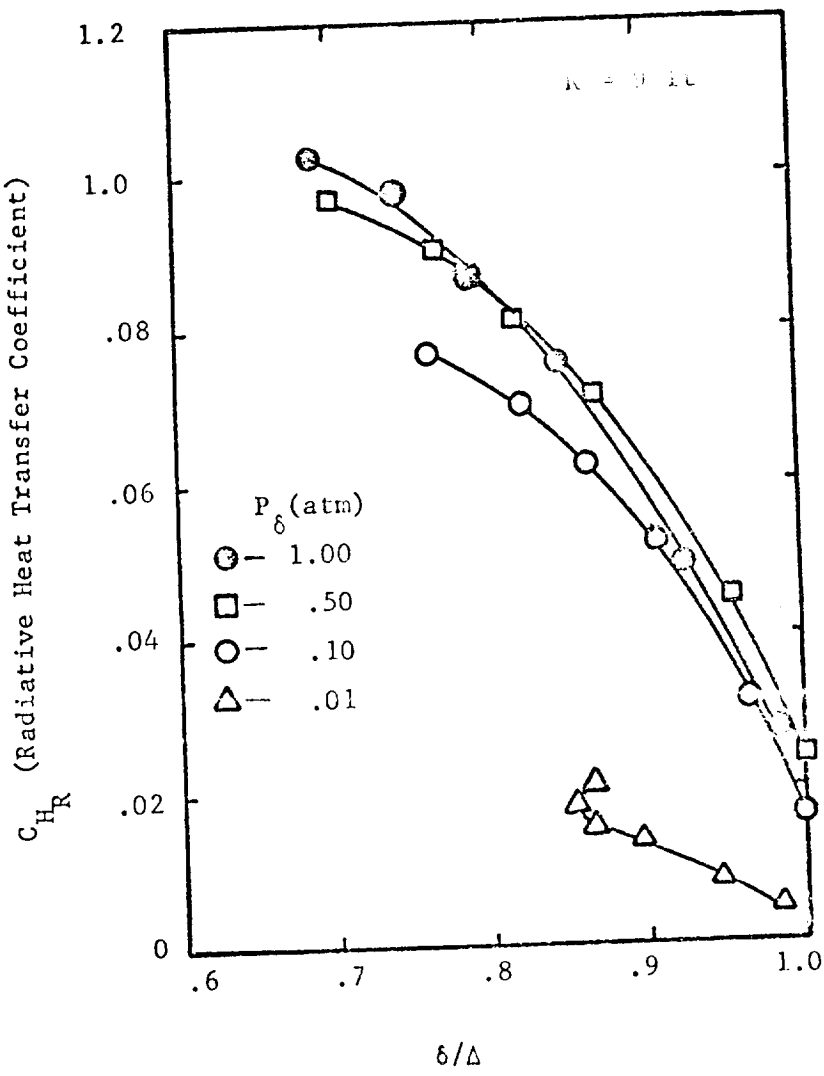

Fig. 5.3 Radiative Heat Transfer Coefficient Variations with δ/Δ

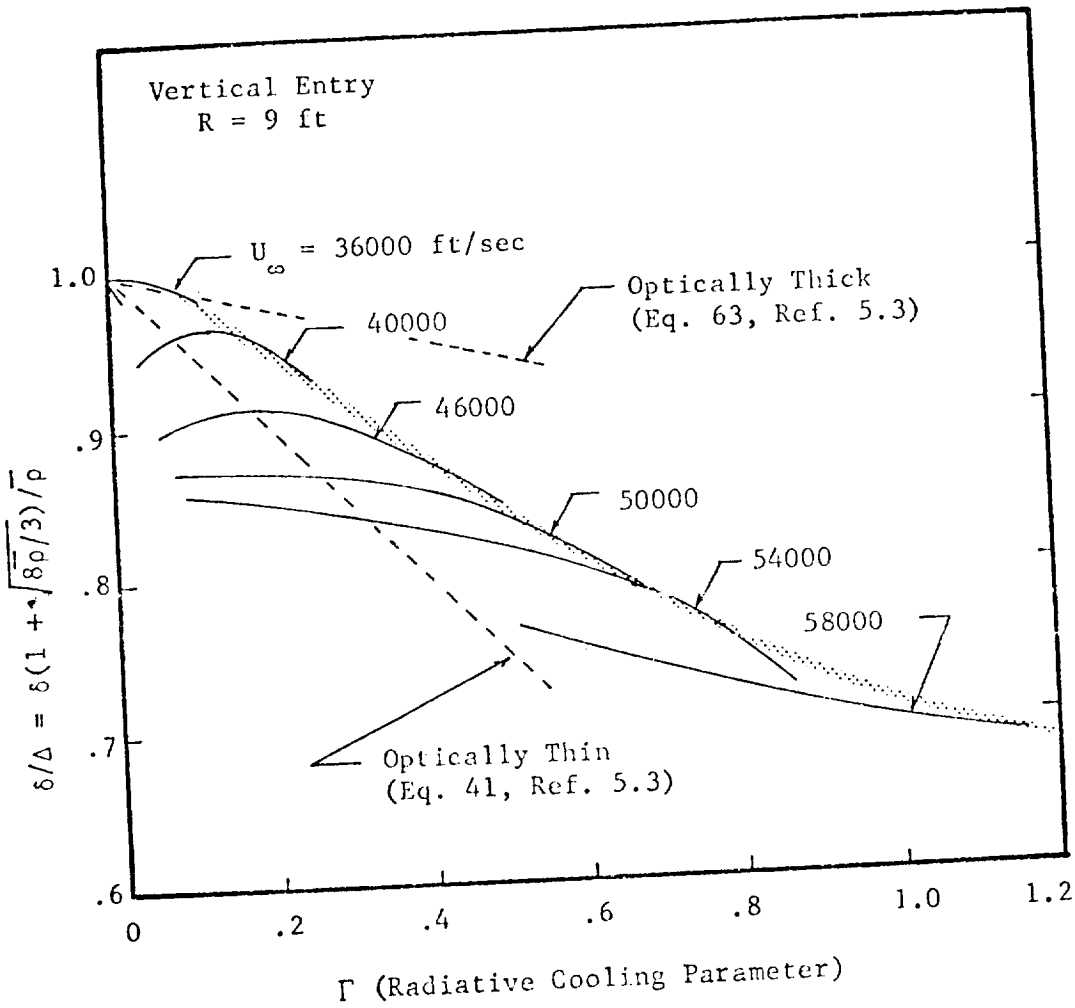

Fig. 5.4 Radiative Cooling Effects on Stand-off Distance for Vertical Entry Flight

of Goulard appear to be in agreement where applicable with the present results for the U_∞ = 36000 ft./sec. curve. The set of curves appears to form a surface which has an asymptotic limit on the optically thick side. Further, the asymtote (i.e. the shaded line in Fig. 5.4) appears nearly linear for values of Γ less than .5 and corresponds to the P_δ = 1.0 and 0.5 atm. line in Fig. 5.2. For larger values of Γ a minimum value in the asymtote for δ/Δ appears to be approached. It is anticipated that for flight velocities higher than 58000 ft./sec. precursor radiation will become significant resulting in an increase in δ/Δ, since a portion of the energy lost by radiation through the shock wave which reduces the stand-off distance will be absorbed by the on coming gas and returned to the shock layer. It might be pointed out that this minimum was understandably not predicted by the analysis of Goulard. This minimum appears to occur for large values of Γ while Goulard's analysis was limited by the assumption that $\Gamma \ll 1$.

Figure 5.5 points out features not apparent in Fig. 5.4. The actual nondimensional stand-off distance and δ/Δ are plotted against post shock pressure for an intermediate velocity of 50000 ft./sec. in Fig. 5.5. The stand-off distance for this vertical flight case exhibits a maximum whereas δ/Δ monotomically decreases with increasing post shock pressure.

To this point in this section of the results presented are for a single body radius, R = 9 ft. Figure 5.6 presents the functional dependence of the stand-off distance on Γ for various values of body

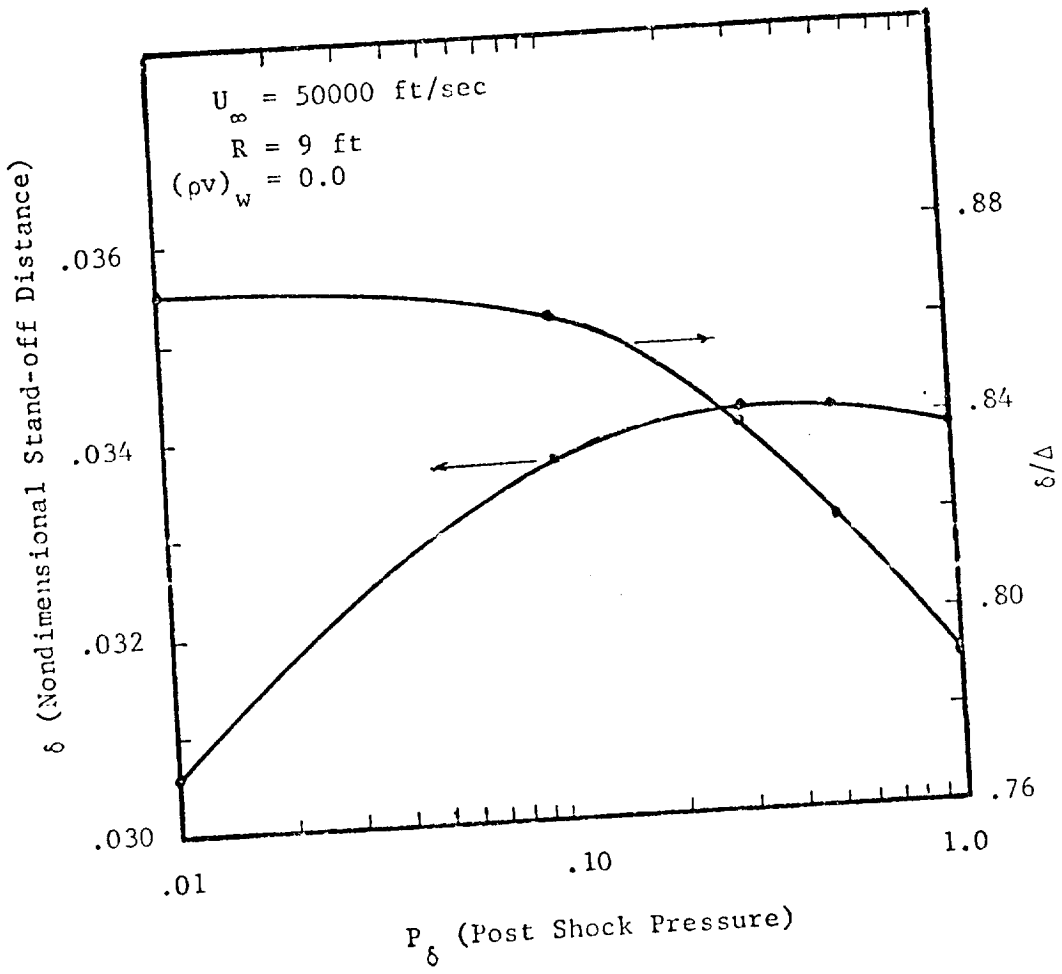

Fig. 5.5 Stand-off Distance and δ/Δ as a Function of Post Shock Pressure

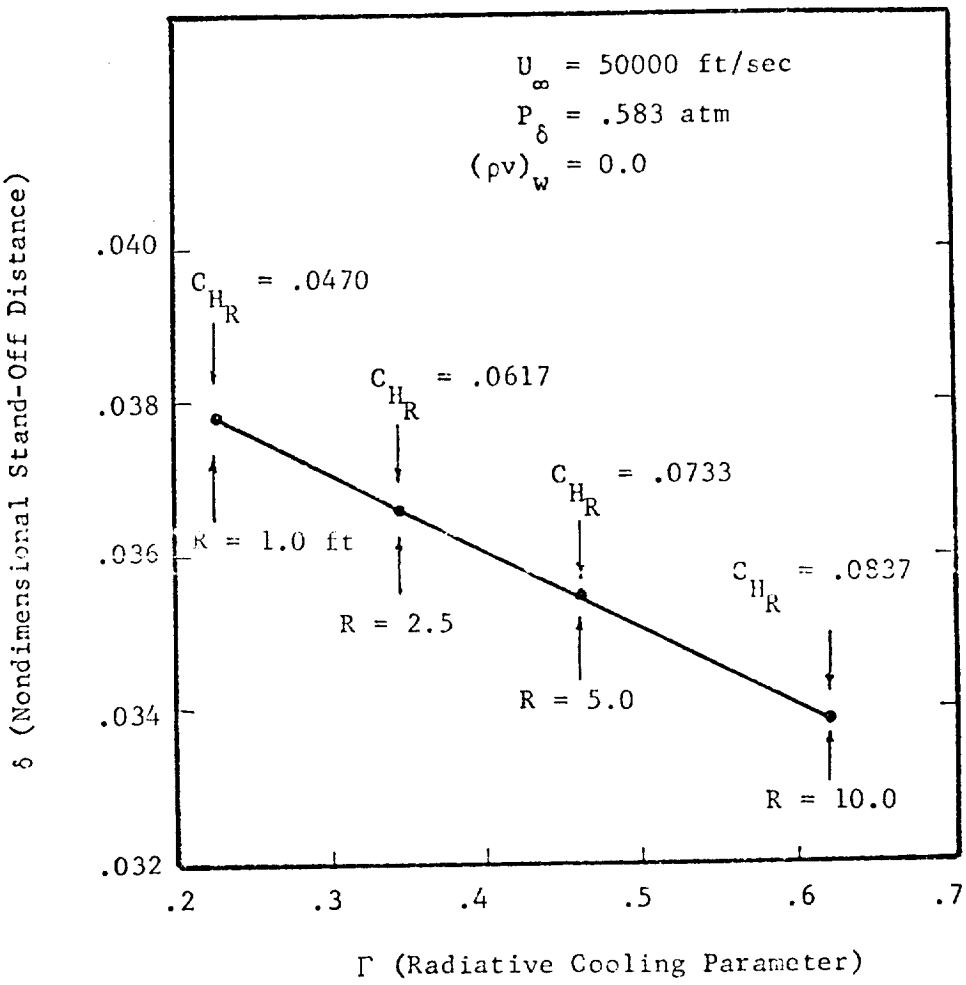

Fig. 5.6 Effect of Radiative Cooling on Stand-off Distance for Various Body Radii

radius. Even though δ verses Γ is linear, plots of δ verses the corresponding R or C_{H_R} would not show a linear dependence. Also, since Fig. 5.6 is for one flight condition, δ/Δ exhibit the same dependencies. It is interesting to observe that the smaller nose radius body will produce the largest nondimensional stand-off distance. This, of course, is a result of the smaller radiative loss experienced by the smaller shock layer. It should be pointed out that although the results given in Fig. 5.6 show a linear relationship, the flight conditions lie along the asymtote shown in Fig. 5.4. Consequently, for flight conditions other than those along the asymtote one might well expect a nonlinear relation between δ and Γ.

During the development of the stagnation equations in Chapter 2, the shock bluntness at the stagnation line was demonstrated to be unknown. The bluntness parameter, $(d\epsilon/d\xi)_{\xi=0}$, has been assumed zero corresponding to a concentric shock in most of the present work. To evaluate the effect of this assumption on the stand-off distance and radiative heating rate, $(d\epsilon/d\xi)_{\xi=0}$ was left as a parameter in the momentum equation (Eq. 2.153) where $d\varphi/d\xi = 1. - d\epsilon/d\xi$. Parametric variation of $(d\epsilon/d\xi)_{\xi=0}$ resulted in the effects shown in Fig. 5.7. The results indicate that the shock stand-off distance and radiative heat transfer coefficient both increase in a near proportionate manner with $(d\epsilon/d\xi)_{\xi=0}$. Further, the effect of $(d\epsilon/d\xi)_{\xi=0}$ is approximately the same for the two radiation models used. The work of Burns and Oliver (Ref. 5.4) indicated that

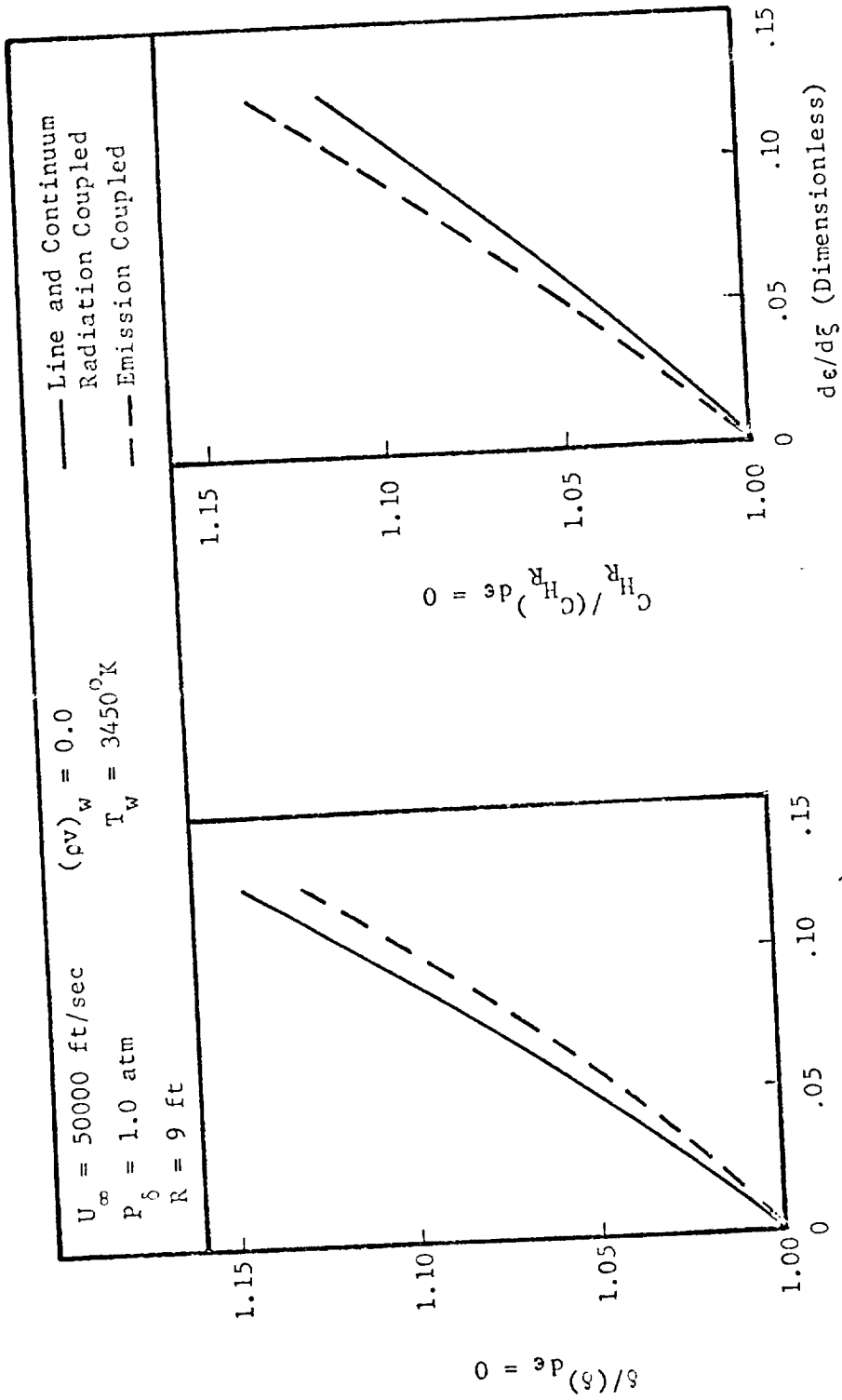

Fig. 5.7 The Effect of Stagnation Line Shock Bluntness on Stand-off Distance and Heating Rate

$(d\epsilon/d\xi)_{\xi=0}$ = .0705 for a hemispherical shaped body at the same flight conditions used to obtain Fig. 5.7. Consequently one would expect a 5 to 10% increase in stand-off distance and heating rate coefficient because of non-concentric effects. This percentage may, of course, change somewhat with flight conditions and body size. Additional observations related to the stagnation line shock bluntness are given in Chapter 6.

The shock stand-off distance is, in addition to the previously stated variables, determined by the amount of ablation products being injected into the shock layer. Mass injection essentially translates the shock wave away from the body with ablation products existing on the wall side of the stagnation point and air species on the shock side. Figures 5.8 and 5.9 show the stagnation point location as a function of mass injection rate and free stream velocity respectively. The nondimensional stagnation point location, $(y/\delta)_{v=0}$, is shown as a function of $(\rho v)_w$ for three post shock pressure levels in Fig. 5.8. The results indicate that the stagnation point location is essentially independent of shock layer pressure level. Also shown in Fig. 5.8 are results from Ref. 5.5 at $(\rho v)_w$ = .20 for a slightly different body radius and carbon phenolic ablation products.

The stagnation point location, for a given post shock pressure level, as a function of free stream velocity is given in Fig. 5.9. Present results are compared to those of Ref. 5.5 which are for different pressure levels shown. The present results and those of

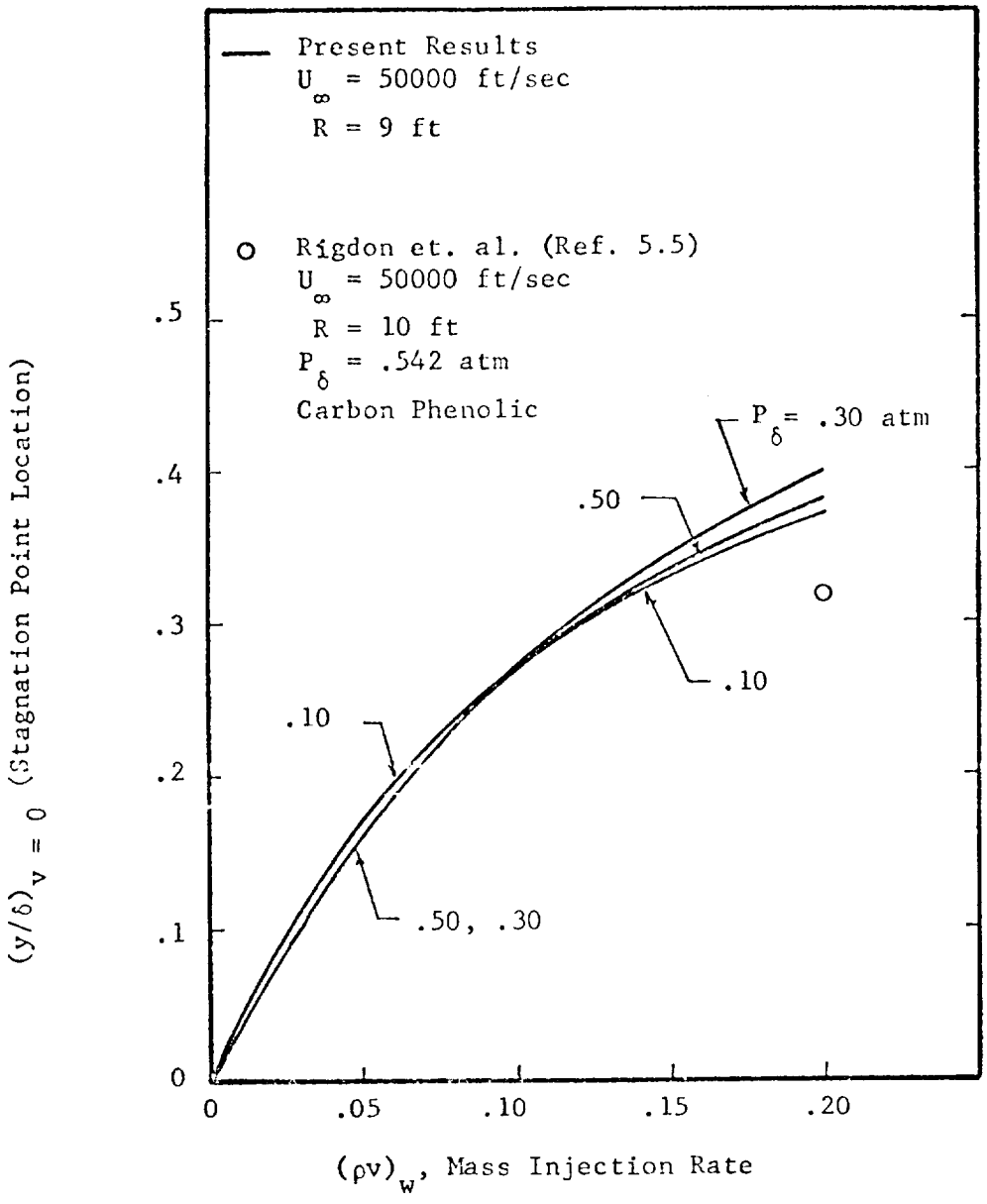

Fig. 5.8 Stagnation Point Location as a Function of Mass Injection Rate

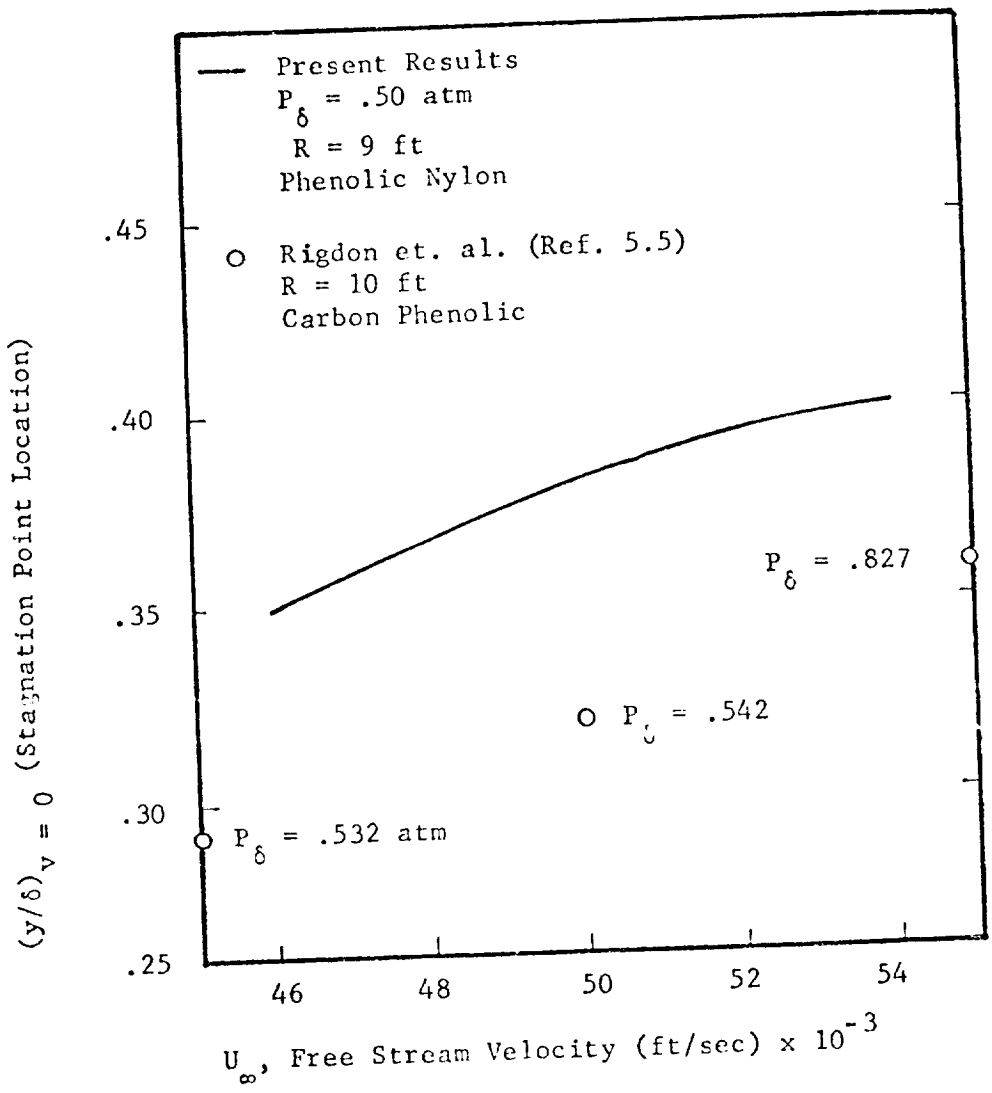

Fig. 5.9 Stagnation Point Location as a Function of Free Stream Velocity

Ref. 5.5 indicate that for the given mass injection rate the ablation product layer thickness increases on a percentage basis as the free-stream velocity is increased. Moreover, the ablation layer thickness reported by Ref. 5.5 is approximately 6.0 to 7.0% of the shock layer smaller than the present results. This agreement appears quite reasonable in the light that Ref. 5.5 results are for a different ablator and slightly larger body radius. The results presented in Figs. 5.8 and 5.9 may be of benefit for investigators using inviscid analysis approximating the inner and outer regions of the shock layer.

HEATING RATES AND ABLATOR COUPLING

The main concern in designing an ablative heat protection system is the prediction of the rate and total amount of energy which would be transferred to the ablator during atmospheric entry. For hyperbolic entry conditions the main mode of energy transfer to the ablator surface is by radiation as illustrated in Fig. 1.7 for no ablation. The effect of mass injection due to ablation is to reduce the convective heating to a negligible level compared to radiative heating. Accordingly, the results presented in this section concern the quantitative definition of radiative heating levels for typical hyperbolic entry flight conditions. A systematic variation of problem defining variables was made to establish cause and effect relationships. Coupled ablator and shock layer solutions were obtained for flight conditions typical of vertical entry.

Many of the radiative heating rates results presented in this section and others are in terms of the nondimensional radiative heat transfer coefficient which has been defined as

$$C_{H_R} = \frac{q_R}{\frac{1}{2} \rho_\infty U_\infty^3} \tag{5.4}$$

This coefficient represents the fraction of the flux of flow energy entering the shock layer per unit area which is transferred to the surface by radiation. The energy not transferred to the surface by radiation or convection is radiatively lost through the shock or retained by the gases surrounding the vehicle*. These gases flow over the vehicle and equilibrate in its wake with the atmosphere.

Radiative heating rate results, for no mass injection, are presented in Fig. 5.10 for conditions which through traditional use have become a standard for comparing radiation calculation methods. The results presented all contain line and continuum radiation and agree to within $\pm$ 10% of the average. The comparison made is essentially between computational methods since as pointed out by Wilson (Ref. 5.6) the basic data for the radiation calculation is common in the work compared. It is noted that C_{H_R} tends to an asymtotic limit at the higher free stream velocities.

This asymtotic behavior is exhibited to a lesser extent as the post shock pressure is lowered for the same flight velocities as shown in Fig. 5.11. Figure 5.11 presents results from the radiative cooling parameter calculations and shock layer calculations. The shock layer calculation results are in general slightly larger than the correlation results except at the lowest pressure. The results

---

* Neglecting precursor heating effects.

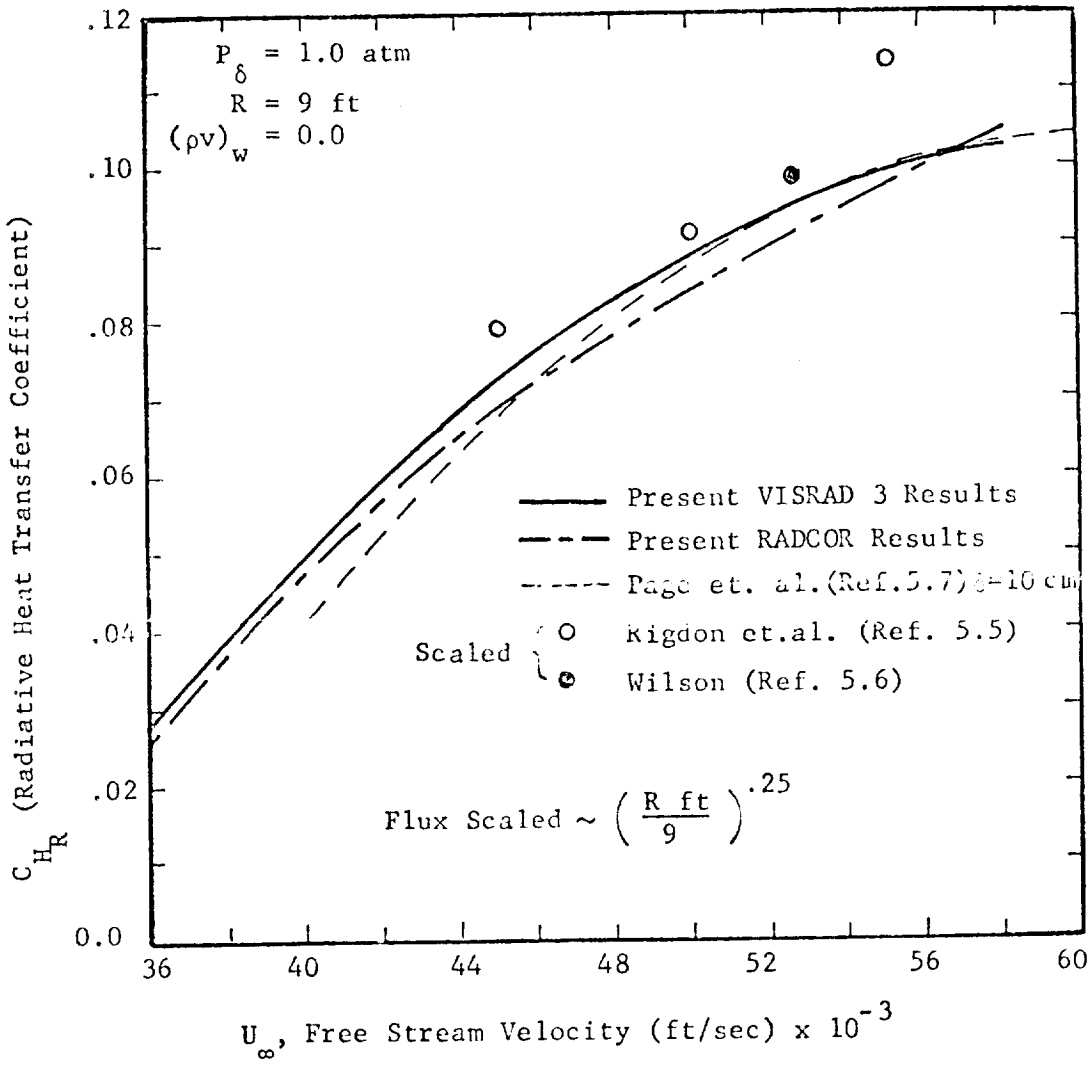

Fig. 5.10 Methods Comparison of Computed Radiative Heat Transfer Coefficients for No Mass Injection

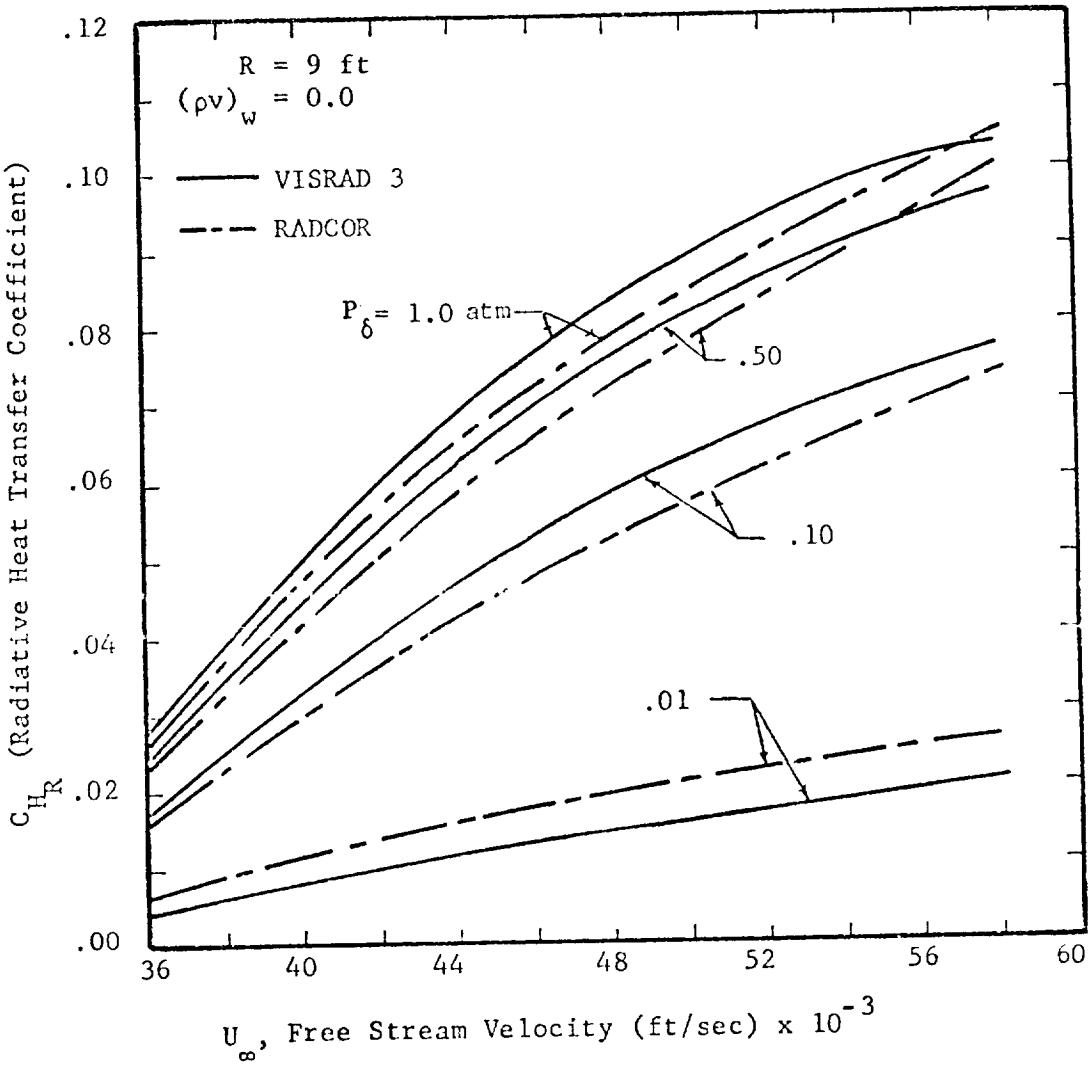

Fig. 5.11 Radiative Heat Transfer Coefficient for Various Post Shock Pressure Levels

demonstrate the nonnegligible effect of the shock layer pressure level on radiative heating.

The effect of body size on radiative heating without ablation is demonstrated in Fig. 5.12 for one set of flight conditions. All of the results presented contain line and continuum radiation coupling. The results are markedly different than the linear body radius dependency predicted by adiabatic shock layer calculations. In fact the present results show a near linear dependence on (ℓn R). The results of Ref. 5.7 also appear linearly dependent on (ℓn R) for values of R greater than 1.5. Calculations at additional flight conditions are necessary to determine if the ℓn(R) relation is characteristic of coupled shock layer solutions which include both line and continuum radiation.

The role of line and continuum radiation coupling is important throughout the peak heating period of hyperbolic entry. To illustrate this point, stagnation line heating rates were computed for a 10-g undershoot boundary trajectory with an initial entry velocity of 55,000 fps. The undershoot trajectory, presented in Fig. 11 of Ref. 5.8, was used by Engel and Spradley (Ref. 5.9) to assess the role of radiative absorption effects on heating loads. This earlier work did not include the effects of line radiation. Fig. 5.13 presents a comparison between the present results and those of Ref. 5.9. All of the results presented account for radiative losses and thus point out the importance of using a radiation model which includes line and continuum radiation without optical depth restrictions. From

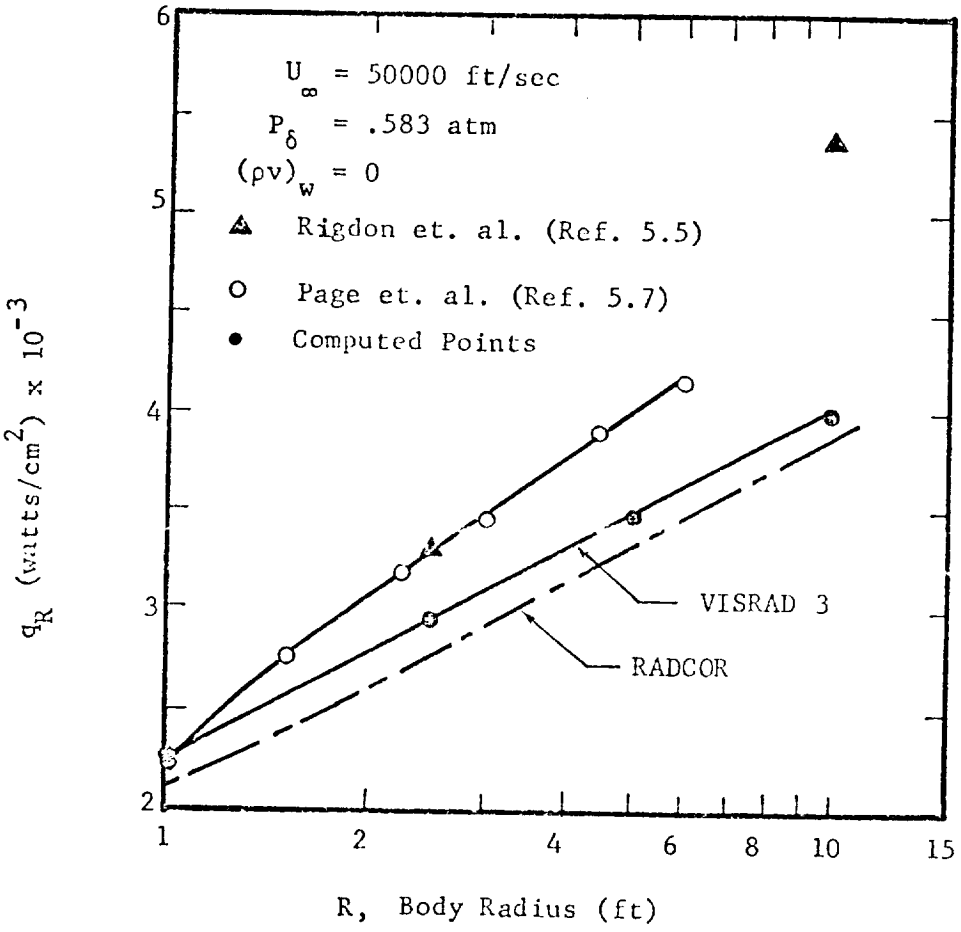

Fig. 5.17 Radiative Heating as a Function of Body Radius

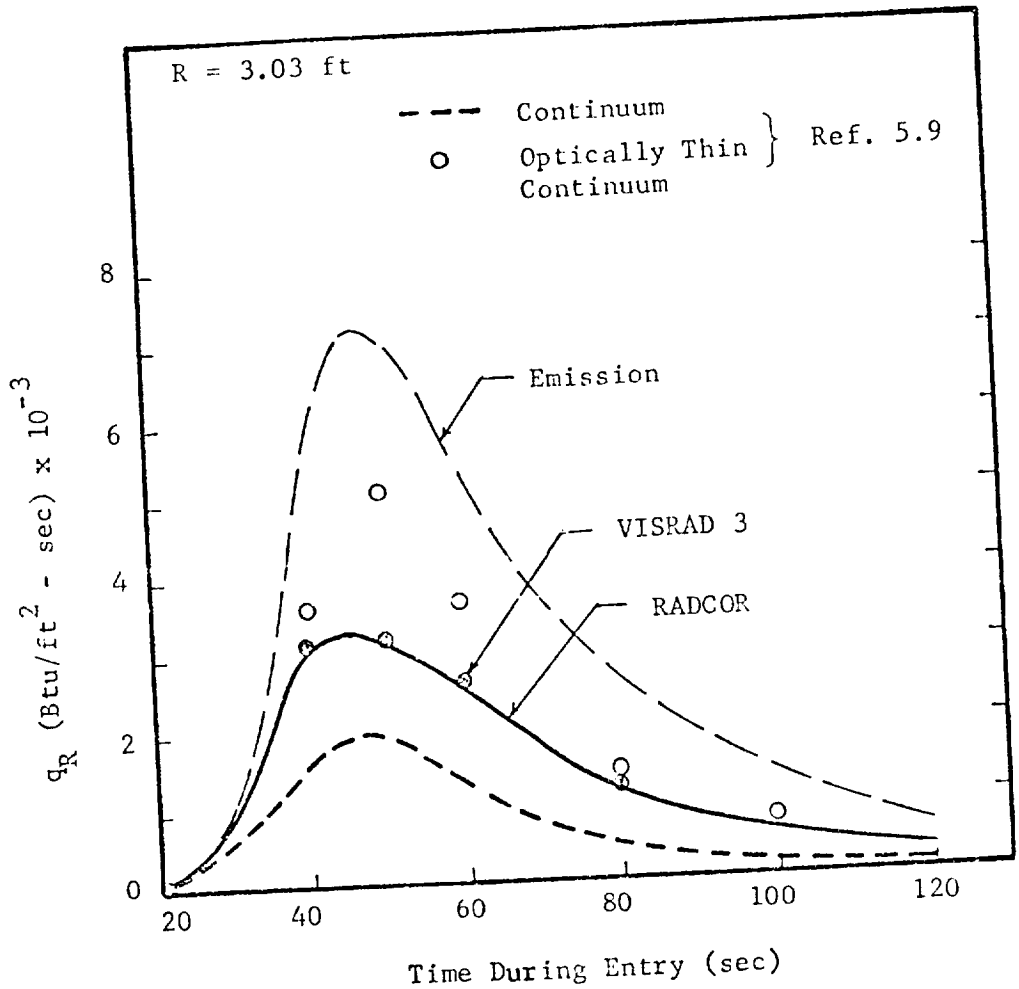

Fig. 5.13 Heating Rates for a 10-g Undershoot Earth Entry Trajectory (W/C_DA = 100 psf, L/D = .5, V_i = 55000 ft/sec)

Fig. 5.13 it is observed that both the emission model and the optically thin continuum model of Ref. 5.9 overpredict the radiative heating rates computed with the RADCOR and VISRAD 3 programs. Further, it is noted that the results of Ref. 5.9, using continuum radiation only, significantly underpredicts the line and continuum heating rates. The present results obtained using the radiative cooling parameter agree quite well with the results from the shock layer solution. It is interesting to note that the present results and those of Ref. 5.9 show a net absorption in approximately 9% of the shock layer near the wall. Thus the line and continuum and continuum only results indicate that including line radiation does not significantly change this observation.

One of the principle objectives of the current research is to evaluate the the effects of ablation product mass injection and to obtain ablator shock layer coupled solutions. It was found that previous work, Ref. 5.5, 5.6, 5.10 and others, obtained heating rates for specified ablation rates from shock layer solutions which exhibited no apparent correlation as demonstrated in Ref. 5.5. Most of the results of the previous work was for various flight velocities, altitudes, body radii and ablation rates of carbon phenolic. Unfortunately either too few results were obtained in one analysis and/or more than one specifying parameter was changed from case to case. This has lead to an incomplete understanding of the effectiveness of ablation products in reducing the radiative heating to the body. Specification of the altitude as an independent parameter

exemplifies the difficulties encountered. If, for example, we were to hold the altitude constant as well as the body size, wall temperature and mass injection rate and vary the flight velocity the following would be observed. As shown in Fig. 2.7 the post shock temperature and pressure levels would both change. This is in addition to a change in post shock velocity as computed using the Rankine-Hugoniot equations. Thus by holding altitude (or free stream density) constant and changing flight velocity, a change in three shock layer parameters occurs rather than one as desired. Since the shock layer pressure level has a considerable effect on radiative heating as shown in Fig. 5.11, it is desirable to specify this parameter rather than altitude. Accordingly, for a constant P_δ a change in free stream velocity changes only one thermodynamic parameter, T_δ, and the post shock velocity. In general it is not possible to change flight conditions without altering at least two shock layer parameters. Consequently the present parametric studies were conducted at specified pressure levels for various free stream velocities.

Radiative heating rate results for U_∞ = 50000 ft/sec, R = 9 ft. and T_w = 3450°K are shown in Figs. 5.14 and 5.15 for different levels of post shock pressure and ablation rate. The results in Fig. 5.14 illustrate the post shock pressure effects on heating at constant $(\rho v)_w$ are somewhat similar in shape but are not similar to the no mass injection line. The results show that an ablation rate $(\rho v)_w$ = .05 reduces the radiative heating rate substantially and additional ablation has a much smaller percentage effect. This effect is also

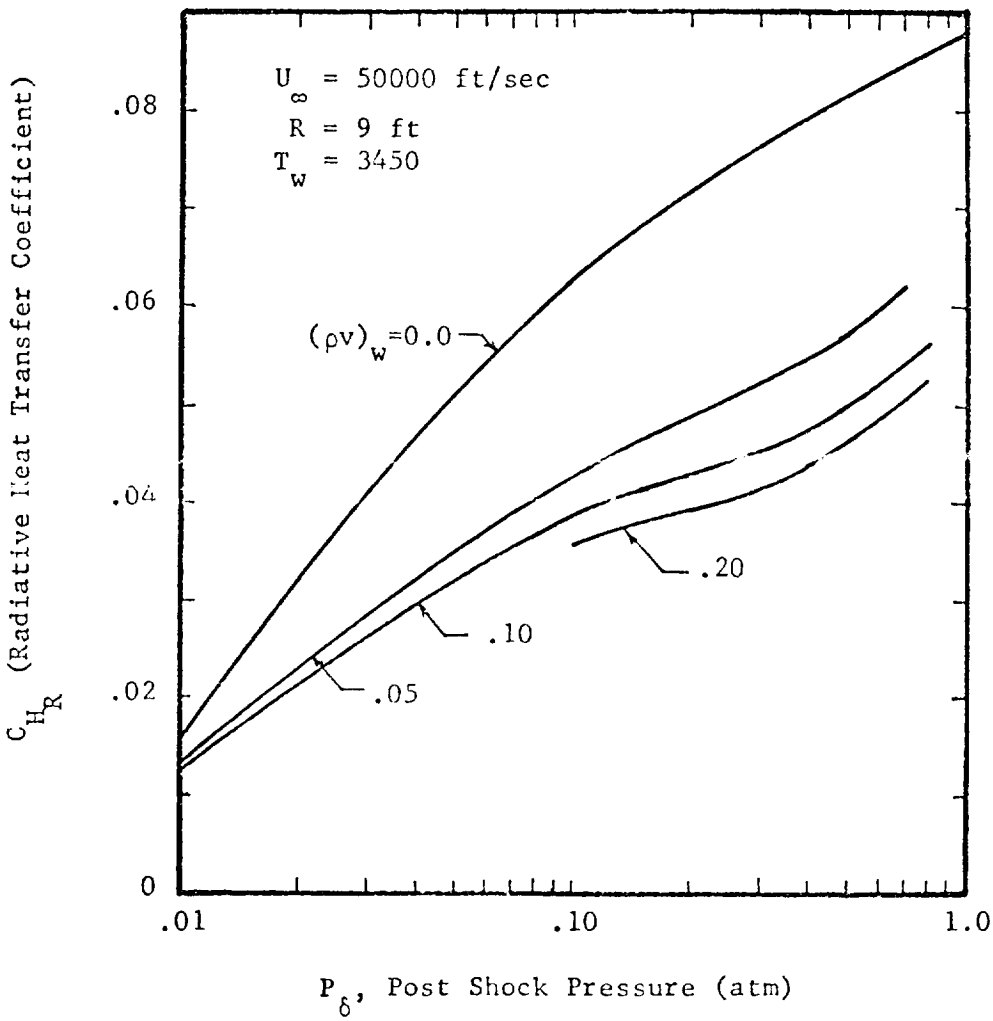

Fig. 5.14 Ablation Rate Effects on C_{H_R} as a Function of Post Shock Pressure

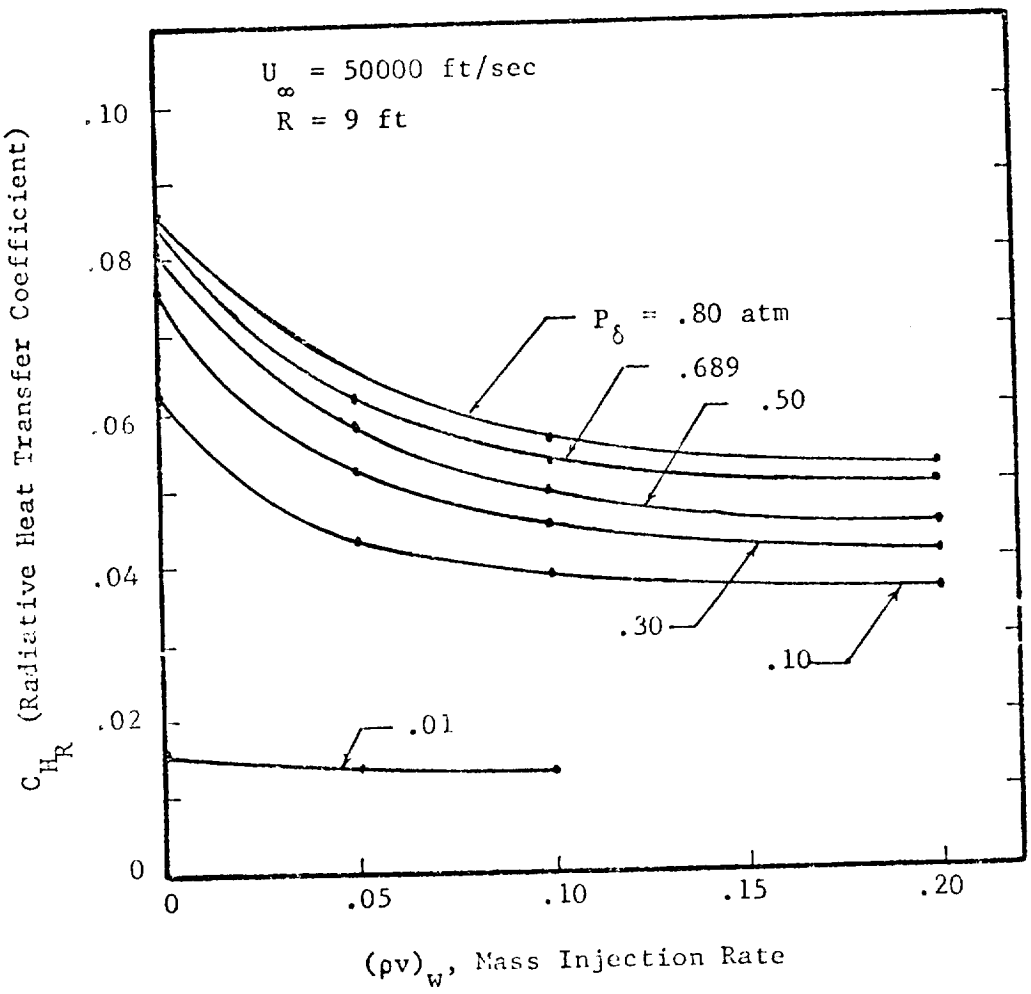

Fig. 5.15 Pressure Level Effects on C_{H_R} as a Function of Mass Injection Rate

shown in Fig. 5.15 which presents another projection of the C_{H_R}, P_δ, $(\rho v)_w$ surface. The constant P_δ curves exhibit a characteristic [illegible] with $(\rho v)_w$ but do not overlap when nondimensionalized by the heating rate coefficient for no mass injection, $(C_{H_R})_0$.

Most investigators present heating rate results for mass injection in a plot of $C_{H_R}/(C_{H_R})_0$ verses $(\rho v)_w$ irrespective of the free stream velocity, post shock pressure or body radius. As pointed out above this had led to apparent disagreement between results. The obvious conclusion is that the $(\rho v)_w$ parameter is not sufficient to correlate the results. Fig. 5.16 was prepared to, in part, point out why $(\rho v)_w$ is insufficient. The results show a quite obvious dependence on post shock pressure and exhibit a minimum in the constant $(\rho v)_w$ curves near P_δ = .3 atm. Two values of nondimensional heating for carbon phenolic are also shown in Fig. 5.16. These values, although not at the precise flight conditions and body size of the present results, were thought to be near enough for comparative purposes. The $(\rho v)_w$ = .10 case of Wilson (Ref. 5.6) shows a slightly higher rate of heating than extrapolation of the present results would yield and the $(\rho v)_w$ = .20 case of Rigdon et. al. (Ref. 5.7) is slightly lower than present results. The agreement is quite reasonable since the results are for different ablators. More importantly, the two points indicate that the same kind of post shock pressure dependence is shown. From these observations it is realized that plotting $C_{H_R}/(C_{H_R})_0$ versus $(\rho v)_w$ irrespective of pressure level may lead to erroneous conclusions regarding the effectiveness of ablation in reducing radiative heating.

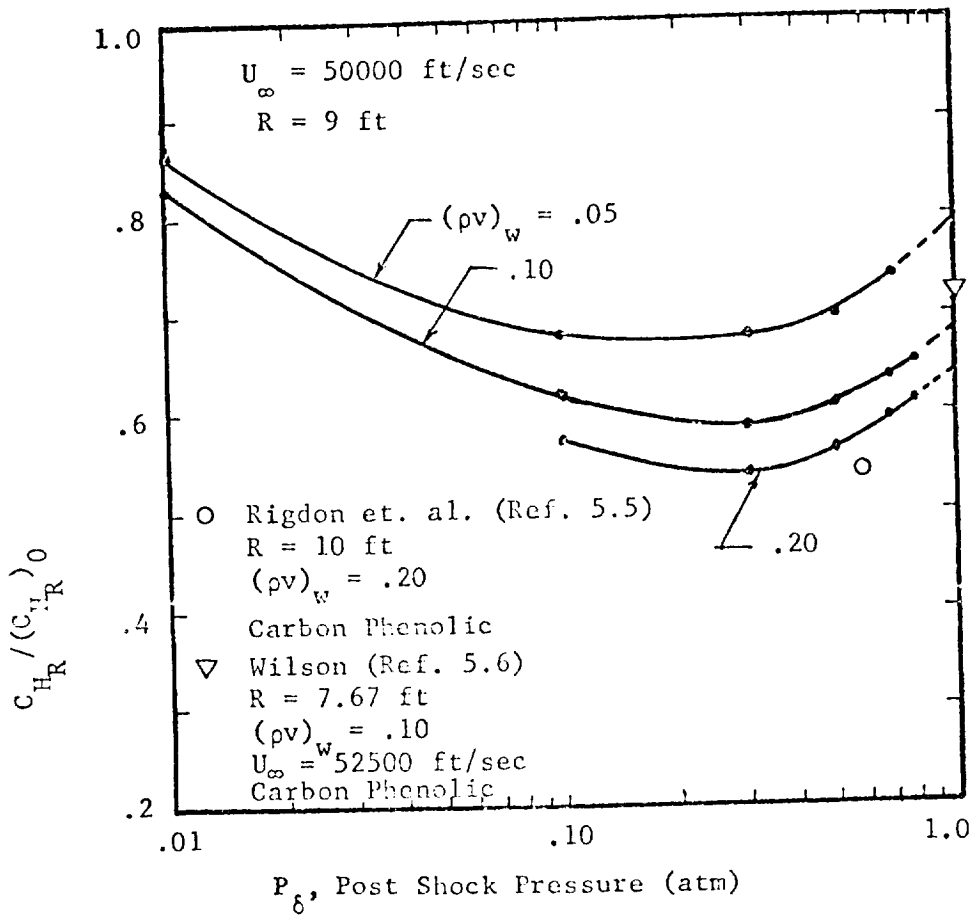

Fig. 5.16 Ablation Rate Effectiveness in Reducing Radiant Heating as a Function of Post Shock Pressure

To examine the effect of free stream velocity on the radiative heating at a constant ablation rate Fig. 5.17 was prepared. As shown in the lower half of the figure the effectiveness of the ablation products for the conditions examined exhibits a minimum (i.e., $C_{H_R}/(C_{H_R})_0$ exhibits a maximum) near 50000 ft/sec. The reason for the maximum in $C_{H_R}/(C_{H_R})_0$ is clear from the plot in the upper half of Fig. 5.17. Even though the actual heating rate increases with velocity for $(\rho v)_w = .20$ its rate of increase is smaller than for no ablation. In the lower half of Fig. 5.17 values of $C_{H_R}/(C_{H_R})_0$ are given for different post shock pressure levels at $U_\infty = 50000$ ft/sec to indicate how the pressure level would shift similar curves verses U_∞. In addition, three computed points from Rigdon, et. al. (Ref. 5.5) for carbon phenolic are shown. These results for a constant altitude are in reasonable agreement if one considers the post shock pressure level shifts.

Of prime importance in the design of an ablative heat shield is the accurate determination of the amount of material which will be lost during entry. To compute the amount of material lost by ablation processes requires a coupled solution of the flow field and ablator. For quasi-steady ablation the coupling is adequately described by the surface balance equations presented in Chapter 3. Fig. 5.18 presents a graphical solution matching the flow field and ablator response for five different post shock pressure levels. The point of crossing of the constant P_δ shock layer lines and the linear segments for the given P_δ of the ablator response as read from Fig. 3.4 yields the

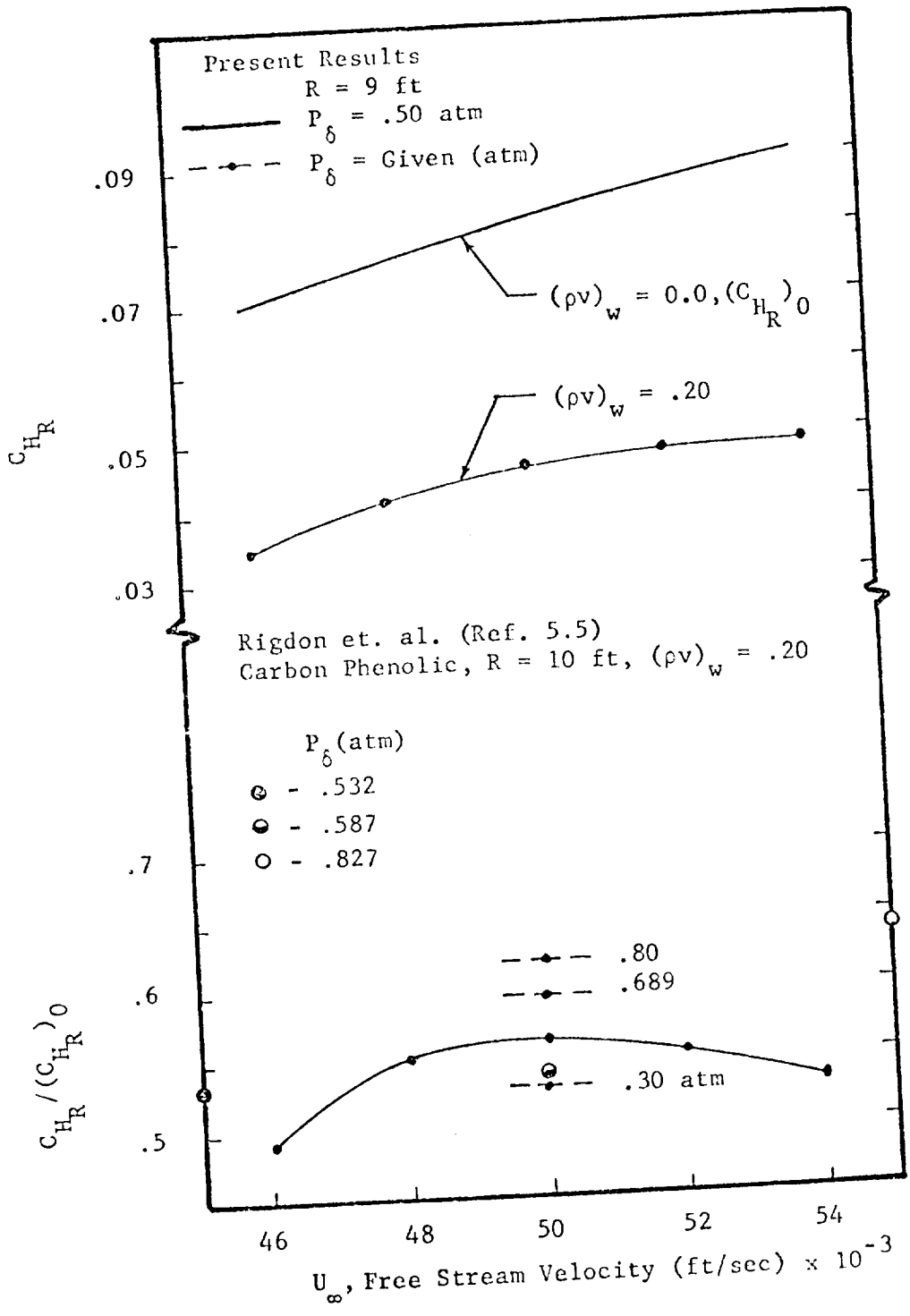

Fig. 5.17 Free Stream Velocity Effects on Radiative Heating for $(\rho v)_w$ = .20

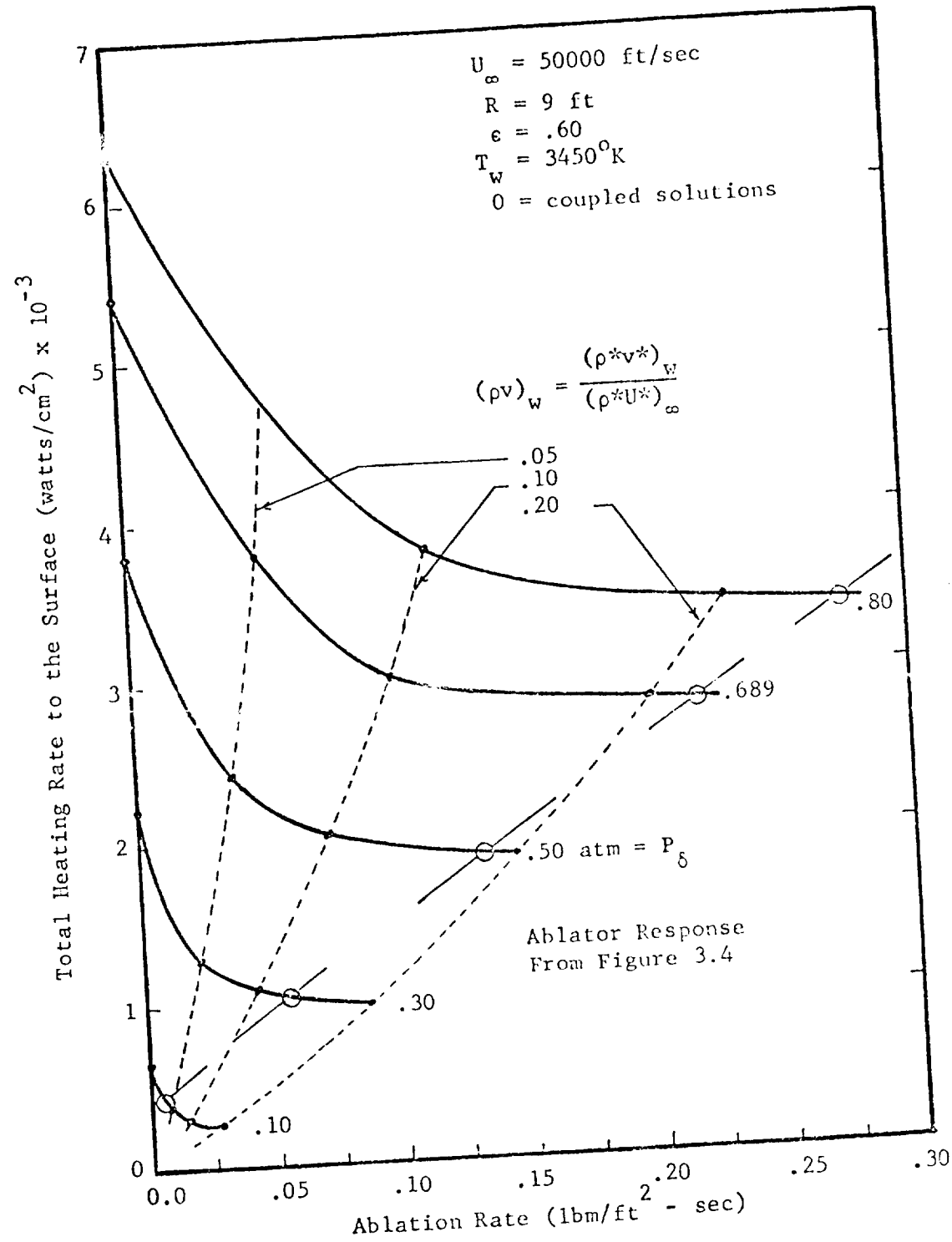

Fig. 5.18 Coupled Ablator - Shock Layer Solutions

coupled solution. Several observations can be made from Fig. 5.18. [illegible] layer coupling becomes important at approximately P_δ = .10 atm. for the flight velocity and body size specified. Further the quasi-steady ablator response assumption would not be valid below P_δ = .10 atm. since the heating is insufficient to maintain the surface at the sublimation temperature unless the char surface is removed by other than the sublimation mechanism such as oxidation. Also for coupled ablation rates at P_δ = .10 and lower the species boundary condition of the third kind at the surface may become important as indicated by Esch (Ref. 5.11). However to obtain coupled ablator-shock layer solutions for P_δ = .10 and larger the surface balance equations used appear quite adequate. In addition, it is observed that as the post shock pressure is increased the intersection angle of the lines from the ablation analysis and the shock layer analysis becomes increasingly acute. Thus errors which are inherent in the heating analysis are reflected in a greater uncertainty in the ablation rate at the higher pressures.

In summary, the results presented provides the most complete description of ablator-shock layer coupling which has been reported.

RADIATIVE COUPLED SHOCK LAYER CHARACTERISTICS

Examining characteristic of radiative coupled shock layers not only leads to a better understanding of the processes which occur but also permits the assessment of the relative importance of the various processes. Accordingly, this section is devoted to observations of shock layer characteristics such as temperature and velocity profiles under a variety of different flight conditions.

The effects of increased radiative coupling is shown in Figs. 5.19 and 5.20. Nondimensional shock layer temperature profiles are shown in Fig. 5.19 for a constant post shock pressure and six free stream velocities. It is noted that as the free stream velocity is increased, the nondimensional temperature profile is lowered as a result of increased radiative loss (i.e. cooling). In general the temperature profiles are approximately linear between $(y/\delta) = .2$ and $(y/\delta) = .8$. This is in contrast with the constant temperature profiles hypothesized by Goulard (Ref. 5.3) for optically thick shock layers. The regions of rapid temperature change near the wall and the shock, anticipated by (Ref. 5.3), are exhibited by the current shock layer solutions. The effects of radiation coupling has a much smaller effect on the momentum transfer in the shock layer as shown in Fig. 5.20. Two observations may be made however. First, the slope of the f' profile at the wall is decreased as the free stream velocity and corresponding radiative cooling is increased. Since the shear at the wall is proportional to f' one concludes that effect of radiative coupling is to reduce the wall shear stress. This is in agreement with previous observations discussed by Anderson (Ref. 5.12). Secondly, radiative cooling effects produce corresponding temperature and thus density changes in the shock layer. The density changes result in a nonlinear variation in f' away from the wall. Stated another way the radiative cooling effect makes the whole shock layer exhibit viscous behavior. Again this concurs with published work of Hoshizakii and Wilson (Ref. 5.13) as well as others.

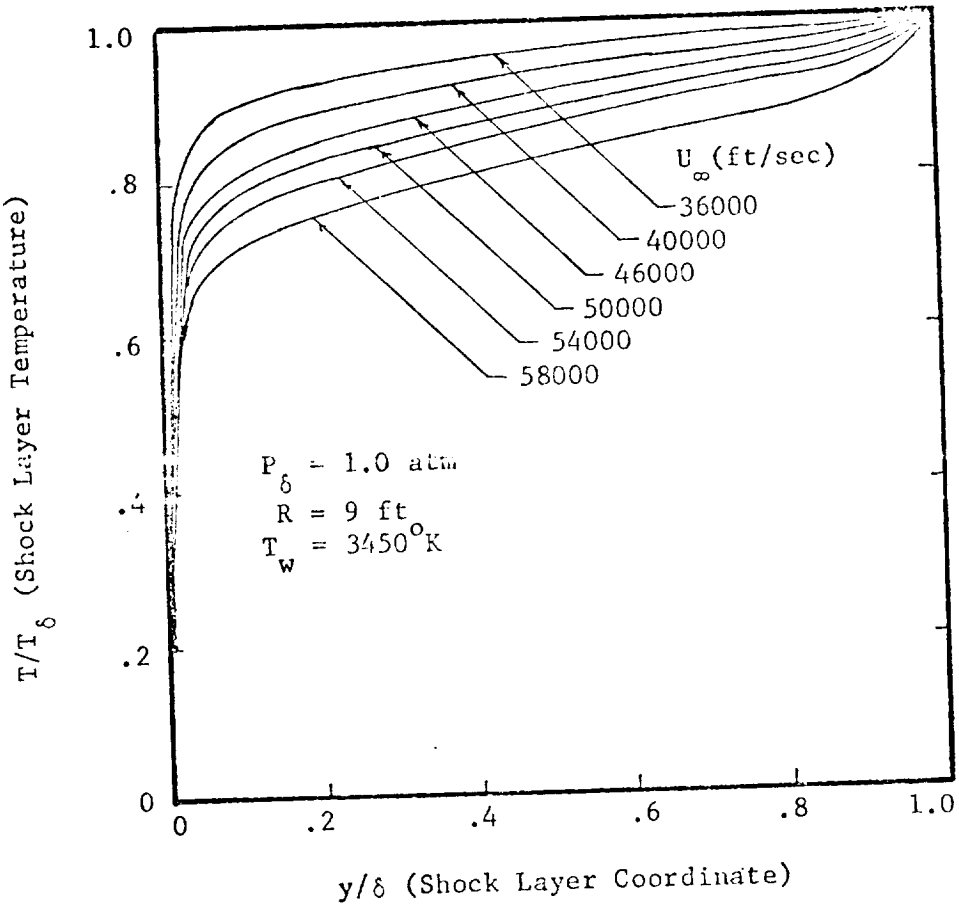

Fig. 5.19 Radiative Coupled Temperature Profiles Without Mass Injection

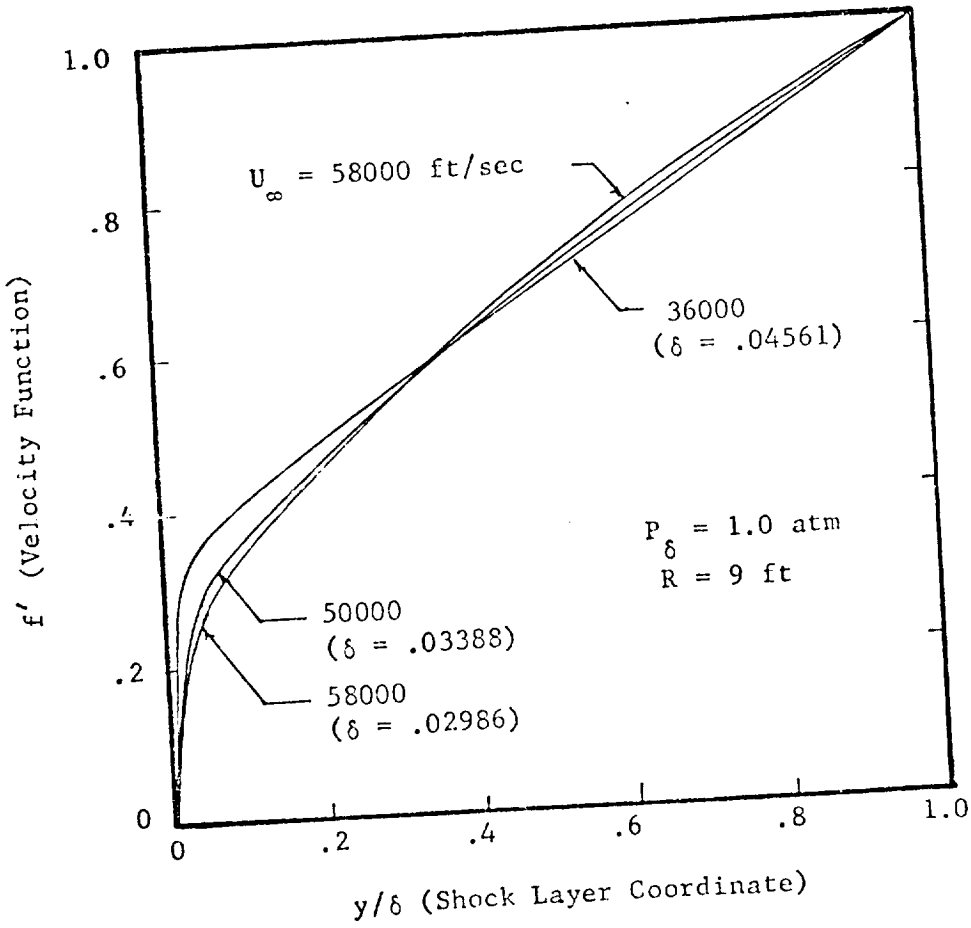

Fig. 5.20 Radiative Coupled f′ Profiles Without Mass Injection

Temperature profiles from shock layer solutions using the emission model are given in Figs. 5.21, 5.22 and 5.23. A comparison of temperature profiles obtained using the emission model and LRAD 3 model is given in Fig. 5.21. The results show that the emission model yields the proper temperature solution behavior even though it tends to overpredict the radiative cooling effect. The use of the emission model to isolate cause and effects is desirable since the model is only dependent on shock layer temperature and pressure*. With the use of the emission radiation model, the effects of including the density variations due to ablation products was examined. The results shown in Fig. 5.22 are for air C_p, k and μ properties. The effect of including ablation products in the density calculation, rather than using an air value, is to shift the temperature profile and stagnation point. Further, the stand-off distance is substantially increased. The effect was considered significant enough that it has been included in all of the ablation coupled results of this work. Rigdon, et. al. (Ref. 5.5) did not isolate this effect and used air values in most of their calculations.

A comparison of the temperature profiles computed using a binary solution of the species equation (Ref. 5.11) and using the constant elemental two zone model of the present work is given in Fig. 5.23. The effects on the temperature profile by including a binary species solution appear negligible. It should be noted that the radiation

---

* It is noted that the model was developed as a correlation of air radiation characteristics only.

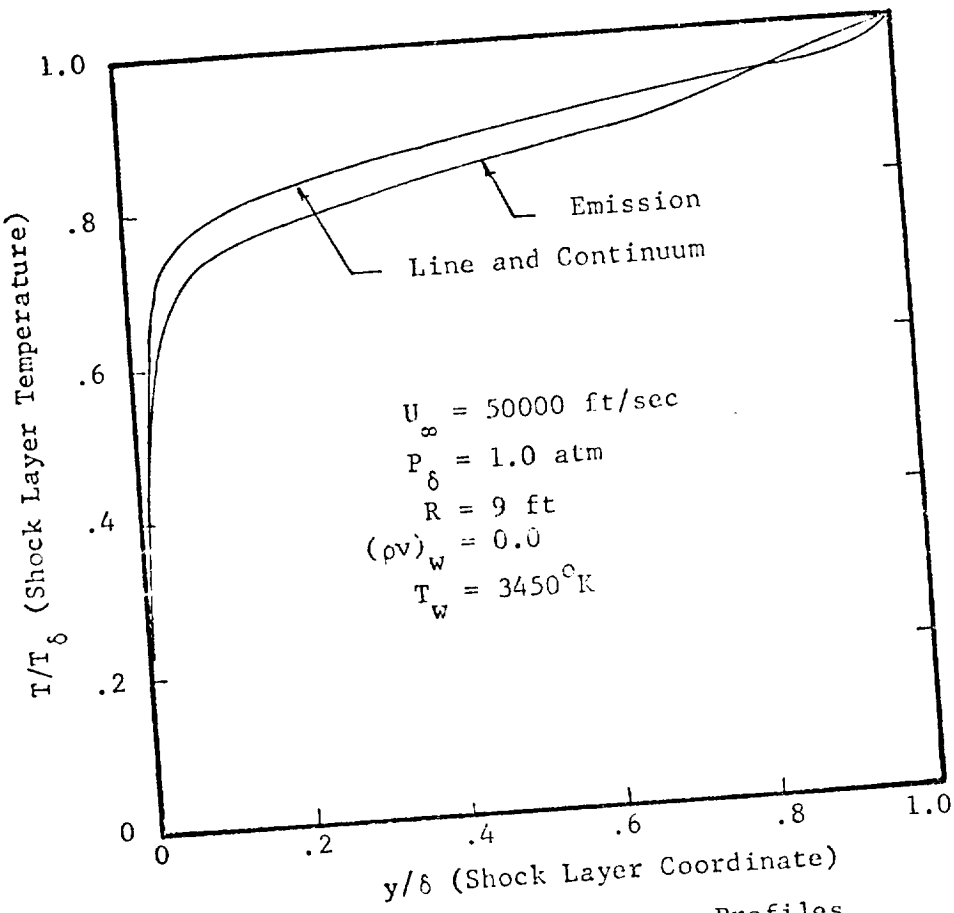

Fig. 5.21 Comparison of Temperature Profiles Resulting From Different Radiation Models

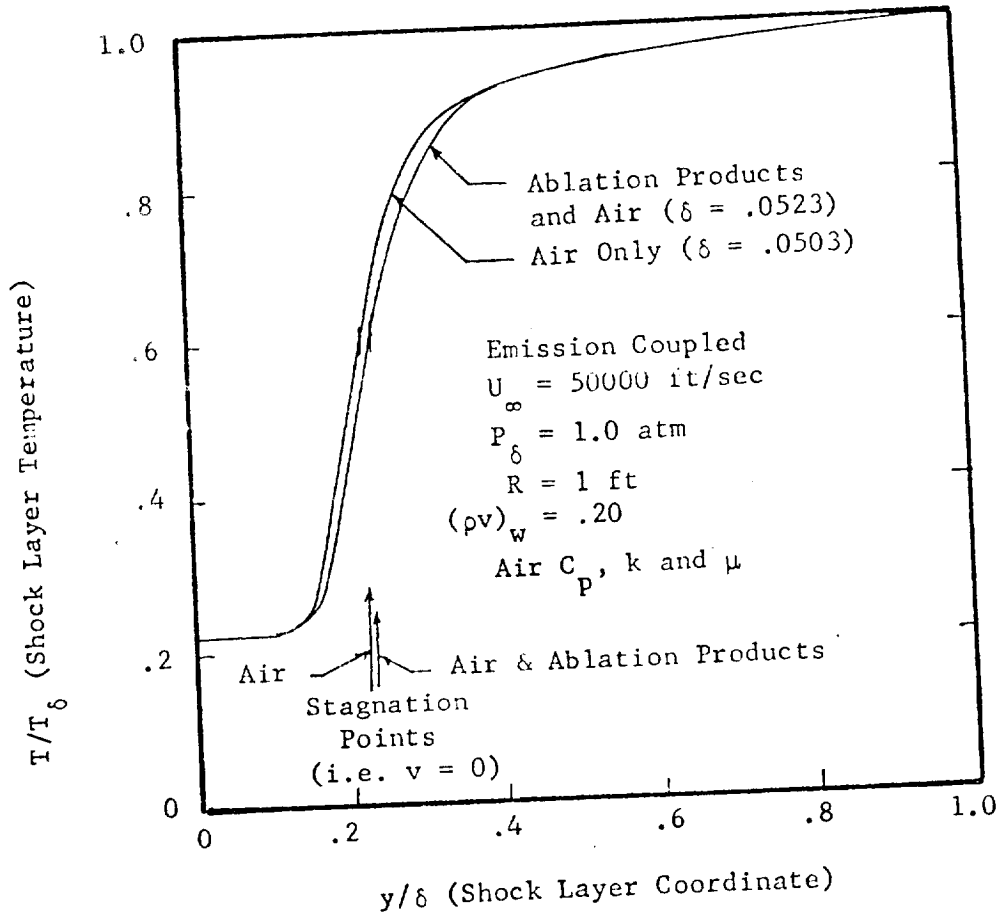

Fig. 5.22 Density Coupling Effects of Ablation Products on the Shock Layer Temperature

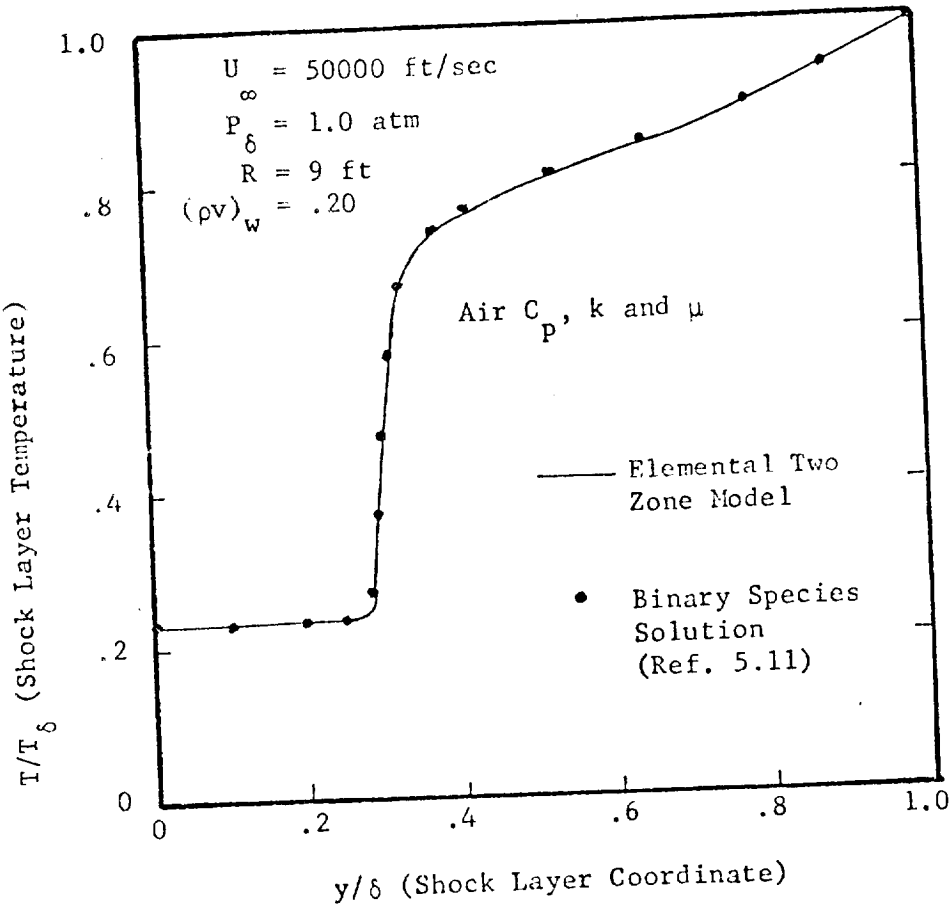

Fig. 5.23 Effects of Elemental Species Solutions on Shock Layer Temperature Using Emission Radiation Coupling

coupling due to species variations is not accounted for since the [illegible] for this comparison. The results indicate, however, that the density variation resulting from diffusion is adequately approximated.

The effects of radiation coupling changes on the temperature profile which arises from the two zone species model approximation is illustrated in Fig. 5.24. It is noted that only a slight change in the temperature profile is observed. Further, the percentage change in the radiative heating rate for the two solutions was observed to be 4.0%. In addition Esch (Ref. 5.11) showed that multicomponent diffusion effects tended to reduce this difference. A comparison is made in Fig. 5.25 of elemental compositions for typical shock layer conditions showing the approximation made in using the two zone constant elemental model. The multicomponent solution, which was an uncoupled analysis, of Ref. 5.11 agrees more closely with the present model than the binary solution*. From the results presented, it is concluded that the two zone constant elemental model appears quite adequate for use in an equilibrium solution of the shock layer equations. It is realized, however, that if finite rate chemistry effects of the ablation species are found to be pronounced, this species approximation would need revision.

An additional discussion regarding properties is in order at this point. The present results are for air mixture values of C_p, k

---

* It is expected that a selection of a heavy-heavy binary diffusion coefficient rather than a light-heavy coefficient as employed by Ref. 5.11 would reduce the difference in the binary and multicomponent concentrations.

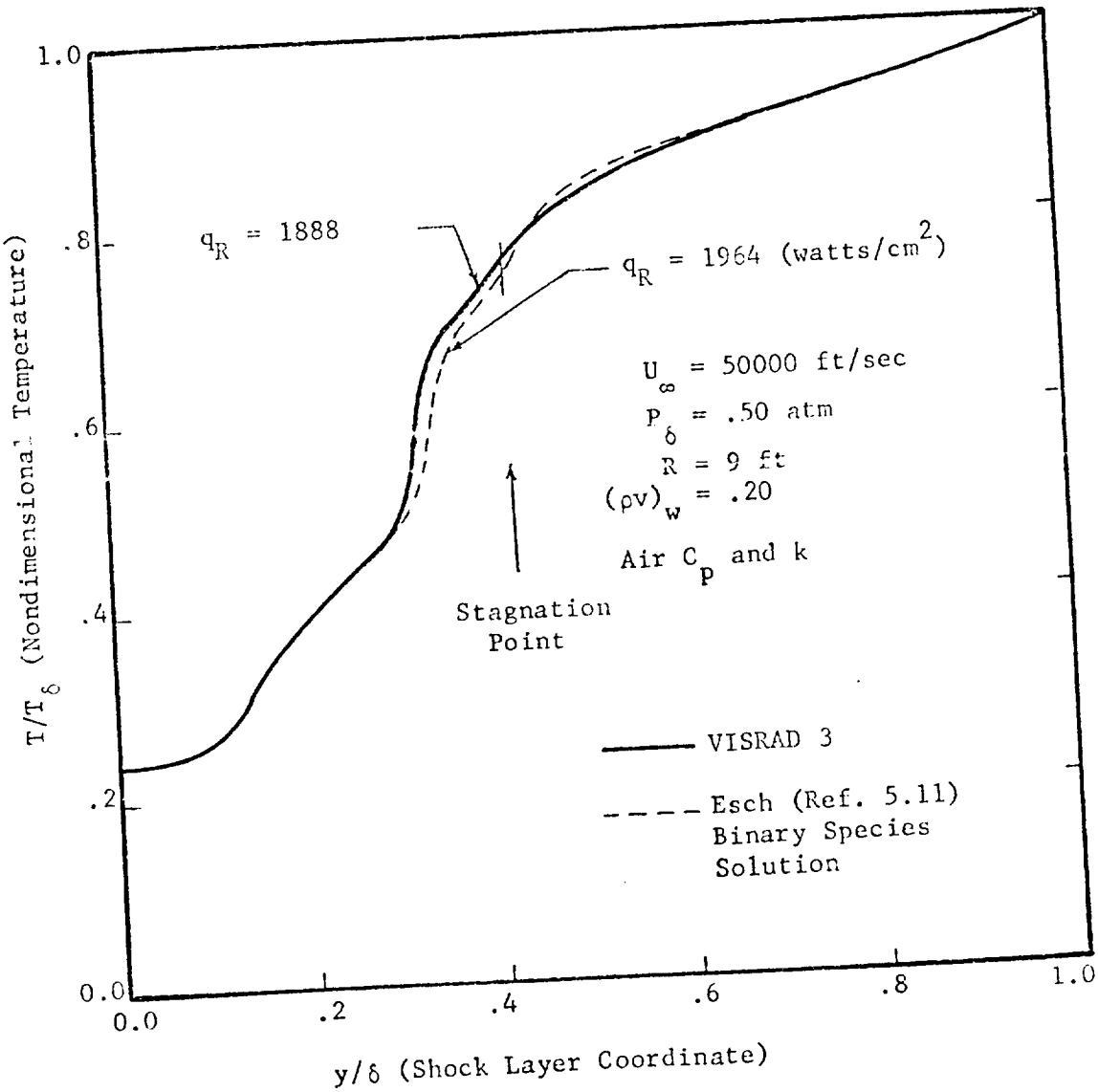

Fig. 5.24 Effects of Elemental Species Solution on Shock Layer Temperature Using Line and Continuum Radiation Coupling

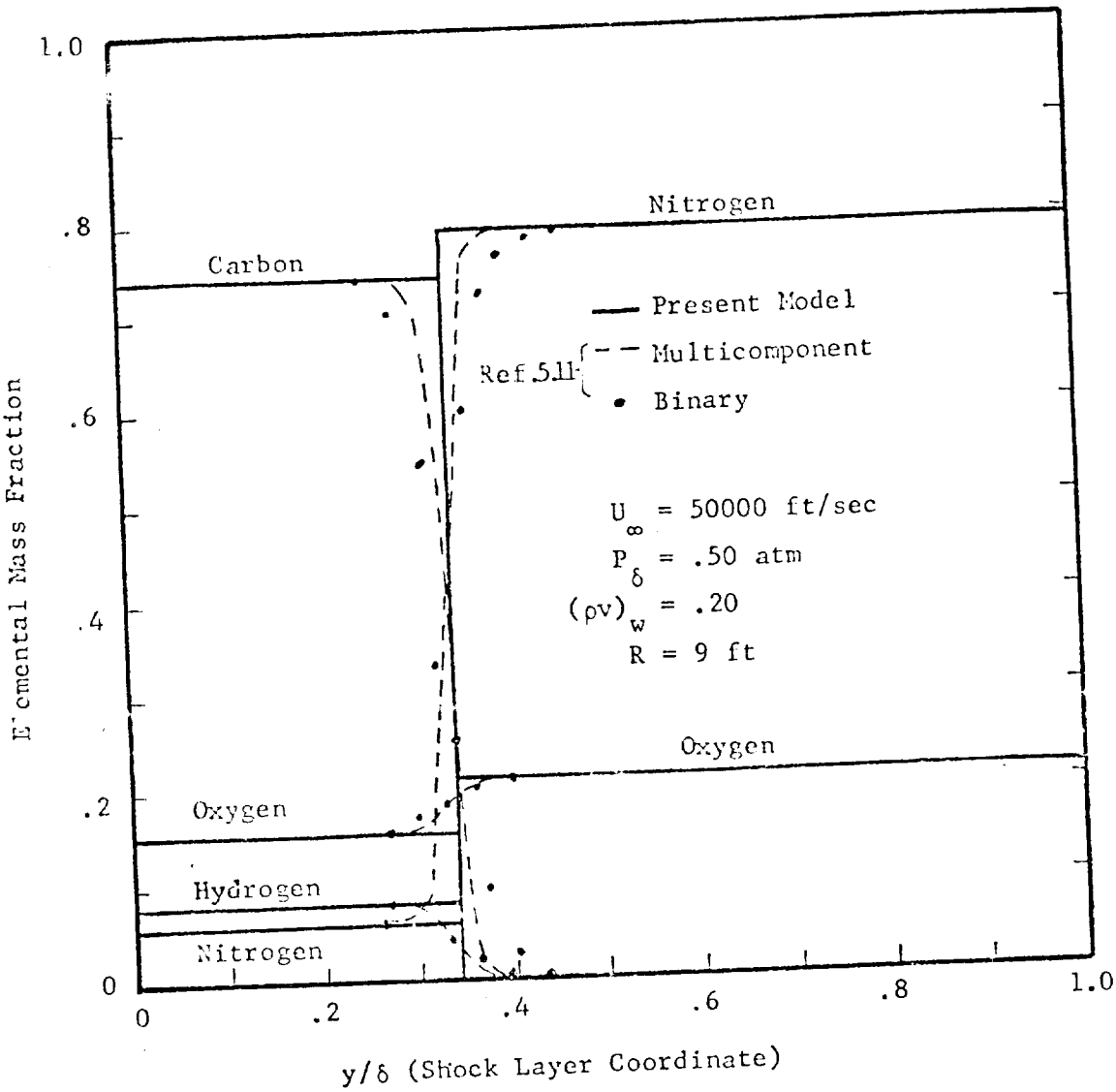

Fig. 5.25 Comparison of Multicomponent, Binary and Two Zone Elemental Solutions

and μ which were used throughout the shock layer. The results and [illegible] by Rigdon, et. al. (Ref. 5.5) for carbon phenolic ablation products and those presented by Esch (Ref. 5.11) for phenolic nylon ablation products indicate the use of air mixture values for k and μ throughout the shock layer is sufficiently adequate for calculation purposes. For the cases examined by Ref. 5.5 and Ref. 5.11 the inclusion of ablation product changes in the mixture thermal conductivity and viscosity changed the heating no more than 1.0 to 2.0 percent. These properties affect the shock layer profiles only in a small region near the stagnation point explaining their small influence on the overall solution. Results presented by Esch (Ref. 5.11) which include ablation species in the heat capacity show a significant decrease in the temperature profile near the wall, from those shown in Fig. 2.23. The reacting heat capacity for phenolic nylon ablation products was reported to be as large as 17 times greater than that of air (Ref. 5.11). The radiative energy absorbed by the ablation products is thus transferred into internal modes rather than translational energy modes as predicted using air C_p. Even though the temperature was decreased significantly near the wall using the ablation product C_p the radiative heat transfer was changed by only 4.8% from the present results for the case given in Fig. 5.24. Other cases reported showed even smaller percentage changes in heating. Consequently the use of air heat capacities in the present work does not appear to have introduced significant changes in the surface heating rate from those which account for ablation product effects on the heat capacity.

It is interesting to examine the effects of the ablation rate and post shock pressure on the shock layer temperature, normal velocity and tangential velocity. Figs. 5.26, 5.27, 5.28 present temperature profiles for different ablation rates at three post shock pressures. Increasing the ablation rate decreases the temperature near the wall as expected. Thus the convective heating is reduced to a negligible level. The temperature profiles exhibit plateaus near the stagnation point and in the ablation layer. The plateaus appear characteristic of the ablation injection cases and were aslo observed by Rigdon et. al. (Ref. 5.5) and Esch (5.11). The plateau near the stagnation point occurs near the peak carbon atom concentration which has a primary role in absorption of radiation. The plateau closer to the wall is a result of molecular absorption of radiant energy which gives rise to the increase in temperature over nonabsorbing results such as those exhibited by the emission model in Fig. 5.23. These plateaus appear more accentuated by increasing shock layer pressure levels. Increasing pressure naturally increases the radiative coupling effects and thus gives rise to the accentuation.

Shock layer pressure levels have a much smaller effect on the velocity field and thus only one pressure level is presented herein. The normal velocity, v/U_∞ and the tangential velocity function, f', are given in Fig. 5.29 for four ablation rates as a function of y/δ. The effect of mass injection is to change the character of the f' profile while the same character is maintained by the normal velocity.

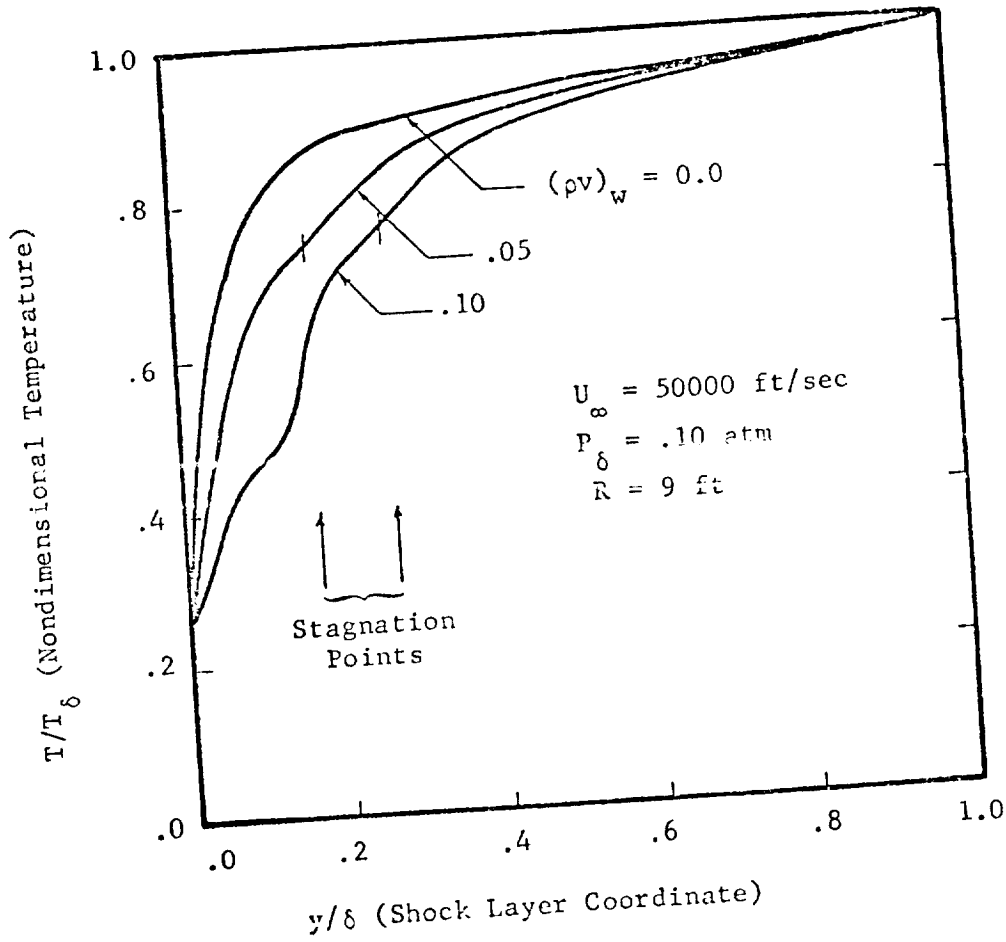

Fig. 5.26 Effects of Ablation Rates on Shock Layer Temperature at P_δ = .10 atm.

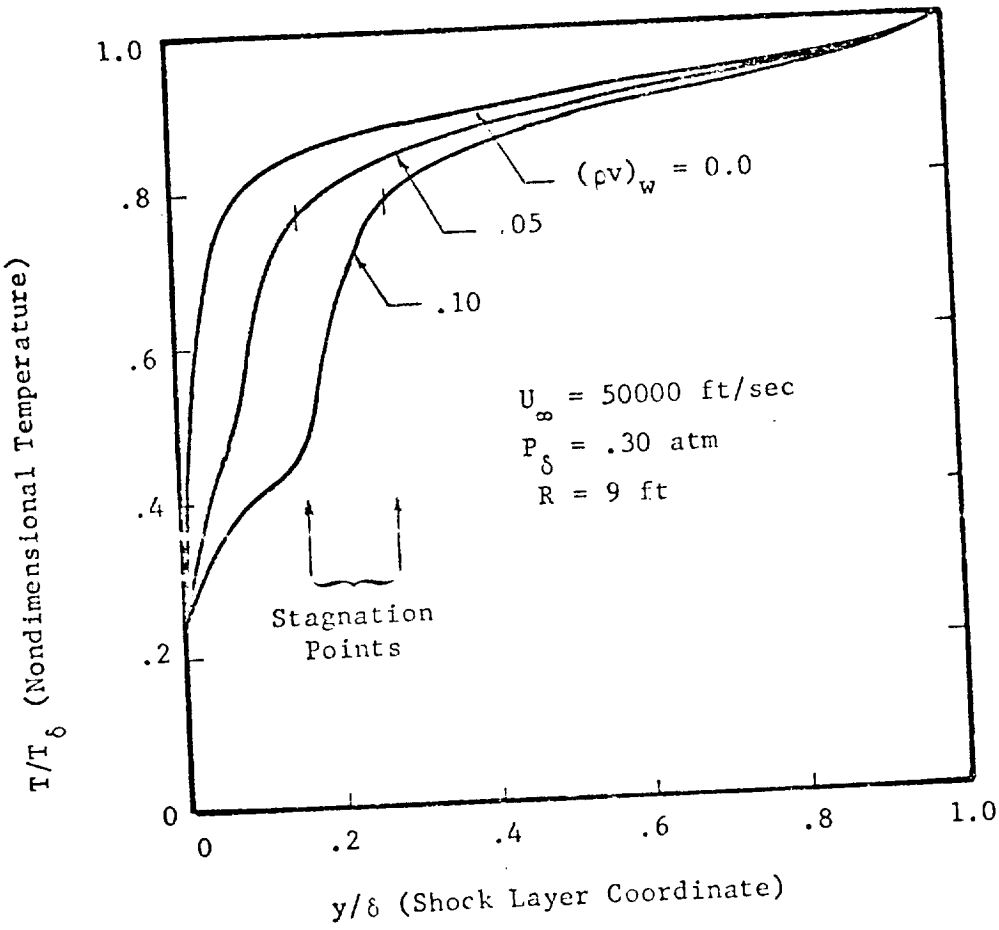

Fig. 5.27 Effects of Ablation Rates on Shock Layer Temperature at P_δ = .30 atm.

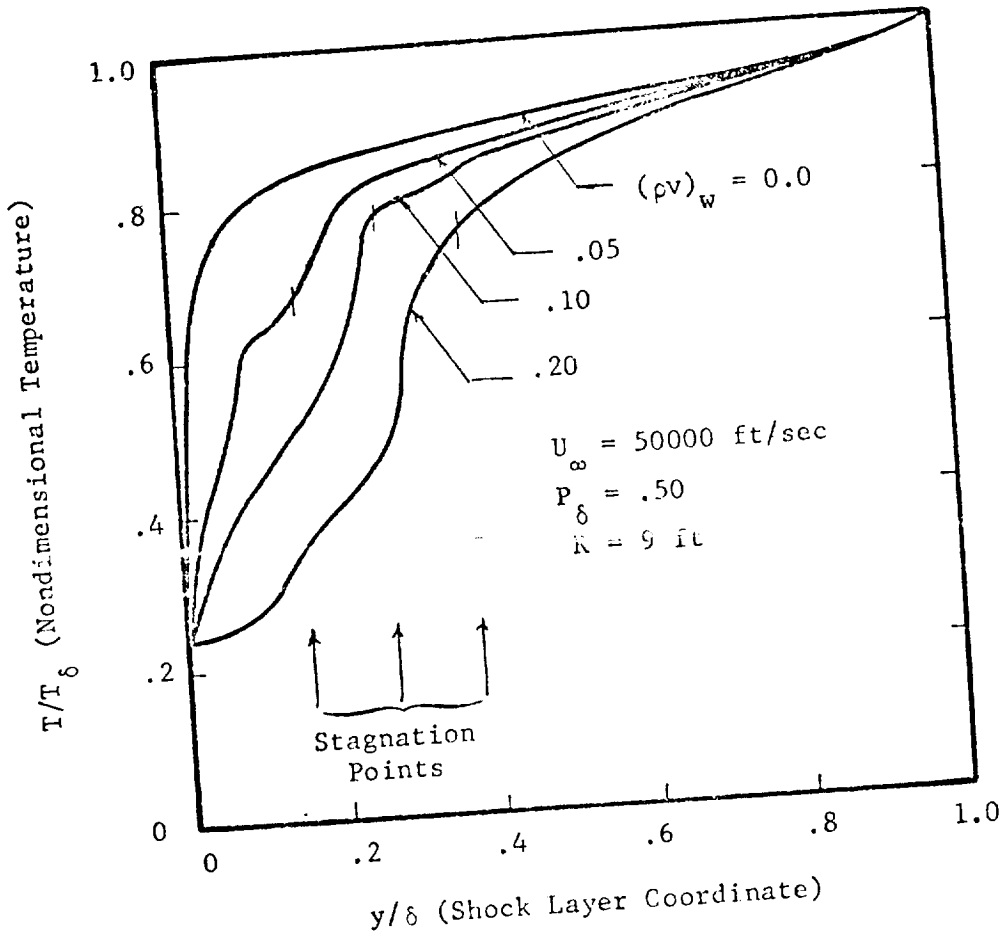

Fig. 5.28 Effects of Ablation Rates on Shock Layer Temperature at P_δ = .50 atm.

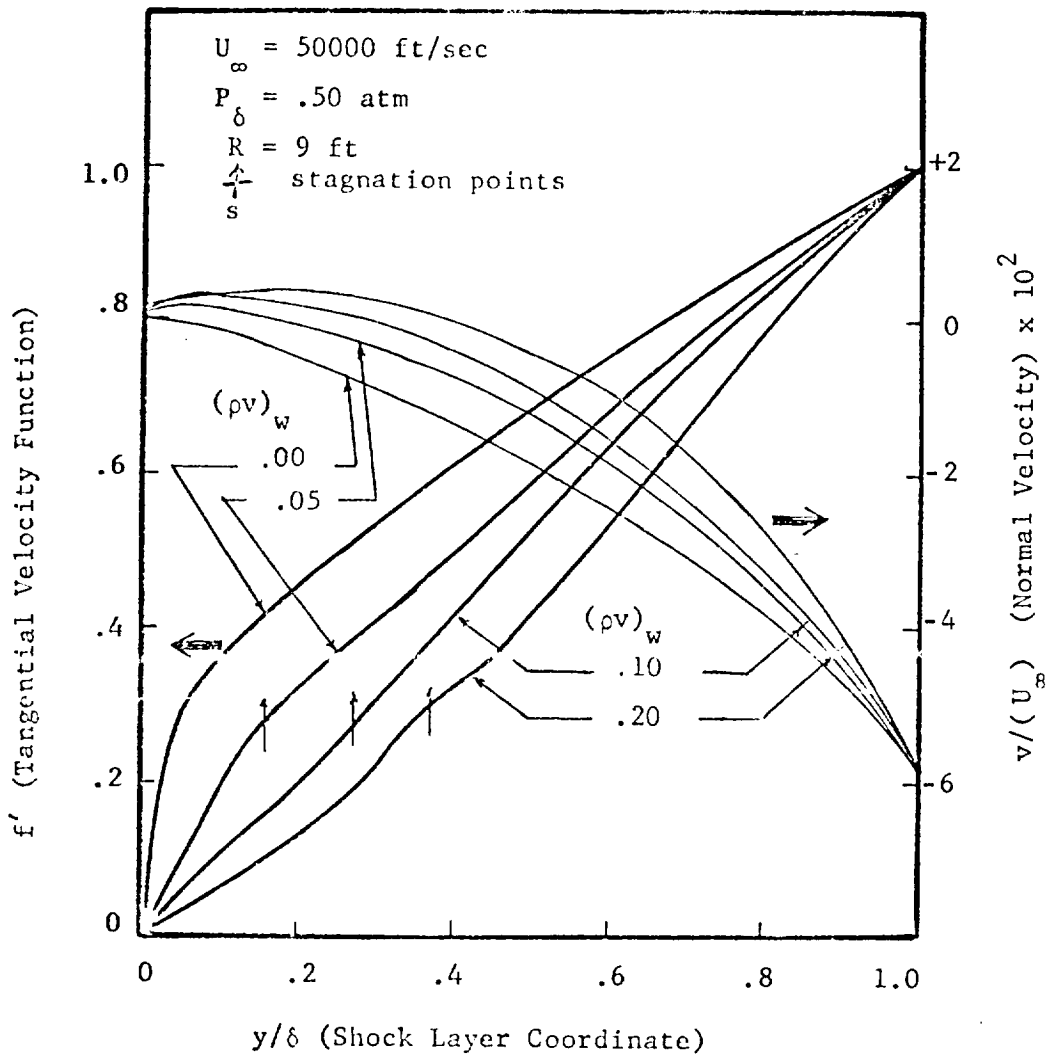

Fig. 5.29 Effects of Ablation Rates on f' and $v/(U_\infty)$ Profiles at P_δ = .50 atm

The character of the f′ profile is changed from one like a boundary layer profile for $(\rho v)_w = 0.0$ to those with mass injection exhibiting linear f′ variations in regions on each side of the stagnation point. The region of significant viscous effects is noted near and on both sides of the stagnation point; this point is indicated by vertical arrows on the f′ profiles. The results in Fig. 5.29 also show a maximum in v/U_∞ profiles between the wall and the stagnation point. This behavior is a result of the density decrease in this region.

RADIATIVE TRANSPORT CHARACTERISTICS

One of the main processes studied in this work is that of radiative energy transfer within the shock layer. The results in this section illustrates the important radiative characteristics observed which determine the radiative heating rates to the body's surface.

The effects of phenolic nylon ablation products on the line and continuum radiative flux to the surface are shown in Tabs. 5.1 and 5.2. The continuum surface flux for the twelve spectral intervals considered is shown in Tab. 5.1. In each spectral interval the magnitude of the flux is given for three different ablation rate cases. By comparing the magnitude of the flux for the three ablation rates in each spectral interval, one observes that the ablation products block most of continuum flux above $h\nu = 8.$ ev. Further, the continuum flux below 5 ev is not absorbed but slightly enhanced by increased ablation rates. Tab. 5.2 presents the line flux counterpart of Tab. 5.1 where the line flux is located in the spectrum at nine

TABLE 5.1

ABLATION PRODUCT EFFECTS ON

CONTINUUM WALL FLUX AT DIFFERENT

SPECTRAL INTERVALS

Frequency interval $h\nu$ (ev)	Continuum Flux* (watts/cm^2)		
	$(\rho v)_w = 0.0$	$(\rho v)_w = .05$	$(\rho v)_w = .10$
0 - 5.	863.9	916.1	935.6
5. - 6.	42.7	43.5	38.8
6. - 7.	26.1	27.8	29.6
7. - 8.	15.9	22.9	11.9
8. - 9.	9.8	7.5	.4
9. - 10.	5.7	10.6	3.2
10. - 10.3	.4	24.2	1.5
10.3 - 11.1	181.4	64.3	58.8
11.1 - 12.0	255.0	.3	.0
12.0 - 13.4	198.8	.1	.0
13.4 - 14.3	17.5	.0	.0
14.3 - 20.0	3.2	.0	.0

* For U_∞ = 50000 ft/sec R = 9 ft

P_δ = .5 atm T_w = 3450°K

TABLE 5.2

ABLATION PRODUCT EFFECTS ON

LINE WALL FLUX IN [illegible] RENT

LINE CENTERS

Frequency center $h\nu$ (ev)	Line Flux* ($watts/cm^2$)		
	$(\rho v)_w = .00$	$(\rho v)_w = .05$	$(\rho v)_w = .10$
1.3	461.7	523.9	487.6
2.7	163.9	185.4	178.2
5.75	.0	15.9	1.0
7.57	282.1	226.5	95.9
9.10	203.8	165.2	79.2
10.4	568.3	95.7	114.0
11.4	85.3	- .1	.0
12.7	- 49.4	.0	.0
13.9	- 9.0	.0	.0

* For U_∞ = 50000 ft/sec R = 9 ft

P_δ = .5 atm $T_w = 3450^oK$

line center frequencies*. At the two lowest frequency line centers the flux is changed only slightly by ablation product injection whereas at larger frequencies the effects are more pronounced. The greatest flux reduction by ablation products is observed at the line center $h\nu$ = 10.4 ev. Thus the nylon phenolic ablation products are the least effective in absorbing energy in the frequency levels below 5 ev. Unfortunately a significant percentage of the radiant energy is shown to be transferred in these lower frequency levels (i.e. 79% for $(\rho v)_w$ = .10).

The solution of the energy equation is directly coupled to the radiative transfer through the radiative flux divergence term in this equation. The radiative flux divergence profiles for zero and 20% ablation rates are shown in Fig. 5.30. It is noted that the effects of ablation products is to reduce both the wall and shock values of the flux divergence. However, the negative area, denoting net absorption, shown in Fig. 5.30 is substantially increased by injection of ablation products. The sharp dip in the profile is evident for both zero and 20% ablation. This sharp change in the profile presents numerical difficulties, if a small step size is not used locally, as discussed in Chapter 4. The small peak near (y/δ) = .38 occurs near the maximum carbon atom concentration and represents small net emission primarily attributed to this species.

The influence of ablation rate on the total line and total

---

* The negative values for line flux for some line groups is a result of line absorption of continuum flux as noted by Ref. 5.6.

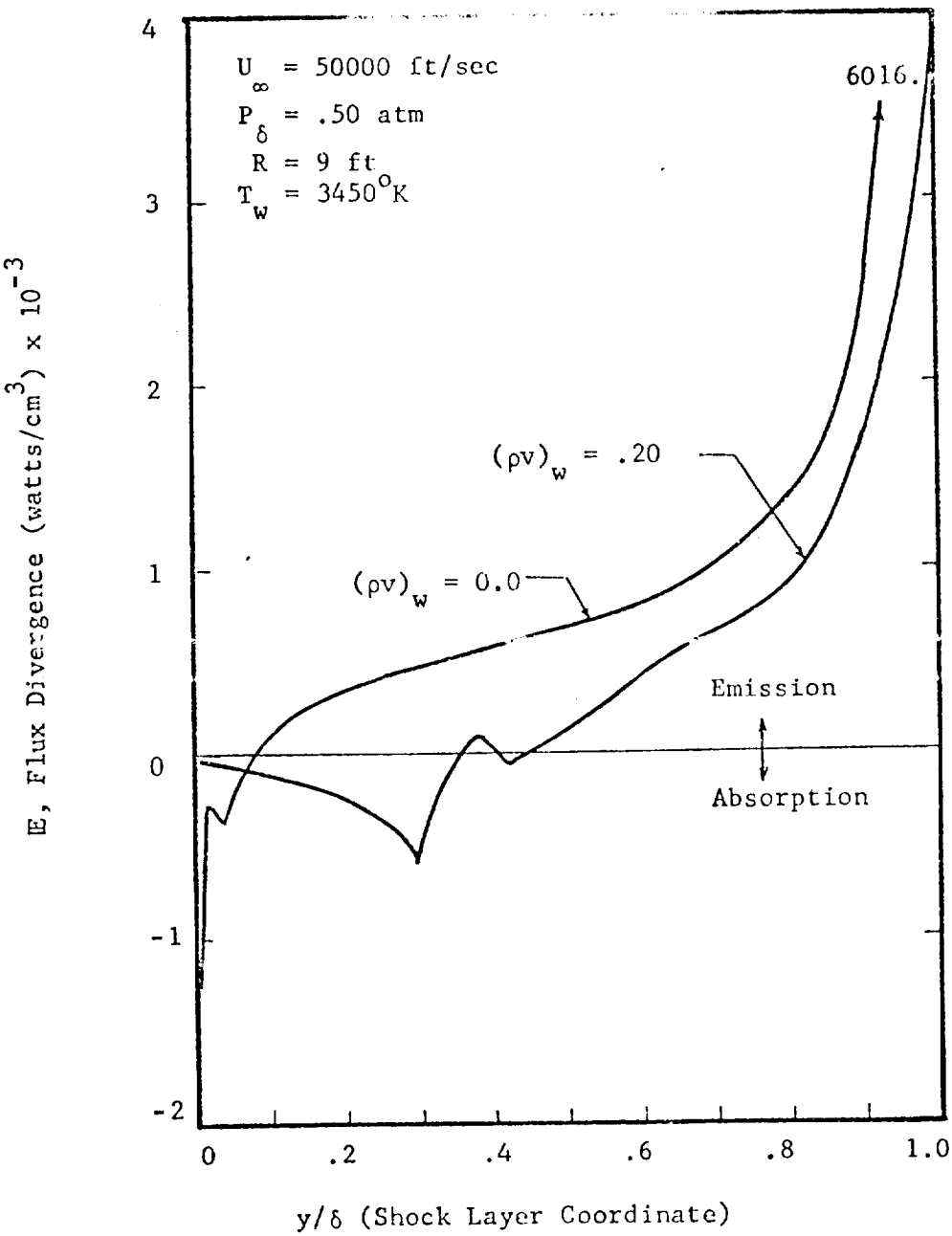

Fig. 5.30 The Effects of Ablation Products on the Radiative Flux Divergence Profile

continuum flux at two locations in the shock layer for two post shock pressure levels are shown in Figs. 5.31 and 5.32. These figures present the line and continuum flux to the surface at $(y/\delta) = 0.0$ and the fluxes toward and away from the surface at stagnation point, $(y/\delta) = (y/\delta)_{v=0}$. In general both the continuum and line flux toward the surface at v = 0 are increased by increasing ablation rates. This is in part due to the flux from the ablation layer to the air layer shown as the lower curves in Figs. 5.31 and 5.32. The upper and lower set of curves gives an indication of the radiative coupling between the ablation and air layer. In a previous section (see Fig. 5.15) it was shown that the total radiative heating to the surface was decreased by increasing the ablation rate. The middle curves of Figs. 5.31 and 5.32 show that both line and continuum contributions to the total flux decrease as a function of increased ablation. However, for the cases shown, increased ablation beyond $(\rho v)_w = .05$ has very little effect on the continuum part of the total flux. Thus regardless of the ablation rate above $(\rho v)_w = .05$ the effectiveness of the ablation products in reducing the total surface heating appears limited by the continuum radiative processes.

It has been demonstrated in previous sections that the post shock pressure is quite important in determining radiative heating rates. To illustrate the pressure dependence of the line and continuum parts of the radiative flux, Fig. 5.33 was prepared. The line and continuum flux toward the body at v = 0 and the resulting two parts which arrive at the surface are shown in the lower half of

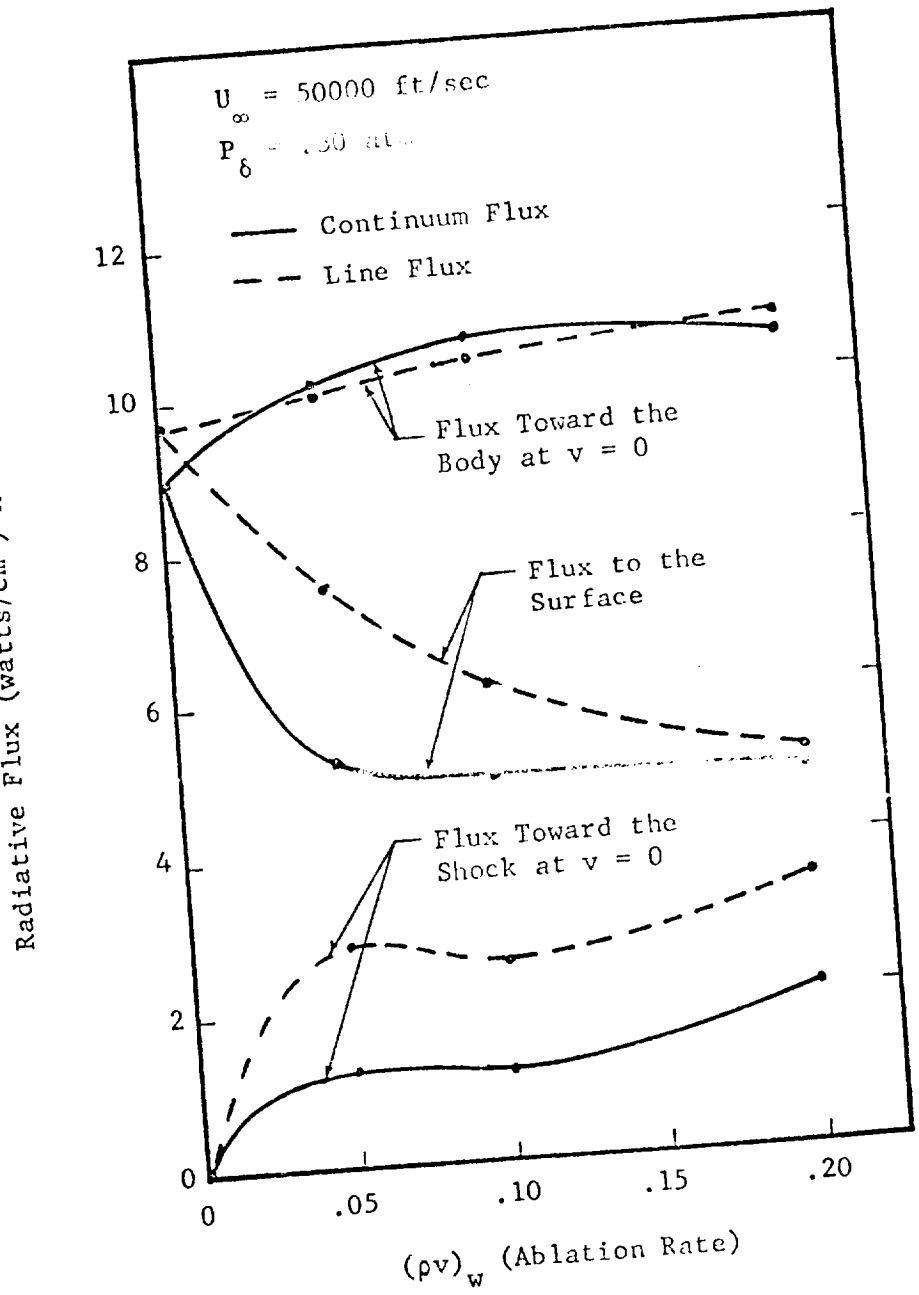

Fig. 5.31 Line and Continuum Flux Dependency on Ablation Rate at P_δ = .30 atm

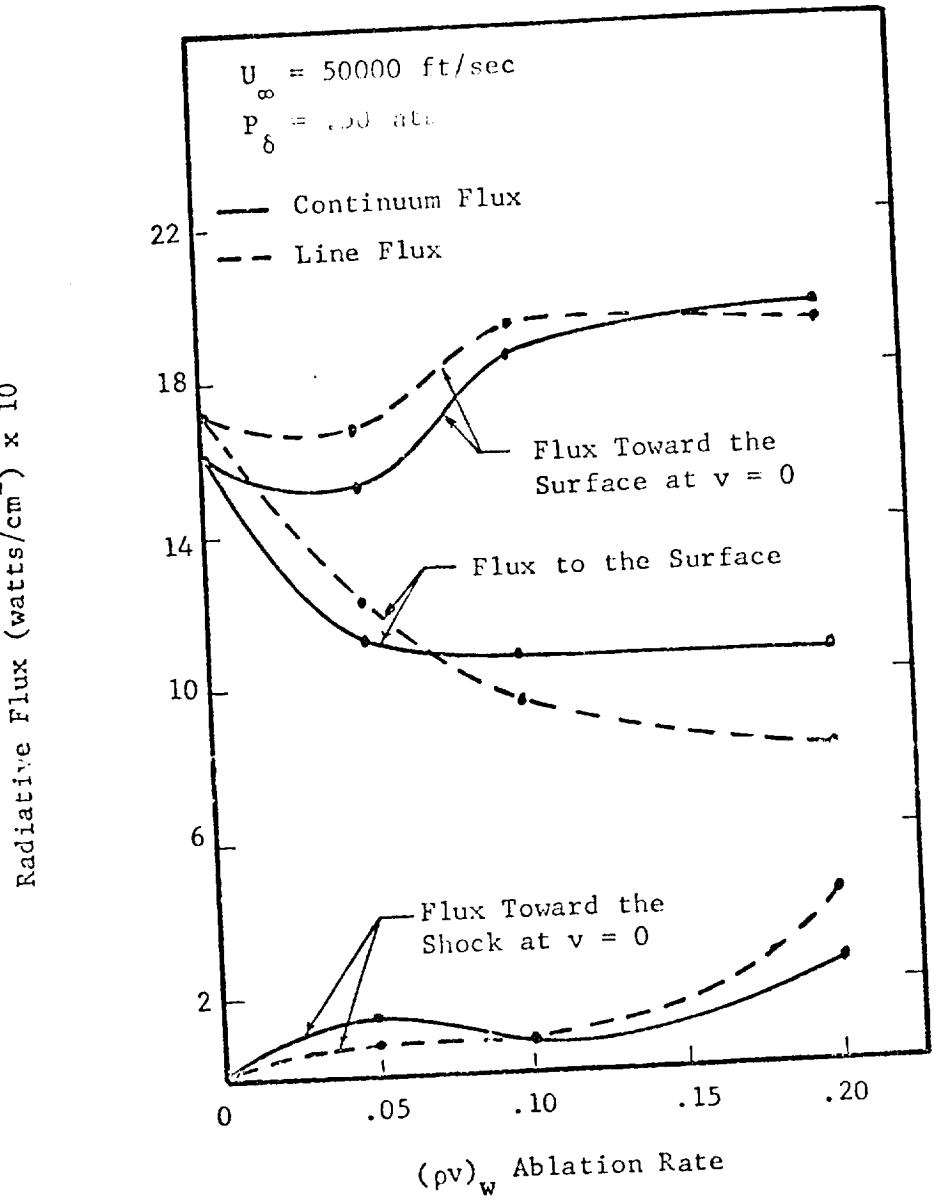

Fig. 5.32 Line and Continuum Flux Dependency on Ablation Rate at P_δ = .50 atm

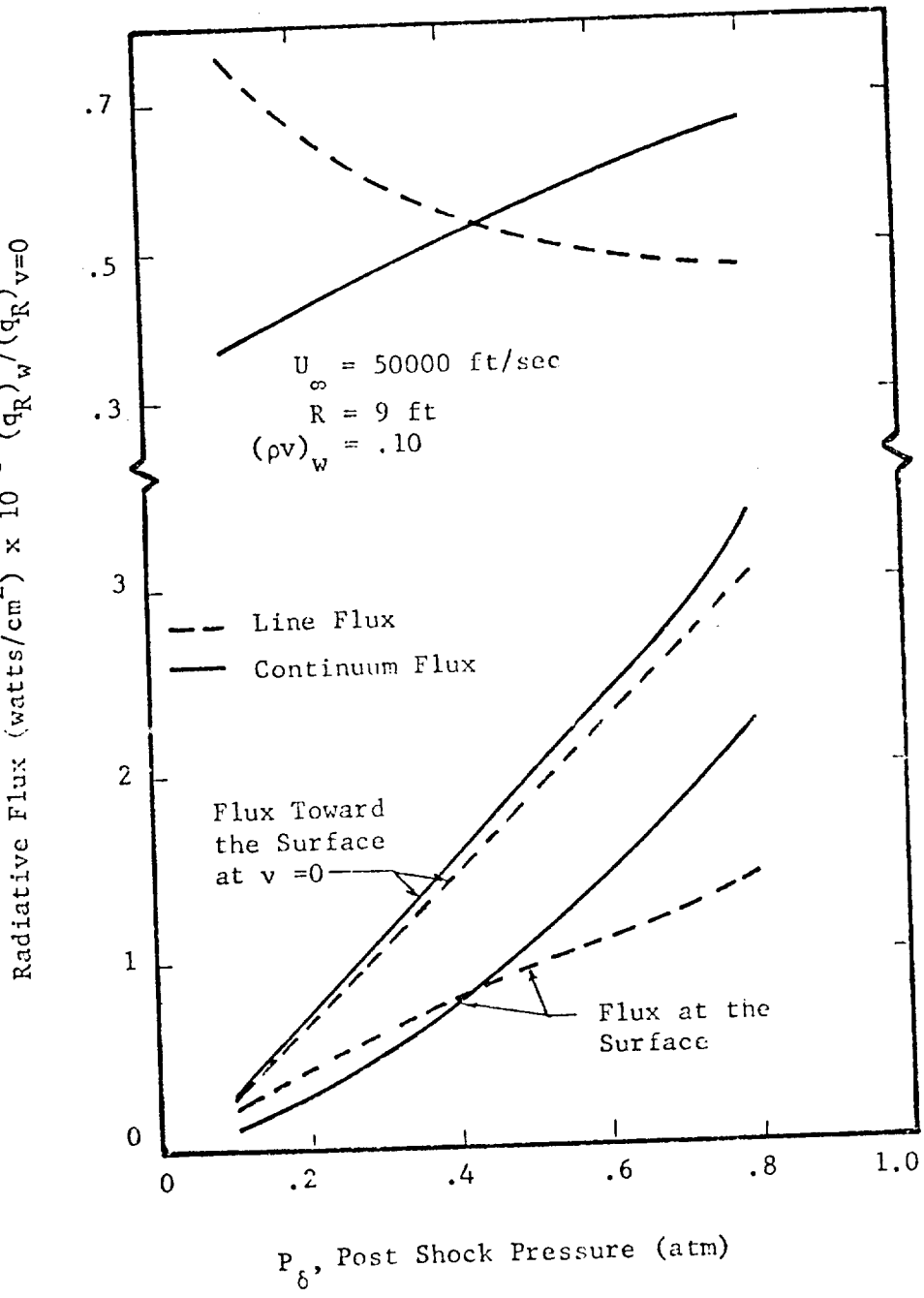

Fig. 5.33 Wall and Stagnation Point Flux as a Function of Post Shock Pressure

Fig. 5.33. These results demonstrate several important effects. In the pressure range considered, the line and continuum flux toward the body at v = 0 vary approximately linearly with pressure. Also the line flux at the wall shows a near linear dependency. The continuum surface flux, however, is lower than the surface line flux at lower pressures and increases nonlinearly to values larger than the surface line flux at higher pressures. This cross over effect with pressure is seen quite clearly from the results in the upper half of Fig. 5.33. The two curves shown are for the line and continuum ratios of the respective flux at the wall, $(q_R)_w$, divided by the respective flux at the stagnation point, $(q_R)_{v=0}$. These curves show, that for a constant ablation rate, line radiation through the ablation layer is attenuated less at low pressures than at higher pressures and the converse is true for continuum radiation. This effect is the reason for the minimum in nondimensional total radiative heating rate curves of Fig. 5.16 as illustrated for one ablation rate in Fig. 5.34. Furthermore, since the continuum flux is essentially unaffected by ablation rates above $(\rho v)_w = .05$ as indicated in Figs. 5.31 and 5.32 the continuum mode for radiant energy transfer is the predominate mode of heating for ablator coupled shock layers at the higher pressure levels considered.

In Chapter 3 an effort was made to select the molecules which would have an effect on the radiative transport. A shock layer calculation was made to assess the importance of including molecules in the radiation calculation. The results shown in Fig. 5.35 indicate

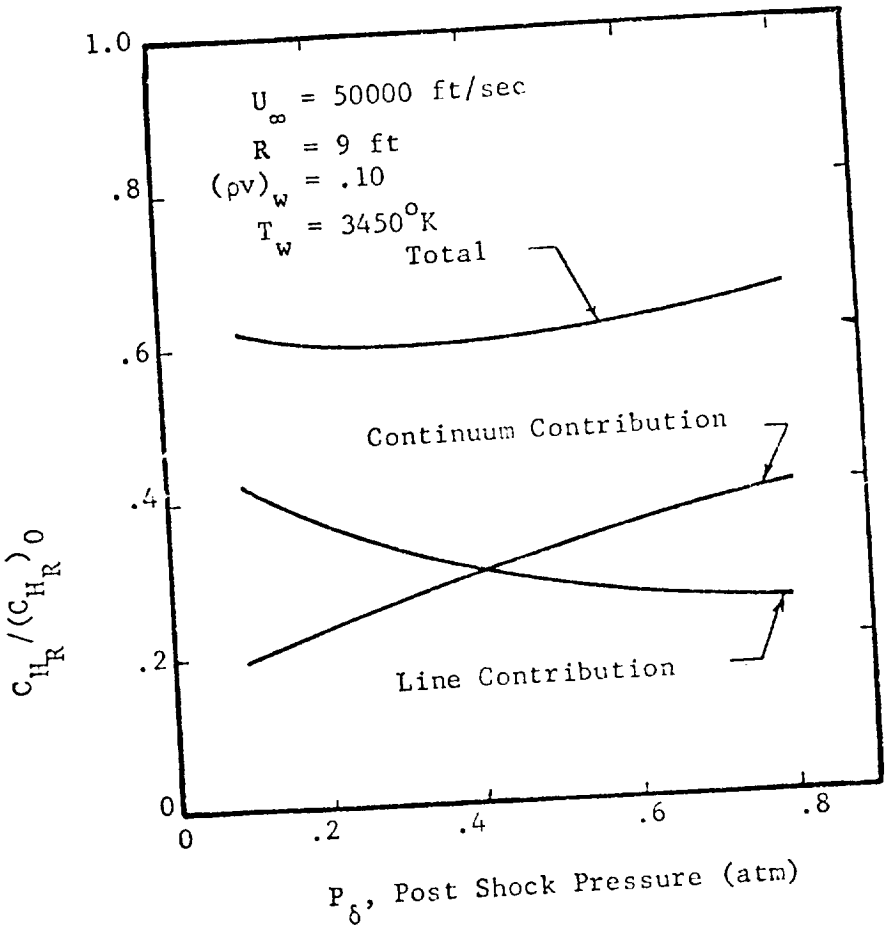

Fig. 5.34 Line and Continuum Contributions to Total Radiative Heating for $(\rho v)_w$ = .10

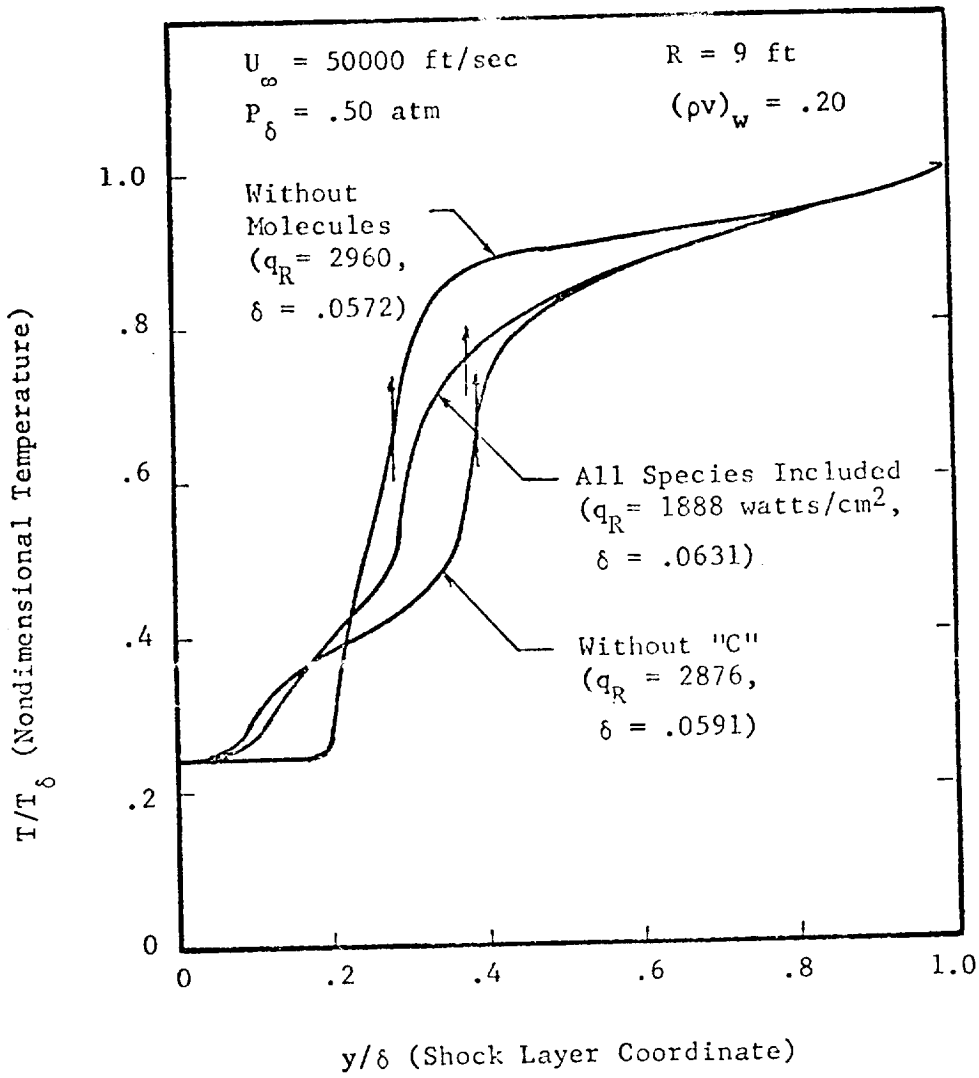

Fig. 5.35 Effects of Carbon Atom and Molecular Radiative Coupling on the Temperature Profile

that the role of molecular radiation is quite important which is in contrast with the assessment made in Ref. 5.6. Excluding molecules in the radiation calculation increased the heating by about 56 percent, reduced the stand-off distance and significantly altered the shock layer temperature profile. It is also noted that the stagnation point is moved toward the body and no rise in the temperature profile near the wall is observed. The assessment of molecular radiation in Ref. 5.6 was made with an uncoupled analysis (i.e. using a temperature profile from a solution not including molecules). This resulted in a small change in total radiative heating and consequently the effects of molecular radiation were considered negligible. The present results show that although the radiant heating may be only slightly changed by molecules for a given temperature profile, the molecular radiation coupling to the temperature profile is significant. The final effect of this coupling is to appreciably change the temperature profile and corresponding shock layer properties and thus change the surface heating significantly.

The results presented in Fig. 5.35 also illustrate the importance of neutral carbon radiation. A 52 percent increase in surface heating results from not including the neutral carbon atoms but including all other species in the radiation calculation for the case studied. Carbon and hydrogen line radiation was not included in the calculations of Ref. 5.10. Smith et. al. (Ref. 5.10) compared their heating rate results for phenolic nylon ablation to results for carbon phenolic of Rigdon et. al. (Ref. 5.5) which includes line

carbon and hydrogen radiation for identical conditions and found the heating rates of (Ref. 5.10) to be substantially larger. The importance of the carbon radiation alone shown in the present investigation suggests that the major difference in these reported results may well be attributed to the differences in species included in their respective radiation models.

Radiative transport results for zero ablation are presented in Fig. 5.36 and 5.37. A maximum in the line contribution to the total surface heating at approximately P_δ = .35 atm. is shown in the upper plot of Fig. 5.36. This behavior is different than the ablation attenuated line contribution to the surface heating seen in Fig. 5.34. The lower plot indicates that the line contribution is larger at the lower free stream velocities than at higher ones. It is also noted that over the entire pressure and velocity ranges considered both line and continuum radiation processes contribute significantly to the total surface heating.

Total radiative heating rates for zero ablation obtained from the present analysis are compared in nondimensional form with results of other investigators in Fig. 5.37. The present results correlates quite well with the radiative cooling parameter, Γ, and lies between the results of two inviscid shock layer analyses (Refs. 5.7 and 5.14). All of the shock layer results presented in Fig. 5.14 lie below the transparent gas theory results of Ref. 5.7. As pointed out by Page et. al. in Ref. 5.7 the transparent theory is not adequate for predicting heating since the true optical properties of the shock

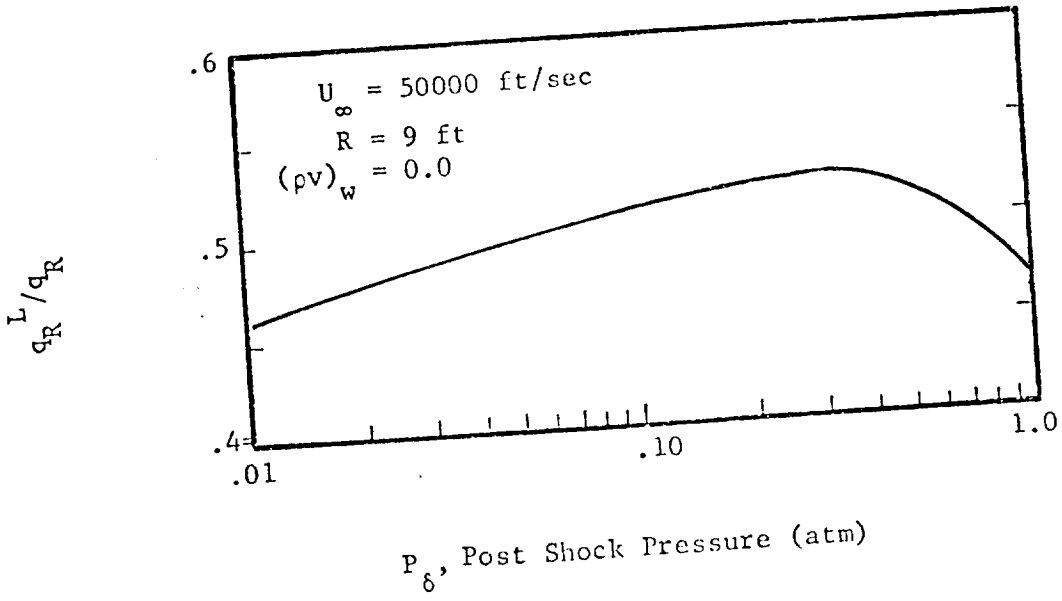

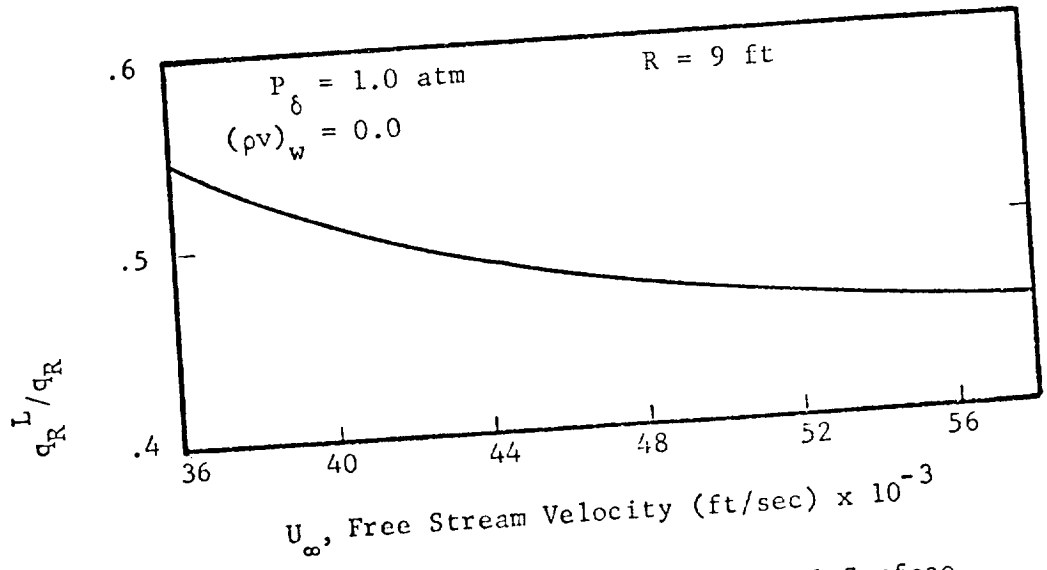

Fig. 5.36 Line Contribution to the Total Surface Flux for $(\rho v)_w = 0.0$

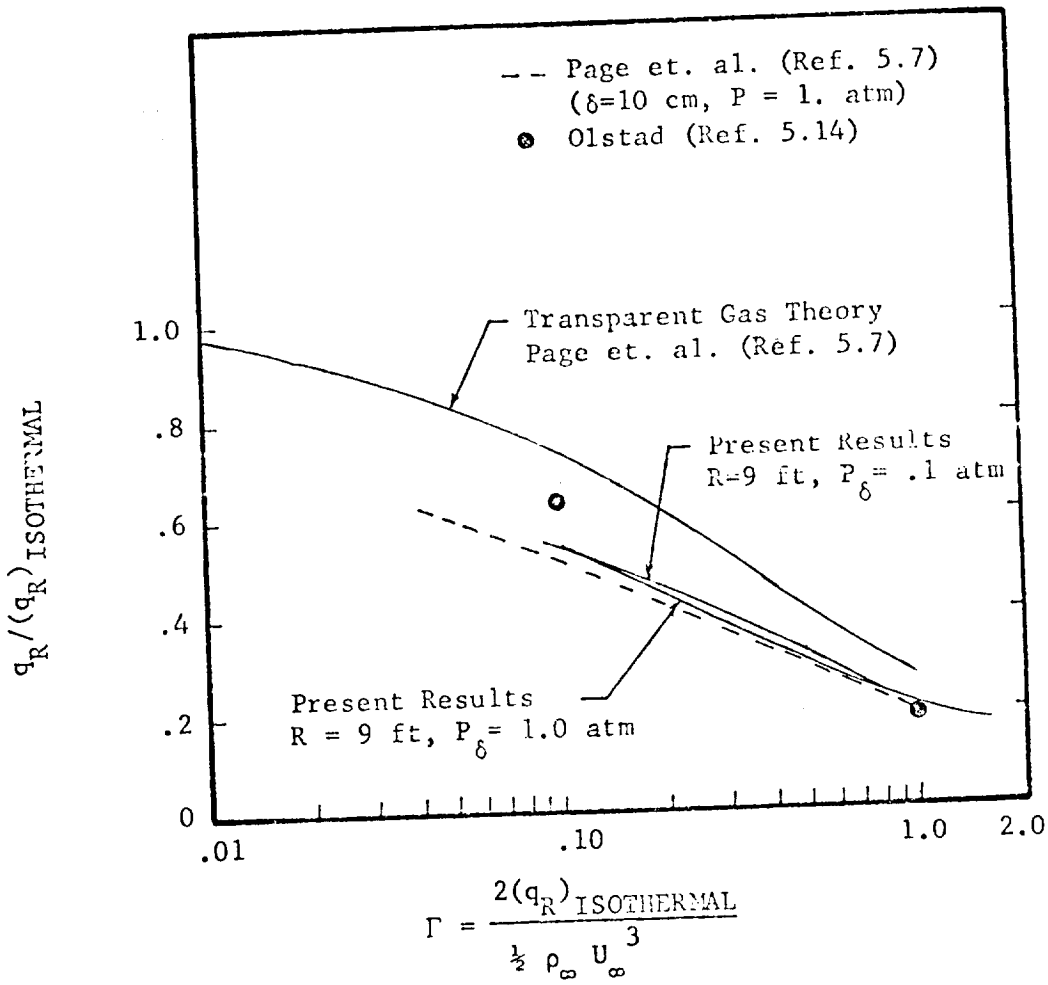

Fig. 5.37 Nonblowing Radiative Cooling Parameter Results

layer are not uniformly optically thin. The important point illustrated in Fig. 5.37 is that the radiative heating for zero ablation can be correlated with a single parameter, Γ, and that both viscous and inviscid analyses yield similar results. The success of this correlative parameter, which is the basis of the RADCOR program calculations, leads to speculation that perhaps a correlation which includes ablation product coupling might be developed.

An attempt was made to determine if the heating rate results of the present work both with and without ablation could be correlated with shock layer parameters. Some of the difficulties encountered are shown in Fig. 5.38. First, the results show that the heat transfer coefficient for the zero ablation cases are correlated rather well by the cooling parameter as expected from the results in Fig. 5.37. The constant ablation rate lines for U_∞ = 50000 ft/sec exhibit an analogous shape and relationship to the zero ablation line as that shown in Fig. 5.14. It was illustrated in the second section of this chapter that C_{H_R} was not a simple function of ablation rate that could be represented by one curve. Thus an appropriate means of reducing the zero ablation curve and the three curves for different ablation rates at U_∞ = 50000 ft/sec has not been found. Moreover, results for a constant pressure, P_δ, and ablation rate for various free stream velocities shown in Fig. 5.38 quite obviously indicates that varying P_δ at constant U_∞ has a different effect on heating than varying U_∞ at constant P_δ when both are done at the same ablation rate. This is different from the zero ablation cases.

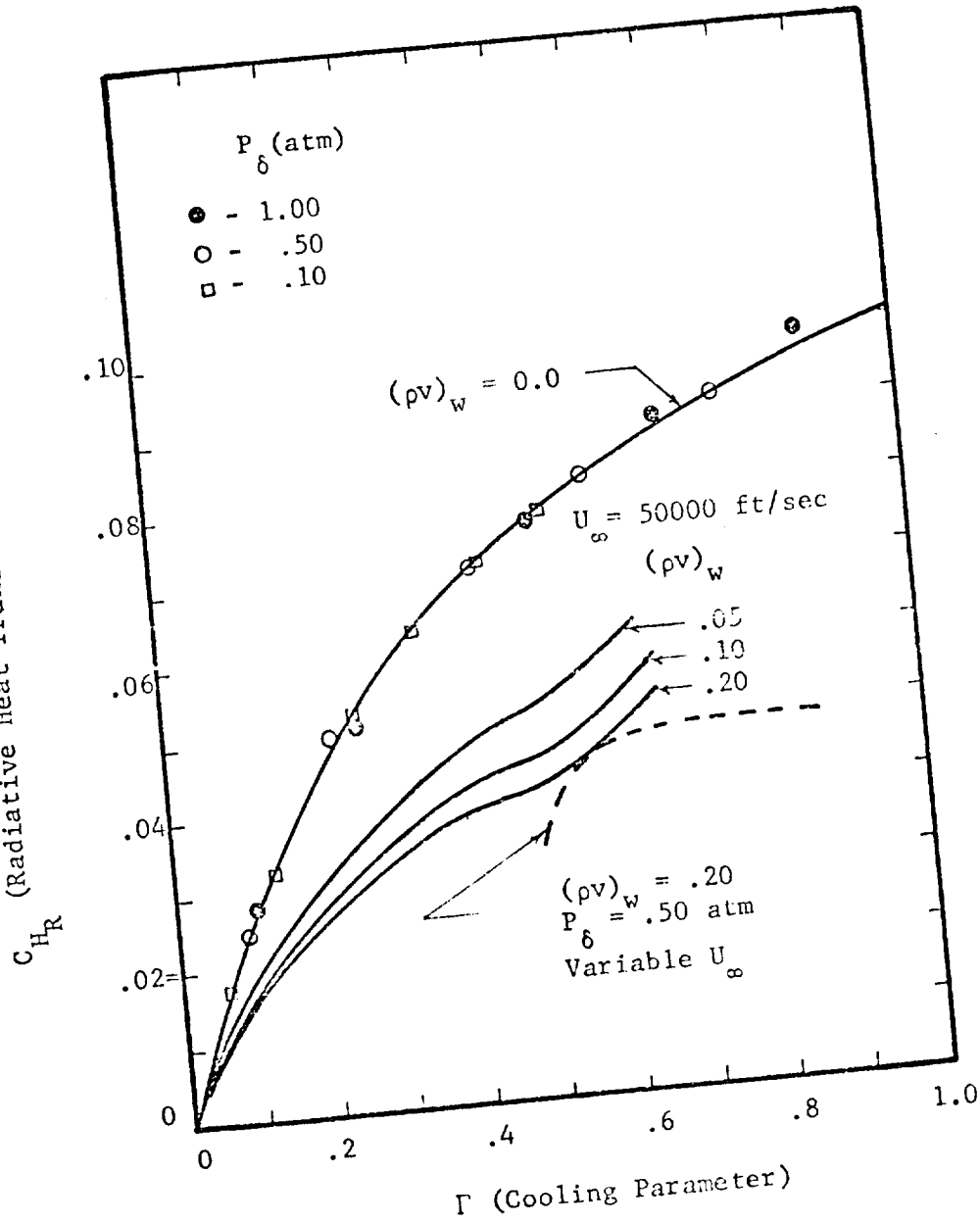

Fig. 5.38 Correlative Effects of the Radiative Cooling Parameter for Several Ablation Rates

Beyond the effects shown in Fig. 5.38 the body radius may also be important in ablation coupled problems. Thus it is concluded that at least two parameters, excluding radius effects, in addition to the radiative cooling parameter would be required to correlate the radiative heating results presented.

HEATING RATES FROM COOLING PARAMETER CORRELATIONS

The complex nature of the shock layer at the stagnation line has been amply demonstrated in previous sections. It is highly desirable to be able to rapidly estimate shock layer heating rates in addition to being able to perform detailed shock layer computations. Accordingly, this section presents radiative heating rate results based on a radiative cooling parameter correlation which permits hand calculations of hyperbolic entry heating. The results presented were computed using the RADCOR computer program documented in Appendix E. The RADCOR program was also used to compute heating rates for a 100% CO_2 atmosphere to demonstrate the effects which may be realized by entry into atmospheres typical of Mars or Venus.

It was shown in the previous section that the radiative heating rates for no ablation were correlated quite well by the radiative cooling parameter. Fig. 5.39 presents a comparison of results from the present shock layer calculations with a correlation equation from Livingston and Willard (Ref. 5.15). The shock layer results show only a small pressure dependence and are slightly above the correlation. Heating rate results from using the correlation are certainly within the present uncertainty limits, i.e. $\pm$ 10%, of

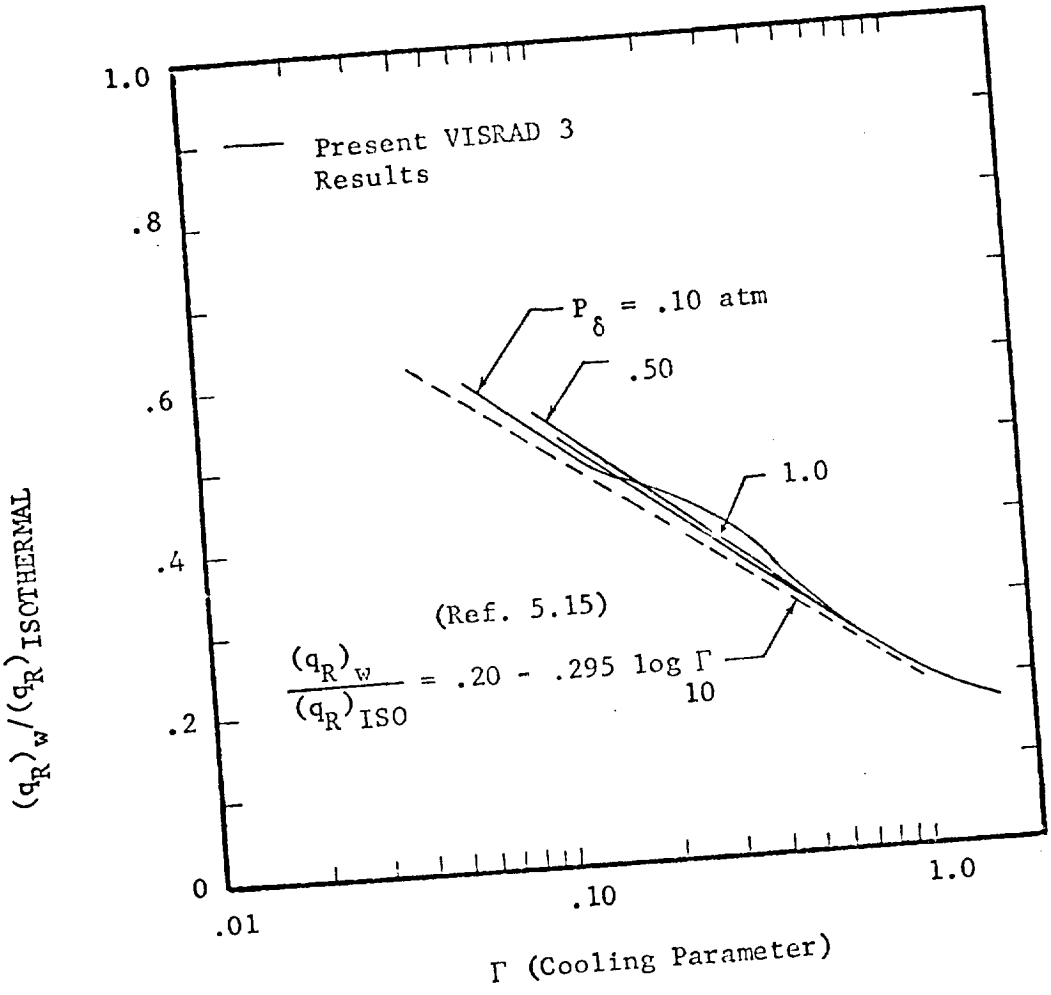

Fig. 5.39 Comparison of Cooling Parameter Correlation and Present Results

current shock layer results as demonstrated in Fig. 5.10. Therefore, the use of the cooling parameter correlation to compute radiative heating rates for preliminary design work appears justified.

A set of figures which can be used for hand calculations of radiative heating rates were developed using the RADCOR program and are designated as Figs. 5.40 to 5.45. These figures present the radiative heat transfer coefficient as a function of free stream velocity for seven post shock pressures from .05 to 2.0 atmospheres. Each of the six figures is for a specific body radius ranging from 1.0 to 11.0 feet.

Given a specific trajectory, defined by ρ_∞, U_∞ and time, and a body radius, a heating rate history can be developed from Figs. 5.40 to 5.45. The heating rate for one point in a trajectory is determined by using U_∞ and P_δ and reading C_{H_R} from the figure for the appropriate body radius. The actual heating rate can then be computed from the definition of C_{H_R} using ρ_∞ and U_∞. The required values for the post shock pressure, P_δ, are usually computed from ρ_∞ and U_∞ in the trajectory analysis. However, if the normal shock information for P_δ is not readily available, Fig. 2.7 can be used to obtain P_δ from the free stream conditions. This process may be repeated for selected points in a trajectory resulting in a radiative heating rate history similar to that shown in Fig. 5.13. Graphical integration of the heating rate curve yields the total heating load at the stagnation point neglecting ablation effects.

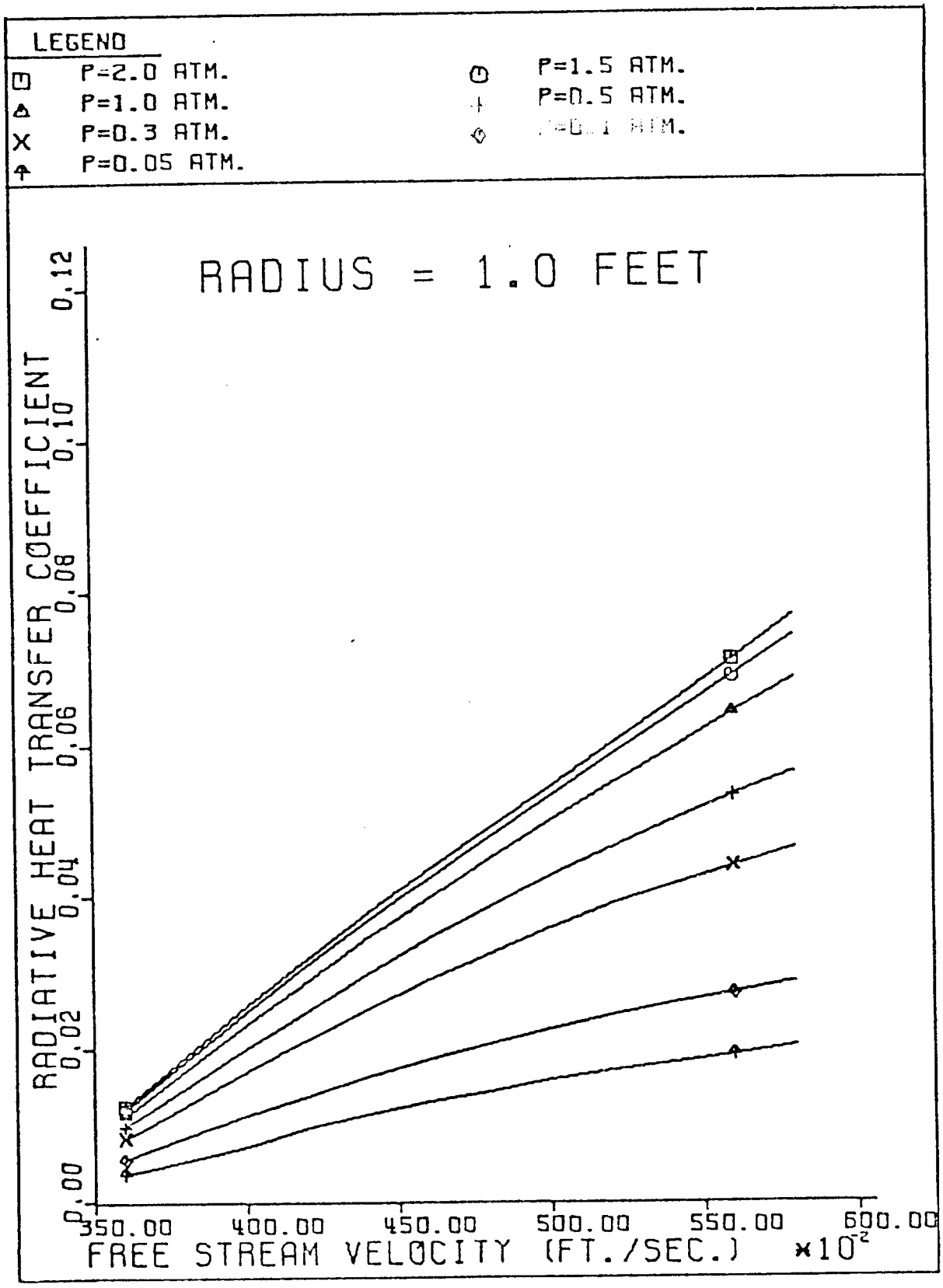

Fig. 5.40 RADCOR Radiative Heat Rate Results for a Body Radius = 1.0 Feet

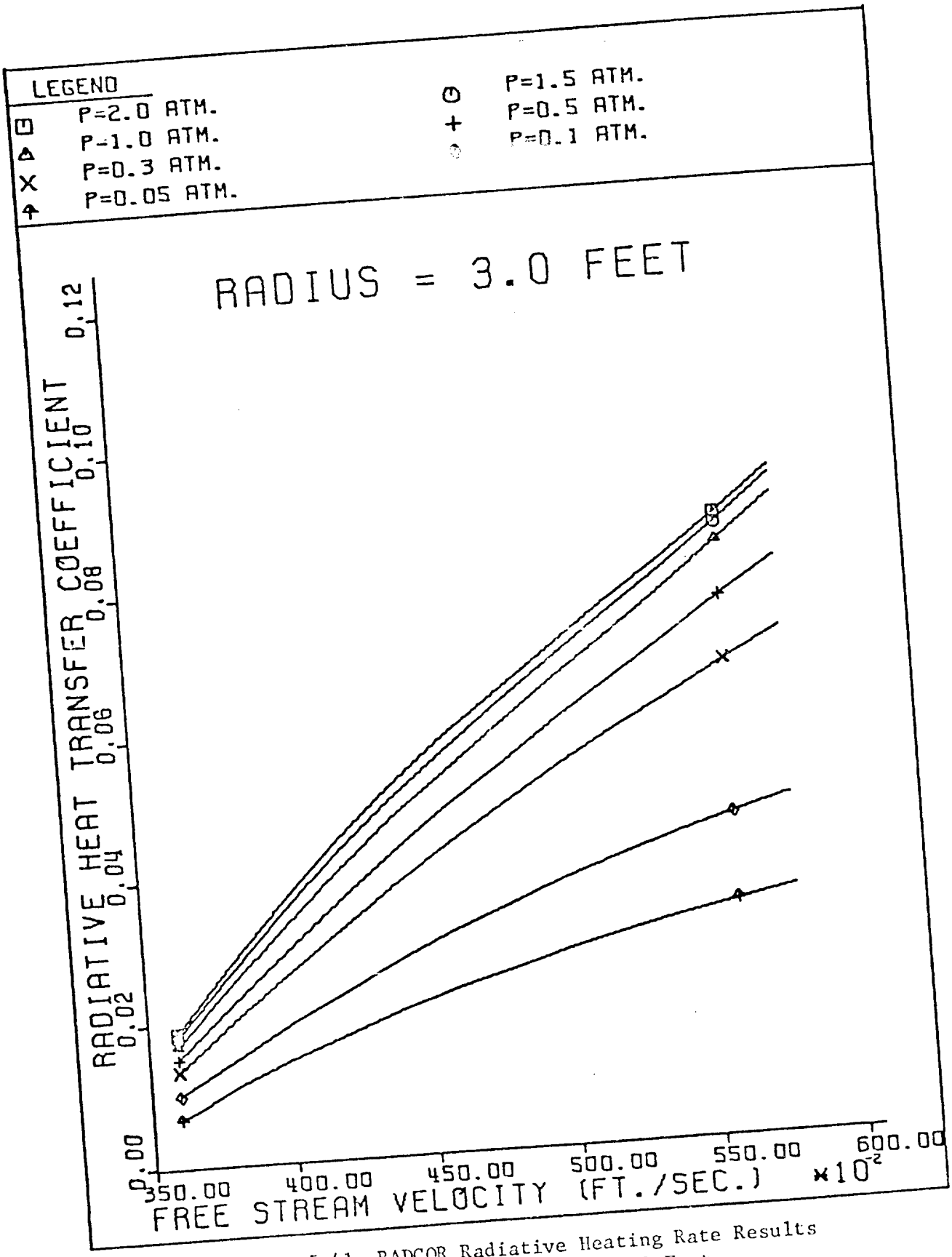

Fig. 5.41 RADCOR Radiative Heating Rate Results for a Body Radius = 3.0 Feet

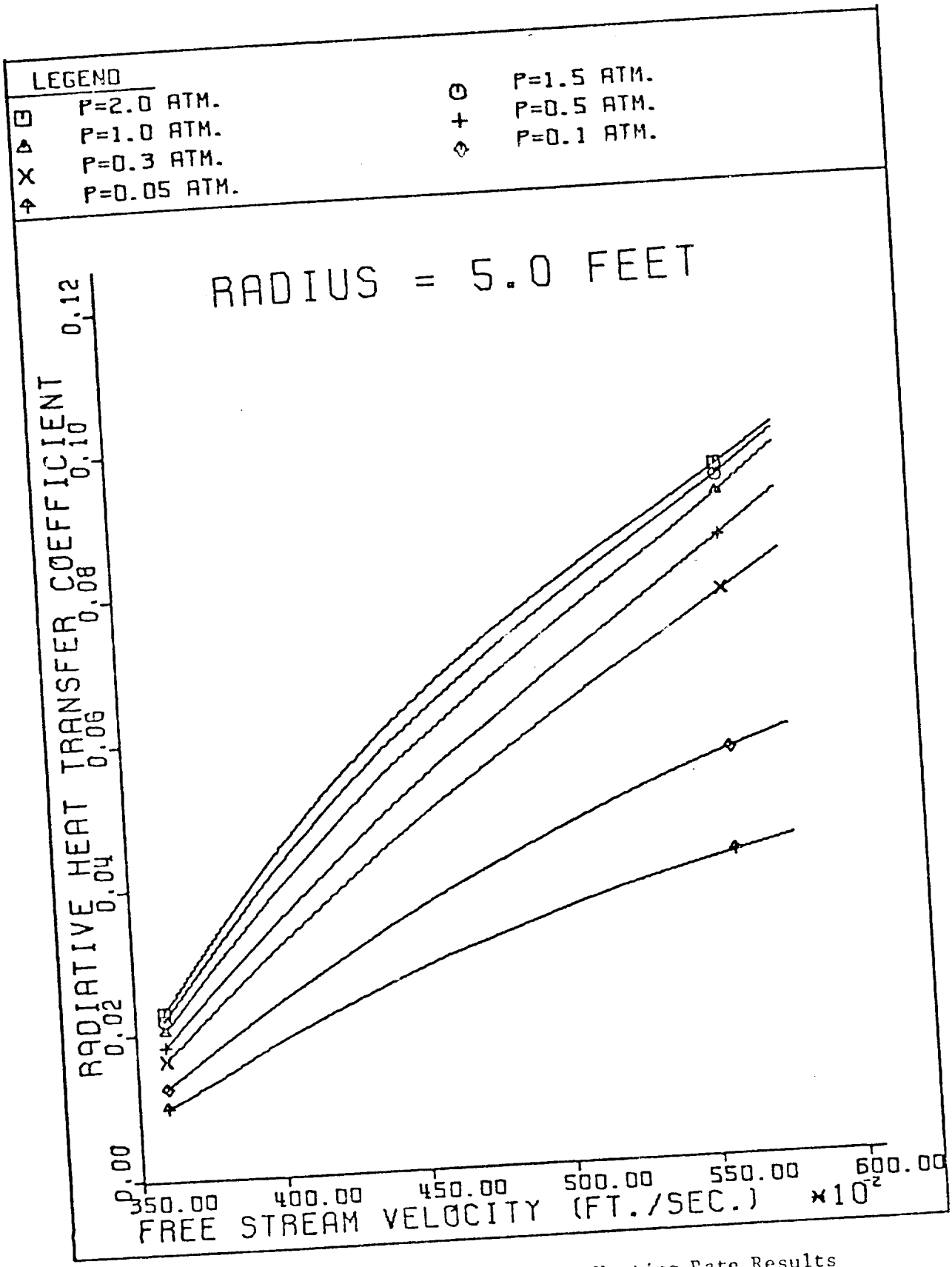

Fig. 5.42 RADCOR Radiative Heating Rate Results for a Body Radius = 5.0 Feet

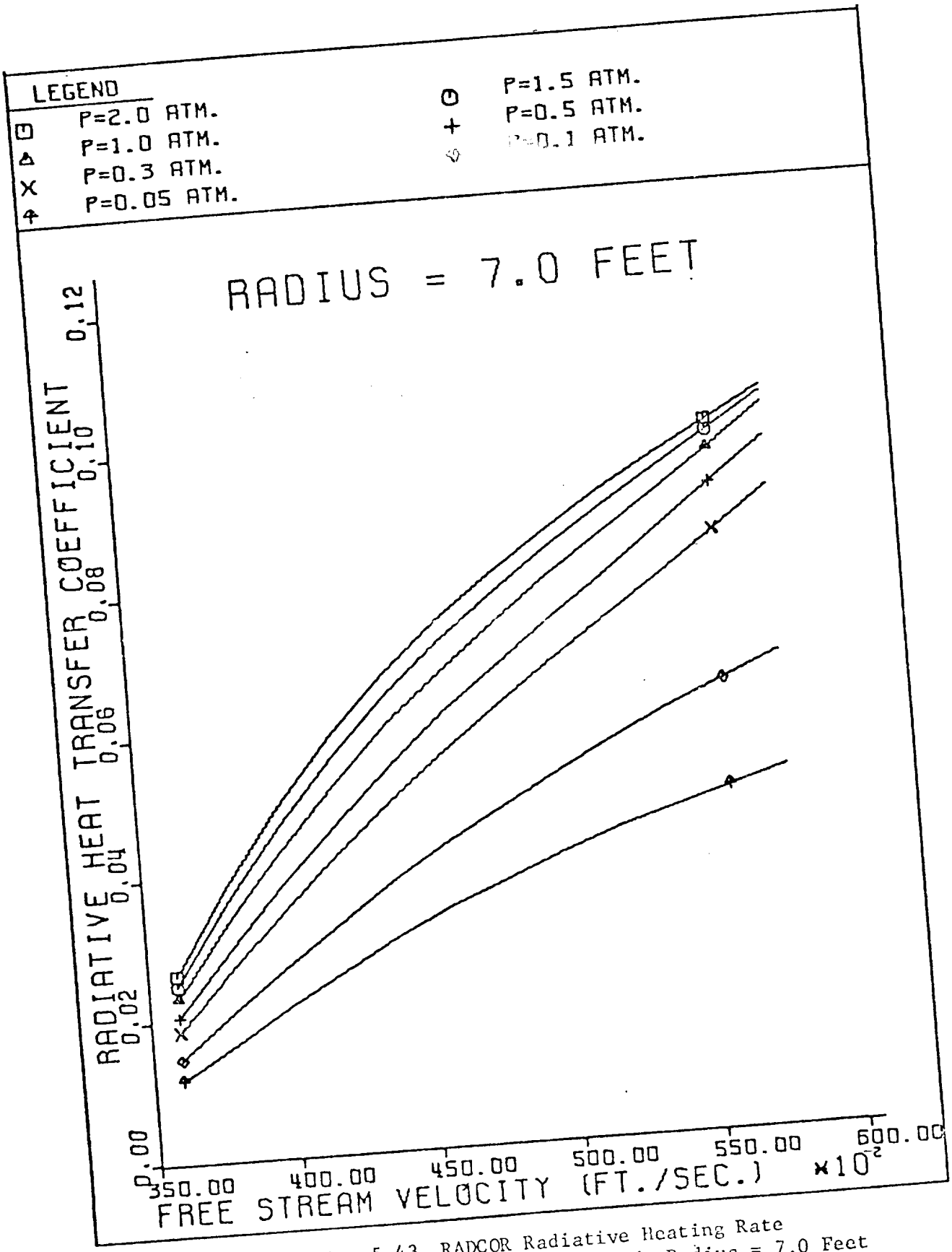

Fig. 5.43 RADCOR Radiative Heating Rate Results for a Body Radius = 7.0 Feet

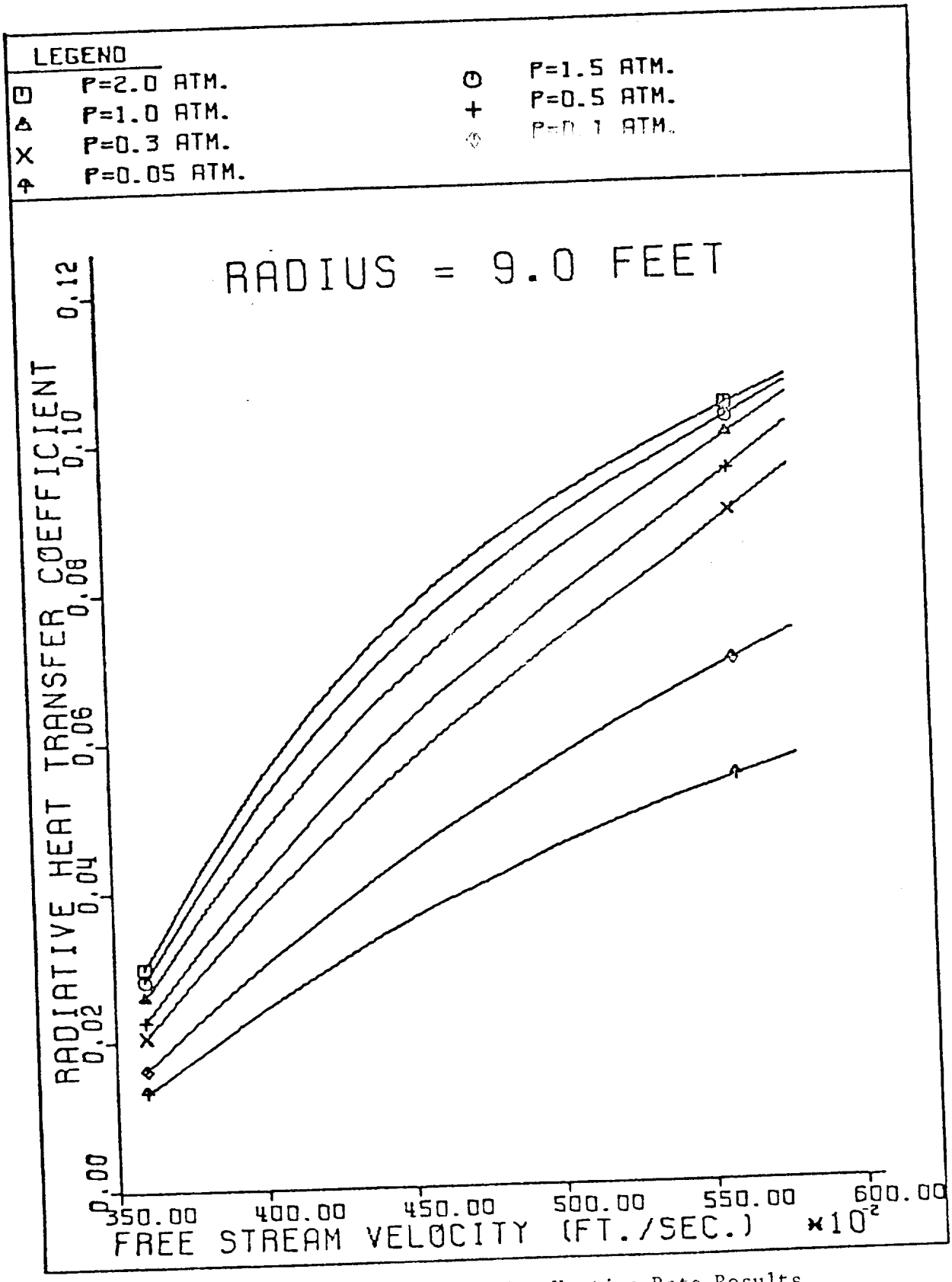

Fig. 5.44 RADCOR Radiative Heating Rate Results for a Body Radius = 9.0 Feet

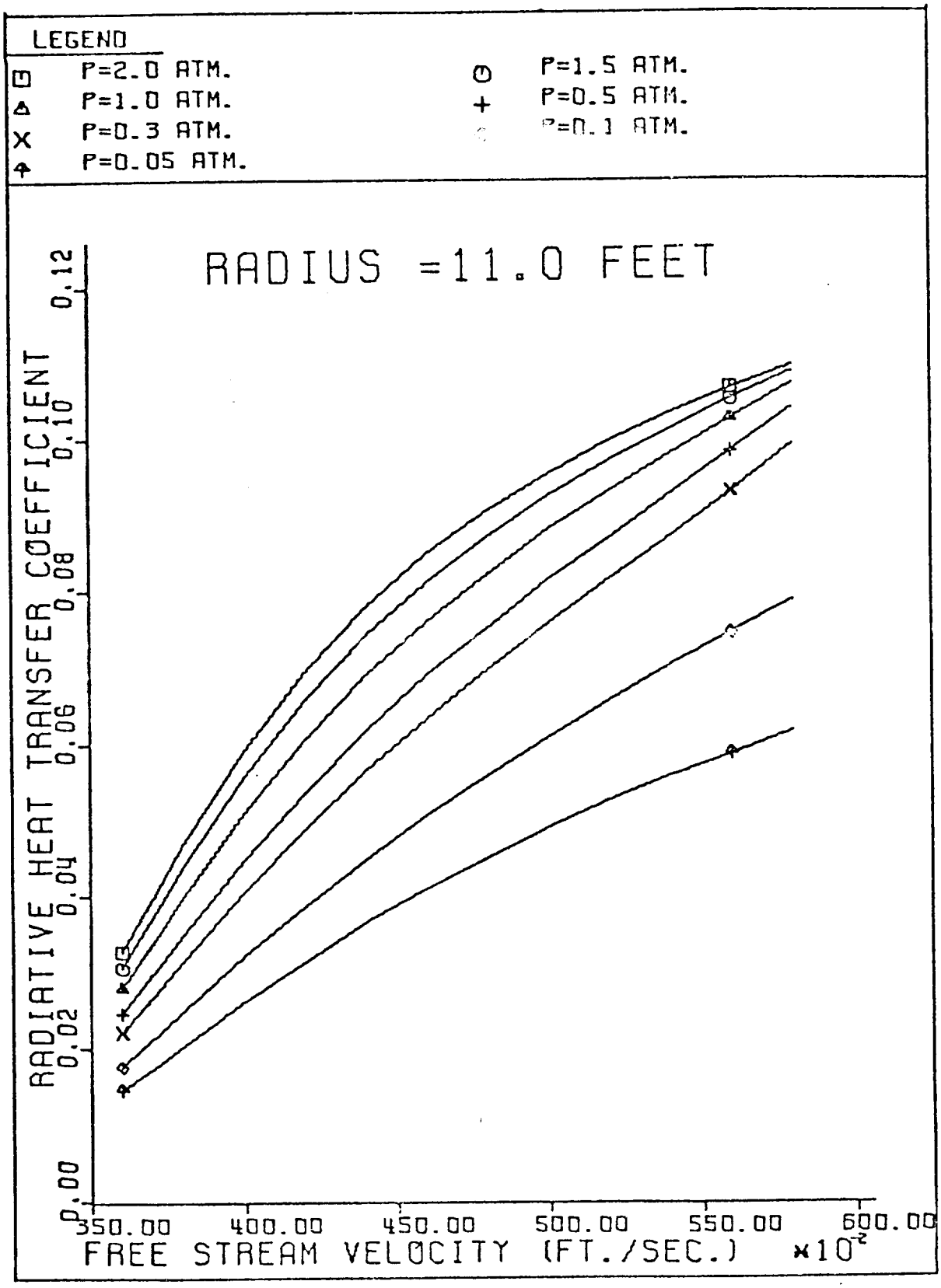

Fig. 5.45 RADCOR Radiative Heating Rate Results for a Body Radius = 11.0 Feet

An estimate of ablation adjusted heating rates may be made using Fig. 5.16 and 5.17. If quasi-steady ablation appears appropriate for the conditions under consideration, sufficient information is presented herein to estimate ablator coupled heating rates and ablation rates. From the results presented in Figs. 5.16, 5.17, and 5.18, setting $C_{H_R}/(C_{H_R})_0 = .7$ for all values of P_δ and U_∞ would yield a conservative estimate of the ablator-shock layer coupling. Ablation adjusted heating rates could then be computed using $C_{H_R}/(C_{H_R})_0 = .7$. An estimate of the ablation rate can then be made using Fig. 3.4. Finally, the total mass loss can then be estimated by graphical integration of an ablation rate verses time plot. This procedure may be useful in defining a body size and ranges flight condition for more detailed analysis. The radiative cooling correlation has been used by Livingston and Williard (Ref. 5.15) and Stickford (Ref. 5.16) to calculate stagnation point heating rates for atmospheres containing different percentages of CO_2 and N_2. The radiative cooling parameter correlation was shown to predict experimentally measured radiative heating rates within the scatter of the data for both air and a 90% CO_2 - 10% N_2 atmospheres. The experimental heating rate data was obtained for a 5 inch diameter hemisphere and a 1.25 in. diameter truncated cylinder in a shock tube. Data was taken over a free stream velocity range of 18,000 to 30,000 ft/sec and a post shock temperature of 7,500 to 15,000^{o}K and pressure range 1.0 to 7.0 atmospheres. Thus, although the free stream velocities are lower than those considered in the present work,

the post shock conditions are similar. The agreement between theory and data shown by Ref. 5.15 lends validity to the use of the cooling parameter correlation in the present work. Furthermore, extension of the present work using the RADCOR program to include CO_2 - N_2 atmospheres is justified by the agreement of these results.

To illustrate the difference in radiative heating rates resulting from different atmospheres Fig. 5.46 was prepared. The results shown are for air and 100% CO_2 at the same post shock conditions which correspond to a representative flight condition for Venus entry. The radiative heat transfer coefficient is given as a function of stand-off distance which, of course, is a function of body radius. The results show a much larger radiative heating for the 100% CO_2 atmosphere than for air at the specified conditions. Further, the heating rate increases more rapidly for air as a function of stand-off distance than for 100% CO_2.

CHAPTER CLOSURE

To recapitulate, stagnation line shock layer solutions were presented for various specified ablation rates and for coupled ablator-shock layer conditions. The characteristics of radiation and ablation coupling in the shock layer were quantitatively shown and discussed. These characteristics included the radiation and ablation effects on the stand-off distance, temperature profile, velocity profile and radiant heating. A simplified heating rate calculation method, based on the radiative cooling parameter, was used to develop a set of graphs which can be used to make hand calculation estimates of hyperbolic entry heating rates.

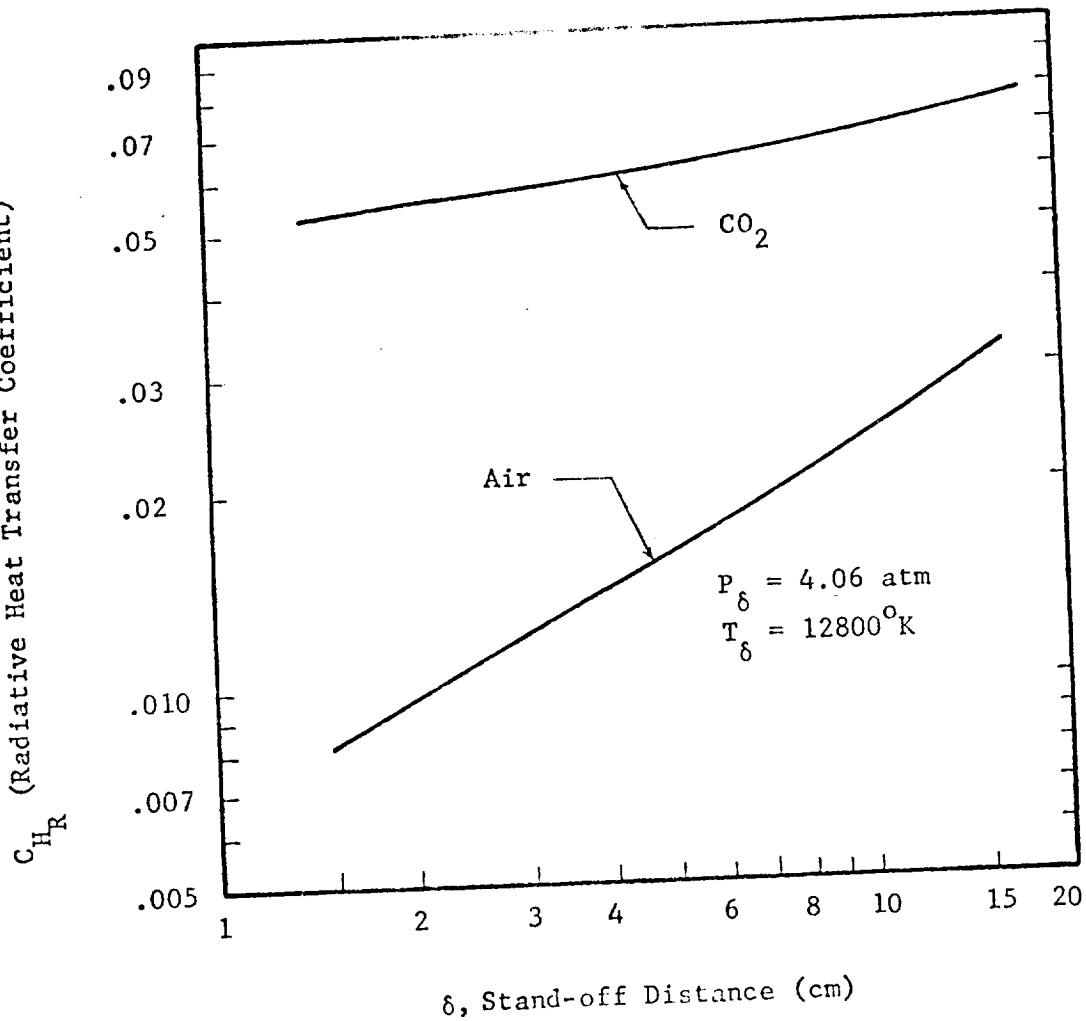

Fig. 5.46 Comparison of Radiative Heating Rates for Air and CO_2 Atmospheres

CHAPTER 5

References

5.1 Inouye, M., "Blunt Body Solutions for Spheres and Ellipsoids in Equilibrium Gas Mixtures," NASA TN D-2780, 1965.

5.2 Hayse, W. D. and R. F. Probstein, Hypersonic Flow Theory, 2nd Ed., Academic Press, New York (1966).

5.3 Goulard, R., "Preliminary Estimates of Radiative Transfer Effects on Detached Shock Layers," AIAA J., 2, No. 3, March 1964.

5.4 Burns, R. K. and C. C. Oliver, "Downstream Radiation to Blunt Entry Vehicles," AIAA J., 6, No. 12, Dec. 1968.

5.5 Rigdon, W. S., R. B. Dirling, Jr. and M. Thomas. "Stagnation Point Heat Transfer During Hypervelocity Atmospheric Entry," NASA CR-1462, Feb. 1970.

5.6 Wilson, K. H., "Stagnation Point Analysis of Coupled Viscous-Radiating Flow with Massive Blowing," NASA CR-1548, June 1970.

5.7 Page, W. A., D. L. Compton, W. J. Borucki, D. L. Cliffone and D. M. Cooper, "Radiative Transport in Inviscid Nonadiabatic Stagnation-Region Shock Layers," AIAA 3rd Thermophysic Conference, Paper No. 68-784, June 1968.

5.8 Korkan, K.D. and G. M. Hanley, "Apollo Command Module Aero-thermodynamics Characteristics at Hyperbolic Earth Entry Velocities," J. of Spacecraft and Rockets, 3, No. 8, Aug. 1966.

5.9 Engel, C. D. and L. W. Spradley, "Radiation Absorption Effects on Heating Loads Encountered During Hyperbolic Entry," J. Spacecraft Roc., Vol. 6, No. 6, 1969, pp. 764-765.

5.10 Smith, G. L., J. T. Suttles, and E. M. Sullivan, "Viscous Radiating Flow-Field on an Ablating Blunt Body," AIAA Paper No. 70-218, Jan. 1970.

5.11 Esch, D. D., Stagnation Region Heating of a Phenolic-Nylon Ablator During Returns From Planetary Missions, Ph.D. Dissertation, Louisiana State University, Baton Rouge, La., Aug. 1971.

5.12 Anderson, J. D. Jr., "An Engineering Survey of Radiating Shock Layers," AIAA J., 7, No. 9, Sept. 1969.

5.13 Hoshizaki, H. and K. H. Wilson, "Viscous Radiating Shock Layer About a Blunt Body," AIAA J., 3, No. 9, Sept. 1965.

5.14 Olstad, W. B., "Correlations for Stagnation-Point Radiative Heat Transfer," AIAA J., 7, No. 1, Jan. 1969.

5.15 Livingston F. and J. Williard, "Planetary Entry Body Heating Rate Measurements in Air and Venus Atmospheric Gas up to T = 15000°K," AIAA J., 9, No. 3, March 1971.

5.16 Stickford, G. H. Jr., "Total Radiative Intensity Calculations for 100% CO_2 and 90% CO_2 - 10% N_2," J. Quant. Spectrosc. Radiat. Transfer, Vol. 10, pp 249-270, 1970.

5.17 Hansen, C. F., "Approximations for Thermodynamic Properties of High Temperature Air," NASA TR R-50, 1959.

CHAPTER 6

AROUND THE BODY RESULTS

The purpose of this chapter is two-fold. First, procedures used to compute the shock shape around the body are discussed and results comparing different methods are presented. The effects of post shock pressure distributions on the shock shape are studied parametrically demonstrating shock location sensitivity to such variations. Secondly, radiative heating rate distribution results from radiative cooling parameter calculations are presented. These results are compared with more detailed analyses which require flow-field solutions and at most are found to differ by about $\pm$ 6%.

SHOCK SHAPE CALCULATIONS

Any discussion of calculations of the location of the bow shock wave produced by a blunt body naturally involves a discussion of the post shock pressure and surface pressure distributions. This is true since the location of the bow shock is determined by the post shock pressure which in turn is to a first approximation directly determined by the surface pressure.

There are three methods which may be used to determine the shock shape and pressure distribution around the body. First, we will consider the technique used in Refs. 6.1 and 6.2 and others. The shock shape is specified *a priori* from which the wall pressure distribution is calculated as the solution proceeds around the body. An output shock shape is calculated from the geometrically relation (Ref. 6.3)

$$\epsilon = \tan^{-1}\left[(d\delta/d\xi)/(1 + \varkappa\delta)\right] \tag{6.1}$$

where δ is calculated as a result of the x - momentum solution. This output angle is compared with the input angle. If the input and output are nearly the same the solution is said to be converged. A second technique involves specifying a wall pressure distribution a priori. Preferably this distribution is known from experimental data for hypersonic Mach numbers. The change in pressure due to radiation coupling is justifiably neglected (Ref. 6.1). A shock shape is also assumed. The shock layer equations are solved around the body and the calculated and input pressure distributions are compared. The shock shape is numerically adjusted according to the pressure difference. The solution is repeated until satisfactory pressure convergence is obtained. The third technique involved is a simultaneous solution of the geometrical relation

$$\delta = \int_0^{\xi} (1 + \varkappa\delta) \tan \epsilon d\xi + \delta_0 \tag{6.2}$$

with the shock layer equations. The post shock and surface pressure distributions are automatically calculated as part of the shock layer equations solution. Only one around the body iteration is needed for this technique.

The first two techniques have been implemented in a modified version of the computer program described in Ref. 6.1 and 6.2. Unfortunately both of these techniques have limitations. The first technique consumes computer time because of the many around the

body iterations which are necessary. In addition, each estimate of the shock shape must be made by hand thus consuming man-hours. The second technique also consumes a great deal of computer time because of the many iterations around the body that are necessary for convergence. The second technique does have an advantage over the first since the input and output pressures are smooth; thus updating of the shock shape can be done automatically. However, this technique does not necessarily satisfy the geometrical differential equation stated above. Since the first two techniques are subject to undesirable limitations, it is the purpose here to explore the feasibility of implementing the third technique.

The post shock pressure, P_δ differs, in general, from the surface pressure, P_w, for the same body angle location. The pressure and temperature variations across the shock layer are shown in Fig. 6.1. These results, obtained from unpublished work of Spradley and Engel (Ref. 6.4), show that the post shock pressure is smaller than the wall pressure for post shock Mach numbers less than one and is greater than the wall pressure for larger Mach numbers. The results presented in Fig. 6.1 were obtained using a computer solution of the shock layer equations documented in Ref. 6.1 and 6.2 The referenced method used a modified Karman-Pohlhausen integral method to solve the x - momentum equation and a finite difference relaxation procedure to evaluate the energy equation. An inviscid y - momentum

Emission Radiation Coupled

U_∞ = 41000 ft/sec

$\rho_\infty = 1.03 \times 10^{-6}$ slug/ft^3

R = 1 ft

$(\rho v)_w = 0.0$

$T_w = 1500^\circ K$

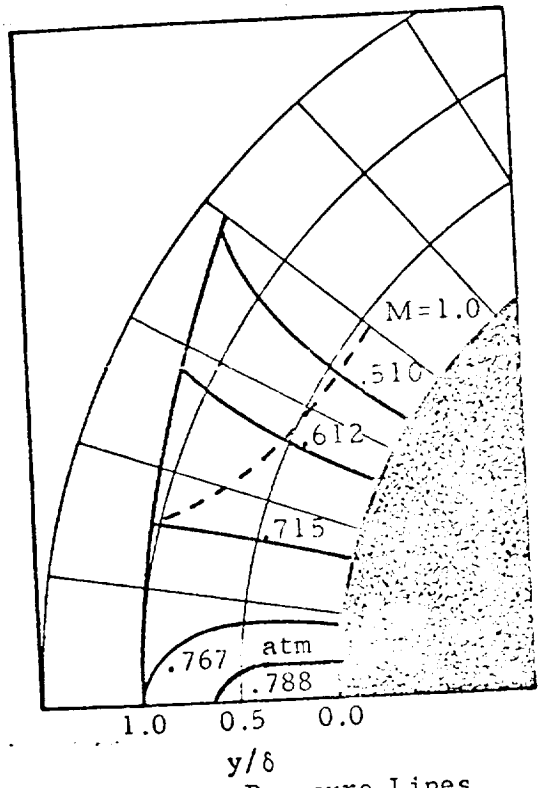

a) Constant Pressure Lines

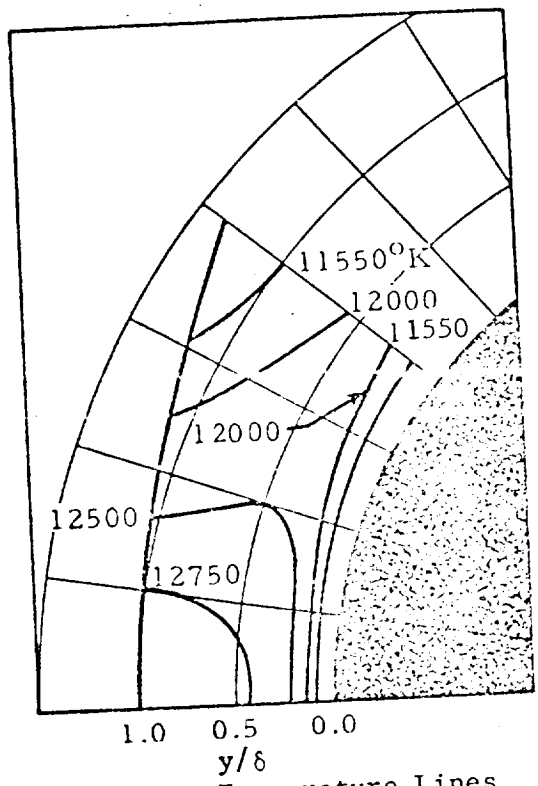

b) Constant Temperature Lines

Fig. 6.1 Shock Layer Pressure and Temperature Lines in a Radiatively Coupled Flow-Field (From Ref. 6.4)

equation solution for the given x - momentum solution is used to obtain the y pressure variation. Results from this program yield the required post shock pressure variation for the present investigation of shock shape calculations.

The geometrical integral equation (6.2) was integrated with a simultaneous Rankine-Hugoniot solution to obtain the bow shock shape for a given post shock pressure distribution. Specifying the free-stream velocity and density and the post shock pressure is sufficient to solve for the shock angle, ϵ, (from Eqs. 2.79 to 2.82) using a thermal and caloric equations of state. This shock angle is then used in Eq. 6.2 to solve for the local stand-off distance, δ. The integration of Eq. 6.2 was carried out using a simple predictor corrector method. Numerical experiments showed that a step size of $\Delta\theta = .5$ deg. was sufficiently small to insure convergence to a unique solution.

Figure 6.2 presents results of the integration and Rankine-Hugoniot solution. Two aspects of shock shape calculations are demonstrated in this figure. First, a comparison of the present integration method and the shock shape computed using the flow-field numerical solution of Ref. 6.2 is presented (i.e. PR = 0.0). The results are in quite good agreement as expected for the following reason. The post shock pressure distribution used in the shock shape integration was obtained from the flow-field solution. The flow-field solution was obtained by specifying the wall pressure

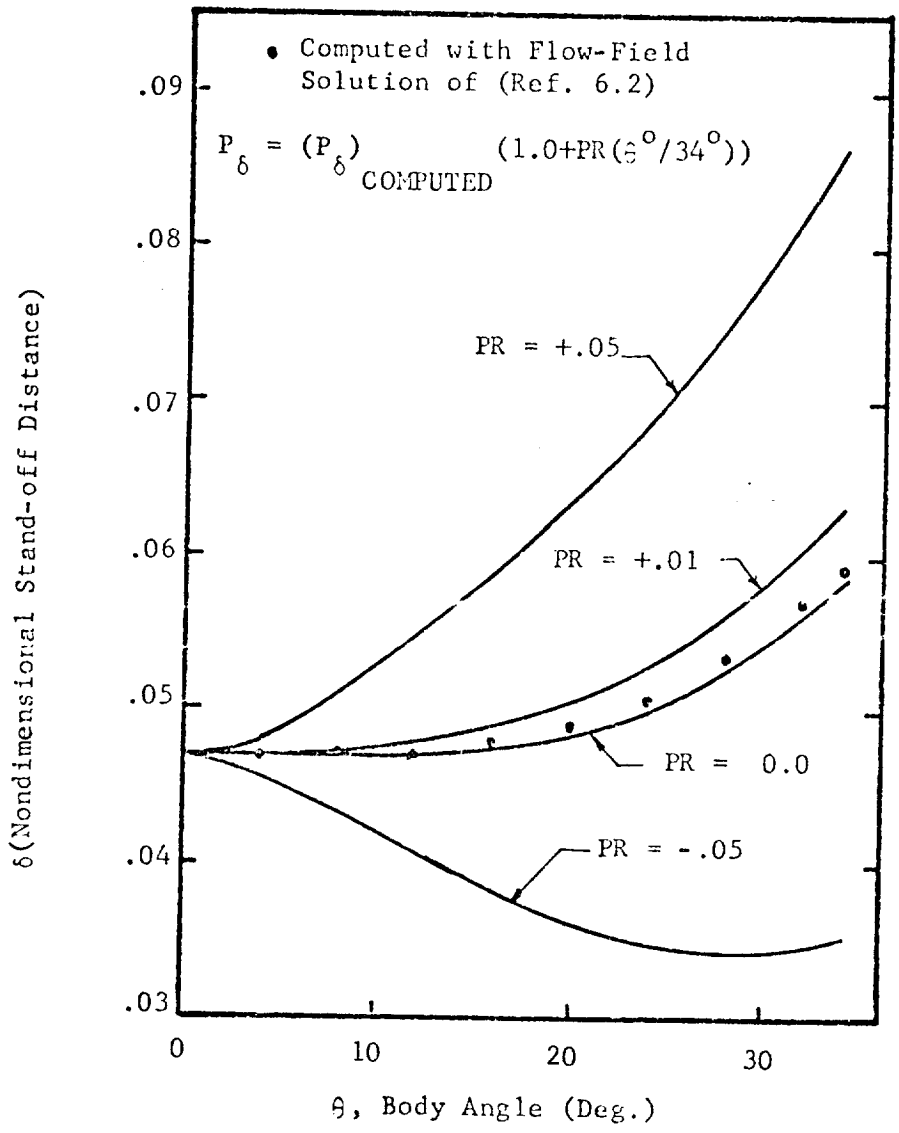

Fig. 6.2 Calculated Shock Shapes

distribution and iterating on the shock shape until the wall pressure converged. The wall pressure was specified using

$$P_w = P_{w_o} (1.0 - 1.25 \sin^2 \theta + 0.284 \sin^4 \theta) \qquad (6.3)$$

which is an inverse solution correlation of Inouye (Ref. 6.5). Thus one aspect demonstrated in Fig. 6.2 is that the numerical integration of Eq. 6.2 does yield a solution comparable to the flow-field solution.

The second aspect of shock shape calculations shown in Fig. 6.2 is the sensitivity of the stand-off distance to the post shock pressure distribution which was studied by parametrically varying this distribution with the equation:

$$P_\delta = (P_\delta)_{\text{COMPUTED}} (1 + PR\ (\theta^0/34^0)) \qquad (6.4)$$

In the above expression PR represents an error that might be experienced by the forward integration procedure in any flow-field solution. The resulting stand-off distances for PR = $\pm$ .05 and + .01 are shown in Fig. 6.2 These results indicate that the normal direction variations in pressure as those shown in Fig. 6.1 are quite important in determining the shock shape. Moreover, a high degree of accuracy must be maintained in a flow-field calculation to prevent computational inaccuracies from being amplified in the resulting shock location.

Assuming that numerical accuracy can be maintained, results presented in Fig. 6.3 indicate that the present integration method is to be preferred over the two other methods previously used with

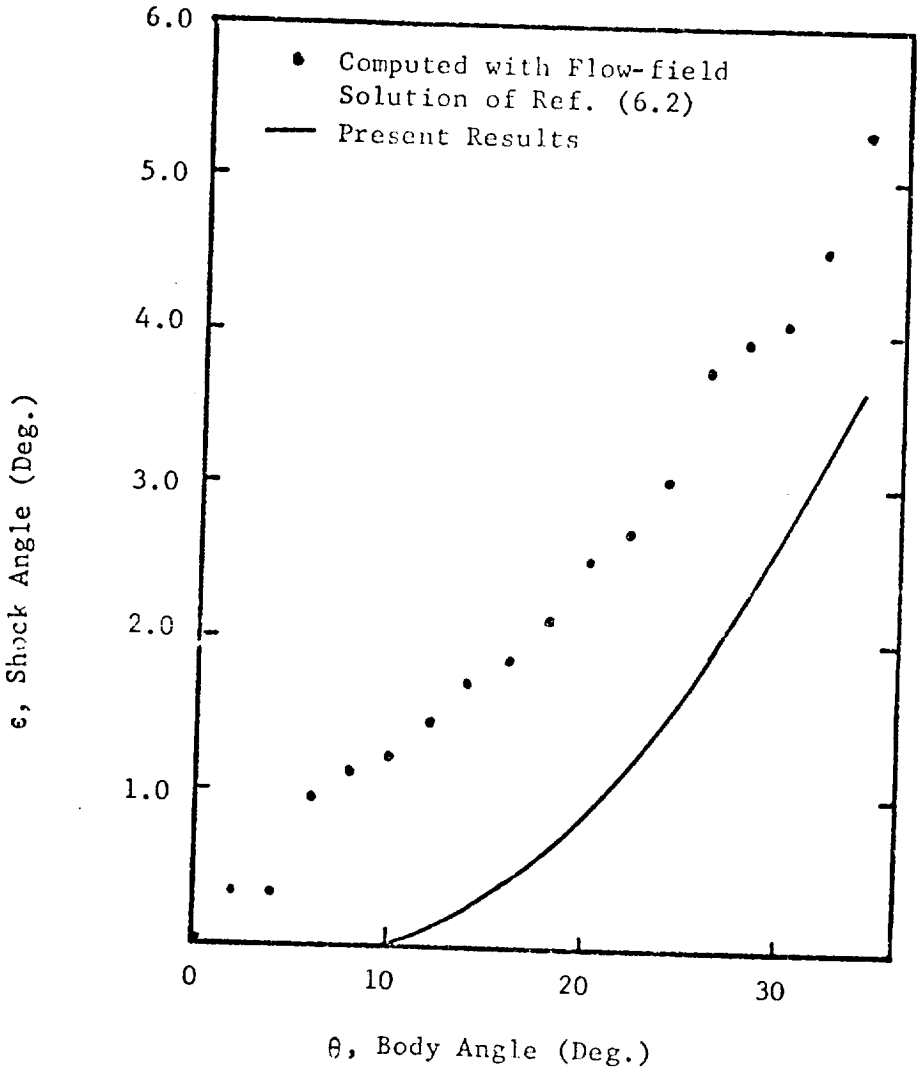

Fig. 6.3 Shock Angle Distributions

flow-field solutions. This figure presents the shock angle computed by the present method and the output shock angle from the flow-field solution. [illegible] computed from differencing the output stand-off distance of the flow-field solution and using a two point difference derivative in Eq. 6.1. Small fluxuations in the output stand-off distance result in the irregular changes in ϵ and acculumutive error. Using the present method a smooth shock angle is computed; this is necessary if the shock shape is to be updated by an iteration procedure in a computer program.

The set of thin shock layer equations for around the body flow are parabolic. Thus, one expects the initial conditions, i.e., stagnation line conditions, to influence the down stream solution. The initial conditions are determined, in part, by the shock curvature at the stagnation line. As pointed out in Chapter 2 this stagnation boundary condition is unknown, and it is usually assumed. The true elliptic nature of the problem indicates that this boundary condition is determined by downstream effects. As pointed out in some early work of Hoshizaki (Ref. 6.6) a downstream boundary condition could theoretically be substituted for the initial shock curvature. This downstream condition is the inviscid shock angle far from the body where all disturbances from the body are negligible. Since it is not practical to attempt to satisfy this downstream boundary condition, the initial shock curvature, $(d\epsilon/d\xi)_{\xi=0}$, must be specified.

In order to examine uncertainty in the post shock pressure distribution resulting from uncertainty in the shock curvature at the stagnation line, Fig. 6.[illegible]d. The flow-field solution of Ref. 6.2 was used to compute the post shock pressure distribution for a given initial shock curvature, $(d\epsilon/d\xi)_{\xi=0}$. The three distributions shown were obtained using Eq. 6.3 and the surface pressure convergence method. The maximum percent difference in pressure noted at $\theta = 34^{\circ}$ is approximately -5%. As was demonstrated in Fig. 6.2 a change of pressure of this magnitude causes a very major change in the shock shape. Accordingly, we may conclude that uncertainties in the initial shock curvature, which result from the elliptic nature of the problem, may preclude an accurate estimate of the shock shape.

As a practical matter the shock shape must be approximated to compute the surface heating rates. Therefore, it is suggested that the initial curvature be assumed such that calculations may be made. The accuracy of the results should be regarded with an awareness of the error which may be introduced by the assumed curvature.

To conclude, it is observed that the integration of the geometrical equation (Eq. 6.2) results in a smooth shock shape. This is important if the shock location is to be iterated upon numerically. Further the shock shape location is strongly coupled to both the initial shock curvature and pressure changes across the shock layer.

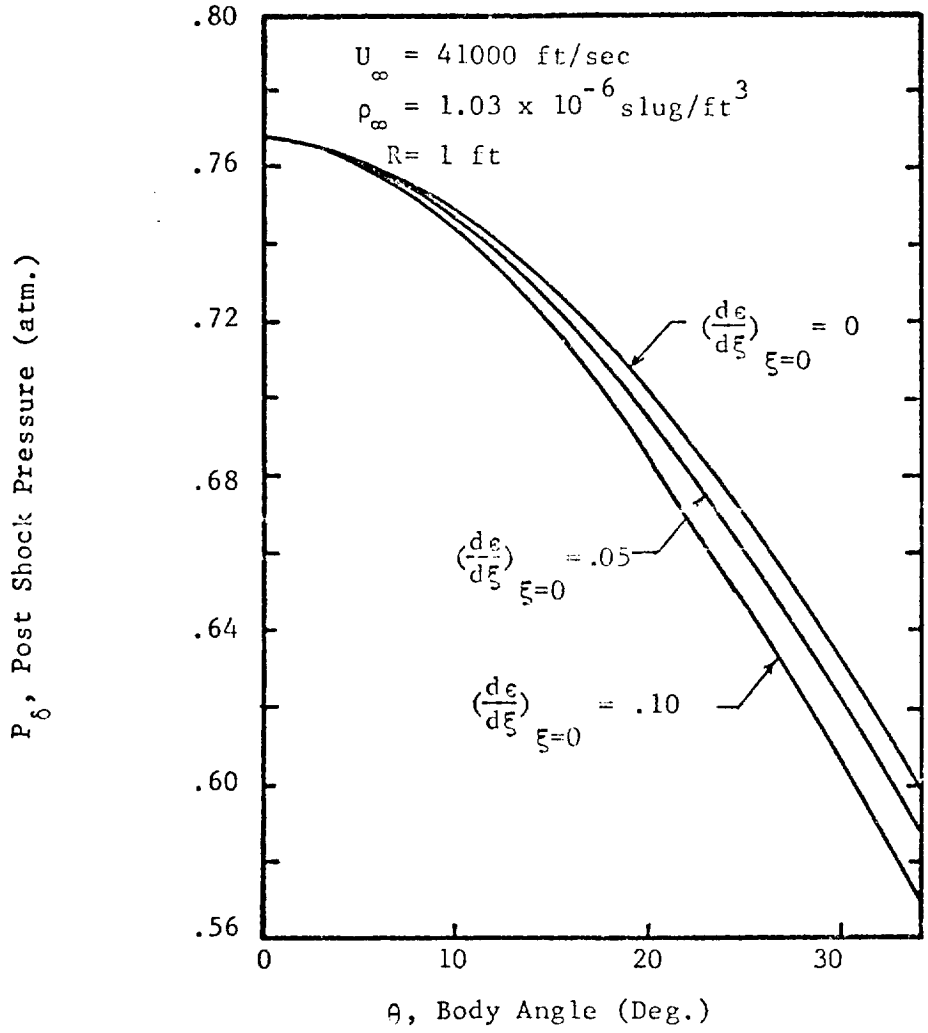

Fig. 6.4 Post Shock Pressure Distributions
for Different Initial Shock Curvatures

RADIATIVE HEATING RATE DISTRIBUTIONS

The success of using a radiative cooling parameter correlation to compute stagnation lin[illegible]rompted an investigation into its applicability to non-stagnation line calculations. The goal here is to obtain a computationally rapid means of estimating distributed heating rates for no mass injection. The effects of mass injection may be accounted for by using stagnation line results presented in Chapter 5 or correlations when available to determine the ablation - shock layer coupled heating rates.

One of the basic assumptions usually made in calculations of shock layer radiative transfer is that the shock layer can be treated locally as a planar infinite slab for calculations along the stagnation line or around the body. This assumption is inherent in the radiative cooling parameter correlation presented in Chapter 3. Thus this assumption is consistent with radiative transfer calculations made in flow-field analysis. In order to use the radiative cooling parameter correlation, developed from stagnation line calculations, for nonstagnation line calculations it is necessary to assume that the radiative transfer process and the local temperature profile are similar to those of the stagnation line. Fig. 6.1b provides a qualitative basis for judging such an assumption. The constant temperature lines shown in Fig. 6.1b were computed using the flow-field analysis of Ref. 6.2 with radiative coupling of the emission model. The results indicate that although there is a change in character of the temperature along constant ξ-lines, the temperature level changes rather slowly as a function of distance

along the body. This is in contrast to the more rapid change in pressure as shown in Fig. 6.1a. Consequently one expects the similarity assumption to be qualitatively correct.

Given the expected limitations, the radiative cooling parameter was used in the computer program RADCOR (see Appendix E) to compute radiative heating distributions. The isothermal flux was computed locally using the post shock temperature and pressure across a slab of thickness equal to the chosen stand-off distance. In the event of the lack of a better estimate a concentric shock is assumed. No provisions have been made to account for radiative transfer blockage by ablation products. Radiative heating distributions computed with this method are presented in Figs. 6.5, 6.6 and 6.7.

Figure 6.5 presents a comparison of heating rate distributions from the present method and an inviscid flow-field solution of Barnwell (Ref. 6.7). Barnwell used a time-dependent finite-difference technique to obtain numerical solutions for the problem of inviscid flow of radiating equilibrium air past spheres at hyperbolic speeds. The results of Ref. 6.7 were computed using a two step absorption coefficient model which included the effects of line and continuum air radiation. The results of the present method were obtained using the shock shape computed by Barnwell.

Fig. 6.6 presents a comparison of the radiative heating distributions about a sphere from the present method and the viscous shock layer solution reported by Chou and Blake (Ref. 6.8).

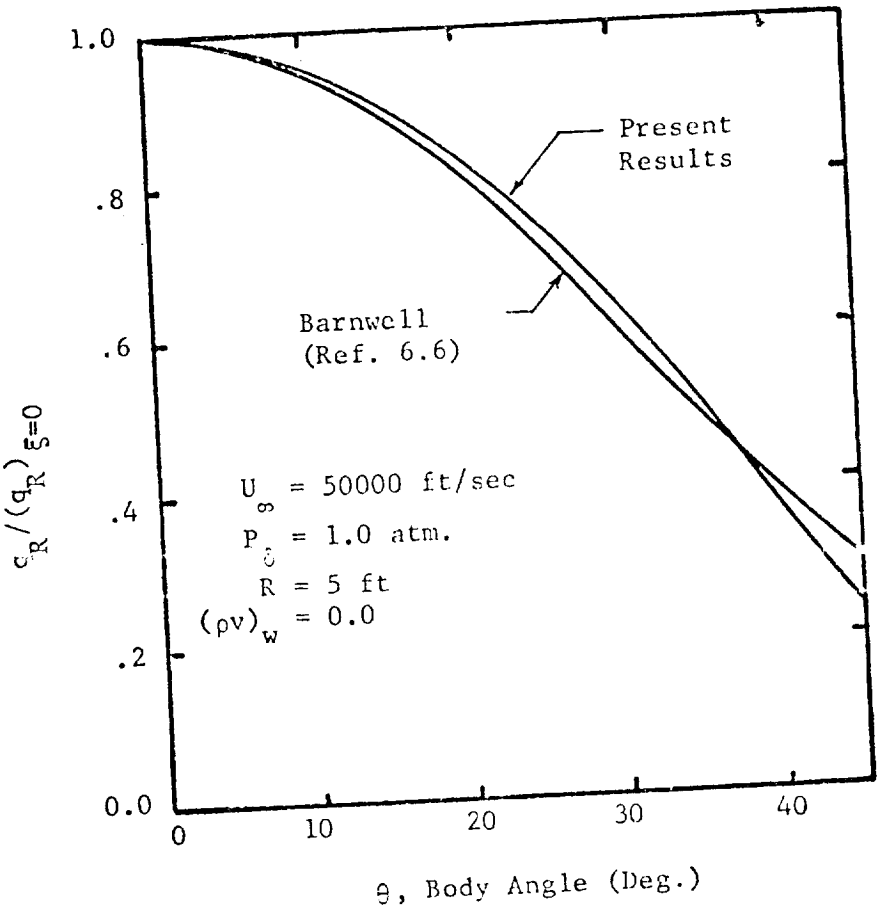

Fig. 6.5 Radiative Surface Heating Rate Distribution Around a Sphere (Comparison 1)

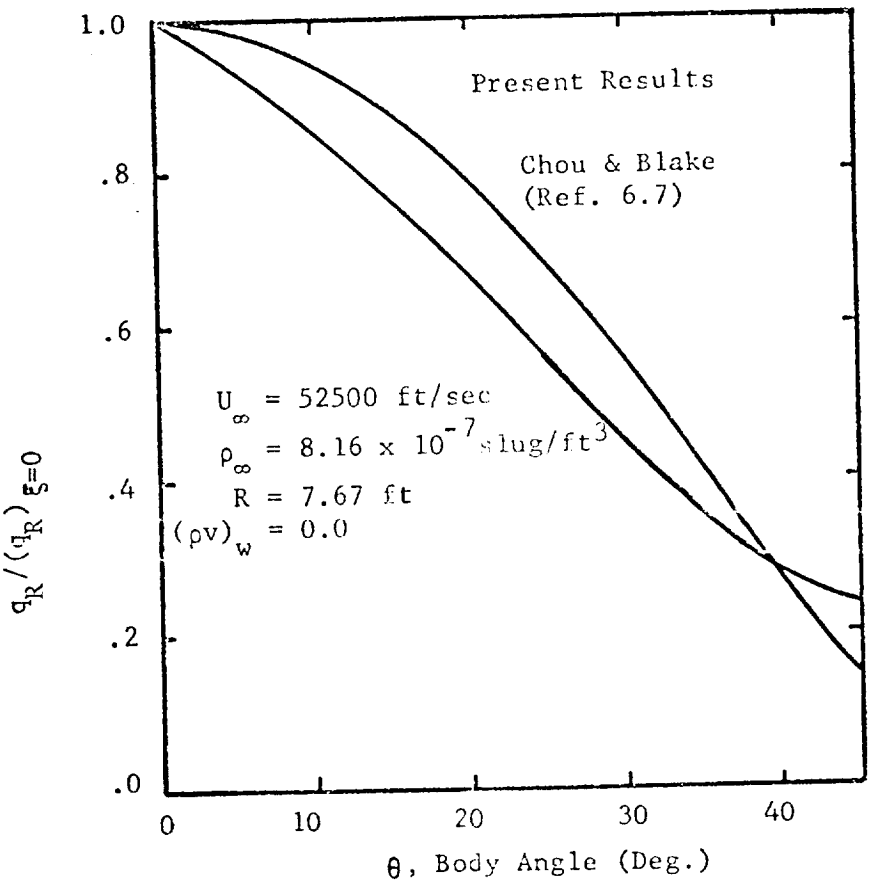

Fig. 6.6 Radiative Surface Heating Distributions Around a Sphere (Comparison 2)

Chou and Blake solved the thin shock layer equations using a Blasius type series expansion technique. Solutions were obtained using three terms in this series. Radiative transport was computed using a three band continuum model for the absorption coefficient of air. The agreement shown in Fig. 6.6 is not as good as in Fig. 6.5; however, it is noted that line radiation effects were not accounted for in the results of Ref. 6.7. As demonstrated by Chou and Blake, viscous effects do not significantly alter the radiative heating distribution for these no ablation cases. This provides additional credence to simularity assumptions inherent in the present method.

Fig. 6.7 presents results for three flight conditions using the present method. Each heating rate distribution case presented took less than 2.0 minutes of IBM 360-65 computer time. The heating rate distributions were computed assuming a concentric shock for a spherical body. The results show the same trends reported using more detailed models. The main trend demonstrated is that the heating rate decreases, as a function of body angle, more rapidly for lower flight velocities than higher ones. Additional cases not presented indicated a weak dependence of the heating rate distribution on body radius which agrees with the results of Ref. 6.7, 6.8 and others.

In order to estimate the effects of initial shock curvature on the heating rate distribution, equilibrium around-the-body solutions were obtained using the computer program documented in Ref. 6.2 Figure 6.8 presents the results of this parametric study. The initial shock curvature, $(d\epsilon/d\xi)_{\xi=0}$, was varied from zero, the concentric

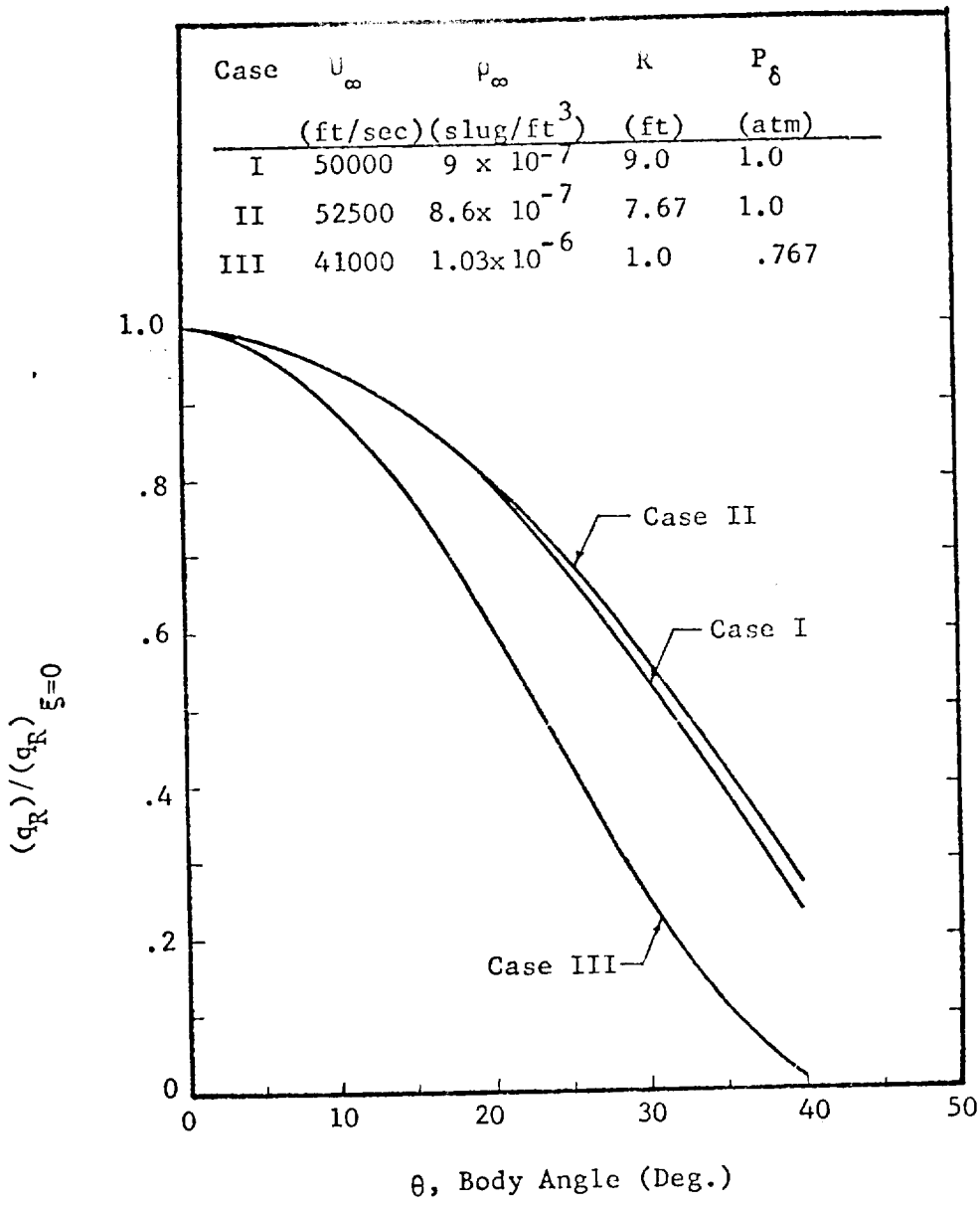

Fig. 6.7 Radiative Surface Heating Rate Distribution Around a Sphere for Different Flight Conditions

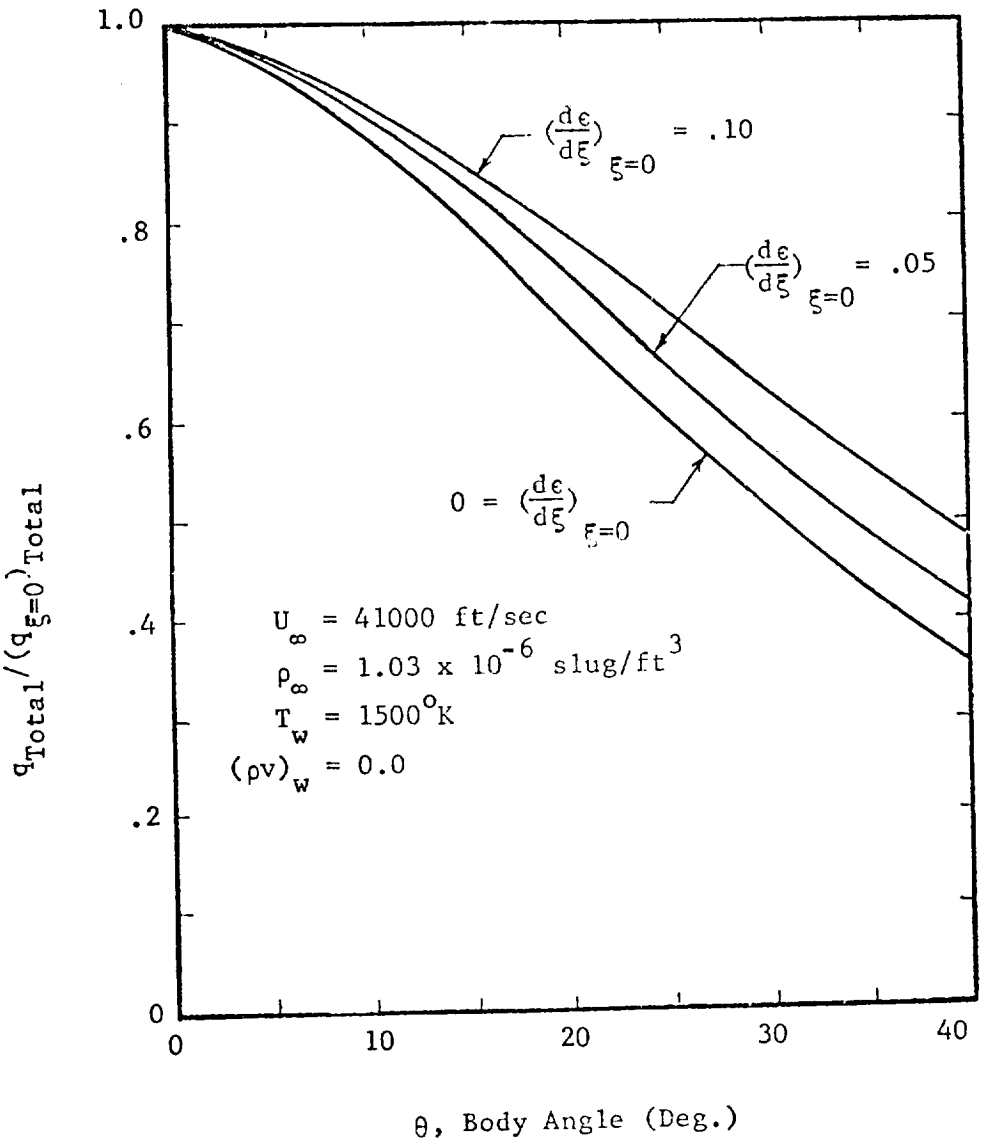

Fig. 6.8 Comparison of Heating Rate Distribution for Different Initial Shock Curvatures

shock assumption, to a value of 0.1. The heating rates, for the 1 foot sphere considered, was significantly increased, ~ 25% higher at 40^{o}, by assuming an initial curvature of 0.1 rather than zero. The initial shock curvature was reported by Burns and Oliver (Ref. 6.9) to be approximately 0.0705 for a hemispherical body at similar flight conditions. It should be noted that the emission radiation model was used in these calculations and therefore only trends, not a quantitative measures, are established. Nevertheless, the large changes shown in Fig. 6.8 indicate that one may safely conclude that the shock curvature at the stagnation line can have a significant effect on the heating rate distribution.

From the results presented in this section one can conclude that the use of a radiative cooling parameter to compute heating rate distributions appears to yield satisfactory results for preliminary design work. This conclusion is indicated by the agreement with other methods shown, the small computation time required and the remaining uncertainty in downstream heating rates resulting from initial shock curvature uncertainties. Although it has not been studied in this section, the present method of using the cooling parameter might well be applicable to non-zero angle of attack problems near the stagnation line if a shock location estimate is available.

CHAPTER 6

References

6.1 Spradley, L. W. and C. D. Engel, "The Effects of Shock Layer Radiation and Viscous Coupling on the Total Heating Rate to a Reentering Blunt Body," NASA CR 61224, April 1968.

6.2 Spradley, L. W. and C. D. Engel, "A Computer Program for Predicting Coupled Convective and Radiative Heat Transfer to a Blunt Body During Superorbital Reentry," LMSC/HREC A791350, Lockheed Missiles & Space Company, Huntsville, Ala., May 1968.

6.3 Hoshizaki, H. and K. H. Wilson, "Viscous, Radiating Shock Layer about a Blunt Body," AIAA J. Vol. 3, No. 9, Sept. 1965, p. 1614-1622.

6.4 Spradley, L. W. and C. D. Engel, Unpublished blunt body work, Lockheed Missiles & Space Company, Huntsville, Ala., 1969.

6.5 Inouye, M., "Blunt Body Solutions for Spheres and Ellipsoids in Equilibrium Gas Mixtures," NASA TN D-2780, 1965.

6.6 Hoshizaki, H., "The Viscous Blunt Body Problem," Proceedings of Symposium on Aerothermoelasticity, ASD TR 61-645, 1961.

6.7 Barnwell, R. W., "Inviscid Radiating Shock Layers About Spheres Traveling at Hyperbolic Speeds in Air," NASA TR R-311, May 1969.

6.8 Chou, Y. S. and L. H. Blake, "Energy-Momentum Coupling in Radiating Shock Layers about a Blunt Body," AIAA J., Vol. 8, No. 9, Sept. 1970.

6.9 Bums, R. K. and C. C. Oliver, "Downstream Radiation to Blunt Entry Vehicles," AIAA J., Vol. 6, No. 12, Dec. 1968.

CHAPTER 7

CONCLUSIONS AND RECOMMENDATIONS

The results in the previous chapters give a more extensive and detailed quantitative description of hyperbolic entry heating than any previously reported studies. The shock layer and ablator analysis includes all of the known significant processes. These processes include ablation and radiative coupling effects within the viscous shock layer, radiative line and continuum processes of both air and ablation species, local chemical equilibrium throughout the shock layer and quasi-steady ablator behavior. The overall analysis includes the best available models of each process and no single other analysis has included all of these processes. Specific processes were studied with respect to their contribution to the shock layer heating. Where several models of the same process were found to yield comparable results the most simple one was incorporated into the overall analysis. The detailed discussion of the mathematical model used and the results obtained provide a sound basis for understanding many of the characteristic processes of hyperbolic entry heating. In addition to the stagnation line work, the radiative cooling parameter, previously used only for the stagnation line, was shown to be applicable in computing heat rate variations around the body. The computer programs developed are engineering tools which can be used to quantitatively define aerothermal environments not already considered in this study.

CONCLUSIONS

Based on the results presented in this work the following conclusions are drawn. The conclusions are for the stagnation line unless stated otherwise.

Mathematical Model

1. As demonstrated in Chapter 4, the thin viscous shock layer flow processes which occur on the front face of a bluff body during hyperbolic planetary entry are accurately described by the bluff body first order shock layer equations stated in Tab. 2.6.
2. Numerical solution of the stagnation line momentum and energy equations using quasilinearization and implicit finite differences was found to be both satisfactory and reliable. In contrast with other reported methods, no numerical difficulties were encountered in using this method for the momentum equation. Thus quasilinearization used with implicit finite differences to obtain a numerical solution to the momentum equation is highly recommended.

Shock Location

1. The shock stand-off distance as a function of the radiative cooling parameter approaches an asymtote at high free stream velocities. The asymtote appears to approach a minimum as the cooling parameter nears a value of one. The radiation perturbation results of Goulard show the

same trends due to optical depth changes as the present results but they do not yield the same radiation coupled stand-off distance.

2. The uncertainties present in the initial shock curvature result in a 5 to 10% increase in the no mass injection stand-off distance and a corresponding 5 to 10% increase in radiative heating above values obtained assuming a concentric shock.

3. To obtain shock shapes around the body, integration of the shock geometrical relation (Eq. 6.2) appears computationally superior to previous methods used.

4. Small changes in the initial shock curvature (i.e. $0.0 \leq (dc/d\xi)_{\xi=0} \leq .1$) result in significant changes in the pressure and heating rate distributions around the body.

Ablation and Radiative Heating

1. The current state of the art analyses yield stagnation line radiative heating rates for no mass injection which agree with $\pm$ 10% of the average.

2. The radiative cooling parameter correlates stagnation line heating rates for no mass injection from the present viscous analysis and from other inviscid analyses rather well over the pressure range of interest.

3. Correlations of the radiative cooling parameter may be used in conjunction with a planar slab radiation model

which accounts for line and continuum transport to obtain estimates of the radiative heating rate variations away from the stagnation line by methods described in Chapter 6.

4. The stagnation point location as a function of mass injection rate is essentially independent of the shock layer pressure level at U_∞ = 50000 ft/sec. The stagnation point location was observed to move slightly away from the body as the flight velocity is increased at a specified ablation rate.

5. The nondimensional ablation rate parameter $(\rho v)_w$, is insufficient to correlate the nondimensional heating rate, $C_{H_R}/(C_{H_R})_{(\rho v)_w = 0}$. The nondimensional heating rate changes with post shock pressure and free stream velocity in addition to $(\rho v)_w$. The results available for comparison indicated that computations for carbon phenolic ablators exhibited the same pressure and free stream velocity dependencies as the present result for phenolic nylon ablators.

6. The ablator-shock layer coupled results indicates that below P_δ = .10 atm at U_∞ = 50000 ft/sec the surface heating is insufficient to maintain the surface at the sublimation temperature. Consequently the quasi-steady approximation will not be valid unless other mechanisms, such as oxidation, remove the surface rapidly enough to

maintain a constant char thickness. In addition, the ablator coupled results showed that at larger pressures (i.e. $P_\delta > .5$ atm) the ablation rate becomes increasingly sensitive to small changes in surface heating rate.

7. Ablation products of phenolic nylon are least effective in absorbing radiant energy in frequency levels below $h\nu = 5.0$ ev. For a typical case considered ($P_\delta = .5$ atm, $(\rho v)_w = .10$, $U_\infty = 50000$ ft/sec) approximately 79 percent of the radiative flux arriving at the surface was in the frequency range below $h\nu = 5.0$ ev.

8. As the shock layer pressure is increased the continuum contribution to the surface flux is increased and the line contribution is decreased at a constant U_∞ and $(\rho v)_w$. This change in the relative contributions from the two radiative mechanisms is responsible for the presssure dependence of the nondimensional heating, $C_{H_R}/(C_{H_R})_0$.

9. The continuum contribution to the surface radiative heating is essentially unchanged by increasing the ablation rate above $(\rho v)_w = .05$. Thus any reduction in radiative heating rate below that for $(\rho v)_w = .05$ is primarily due to blockage of line radiation.

10. Sufficient information is given graphically to permit hand computations of hyperbolic earth entry heating rates for no mass injection. A method of obtaining an adjusted estimate of the ablator coupled radiative heating is suggested.

Gas Properties

1. Comparison with multicomponent and binary diffusion species equation solutions indicates that the two zone constant elemental approximation of this work is sufficiently accurate to predict ablative coupled heating rates (i.e. within 4.0% of calculations using binary diffusion).
2. The use of air values for viscosity and thermal conductivity rather than including ablator species effects is justified for engineering analysis of the shock layer when the main concern is prediction of surface heating rates. The maximum heating rate percentage change observed was 2.0 percent.
3. The influence of ablation product species referenced to that of air on the reacting heat capacity and thus the temperature profile and radiative heating is more significant than the influence produced by the transport properties. For the case studies the maximum change in heating rate due to difference between air and ablation product heat capacities was 4.8 percent.
4. Molecular absorption of radiant energy in the ablation layer reduces the radiative heating rate significantly (i.e. 52% for the case studied).

RECOMMENDATIONS

Recommendations for improving current ablation coupled heating rate calculation capability are as follows:

1. An analysis to determine the magnitude of the initial shock curvature for different ablation rates is recommended. The stagnation line and distributed heating rates are influenced significantly enough by this parameter to warrent a better definition than presently available.
2. Additional experimental verification of frequency dependent radiation data is needed to improve heating rate calculation reliability. For some species, C_3H and C_4H, a complete lack of data was found. In addition, carbon soot has been experimentally observed in the shock layers of ablative models. Since carbon soot is a strong absorber and radiatively active below 5 ev, mechanisms for carbon soot injection into the shock layer from the ablator need mathematical definition.
3. Additional cases could be run with the VISRAD 3 computer program for flight velocities and body radii not considered herein to provide a larger range of calculated results for hand calculations. The effects of ablation products on heat capacity should be included in these additional calculations.

Recommendations for future analyses of ablative heat protection systems are as follows:

1. Establishment by NASA of a set of flight conditions and body sizes for analysis by investigators would permit more direct comparisons of results and numerical methods than can now be achieved. This type of coordinated work has been achieved for orbital entry conditions by AGARD.
2. Studies for entry into the planetary atmospheres of Mars and Venus could be conducted using the VISRAD 3 program. Only minor changes to the program to account for arbitrary free stream gases would be necessary to obtain this additional analytical capability.
3. The VISRAD 3 program has the flexibility to be used for different ablator composition. A comparative analysis with this program to examine the effectiveness of ablation products of different ablators in reducing radiative heating rates would yield information complementing test results.

APPENDIX A

GENERAL CONSERVATION EQUATIONS

CONSERVATION EQUATIONS OF A MULTICOMPONENT, RADIATING, CHEMICALLY REACTING FLUID

The conservation laws for mass, momentum, and energy will be presented for a continuum, multicomponent fluid whose internal degrees of freedom are in thermodynamic equilibrium. The assumption of thermodynamic equilibrium implies that no matter how small a volume of fluid we are interested in there are enough molecules within the volume to give meaningful average properties and that regardless of the flow velocities of interest a temperature may be ascribed to the fluid. This is roughly equivalent to assuming the first postulate of nonequilibrium thermodynamics, see Fitts Ref. A.1.

A general property balance can be made on an element of volume $\forall$ moving with an arbitrary velocity similar to that given in Ref. A.2. The property (mass, momentum, or energy) per unit volume is designated by β . The flux of a property through a control surface is denoted by $\overline{B}$ (property x length)/(volume x time), and the generation of a property within the control volume is denoted by $\mathbb{B}$ (property)/(volume x time). The differential form of the general property balance can be written in terms of the above definitions (p 31, Ref. A.2).

$$\frac{\partial \beta}{\partial t} + \nabla \cdot \beta \overline{V} + \nabla \cdot \overline{B} - \mathbb{B} = 0 \qquad (A.1)$$

if the control volume is subsequently assumed fixed in space. Thus for a control volume stationary in space there is a convective flow

through the control volume which is identifical to the motion term associated with the moving control volume. This means that if the general balance is derived for a moving control volume it may be used for a fixed control volume, with $\bar{B}$ maintaining exactly its same definition. This allows $\bar{B}$ to be interpreted as a diffusive flow. This is obvious for the moving control volume, but the common practice of lumping all kinds of effects into this flux term for a fixed control volume effectively redefines $\bar{B}$. Therefore, the general balance equation is derived in the form for a moving control volume, but it is fully intended to be used to describe a stationary volume in space.

The general property balance Eq. A.1 can also be written:

$$\frac{\partial \beta}{\partial t} + \bar{V}\cdot\nabla\beta + \beta\nabla\cdot\bar{V} + \nabla\cdot\bar{B} - \mathbb{B} = 0 \qquad \text{(A.2)}$$

(1) (2) (3) (4) (5)

The meaning of these terms is, for a control volume:

(1) the accumulation of β,

(2) the convective flow of β,

(3) the dilation of the flow, i.e. the change of β when the fluid is compressed or expanded,

(4) the diffusional flux,

(5) the generation of β.

Using Eq. A.2 and specifying β, $\bar{B}$, and $\mathbb{B}$ we now can write the conservation equations. Consider first the conservation of mass by specifying $\beta = \rho$ (mass/volume), $\bar{B} = \mathbb{B} = 0$.

Substitution into Eq. A.2 yields

Continuity:

$$\frac{\partial \rho}{\partial t} + \bar{V}\cdot\nabla\rho + \rho\nabla\cdot\bar{V} = 0 \qquad (A.3)$$

Before proceeding to the other conservation equations let us rewrite the general property balance equation in another form by substituting $\beta = b\rho$ into Eq. A.2. By using this substitution and noting the continuity equation appears as a product of b, the general property balance relation can be expressed as:

$$\rho \frac{Db}{Dt} + \nabla\cdot\bar{B} - \mathbb{B} = 0 \qquad (A.4)^{+}$$

This equation will be used to evaluate the remainder of the conservation equations.

Consider now species conservation by specifying

$$b = C_i$$
$$\bar{B} = \bar{J}_i$$
$$\mathbb{B} = \dot{\omega}_i$$

where

$$\sum \bar{J}_i = 0$$

Substitution of the above relations into Eq. A.4 yields

Species Continuity:

$$\rho \frac{DC_i}{Dt} + \nabla\cdot\bar{J}_i - \dot{\omega}_i = 0 \qquad (A.5)$$

$^{+}$ $\frac{Db}{Dt}$ is the substantial derivative of b which equals $\frac{\partial b}{\partial t} + \bar{V}\cdot\nabla b$.

Let us accept the second postulate of thermodynamics of irreversible processes which states that if the fluid is not too far from equilibrium, fluxes and curr[illegible]eous functions of the driving force. Using this postulate the mass flux vector of specie i, Eq. A.5, can be written as the sum of contributing vectors.

$$\bar{J}_i = (L_{D1}\,\bar{X}_1)_i + (L_{D2}\,\bar{X}_2)_i + \cdots \tag{A.6}$$

where

L_{lm} = Transport Coefficient

$\bar{X}_m$ = Driving Force

and where subscript "D" indicates diffusional transport coefficients.

The number of necessary terms to consider can only be discussed in reference to a particular application. Four terms are stated below from Bird et al., Ref. A.3, for consideration.

$$(L_{11}\bar{X}_1)_i = \bar{J}_i^{(D)} = \frac{n_t^2}{\rho RT} \sum_j M_i M_j D_{ij} \left[Y_i \sum_{\substack{k=1 \\ k\neq j}} \left(\frac{\partial G_j}{\partial Y_k}\right)_{T,\forall,Y_l} \nabla Y_k \right] \tag{A.7}$$

$$(L_{12}\bar{X}_2)_i = \bar{J}_i^{(T)} = - D_i^T \nabla \ell n\, T \tag{A.8}$$

$$(L_{13}\bar{X}_3)_i = \bar{J}_i^{(P)} = \frac{n_t^2}{\rho RT} \sum M_i M_j D_{ij} \left[Y_j M_j \left(\frac{\bar{v}_j}{M_j} - \frac{1}{\rho}\right) \nabla P \right] \tag{A.9}$$

$$(L_{14}\bar{X}_4)_i = \bar{J}_i^{(g)} = \frac{-n_t^2}{\rho RT} \sum M_i M_j D_{ij} \left[Y_j M_j (\bar{g}_j - \sum \frac{\rho_k}{\rho} \bar{g}_k) \right] \tag{A.10}$$

where

n_t = Concentration in total no. of moles/volume (C in Ref. A.3)

Y_j = Mole fraction (X_j in Ref. A.3)

G_j = Gibbs' free energy

D_{ij} = Multicomponent diffusion coefficient

D_i^T = Thermal diffusion coefficient

Eq. A.7 expressed the mass diffusion vector. Since the driving force is of the same measure as the flux, they are called "conjugate". The conjugate transport coefficients, L_{aa}, are the largest, i.e. mass is diffused primarily by mass concentration gradients. Eq's. A.8, A.9, and A.10 represent the mass flux vector contribution from thermal diffusion, pressure diffusion, and forced diffusion respectively. There are also fluxes due to inertia and viscous terms, but they are very small, see appendix in Fitts Ref. A.1. Electrical and magnetic effects can also create fluxes.

The definition of flux as a linear function of coefficients and potentials and the realization that fluxes are tensors of various ranks leads one to speculate on what type of cross effects can exist. Curie's theorem states that "fluxes whose tensorial characters differ by an odd integer cannot interact in isotropic systems," Ref. A.1. This means that the mass flux tensor and the heat flux tensor which are both vectors are not coupled to the reaction rate tensor (a scalar), or the momentum flux tensor (a second order tensor) but may be coupled to each other. Also, it should be observed that momentum flux tensor either as a second order tensor or in contracted form as a scalar may be coupled to the reaction rate tensor.

With the foregoing information in mind consider the conservation of momentum. For substitution into the general balance equation

$$b = \beta/\rho = \bar{V}$$

$$\bar{\bar{B}} = -\bar{\bar{\tau}} + \bar{\bar{I}}P - \bar{\bar{P}}_R$$

$$B = \sum_i \rho_i \bar{g}_i$$

Using Eq. A.4 for momentum conservation yields

Momentum:

$$\rho \frac{D\bar{V}}{Dt} - \nabla \cdot (\bar{\bar{\tau}} - \bar{\bar{I}}P + \bar{\bar{P}}_R) - \sum_i \rho_i \bar{g}_i = 0 \qquad (A.11)$$

Note that in the above equation the radiative pressure tensor, $\bar{\bar{P}}_R$, is included for completeness. This term is negligible for practically all non-nuclear problems (Ref. A.5).

Let us now apply the general balance equation to conservation of energy by specifying

$$b = Q + \frac{V^2}{2} + \sum_i \rho_i \bar{V} \cdot \bar{g}_i = E \qquad \text{(energy/mass)}$$

$$\bar{B} = \bar{q}_D \qquad \text{(energy/volume)(length/time)}$$

$$-B = \nabla \cdot \bar{q}_R - \nabla \cdot (\bar{\bar{\tau}} - \bar{\bar{I}}P + \bar{\bar{P}}_R) \cdot \bar{V} + \sum \bar{g}_i \cdot \bar{J}_i$$

$$- S\rho \qquad \text{(energy/volume - time)}$$

= generation by radiation + pressure tensors + external forces + heat sources internal to the C.V.; i.e. induction heating, resistance heating, etc.

Substitution of the above into Eq. A.4 yields the total internal energy form of the energy equation

$$\rho \frac{DE}{Dt} + \nabla \cdot \bar{q}_D + \nabla \cdot \bar{q}_R - \nabla \cdot (\bar{\bar{\tau}} - \bar{\bar{I}}P + \bar{\bar{P}}_R) \cdot \bar{V}$$

$$+ \sum_i \bar{g}_i \cdot \bar{J}_i - S\rho = 0 \qquad (A.12)$$

where

$\bar{q}_D$ = diffusional heat flux vector

$\bar{q}_R$ = radiative heat flux vector

$\sum_i \bar{g}_i \cdot \bar{J}_i$ = heat generated in the system by a gravitational field

Let us investigate further the diffusional and radiative heat flux vectors. Again imposing restrictions from thermodynamics of irreversible processes, the diffusional heat flux vector may be written as a sum of vectors

$$\bar{q}_D = (L_{T1}\bar{X}_1) + (L_{T2}\bar{X}_2) + \ldots \tag{A.13}$$

where

$$L_{T1}\bar{X}_1 = \sum_i h_i \bar{J}_i - k' \nabla T$$

$L_{T2}\bar{X}_2$ = energy transport due to the Dufour effect

The $L_{T1}\bar{X}_1$ term is the conjugate term for this flux vector. It should be noted however that the right hand side definition is an arbitrary one. The Dufour effect arises due as the conjugate of the Soret effect in mass diffusion. Additional cross effects from other coefficients and potentials will not be considered.

Radiative transfer of heat is propogated in an entirely different manner than diffusional heat transfer. Duffusional heat transfer mechanism depends on gradients in the gas, such as temperature, species, pressure or external forces as pointed out by Planck, Ref. A.4.

Radiative transfer of heat is in itself entirely independent of these gradients in the medium through which it passes. In general, radiation is a far more complicated phenomenon than diffusional heat transfer. The reason for this is that the state of the radiation at a given instant and at a given point of the gas can not be represented by a single vector as the diffusional mechanisms can. All radiative energy rays which at a given time pass through the same point in a gas are independent of each other. Therefore, to specify completely the state of the radiation at a point the radiation intensity must be known in all directions which pass through the point under consideration.

Special attention will now be given to the development of the radiative flux and flux divergence terms which are needed in the evaluation of energy conservation. Starting with the basic concepts of radiative transfer in an absorbing and emitting medium, Ref. A.4 and A.5, a definition of the spectral radient energy density is developed.

Let $f(\nu,\bar{r}, \bar{\Omega}_1,t)d\nu\, d\Omega$ be the number of photons in the frequency interval ν to $\nu + d\nu$, contained at time t in the volume element dV located about the point $\bar{r}$, and having a direction of motion within an element of solid angle $d\Omega$ about the unit vector $\bar{\Omega}_1$. The function f is called the distribution function. For this definition to be meaningful the linear dimensions of the volume element must be larger than the largest wavelength C/ν .

Each photon possesses an energy $h\nu$. Therefore, the <u>spectral radiant energy density</u> may be defined as the radiant energy of frequency

ν included in a unit spectral interval and contained in a unit volume at the point $\bar{r}$ and at the time t by:

$$\mathbb{U}_\nu (\bar{r}, t) = h\nu \int_{4\pi} f \, d\Omega \tag{A.14}$$

In a like manner, the spectral radiation intensity can be defined. First recall each photon possesses a velocity equal to that of light c. Therefore the quantity

$$h\nu c \, f(\nu, \bar{r}, \bar{\Omega}_1, t) \, d\nu \, d\Omega \tag{A.15}$$

represents the radiant energy in the spectral interval $d\nu$ passing through a unit area in a unit time in the direction within the solid angle $d\Omega$ about $\bar{\Omega}_1$. The area is located at $\bar{r}$ and is normal to $\bar{\Omega}_1$. This statement is not necessarily obvious. In order to clearly indicate how and what area is located at point $\bar{r}$ let us follow the derivation of the spectral radiant energy density given by Planck Ref. A.4.

Consider an infinitely small element of volume $d\mathbb{V}$, at the point which has an arbitrary shape Fig. A.1. In order to allow for all rays to pass through the volume $d\mathbb{V}$, we can construct about any point $\bar{r}$ of $d\mathbb{V}$ a sphere of radius σ . The radius σ is selected to be large compared with the linear dimensions of $d\mathbb{V}$ but still so small that no appreciable absorption or scattoring of radiation occurs in the sphere. Each ray which reaches $d\mathbb{V}$ must then originate from some point on the surface of the sphere.

Let us determine the amount of energy contained in $d\mathbb{V}$ which originated from an element of surface area da. The surface area is

chosen such that its linear dimensions are small compared to those of $d\forall$. Consider the cone of rays which start at a particular point on da and pass through the volume $d\forall$. This cone consists of an infinite number of conical elements with a common vertex at a point on da each cutting out of the volume $d\forall$ a certain element of length s. The solid angle of such a conical element is $\Delta A/\sigma^2$ where ΔA denotes the area of cross section normal to the axis of the cone at a distance σ from the vertex Fig. A.1.

In order to find the energy radiated through an element of area let us first define $h\nu cf$

$$I_\nu (\bar{r},\bar{\Omega}_1,t) = h\nu cf \tag{A.16}$$

which is called the spectral radiation intensity. Using Eq. A.15 and A.16 the monochromatic energy which has passed through da and is in $d\forall$ is:

$$I_\nu \, d\Omega \, (s/c) \, da = h\nu cf \, d\Omega \, (s/c) \, da \tag{A.17}$$

where $d\Omega = \dfrac{\sum \Delta A}{\sigma^2}$ and s is the path length in $d\forall$. The energy which enters the conical element in $d\forall$ spreads out into a volume ΔAs. Summing up over all conical elements which originate in da and enter $d\forall$ yields

$$\frac{I_\nu}{c}\frac{da}{\sigma^2}\sum \Delta As = \frac{I_\nu}{c}\frac{da}{\sigma^2}\, d\forall = \frac{I_\nu}{c}\, d\Omega\, d\forall \tag{A.18}$$

The symbol, $d\Omega$, used in Eqs. A.17 and A.18 has two different meanings; this difference is seldom noted in the literature. This represents the entire

monochromatic radiant energy contained in volume $d\forall$ resulting from radiation through the element of area da. To determine the total monochromatic radiant energy contained in $d\forall$ we must integrate over all elements of area da contained in the surface of the sphere. For the procedure of this integration observe Fig. A.2. In this case the increment in solid angle $d\Omega = \frac{da}{\sigma^2}$ which corresponds to a cone with a vertex at $\bar{r}$. Integrating the right hand side of Eq.'s A.18 yields the total energy:

$$\frac{d\forall}{c} \int I_\nu \, d\Omega$$

The monochromatic radiant energy density is obtained by dividing by $d\forall$.

$$\mathbb{U}_\nu = \frac{1}{c} \int I_\nu \, d\Omega \tag{A.19}$$

Since the radius σ does not appear in Eq. A.19 we can think of I_ν as the intensity of radiation at the point $\bar{r}$ itself or the intensity of radiation passing thru a unit area at $\bar{r}$ in the direction $\bar{\Omega}_1$. This clarifies a difficult concept which is avoided in many derivations.

From the definition of I_ν it follows that the radiation heat flux is a vector of magnitude

$$q_R(\bar{r},t) = \int c \, \mathbb{U}_\nu d\nu = \int\int I_\nu \, d\Omega \, d\nu \tag{A.20}$$

in the direction $\bar{\Omega}_1$ of photon propagation. Let the normal to any surface thru point $\bar{r}$ be called $\bar{n}$. Therefore the magnitude of the heat flux passing thru a unit surface area normal to $\bar{n}$ from photon propagation in the $\bar{\Omega}_1$ direction is:

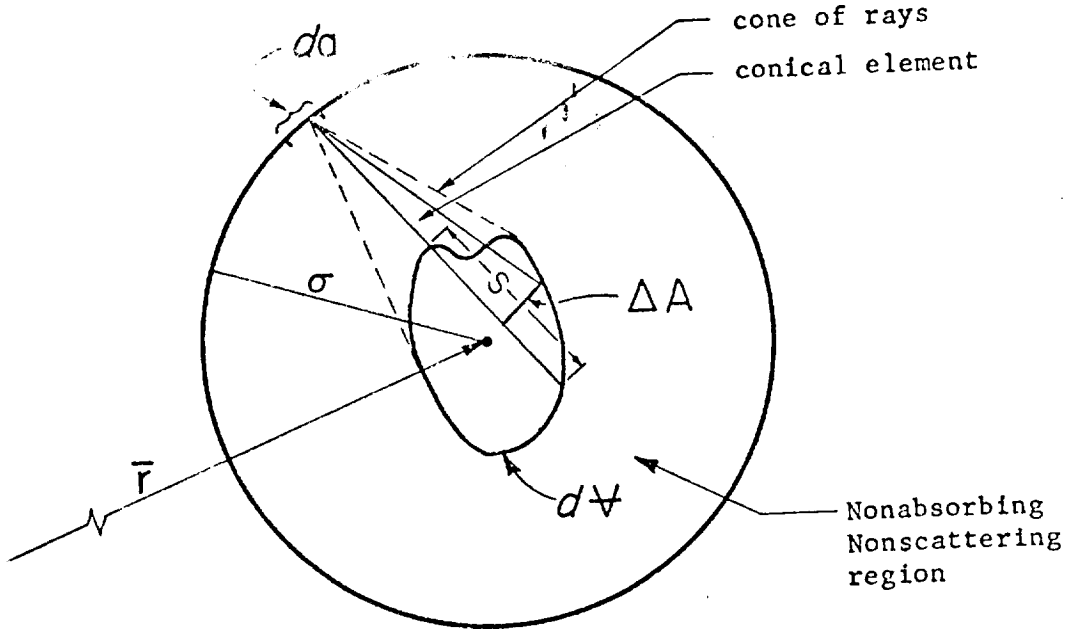

Fig. A.1 Radiation to dV From Its Surroundings

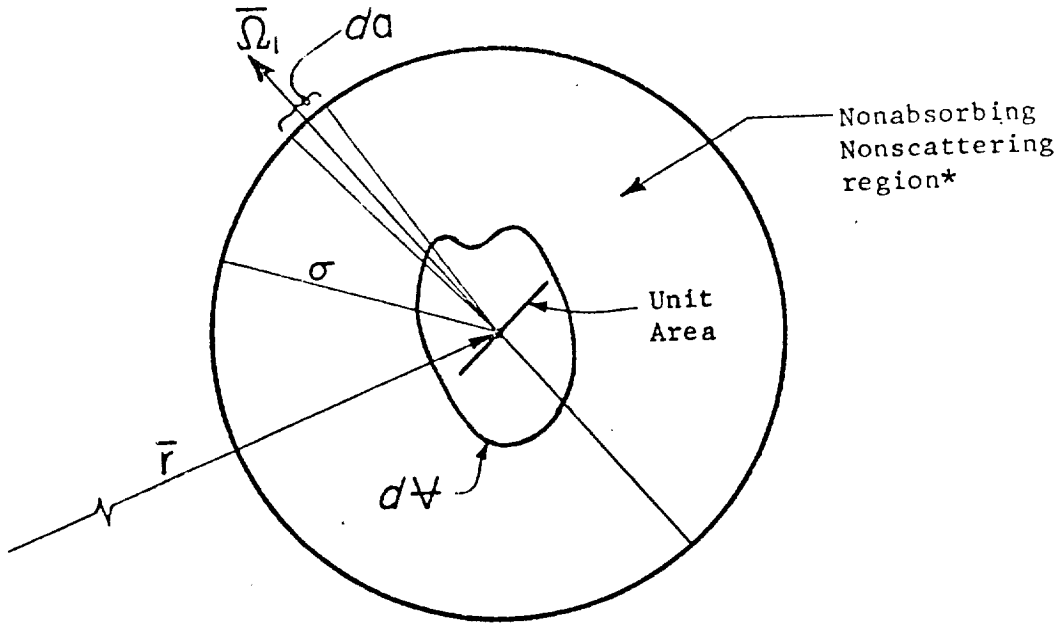

*Radiation in minus $\bar{\Omega}_1$ direction to the unit area equals the radiation from the unit area in the minus $\bar{\Omega}_1$ direction.

Fig. A.2 Geometric Relations for Calculation of Radiation to dV

$$(\bar{n}\cdot\bar{q}_R) = q_R(\bar{r},\bar{n},t) = \int\int_{4\pi} (\bar{n}\cdot\bar{\Omega}_1)\, I_\nu\,(\bar{r},\bar{\Omega}_1,t)\, d\Omega\, d\nu \qquad (A.21)$$

Finally the radiation flux vector can be written

$$\bar{q}_R(\bar{r},t) = \int_{\nu=0}^{\infty}\int_{\Omega=0}^{4\pi} I_\nu(\bar{r},\bar{\Omega}_1,t)\,\bar{\Omega}_1\, d\Omega\, d\nu \qquad (A.22)$$

Therefore $\bar{q}_R$ is defined at any point $\bar{r}_1$ and time t in space.

For the use of the radiative heat flux vector in the energy equation, it is desirable to be able to calculate a component of $\bar{q}_R$ in any coordinate direction of an orthogonal coordinate system and to calculate $\nabla\cdot\bar{q}_R$. These calculations may be accomplished in a more expeditious fashion by first writing the equation of radiative transfer.

The radiative transfer equation states that the rate of radiative energy accumulated in a volume element plus the rate that it flows thru the element equals the rate of generation within the element. The generation of radiative energy is accomplished by emission and absorption. The general property balance can be used by defining

$$\beta = I_\nu$$

$$\bar{B} = 0$$

$$\mathbb{B} = c\left[\mathcal{J}_\nu\,(1 + \frac{c^2}{2h\nu^3}\, I_\nu) - K\, I_\nu\right]$$

where

$\mathcal{J}_\nu$ = Radiative emission coefficient

K = Radiative absorption coefficient

Substituting into Eq. A.2

$$\frac{\partial I}{\partial t} + (\bar{\Omega}_1) \cdot \nabla I_\nu + \nu \frac{\partial}{\partial \nu} (\bar{\Omega}_1) =$$

$$c\left[\mathcal{J}_\nu \left(1 + \frac{c^2}{2h\nu^3} I_\nu\right) - K I_\nu \right] \tag{A.23}$$

and noting that

$$\nabla \cdot \bar{\Omega}_1 = 0$$

we can write

$$\frac{1}{c}\left[\frac{\partial I_\nu}{\partial t} + c\bar{\Omega}_1 \cdot \nabla I_\nu \right] = \mathcal{J}_\nu \left(1 + \frac{c^2}{2h\nu} I_\nu\right) - K I_\nu \tag{A.24}$$

which is identical to the expression given by Zel'dovich and Raizer Ref. A.5. In order to simplify Eq. A.24 the following observations are made. The emission term $\mathcal{J}_\nu$ can be expressed

$$\mathcal{J}_\nu = \alpha_\nu B_\nu \tag{A.25}$$

by using Kirchoff's law and assuming local thermodynamic equilibrium. Note that the effective volumetric absorption coefficient

$$\alpha_\nu = K\left[1 - \exp(-h\nu/k_c T) \right] \tag{A.26}$$

is the product of the absorption coefficient and the induced emission term. Therefore the emission term $\mathcal{J}_\nu$ has both spontaneous and induced emission taken into account. The spontaneous emission term is the Planck function.

$$B_\nu = \frac{2h\nu^3}{c^2} \frac{1}{\exp(+h\nu/k_c T) - 1} \tag{A.27}$$

Using these definitions Eq. A.24 can be rewritten as:

$$\frac{1}{c}\frac{\partial I_\nu}{\partial t} + \bar{\Omega}_1 \cdot \nabla I_\nu = \alpha_\nu (B_\nu - I_\nu) \tag{A.28}$$

If the radiative transfer Eq. A.28 is multiplied by $d\Omega$ and integrated over all directions the conservation of radiation equations is obtained

$$\frac{\partial \mathbb{U}_\nu}{\partial t} + \nabla \cdot \bar{q}_{R,\nu} = c\,\alpha_\nu (\mathbb{U}_{\nu p} - \mathbb{U}_\nu) \tag{A.29}$$

where

$$\mathbb{U}_{\nu p} = \frac{4\pi B_\nu}{c}$$

Let us assume

$$\frac{\partial \mathbb{U}_\nu}{\partial t} = \frac{1}{c}\int \frac{\partial I_\nu}{\partial t}\, d\Omega = 0$$

since c is very large. Then we may solve Eq. A.26 for the radiative flux divergence.

$$\nabla \cdot \bar{q}_R(\bar{r}_1) = \int_0^\infty \alpha_\nu \left(4\pi B_\nu - \int_0^{4\pi} I_\nu(\bar{r})\, d\Omega\right) d\nu \tag{A.30}$$

The contribution of the radiative flux divergence term in the energy equation has important mathematical ramifications. It should be noticed that the flux divergence term is evaluated by integrating over all space. The other terms in the energy equation are differentials calculated locally. The radiative flux divergence term therefore makes the energy equation an integro-partial-differential equation.

CONSERVATION EQUATIONS IN GENERAL ORTHOGONAL COORDINATES

From the previous section we have a vector formulation of the basic conservation equations for a reacting, radiating, conducting fluid. Most flow problems are represented by the conservation equations in orthogonal coordinates. In this section the basic conservation laws will be written in general curvilinear orthogonal coordinates. This permits one to select a useful coordinate system for a particular problem and thus determine the appropriate coordinate stretching functions. Substitution of the stretching functions into the conservation equations in curvilinear orthogonal coordinates will yield the appropriate governing equations for the problem of interest.

Table A.1 presents a set of physical tensor operations for orthogonal coordinate systems. By using the information in this table we are able to write the conservation equations in curvilinear orthogonal coordinates. The statement of these equations have been made in part by Back, Tsien, Brodkey, Ref's: A.6, A.7, and A.2 respectively, and others.

The steady state conservation equations can be stated as follows:

Global Continuity:

$$\nabla\cdot\rho\bar{V} = 0 \tag{A.31}$$

Species Continuity:

$$\nabla\cdot(\rho_i\bar{V}) + \nabla\cdot\bar{J}_i = \omega_i \tag{A.32}$$

TABLE A.1

Physical Tensor Operations in Orthogonal Coordinates

Vector Operation	Geometrical Components
1. Vector, $\bar{a}$ =	$\bar{E}_1 A_1 + \bar{E}_2 A_2 + \bar{E}_3 A_3$
2. Scalar or dot product, $\bar{a} \cdot b$ =	$\frac{A_1 B_1}{h_1^2} + \frac{A_2 B_2}{h_2^2} + \frac{A_3 B_3}{h_3^2}$
3. Vector or cross product, $\bar{a} \times b$ =	$(A_2 B_3 - A_3 B_2)\bar{E}_1 + (A_3 B_1 - A_1 B_3)\bar{E}_2 + (A_1 B_2 - A_2 B_1)\bar{E}_3$
4. Gradient of scalar, ∇U =	$\frac{\bar{E}_1}{h_1}\frac{\partial U}{\partial \xi_1} + \frac{\bar{E}_2}{h_2}\frac{\partial U}{\partial \xi_2} + \frac{\bar{E}_3}{h_3}\frac{\partial U}{\partial \xi_3}$
5. Gradient of vector, $\nabla \bar{a}$ =	W_{ij}; elements of W_{ij} are: $W_{ii} = \frac{1}{h_i}\frac{\partial A_i}{\partial \xi_i} + \frac{1}{h_j}\frac{\partial h_i}{\partial \xi_j}\frac{A_j}{h_i} + \frac{1}{h_k}\frac{\partial h_i}{\partial \xi_k}\frac{A_k}{h_i}$ $W_{ij} = \frac{1}{h_j}\frac{\partial A_i}{\partial \xi_j} - \frac{1}{h_i}\frac{\partial h_j}{\partial \xi_i}\frac{A_j}{h_j}$
6. Divergence of $\bar{a}$, $\nabla \cdot \bar{a}$ =	$\frac{1}{h_1 h_2 h_3}\left[\frac{\partial(h_2 h_3 A_1)}{\partial \xi_1} + \frac{\partial(h_1 h_3 A_2)}{\partial \xi_2} + \frac{\partial(h_1 h_2 A_3)}{\partial \xi_3}\right]$

(Table A.1 continued)

7. Curl of $\bar{a}$, $\nabla \times \bar{a} =$

$$\frac{1}{h_1 h_2 h_3}\begin{vmatrix} h_1\bar{E}_1 & h_2\bar{E}_2 & h_3\bar{E}_3 \\ \partial/\partial\xi_1 & \partial/\partial\xi_2 & \partial/\partial\xi_3 \\ h_1A_1 & h_2A_2 & h_3A_3 \end{vmatrix}$$

8. Laplacian of U,

$$\nabla^2 U = \nabla \cdot (\nabla U) = \frac{1}{h_1 h_2 h_3}\left[\frac{\partial}{\partial\xi_1}\left(\frac{h_2 h_3}{h_1}\frac{\partial U}{\partial\xi_1}\right) + \frac{\partial}{\partial\xi_2}\left(\frac{h_3 h_1}{h_2}\frac{\partial U}{\partial\xi_2}\right) + \frac{\partial}{\partial\xi_3}\left(\frac{h_1 h_2}{h_3}\frac{\partial U}{\partial\xi_3}\right)\right]$$

9. Laplacian of $\bar{a}$,

$$\nabla^2\bar{a} = \nabla(\nabla\cdot\bar{a}) - \nabla\times(\nabla\times\bar{a}) = \left\{\frac{1}{h_1}\frac{\partial}{\partial\xi_1}(\nabla\cdot\bar{a}) + \frac{1}{h_2 h_3}\left[\frac{\partial}{\partial\xi_3}\left\{\frac{h}{h_3 h_1}\left(\frac{\partial h_1 A_1}{\partial\xi_3} - \frac{\partial h_3 A_3}{\partial\xi_1}\right)\right\}\right.\right.$$

$$\left.\left. - \frac{\partial}{\partial\xi_2}\left\{\frac{h_3}{h_1 h_2}\left(\frac{\partial h_2 A_2}{\partial\xi_1} - \frac{\partial h_1 A_1}{\partial\xi_2}\right)\right\}\right]\right\}\bar{E}_1$$

$$+ \left\{\frac{1}{h_2}\frac{\partial}{\partial\xi_2}(\nabla\cdot\bar{a}) + \frac{1}{h_3 h_1}\left[\frac{\partial}{\partial\xi_1}\left\{\frac{h_3}{h_1 h_2}\left(\frac{\partial h_2 A_2}{\partial\xi_1} - \frac{\partial h_1 A_1}{\partial\xi_2}\right)\right\} - \frac{\partial}{\partial\xi_3}\left\{\frac{h_1}{h_2 h_3}\left(\frac{\partial h_3 A_3}{\partial\xi_2} - \frac{\partial h_2 A_2}{\partial\xi_3}\right)\right\}\right]\right\}\bar{E}_2$$

$$+ \left\{\frac{1}{h_3}\frac{\partial}{\partial\xi_3}(\nabla\cdot\bar{a}) + \frac{1}{h_1 h_2}\left[\frac{\partial}{\partial\xi_2}\left\{\frac{h_1}{h_2 h_3}\left(\frac{\partial h_3 A_3}{\partial\xi_2} - \frac{\partial h_2 A_2}{\partial\xi_3}\right)\right\} - \frac{\partial}{\partial\xi_1}\left\{\frac{h_1}{h_3 h_1}\left(\frac{\partial h_1 A_1}{\partial\xi_3} - \frac{\partial h_3 A_3}{\partial\xi_1}\right)\right\}\right]\right\}\bar{E}_3$$

(Table A.1 continued)

10. $$(\bar{a} \cdot \nabla) U = \frac{A_1}{h_1} \frac{\partial U}{\partial \xi_1} + \frac{A_2}{h_2} \frac{\partial U}{\partial \xi_2} + \frac{A_3}{h_3} \frac{\partial U}{\partial \xi_3}$$

11. $$(\bar{a} \cdot \nabla) \bar{b} = \frac{1}{h_1} \left\{ \left(A_1 \frac{\partial B_1}{\partial \xi_1} + A_2 \frac{\partial B_2}{\partial \xi_1} + A_3 \frac{\partial B_3}{\partial \xi_1} \right) - \frac{A_2}{h_2} \left(\frac{\partial h_2 B_2}{\partial \xi_1} - \frac{\partial h_1 B_1}{\partial \xi_2} \right) \right.$$
$$\left. + \frac{A_3}{h_3} \left(\frac{\partial h_1 B_1}{\partial \xi_3} - \frac{\partial h_3 B_3}{\partial \xi_1} \right) \right\} \bar{E}_1 + \frac{1}{h_2} \left\{ \left(A_1 \frac{\partial B_1}{\partial \xi_2} + A_2 \frac{\partial B_2}{\partial \xi_2} + A_3 \frac{\partial B_3}{\partial \xi_2} \right) \right.$$
$$\left. - \frac{A_3}{h_3} \left(\frac{\partial h_3 B_3}{\partial \xi_2} - \frac{\partial h_2 B_2}{\partial \xi_3} \right) + \frac{A_1}{h_1} \left(\frac{\partial h_2 B_2}{\partial \xi_1} - \frac{\partial h_1 B_1}{\partial \xi_2} \right) \right\} \bar{E}_2$$
$$+ \frac{1}{h_3} \left\{ \left(A_1 \frac{\partial B_1}{\partial \xi_3} + A_2 \frac{\partial B_2}{\partial \xi_3} + A_3 \frac{\partial B_3}{\partial \xi_3} \right) - \frac{A_1}{h_1} \left(\frac{\partial h_1 B_1}{\partial \xi_3} - \frac{\partial h_3 B_3}{\partial \xi_1} \right) \right.$$
$$\left. + \frac{A_2}{h_2} \left(\frac{\partial h_3 B_3}{\partial \xi_2} - \frac{\partial h_2 B_2}{\partial \xi_3} \right) \right\} \bar{E}_3$$

(Table A.1 continued)

12. Divergence of a symmetric tensor, $\nabla \cdot \bar{\bar{W}}$
Note: $W_{ij} = W_{ji}$

$$\nabla\cdot\bar{\bar{W}} = (\nabla\cdot\bar{\bar{W}})_1\bar{E}_1 + (\nabla\cdot\bar{\bar{W}})_2\bar{E}_2 + (\nabla\cdot\bar{\bar{W}})_3\bar{E}_3$$

$$(\nabla\cdot\bar{\bar{W}})_1 = \frac{1}{h_1h_2h_3}\left[\frac{\partial}{\partial\xi_1}(h_2h_3W_{11}) + \frac{\partial}{\partial\xi_2}(h_1h_3W_{12}) + \frac{\partial}{\partial\xi_3}(h_1h_2W_{13})\right]$$
$$+ \frac{W_{12}}{h_1h_2}\frac{\partial h_1}{\partial\xi_2} + \frac{W_{31}}{h_1h_3}\frac{\partial h_1}{\partial\xi_3} - \frac{W_{22}}{h_1h_2}\frac{\partial h_2}{\partial\xi_1} - \frac{W_{33}}{h_1h_3}\frac{\partial h_3}{\partial\xi_1}$$

$$(\nabla\cdot\bar{\bar{W}})_2 = \frac{1}{h_1h_2h_3}\left[\frac{\partial}{\partial\xi_1}(h_2h_3W_{12}) + \frac{\partial}{\partial\xi_2}(h_1h_3W_{22}) + \frac{\partial}{\partial\xi_3}(h_1h_2W_{23})\right]$$
$$+ \frac{W_{12}}{h_1h_2}\frac{\partial h_2}{\partial\xi_1} + \frac{W_{23}}{h_2h_3}\frac{\partial h_2}{\partial\xi_3} - \frac{W_{11}}{h_1h_2}\frac{\partial h_1}{\partial\xi_2} - \frac{W_{33}}{h_2h_3}\frac{\partial h_3}{\partial\xi_2}$$

$$(\nabla\cdot\bar{\bar{W}})_3 = \frac{1}{h_1h_2h_3}\left[\frac{\partial}{\partial\xi_1}(h_2h_3W_{31}) + \frac{\partial}{\partial\xi_2}(h_1h_3W_{32}) + \frac{\partial}{\partial\xi_3}(h_1h_2W_{33})\right]$$
$$+ \frac{W_{31}}{h_1h_3}\frac{\partial h_3}{\partial\xi_1} + \frac{W_{23}}{h_2h_3}\frac{\partial h_3}{\partial\xi_2} - \frac{W_{11}}{h_1h_2}\frac{\partial h_1}{\partial\xi_3} - \frac{W_{22}}{h_2h_3}\frac{\partial h_2}{\partial\xi_3}$$

(Table A.1 continued)

13. $\bar{\bar{w}}:(\nabla\bar{b})$ =

For $\bar{\bar{w}}$ being a symmetric tensor

$$W_{11}\left(\frac{1}{h_1}\frac{\partial B_1}{\partial \xi_1} + \frac{B_2}{h_1 h_2}\frac{\partial h_1}{\partial \xi_2} + \frac{B_3}{h_1 h_3}\frac{\partial h_1}{\partial \xi_3}\right)$$

$$+ W_{22}\left(\frac{1}{h_2}\frac{\partial B_2}{\partial \xi_2} + \frac{B_1}{h_1 h_2}\frac{\partial h_2}{\partial \xi_1} + \frac{B_3}{h_2 h_3}\frac{\partial h_2}{\partial \xi_3}\right)$$

$$+ W_{33}\left(\frac{1}{h_3}\frac{\partial B_3}{\partial \xi_3} + \frac{B_1}{h_1 h_3}\frac{\partial h_3}{\partial \xi_1} + \frac{B_2}{h_2 h_3}\frac{\partial h_3}{\partial \xi_2}\right)$$

$$+ W_{12}\left(\frac{1}{h_2}\frac{\partial B_1}{\partial \xi_2} + \frac{1}{h_1}\frac{\partial B_2}{\partial \xi_1} - \frac{B_2}{h_1 h_2}\frac{\partial h_2}{\partial \xi_1} - \frac{B_1}{h_1 h_2}\frac{\partial h_1}{\partial \xi_2}\right)$$

$$+ W_{13}\left(\frac{1}{h_3}\frac{\partial B_1}{\partial \xi_3} + \frac{1}{h_1}\frac{\partial B_3}{\partial \xi_1} - \frac{B_3}{h_1 h_3}\frac{\partial h_3}{\partial \xi_1} - \frac{B_1}{h_1 h_3}\frac{\partial h_1}{\partial \xi_3}\right)$$

$$+ W_{23}\left(\frac{1}{h_3}\frac{\partial B_2}{\partial \xi_3} + \frac{1}{h_2}\frac{\partial B_3}{\partial \xi_2} - \frac{B_3}{h_2 h_3}\frac{\partial h_3}{\partial \xi_2} - \frac{B_2}{h_2 h_3}\frac{\partial h_2}{\partial \xi_3}\right)$$

(Table A.1 continued)

14 $\nabla\cdot\bar{\bar{w}}\cdot\bar{b}$ =

$$\frac{1}{h_1h_2h_3}\left\{\frac{\partial}{\partial\xi_1}\left[h_2h_3(W_{11}B_1 + W_{21}B_2 + W_{31}B_3)\right] + \frac{\partial}{\partial\xi_2}\left[h_1h_3(W_{12}B_1\right.\right.$$

$$\left.\left. + W_{22}B_2 + W_{32}B_3)\right] + \frac{\partial}{\partial\xi_3}\left[h_1h_2(W_{13}B_1 + W_{23}B_2 + W_{33}B_3)\right]\right\}$$

For $\bar{\bar{w}}$ being a symmetric tensor

scalar	U	tensor	$\bar{\bar{w}}$ components $\{W_{ij}\}$
unit vectors	$\bar{E}_1, \bar{E}_2, \bar{E}_3$	orthogonal coordinates	ξ_1, ξ_2, ξ_3
vectors $\bar{a}$, $\bar{b}$	components $\{A_1, A_2, A_3\}$, $\{B_1, B_2, B_3\}$	stretching functions	h_1, h_2, h_3

Momentum:

$$\rho(\bar{V}\cdot\nabla)\bar{V} - \bar{g} - \bar{\bar{\tau}} - \bar{\bar{P}}_R) - \sum_i \rho_i \bar{g}_i = 0 \qquad \text{(A.33)}$$

Energy:

$$\rho(\bar{V}\cdot\nabla)E + \nabla\cdot(\bar{q}_D + \bar{q}_R) + \sum_i \bar{g}_i\cdot\bar{J}_i - \nabla\cdot(\bar{\bar{\tau}} - \bar{\bar{I}}P + \bar{\bar{P}}_R)\cdot\bar{V} - S\rho = 0 \qquad \text{(A.34)}$$

The energy equation may also be written as follows:

$$\rho(\bar{V}\cdot\nabla)H + \nabla\cdot(\bar{q}_D + \bar{q}_R) + \sum_i \bar{g}_i\cdot\bar{J}_i - \nabla\cdot(\bar{\bar{\tau}} + \bar{\bar{P}}_R)\cdot\bar{V} - S\rho = 0 \qquad \text{(A.35)}$$

This form is presented by Ref. A.3 without the radiation or internal heat source term.

For the purpose of writing the conservation equations in curvilinear orthogonal coordinates, the coordinates are chosen to be ξ_1, ξ_2, and ξ_3 corresponding to ξ_1, ξ_2, and ξ_3 of Tab. A.1 respectively. The differential elements of length in the respective coordinate directions are $h_1 d\xi_1$, $h_2 d\xi_2$, and $h_3 d\xi_3$ such that a differential arc length can be expressed as

$$(d\zeta)^2 = h_1^2(d\xi_1)^2 + h_2^2(d\xi_2)^2 + h_3^2(d\xi_3)^2 \qquad \text{(A.36)}$$

where h_1, h_2, and h_3 are called the "stretching functions" in the respective coordinate directions. In the following equations u, v, and w are the velocity components of $\bar{V}$ in the direction of increasing ξ_1, ξ_2, and ξ_3.

Applying the ∇ operator from Tab. A.1 the global continuity equation becomes

$$\frac{1}{h_1 h_2 h_3}\left[\frac{\partial(h_2 h_3 \rho u)}{\partial \xi_1} + \frac{\partial(h_1 h_3 \rho v)}{\partial \xi_2} + \frac{\partial(h_1 h_2 \rho w)}{\partial \xi_3}\right] = 0 \qquad \text{(A.37)}$$

In a similar manner the species continuity equation can be written

$$\frac{1}{h_1 h_2 h_3}\left[\frac{\partial(h_2 h_3 \rho_i u)}{\partial \xi_1} + \frac{\partial(h_1 h_3 \rho_i v)}{\partial \xi_2} + \frac{\partial(h_1 h_2 \rho_i w)}{\partial \xi_3}\right] +$$

$$\frac{1}{h_1 h_2 h_3}\left[\frac{\partial(h_1 h_3 J_{i,\xi_1})}{\partial \xi_1} + \frac{\partial(h_1 h_3 J_{i,\xi_2})}{\partial \xi_2} + \frac{\partial(h_1 h_2 J_{i,\xi_3})}{\partial \xi_3}\right] -$$

$$\omega_i = 0 \qquad \text{(A.38)}$$

In order to evaluate the above equation the components J_{i,ξ_1}, J_{i,ξ_2}, and J_{i,ξ_3} of the mass flux vector $\bar{J}_i$ must be specified. The mass flux vector for a wide range of fluid problems is well represented by two terms

$$\bar{J}_{i_{(D)}} = \bar{J}_i^{(D)} + \bar{J}_i^{(T)} \qquad \text{(A.39)}$$

The expressions for there two mass flux vectors are

$$\bar{J}_i^{(D)} = \frac{n_t^2}{\rho \mathbb{R} T} \sum_{j=1}^{n} M_i M_j D_{ij}\left[Y_j \sum_{\substack{k=1 \\ k\neq j}}^{n} \left(\frac{\partial G_j}{\partial Y_k}\right)_{T,\forall,Y_\ell} \nabla Y_k\right] \qquad \text{(A.7)}$$

$$\bar{J}_i^{(T)} = - D_i^T \nabla \ell n\, T \qquad \text{(A.8)}$$

The transformed components of the above equations are

$$J^{(D)}_{i,\xi_1} = \frac{n_t^2}{\rho \mathcal{R} T} \sum_{j=1}^{n} M_i M_j D_{ij} \left[Y_j \sum_{\substack{k=1 \\ k\neq j}}^{n} \left(\frac{\partial G_j}{\partial Y_k}\right)_{T,\forall,Y_{\ell\neq j,k}} \frac{1}{h_1} \frac{\partial Y_k}{\partial \xi_1} \right]$$

$$J^{(D)}_{i,\xi_2} = \frac{n_t^2}{\rho \mathcal{R} T} \sum_{j=1}^{n} M_i M_j D_{ij} \left[Y_j \sum_{\substack{k=1 \\ k\neq j}}^{n} \left(\frac{\partial G_j}{\partial Y_k}\right)_{T,\forall,Y_{\ell\neq j,k}} \frac{1}{h_2} \frac{\partial Y_k}{\partial \xi_2} \right] \qquad \text{(A.40)}$$

$$J^{(D)}_{i,\xi_3} = \frac{n_t^2}{\rho \mathcal{R} T} \sum_{j=1}^{n} M_i M_j D_{ij} \left[Y_j \sum_{\substack{k=1 \\ k\neq j}}^{n} \left(\frac{\partial G_j}{\partial Y_k}\right)_{T,\forall,Y_{\ell\neq j,k}} \frac{1}{h_3} \frac{\partial Y_k}{\partial \xi_3} \right]$$

$$J^{(T)}_{i,\xi_1} = \frac{-D_i^T}{h_1} \frac{\partial(\ell n\ T)}{\partial\ \xi_1}$$

$$J^{(T)}_{i,\xi_2} = \frac{-D_i^T}{h_2} \frac{\partial(\ell n\ T)}{\partial\ \xi_2} \qquad \text{(A.41)}$$

$$J^{(T)}_{i,\xi_3} = \frac{-D_i^T}{h_3} \frac{\partial(\ell n\ T)}{\partial\ \xi_3}$$

For substitution into the species continuity equation

$$J_{i,\xi_1} = J^{(D)}_{i,\xi_1} + J^{(T)}_{i,\xi_1}$$

$$J_{i,\xi_2} = J^{(D)}_{i,\xi_2} + J^{(T)}_{i,\xi_2} \qquad \text{(A.42)}$$

$$J_{i,\xi_3} = J^{(D)}_{i,\xi_3} + J^{(T)}_{i,\xi_3}$$

This completes the necessary operations to explicitly write the species continuity equation in general orthogonal coordinates.

Before writing the momentum and energy equations in general orthogonal coordinates the radiation pressure tensor and external force field terms are dropped.* The resulting vector form of the two equations are

Momentum:

$$\rho(\bar{V} \cdot \nabla)\bar{V} - \nabla \cdot (\bar{\bar{\tau}} - \bar{\bar{I}}P) = 0 \tag{A.43}$$

Energy:

$$\rho(\bar{V} \cdot \nabla)H + \nabla \cdot (\bar{q}_D + \bar{q}_R) - \nabla \cdot (\bar{\bar{\tau}}) \cdot \bar{V} = 0 \tag{A.44}$$

If the need to account for the additional effects should arise, the appropriate terms could be added to the governing equations in an analogous manner to the terms which will be considered.

Using the definitions in Tab. A.1, the momentum equation can be written in the three orthogonal directions.

ξ_1 - momentum:

$$\begin{aligned}
&\frac{u}{h_1}\frac{\partial u}{\partial \xi_1} + \frac{v}{h_2}\frac{\partial u}{\partial \xi_2} + \frac{w}{h_3}\frac{\partial u}{\partial \xi_3} + \frac{uv}{h_1 h_2}\frac{\partial h_1}{\partial \xi_2} + \frac{uw}{h_1 h_3}\frac{\partial h_1}{\partial \xi_3} \\
&- \frac{v^2}{h_1 h_2}\frac{\partial h_2}{\partial \xi_1} - \frac{w^2}{h_1 h_3}\frac{\partial h_3}{\partial \xi_1} + \frac{1}{\rho}\frac{1}{h_1}\frac{\partial P}{\partial \xi_1} \\
&- \frac{1}{\rho}\left[\frac{1}{h_1 h_2 h_3}\left(\frac{\partial(h_2 h_3 \tau_{11})}{\partial \xi_1} + \frac{\partial(h_1 h_2 \tau_{12})}{\partial \xi_2} + \frac{\partial(h_1 h_3 \tau_{13})}{\partial \xi_3}\right)\right. \\
&\left. + \frac{\tau_{12}}{h_1 h_2}\frac{\partial h_1}{\partial \xi_2} + \frac{\tau_{13}}{h_1 h_3}\frac{\partial h_1}{\partial \xi_3} - \frac{\tau_{22}}{h_1 h_2}\frac{\partial h_2}{\partial \xi_1} - \frac{\tau_{33}}{h_1 h_3}\frac{\partial h_3}{\partial \xi_1}\right] = 0
\end{aligned} \tag{A.45}$$

* These terms are not usually significant for gas dynamic problems.

ξ_2 - momentum:

$$\frac{u}{h_1}\frac{\partial v}{\partial \xi_1} + \frac{v}{h_2}\frac{\partial v}{\partial \xi_2} + \frac{w}{h_3}\frac{\partial v}{\partial \xi_3} + \frac{uv}{h_1 h_2}\frac{\partial h_2}{\partial \xi_1} + \frac{vw}{h_2 h_3}\frac{\partial h_2}{\partial \xi_3}$$

$$- \frac{u^2}{h_1 h_2}\frac{\partial h_1}{\partial \xi_2} - \frac{w^2}{h_2 h_3}\frac{\partial h_3}{\partial \xi_2} + \frac{1}{\rho}\frac{1}{h_2}\frac{\partial P}{\partial \xi_2} \qquad \text{(A.46)}$$

$$- \frac{1}{\rho}\left[\frac{1}{h_1 h_2 h_3}\left(\frac{\partial(h_2 h_3 \tau_{12})}{\partial \xi_1} + \frac{\partial(h_1 h_3 \tau_{22})}{\partial \xi_2} + \frac{\partial(h_1 h_2 \tau_{32})}{\partial \xi_3}\right)\right.$$

$$\left. + \frac{\tau_{12}}{h_1 h_2}\frac{\partial h_2}{\partial \xi_1} + \frac{\tau_{23}}{h_2 h_3}\frac{\partial h_2}{\partial \xi_3} - \frac{\tau_{11}}{h_1 h_2}\frac{\partial h_1}{\partial \xi_2} - \frac{\tau_{33}}{h_2 h_3}\frac{\partial h_3}{\partial \xi_2}\right] = 0$$

ξ_3 - momentum:

$$\frac{u}{h_1}\frac{\partial w}{\partial \xi_1} + \frac{v}{h_2}\frac{\partial w}{\partial \xi_2} + \frac{w}{h_3}\frac{\partial w}{\partial \xi_3} + \frac{wu}{h_1 h_3}\frac{\partial h_3}{\partial \xi_1} + \frac{wv}{h_2 h_3}\frac{\partial h_3}{\partial \xi_2}$$

$$- \frac{u^2}{h_1 h_3}\frac{\partial h_1}{\partial \xi_2} - \frac{w^2}{h_2 h_3}\frac{\partial h_2}{\partial \xi_3} + \frac{1}{\rho}\frac{1}{h_3}\frac{\partial P}{\partial \xi_3} \qquad \text{(A.47)}$$

$$- \frac{1}{\rho}\left[\frac{1}{h_1 h_2 h_3}\left(\frac{\partial(h_2 h_3 \tau_{13})}{\partial \xi_1} + \frac{\partial(h_1 h_3 \tau_{23})}{\partial \xi_2} + \frac{\partial(h_1 h_2 \tau_{33})}{\partial \xi_3}\right)\right.$$

$$\left. + \frac{\tau_{31}}{h_1 h_3}\frac{\partial h_3}{\partial \xi_1} + \frac{\tau_{23}}{h_2 h_3}\frac{\partial h_3}{\partial \xi_2} - \frac{\tau_{11}}{h_1 h_3}\frac{\partial h_1}{\partial \xi_3} - \frac{\tau_{22}}{h_2 h_3}\frac{\partial h_2}{\partial \xi_3}\right] = 0$$

In the above equations, the subscripts 1, 2, and 3 in the symmetric stress tensor denote the coordinate directions ξ_1, ξ_2, and ξ_3 respectively. In order to evaluate the three momentum equations the components of the viscous stress tensor must be defined. For a Stokes' fluid the stress tensor is defined by, Ref. A.2, in terms of the rate of strain tensor $\bar{\bar{e}}$.

$$\bar{\bar{\tau}} = f(\bar{\bar{e}})$$

The simplest form for this equation in three dimensions is (Ref. A.2)

$$\bar{\bar{\tau}} = A\bar{\bar{I}} + B\bar{\bar{e}} + C\bar{\bar{e}} \cdot \bar{\bar{e}} \tag{A.48}$$

For a Newtonian fluid

$$A = -\left(\frac{2}{3}\mu - \tilde{\mu}\right)\nabla \cdot \bar{V}, \quad B = +\mu, \quad C = 0 \tag{A.49}$$

The stress tensor may now be written as

$$\bar{\bar{\tau}} = \lambda\bar{\bar{I}}\nabla \cdot \bar{V} + \mu\bar{\bar{e}} \tag{A.50}$$

The components of the stress tensor are

$$\left.\begin{aligned} \tau_{11} &= \lambda\nabla \cdot \bar{V} + \mu e_{11} \\ \tau_{22} &= \lambda\nabla \cdot \bar{V} + \mu e_{22} \\ \tau_{33} &= \lambda\nabla \cdot \bar{V} + \mu e_{33} \end{aligned}\right\} \tag{A.51a}$$

$$\left.\begin{aligned} \tau_{12} &= \tau_{21} = \mu e_{12} \\ \tau_{13} &= \tau_{31} = \mu e_{13} \\ \tau_{23} &= \tau_{32} = \mu e_{23} \end{aligned}\right\} \tag{A.51b}$$

Which may be written

$$\tau_{11} = \frac{\lambda}{h_1 h_2 h_3}\left[\frac{\partial(h_2 h_3 u)}{\partial \xi_1} + \frac{\partial(h_1 h_3 v)}{\partial \xi_2} + \frac{\partial(h_1 h_2 w)}{\partial \xi_3}\right] + 2\mu\left[\frac{1}{h_1}\frac{\partial u}{\partial \xi_1} + \frac{v}{h_1 h_2}\frac{\partial h_1}{\partial \xi_2} + \frac{w}{h_3 h_1}\frac{\partial h_1}{\partial \xi_3}\right] \tag{A.52}$$

$$\tau_{22} = \frac{\lambda}{h_1 h_2 h_3}\left[\frac{\partial(h_2 h_3 u)}{\partial \xi_1} + \frac{\partial(h_1 h_3 v)}{\partial \xi_2} + \frac{\partial(h_1 h_2 w)}{\partial \xi_3}\right]$$

$$+ 2\mu\left[\frac{1}{h_2}\frac{\partial v}{\partial \xi_2} + \frac{w}{h_2 h_3}\frac{\partial h_2}{\partial \xi_3} + \frac{u}{h_1 h_2}\frac{\partial h_2}{\partial \xi_1}\right] \tag{A.53}$$

$$\tau_{33} = \frac{\lambda}{h_1 h_2 h_3}\left[\frac{\partial(h_2 h_3 u)}{\partial \xi_1} + \frac{\partial(h_1 h_3 v)}{\partial \xi_2} + \frac{\partial(h_1 h_2 w)}{\partial \xi_3}\right]$$

$$+ 2\mu\left[\frac{1}{h_3}\frac{\partial w}{\partial \xi_3} + \frac{u}{h_1 h_3}\frac{\partial h_3}{\partial \xi_1} + \frac{v}{h_2 h_3}\frac{\partial h_3}{\partial \xi_2}\right] \tag{A.54}$$

$$\tau_{12} = \tau_{21} = \mu\left[\frac{h_2}{h_1}\frac{\partial}{\partial \xi_1}\left(\frac{v}{h_2}\right) + \frac{h_1}{h_2}\frac{\partial}{\partial \xi_2}\left(\frac{u}{h_1}\right)\right] \tag{A.55}$$

$$\tau_{13} = \tau_{31} = \mu\left[\frac{h_1}{h_3}\frac{\partial}{\partial \xi_3}\left(\frac{u}{h_1}\right) + \frac{h_3}{h_1}\frac{\partial}{\partial \xi_1}\left(\frac{w}{h_3}\right)\right] \tag{A.56}$$

$$\tau_{23} = \tau_{32} = \mu\left[\frac{h_3}{h_2}\frac{\partial}{\partial \xi_2}\left(\frac{w}{h_3}\right) + \frac{h_2}{h_3}\frac{\partial}{\partial \xi_3}\left(\frac{v}{h_2}\right)\right] \tag{A.57}$$

With the preceding definition of the stress tensor, the momentum equations become three equations expressed in the three components of the velocity vector.

The total enthalpy form of the energy equation Eq. A.44 may be written in general orthogonal coordinates by noting the form of the three operators expressed in Tab. A.1.

$$\rho\left[\frac{u}{h_1}\frac{\partial H}{\partial \xi_1} + \frac{v}{h_2}\frac{\partial H}{\partial \xi_2} + \frac{w}{h_3}\frac{\partial H}{\partial \xi_3}\right] = \frac{-1}{h_1h_2h_3}\left[\frac{\partial(h_2h_3q_{D,1})}{\partial \xi_1}\right.$$

$$\left. + \frac{\partial(h_1h_3q_{D,2})}{\partial \xi_2} + \frac{\partial(h_1h_2q_{D,3})}{\partial \xi_3}\right] - \frac{1}{h_1h_2h_3}\left[\frac{\partial(h_2h_3q_{R,1})}{\partial \xi_1}\right.$$

$$\left. + \frac{\partial(h_1h_3q_{R,2})}{\partial \xi_2} + \frac{\partial(h_1h_2q_{R,3})}{\partial \xi_3}\right] + \frac{1}{h_1h_2h_3}\left[\frac{-\partial\{h_2h_3(\tau_{11}u+\tau_{21}v+\tau_{31}w)\}}{\partial \xi_1}\right.$$

$$\left. + \frac{\partial\{h_1h_3(\tau_{12}u+\tau_{22}v+\tau_{32}w)\}}{\partial \xi_2} + \frac{\partial\{h_1h_2(\tau_{12}u+\tau_{23}v+\tau_{33}w)\}}{\partial \xi_3}\right] \qquad (A.58)$$

The components of the shear stress have been defined in the discussion of the momentum equation. Therefore only the components of the heat flux vectors are left to be defined to provide a complete statement of the energy equation.

The heat flux vector as handled previously will be described as the sum of the diffusional and radiative heat flux vectors. The diffusional heat flux vector can be expressed as a function of the mass flux vector by simple manipulation of the equation given by

$$\bar{q}_D = -k'\nabla T + \sum_i h_i\bar{J}_i - Nk_cT\sum_i \frac{D_i^T}{N_im_i}\nabla\left(\frac{N_i}{N}\right) \qquad (A.59a)$$

where k' is not the ordinary thermal conductivity coefficient. The usual form of the diffusional heat flux vector is written in terms of diffusion velocities or mass flux vectors. This form eliminates $\nabla(\frac{N_i}{N})$ from the preceding equation and adds a term to k' yielding the ordinary thermal conductivity. This step also introduces the binary diffusion coefficient into the Dufour effect term. Following Hirschfelder et. al., Ref. A.8, and substituting for the diffusion velocities yields:

$$\bar{q}_D = -k\nabla T + \sum_i h_i \bar{J}_i - \frac{P}{N^2} \sum_i \sum_{j\neq i} \frac{N_i}{m_i} \frac{D_i^T}{\mathbb{D}_{ij}} \left(\frac{\bar{J}_i}{\rho_j} - \frac{\bar{J}_i}{\rho_i} \right) \qquad \text{(A.59b)}^{\#}$$

where $\mathbb{D}_{ij}$ is the binary diffusion coefficient

$$\mathbb{D}_{ij} = \frac{3(M_i + M_j)P}{16N^2 M_i M_j \Omega_{ij}^{(1,1)}} \qquad \text{(A.60)}$$

The diffusional heat flux vector contains terms which respectively represent conductive energy flux, diffusional energy flux, and diffusion-thermo (Dufour) energy flux. The Dufour effect is kept in the above equation to be consistent with keeping the Soret effect in the species continuity equation. At this point it is appropriate to point out that the thermal conductivity in the conductive flux term is in general a tensor. For the case of an isentropic fluid, the conductivity reduces to a scalar. This is the form used in the diffusional energy flux vector above.

Having stated the vector form of the diffusional heat flux vector, the components needed in the energy equation can be expressed.

$$q_{D,1} = -\frac{k}{h_1} \frac{\partial T}{\partial \xi_1} + \sum_i h_i J_{i,\xi_1} - \frac{P}{N^2} \sum_i \sum_{j\neq i} \frac{N_i}{m_i} \frac{D_i^T}{\mathbb{D}_{ij}} \left(\frac{J_{j,\xi_1}}{\rho_j} - \frac{J_{i,\xi_1}}{\rho_i} \right) \qquad \text{(A.61)}$$

The perfect gas equation of state has been used to replace $k_c T$ in these equations from Ref. A.8 with P/N.

$$q_{D,2} = -\frac{k}{h_2}\frac{\partial T}{\partial \xi_2} + \sum_i h_i J_{i,\xi_2} - \frac{P}{N^2}\sum_i \sum_{j\neq i} \frac{N_i}{m_i}\frac{D_i^T}{\mathbb{D}_{ij}}\left(\frac{J_{j,\xi_2}}{\rho_j} - \frac{J_{i,\xi_2}}{\rho_i}\right) \tag{A.62}$$

$$q_{D,3} = -\frac{k}{h_3}\frac{\partial T}{\partial \xi_3} + \sum_i h_i J_{i,\xi_3} - \frac{P}{N^2}\sum_i \sum_{j\neq i} \frac{N_i}{m_i}\frac{D_i^T}{\mathbb{D}_{ij}}\left(\frac{J_{j,\xi_3}}{\rho_j} - \frac{J_{i,\xi_3}}{\rho_i}\right) \tag{A.63}$$

where the components of the mass flux vector used in the above expression are defined in the discussion of the species continuity equation.

To calculate the components of the radiative flux vector q_{R,ξ_i} where ξ_i is an orthogonal coordinate, let us integrate Eq. A.30.

$$\bar{q}_R(\bar{r}_1) = \int_{\bar{r}_0}^{\bar{r}_1} \nabla \cdot \bar{q}_R d\bar{r} = \int_{\bar{r}_0}^{\bar{r}_1} \nabla \cdot \bar{q}_R (h_1 \bar{e}_1 d\xi_1 + h_2 \bar{e}_2 d\xi_2 + h_3 \bar{e}_3 d\xi_3) \tag{A.64}$$

Note that $\nabla \cdot \bar{q}_R$ is a scalar independent of coordinate system. The flux components may be written:

$$q_{R,\xi_i} = \int_{\bar{r}_0}^{\bar{r}_1} (\nabla \cdot \bar{q}_R) h_i d\xi_i \tag{A.65}$$

or by substituting from Eq. A.30

$$q_{R,1} = \int_{\xi(\bar{r}_0)}^{\xi(\bar{r}_1)} \int_0^\infty \alpha_\nu \left(4\pi B_\nu - \int_0^{4\pi} I_\nu(\bar{r}) d\Omega\right) d\nu h_1 d\xi_1 \tag{A.66}$$

$$q_{R,2} = \int_{\xi(\bar{r}_0)}^{\xi(\bar{r}_1)} \int_0^{\infty} \alpha_\nu \left(4\pi B_\nu - \int_0^{4\pi} I_\nu(\bar{r})\, d\Omega \right) d\nu h_2 d\xi_2 \qquad \text{(A.67)}$$

$$q_{R,3} = \int_{\xi(\bar{r}_0)}^{\xi(\bar{r}_1)} \int_0^{\infty} \alpha_\nu \left(4\pi B_\nu - \int_0^{4\pi} I_\nu(\bar{r})\, d\Omega \right) d\nu h_3 d\xi_3 \qquad \text{(A.68)}$$

In addition to the general conservation equations an equation of state is needed to specify the relationship between pressure and temperature. A reasonable approximation for the thermal behavior of a gaseous mixture is the ideal gas equation of state.

$$P = \rho RT \sum C_i / M_i \qquad \text{(A.69)}$$

Another form of the ideal gas equation of state is

$$P = N k_c T \qquad \text{where} \quad \sum_i N_i = N \qquad \text{(A.70)}$$

This last expression has been used previously to state Eq.'s A.59 and A.60.

CONSERVATION EQUATIONS IN BODY ORIENTED COORDINATES

In order to describe the flow over blunt bodies moving at hypersonic velocities, it is found convenient to solve the conservation equations in orthogonal body oriented coordinate systems. The type of body under consideration, i.e. three-dimensional, axisymmetric or two dimensional, thus determine the stretching functions, h_1, h_2, h_3, discussed in the previous section. The class of bodies considered in this development are axisymmetric or two-dimensional and have the following stretching functions, see Tab. A.2:

$$\left.\begin{aligned} \xi_1 &= x, & h_1 &= 1 + \varkappa y \\ \xi_2 &= y, & h_2 &= 1 \\ \xi_3 &= \varphi, & h_3 &= r \end{aligned}\right\} \quad \text{AXISYMMETRIC} \tag{A.71}$$

$$\left.\begin{aligned} \xi_1 &= x, & h_1 &= 1 + \varkappa y \\ \xi_2 &= y, & h_2 &= 1 \\ \xi_3 &= z, & h_3 &= 1 \end{aligned}\right\} \quad \text{TWO-DIMENSIONAL} \tag{A.72}$$

where $\varkappa$ is the local body curvature and r is defined in Fig. A.3. Using Fig. A.3 the following relationship may be found

$$r = r_w + y \sin \theta \tag{A.73}$$

$$dr = \sin \theta \, dy + \tilde{\varkappa} \cos \theta \, dx \tag{A.74}$$

where

$$\tilde{\varkappa} = 1 + \varkappa y \tag{A.75}$$

Table A.2 Coordinate Systems and Stretching Functions

1. Orthogonal coordinate system, and 2. orthogonal coordinates ξ_1, ξ_2, ξ_3	Rectangular coordinates			Stretching functions h_1 h_2 h_3		
	x	y	z	h_1	h_2	h_3
Cylindrical r, θ, z	r cos θ	r sin θ	z	1	r	1
Spherical r, φ, θ	r cos θ sin φ	r sin θ sin φ	r cos θ	1	r	r sin φ
Parabolic cylindrical ξ, η, z	$\frac{1}{2}(\xi^2 - \eta^2)$	$\xi\eta$	z	$\sqrt{\xi^2 + \eta^2}$	$\sqrt{\xi^2 + \eta^2}$	1
Local coordinates along surface x, y, z	-	-	-	$1 + \kappa y$	1	1
Local coordinates along surface Symmetric about axis x, y, φ	-	-	-	$1 + \kappa y$	1	r

Note: Additional coordinate systems are considered by Back, Ref. A.6.

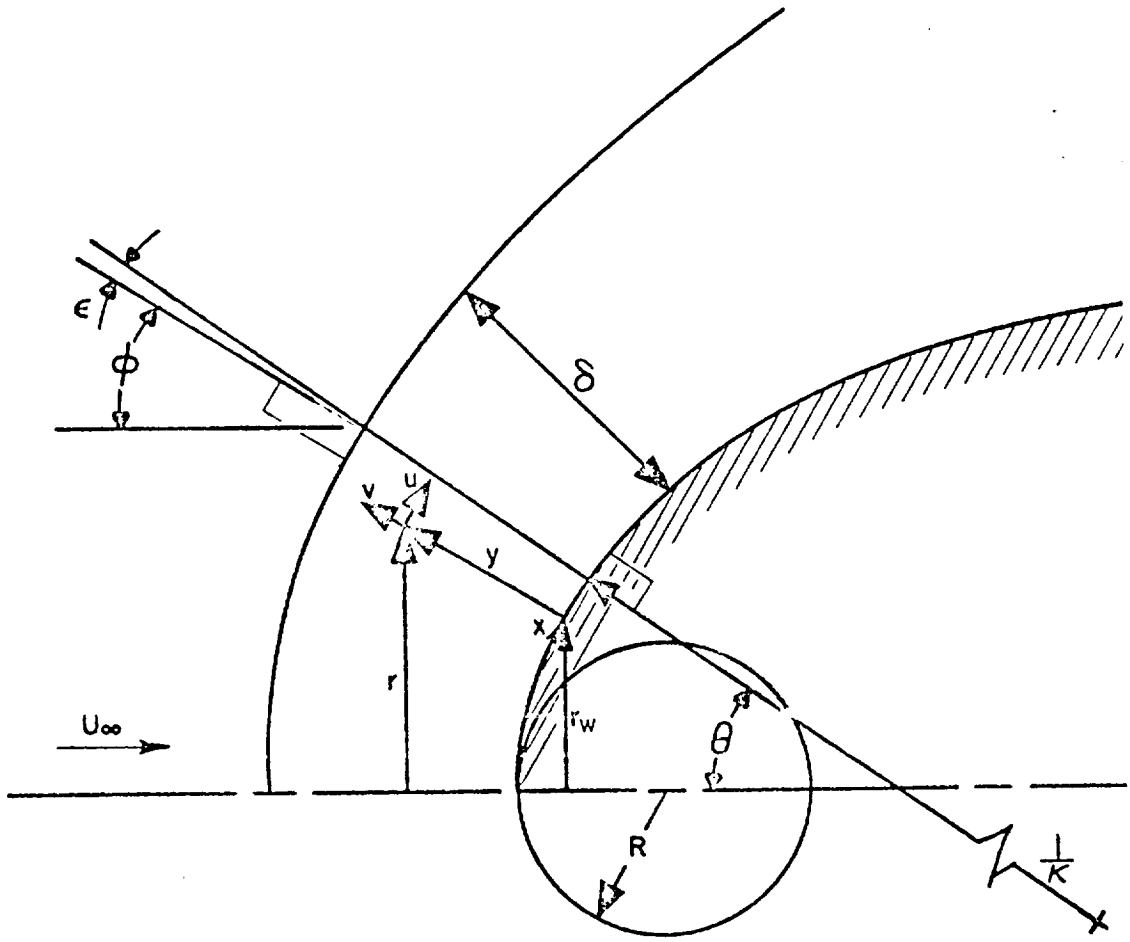

$$\text{Tan}\,\epsilon = \frac{d\delta}{(1+\kappa\delta)\,dx} \qquad \frac{d\theta}{dx} = \kappa(x)$$

$$\delta = \int_0^x (1+\kappa\delta)\,\text{Tan}\,\epsilon\,dx + \delta_0 \qquad \theta = \int_0^x \kappa(x)\,dx$$

Fig. A.3 Body-Oriented Coordinate System

$$(d\zeta)^2 = \tilde{\kappa}^2(dx)^2 + (dy)^2 + (r^A dz)^2 \tag{A.76}$$

For the axisymmetric case z has been substituted for φ. Thus by noting that the superscript A can be either 1 or 0 both the respective axisymmetric and two dimensional cases can be represented by one set of equations.

Substituting the stretching functions A.71 and A.72 and relationships A.73 and A.75 into the general conservation equations for a multicomponent continuum gas in general orthogonal coordinates given in the second section yields the following equations.

Continuity:

$$\frac{\partial(\rho u r^A)}{\partial x} + \frac{\partial(\tilde{\kappa} r^A \rho v)}{\partial y} = 0 \tag{A.77}$$

Species Continuity:

$$\frac{\partial(r^A \rho C_i u)}{\partial x} + \frac{\partial(\tilde{\kappa}\, r^A \rho C_i v)}{\partial y} = \frac{-\partial(r^A J_{i,x})}{\partial x}$$

$$\frac{-\partial(\tilde{\kappa}\, r^A J_{i,y})}{\partial y} + \tilde{\kappa} r^A \omega_i \tag{A.78}$$

where $J_{i,x}$ and $J_{i,y}$ are the mass flux components of species i in the x and y direction respectively. The mass flux vector is the sum of two vectors neglecting force diffusion and pressure diffusion.

$$\bar{J}_i = \bar{J}_i^{(D)} + \bar{J}_i^{(T)} \tag{A.79}$$

The components are

concentration diffusion:

$$J^{(D)}_{i,x} = \frac{n_t^2}{\rho \mathbb{R}T} \sum_{j=1}^{n} M_i M_j D_{ij} \left[Y_i \sum_{\substack{k=1 \\ k\neq j}}^{n} \left(\frac{\partial G_j}{\partial Y_k} \right)_{T,\forall,Y_{\ell \neq j,k}} \frac{1}{\tilde{\kappa}} \frac{\partial Y_k}{\partial x} \right] \tag{A.80}$$

$$J^{(D)}_{i,y} = \frac{n_t^2}{\rho \mathbb{R}T} \sum_{j=1}^{n} M_i M_j D_{ij} \left[Y_i \sum_{\substack{k=1 \\ k\neq j}}^{n} \left(\frac{\partial G_j}{\partial Y_k} \right)_{T,\forall,Y_{\ell \neq j,k}} \frac{\partial Y_k}{\partial y} \right] \tag{A.81}$$

thermal diffusion:

$$J^{(T)}_{i,x} = - \frac{D_i^T}{\tilde{\kappa}} \frac{\partial \ell n\, T}{\partial x} \tag{A.82}$$

$$J^{(T)}_{i,y} = - D_i^T \frac{\partial \ell n\, T}{\partial y} \tag{A.83}$$

The two momentum equations can be expressed in the following manner.

x - momentum

$$\begin{aligned} &\rho r^A u \frac{\partial u}{\partial x} + \rho \tilde{\kappa} r^A v \frac{\partial v}{\partial y} - \rho \kappa r^A uv \\ &+ r^A \frac{\partial P}{\partial x} - \frac{\partial (r^A \tau_{xx})}{\partial x} - \frac{\partial (\tilde{\kappa} r^A \tau_{xy})}{\partial y} \\ &- r^A \kappa \tau_{xy} + \tau_{zz} \frac{\partial r^A}{\partial x} = 0 \end{aligned} \tag{A.84}$$

y - momentum

$$\begin{aligned} &\rho r^A u \frac{\partial v}{\partial x} + \rho \tilde{\kappa} r^A v \frac{\partial v}{\partial y} - \rho \kappa r^A u^2 \\ &+ \tilde{\kappa}\, r^A \frac{\partial P}{\partial y} - \frac{\partial (r^A \tau_{xy})}{\partial x} - \frac{\partial (\tilde{\kappa} r^A \tau_{yy})}{\partial y} \\ &+ \kappa r^A \tau_{xx} + \tilde{\kappa} \tau_{zz} \frac{\partial r^A}{\partial y} = 0 \end{aligned} \tag{A.85}$$

where the components of the stress tensor are

$$\tau_{xx} = \frac{\lambda}{\underset{\sim}{\kappa} r^A}\left[\frac{\partial(r^A u)}{\partial x} + \frac{\partial(\tilde{\kappa} r^A v)}{\partial y}\right] + \frac{2\mu}{\underset{\sim}{\kappa}}\left[\frac{\partial u}{\partial x} + \kappa v\right] \tag{A.86}$$

$$\tau_{yy} = \frac{\lambda}{\underset{\sim}{\kappa} r^A}\left[\frac{\partial(r^A u)}{\partial x} + \frac{\partial(\tilde{\kappa} r^A v)}{\partial y}\right] + 2\mu\,\frac{\partial v}{\partial y} \tag{A.87}$$

$$\tau_{zz} = \frac{\lambda}{\underset{\sim}{\kappa} r^A}\left[\frac{\partial(r^A u)}{\partial x} + \frac{\partial(\tilde{\kappa} r^A v)}{\partial y}\right] + 2\mu\left[\frac{u}{\underset{\sim}{\kappa} r^A}\frac{\partial r^A}{\partial x} + \frac{v}{r^A}\frac{\partial r^A}{\partial y}\right] \tag{A.88}$$

$$\tau_{xy} = \tau_{yx} = \mu\left[\frac{1}{\underset{\sim}{\kappa}}\frac{\partial v}{\partial x} + \frac{\partial u}{\partial y} - \frac{\kappa}{\underset{\sim}{\kappa}}u\right] \tag{A.89}$$

The above stress components are also used in the energy equation.

energy:

$$\rho r^A u\frac{\partial H}{\partial x} + \rho\tilde{\kappa} r^A v\frac{\partial H}{\partial y} = -\frac{\partial(r^A q_{D,x})}{\partial x} - \frac{\partial(\tilde{\kappa} r^A q_{D,y})}{\partial y}$$

$$-\frac{\partial(r^A q_{R,x})}{\partial x} - \frac{\partial(\tilde{\kappa} r^A q_{R,y})}{\partial y} + \frac{\partial}{\partial x}\left[r^A u\tau_{xx} + r^A v\tau_{xy}\right] \tag{A.90}$$

$$+\frac{\partial}{\partial y}\left[\tilde{\kappa} r^A u\tau_{xy} + \tilde{\kappa} r^A v\tau_{yy}\right]$$

The components of the diffusional heat flux vector are

$$q_{D,x} = -\frac{k}{\underset{\sim}{\kappa}}\frac{\partial T}{\partial x} + \sum_i h_i J_{i,x}$$

$$-\frac{P}{N^2}\sum_i\sum_{j\neq i}\frac{N_i}{m_i}\frac{D_i^T}{\mathbb{D}_{ij}}\left(\frac{J_{j,x}}{\rho_j} - \frac{J_{i,x}}{\rho_i}\right) \tag{A.91}$$

$$q_{D,y} = -k\frac{\partial T}{\partial y} + \sum_i h_i J_{i,y} - \frac{P}{N^2}\sum_i \sum_{j\neq i} \frac{N_i}{m_i}\frac{D_i^T}{\mathbb{D}_{ij}}\left(\frac{J_{j,y}}{\rho_j} - \frac{J_{i,y}}{\rho_i}\right) \tag{A.92}$$

From Eq. A.66 and Eq. A.67 the components of the radiative flux vector are:

$$q_{R,x} = \int_{x(\bar{r}_0)}^{x(\bar{r}_1)}\int_0^\infty \alpha_\nu(4\pi B_\nu - \int_0^{4\pi} I_\nu(\bar{r})d\Omega)d\nu\tilde{\kappa}dx \tag{A.93}$$

$$q_{R,y} = \int_{y(\bar{r}_0)}^{y(\bar{r}_1)}\int_0^\infty \alpha_\nu(4\pi B_\nu - \int_0^{4\pi} I_\nu(\bar{r})d\Omega)d\nu dy \tag{A.94}$$

The statement of these vector components completes the set of conservation equations expressed in body oriented orthogonal coordinates. By the use of the stretching functions listed in Tab. A.2, the conservation equations can be written in the coordinate system desired by following the method used for the case under consideration in this section. Furthermore, it is noted that the conservation equations were obtained using orthogonal versions of the tensor terms. Consequently, if a nonorthogonal transformation is desired the equations may be used without fear of neglecting terms.

Subsequent transformation of independent variables using Dorodnitsyn, Von Mises, Lees or one of many other transformations may be made in order to simplify the form of the conservation equations. The selection and use of these transformations will not be discussed here. The reader is referred to Dorrance, Ref. A.9, and Hansen, Ref. A.10, for suitable discussion and listing of similarity transformations.

APPENDIX A

References

A.1 Fitts, Donald D. Nonequilibrium Thermodynamics. New York: McGraw-Hill Book Company, Inc., 1962.

A.2 Brodkey, Robert S. The Phenomena of Fluid Motions. Reading, Massachusetts: Addison-Wesley Publishing Company, 1967.

A.3 Bird, R. Byron, Warren E. Stewart, and Edwin N. Lightfoot. Transport Phenomena. New York: John Wiley & Sons, Inc., 1966.

A.4 Planck, Max. The Theory of Heat Radiation, New York: Dover Publications, Inc., 1959.

A.5 Zel'dovich, Ya. B., and Yu. P. Raiser. Physics of Shock Waves and High-Temperature Hydrodynamic Phenomena, Vol. 1, ed. by Wallace D. Hayes and Ronald F. Probstein, New York: Academic Press, 1966.

A.6 Back, L. H. "Conservation Equations of a Viscous, Heat-Conducting Fluid in Curvilinear Orthogonal Coordinates," JPL Technical Report 32-1332 (Sept. 1968).

A.7 Emmons, H. W., Ed. Fundamentals of Gas Dynamics, Vol. III, Ch. I, Tsien, H.S., "The Equations of Gas Dynamics," Princeton University Press, Princeton, New Jersey, 1958.

A.8 Hirschfelder, C. T. Curtiss and R. B. Bird. Molecular Theory of Gases and Liquids, John Wiley & Sons, Inc., New York, 1954.

A.9 Dorrance, W. H. Viscous Hypersonic Flow, McGraw Hill Book Company, Inc., New York, 1962.

A.10 Hansen, A. G., Similarity Analyses of Boundary Value Problems in Engineering, Prentice-Hall, Inc., Englewood Cliffs, New Jersey, 1964.

APPENDIX B

RADIATIVE TRANSPORT EQUATIONS

The purpose of this appendix is to provide details of the radiative properties and transport equations used in this work which were developed by Wilson (Ref. B.1). Accordingly, the following development provides a synopsis of the radiative transport section of Ref. B.1. The synopsis is complete in itself and provides definition of symbols and terms not found in the main text.

BASIC TRANSPORT EQUATIONS

In Chapter 2 the radiative transport equation was solved in physical space for a one-dimensional slab to yield an equation for intensity. This equation, Eq. 2.49, and the equations for the flux Eq. 2.50, and flux divergence, Eq. 2.51, are the starting place for this development.

In order to calculate intensities the absorption coefficient is separated into a line and continuum contribution.

$$\alpha_\nu = \alpha_\nu^C + \alpha_\nu^L \tag{B.1}$$

Correspondingly, the flux normal to the body* is expressed as a sum of the continuum only process and the line process corrected for continuum attenuation.

$$q_R = q_R^C + q_R^L \tag{B.2}$$

---

* The y subscript on the flux term which was used in the main text has been dropped in Appendix B for convenience.

The continuum flux is then expressed as

$$q_R = \pi \int_0^\infty \left\{ \int_0^{E_\nu(0,y)} B_\nu dE_\nu - \int_0^{E_\nu(y,\delta)} B_\nu dE_\nu \right\} d\nu \qquad (B.3)$$

where the emissive function, E_ν, is

$$E_\nu = 1 - \exp\left[- \frac{1}{f} \int_{y'}^{y} \alpha_\nu^C d\hat{y} \right] \qquad (B.4)$$

The line flux is expressed as*

$$q_R^L = \pi \sum_{\substack{\text{all lines} \\ i}} \int_0^{w_i(0,y)} B_i dw_i(y',y) - \int_0^{w_i(y,\delta)} B_i dw_i(y,y') \qquad (B.5)$$

where the frequency integration has been carried out analytically and incorporated into an equivalent width variable, $w_i(y',y)$, defined as

$$w_i(y',y) = w_i[-(y,y')] = e^{-\frac{1}{f}\int_{y'}^{y} \alpha_\nu^C d\hat{y}} \int_{\Delta\nu} \left[1 - e^{-\frac{1}{f}\int_{y'}^{y} \alpha_\nu^L d\hat{y}} \right] d\nu \qquad (B.6)$$

In this definition it has been assumed that the continuum absorption coefficient and Planck function are frequency independent over the interval $\Delta\nu$.

The flux divergence is expressed as a sum of four terms.

$$\frac{\partial q_R}{\partial y} \equiv Q = Q^{C,C} + Q^{C,L} + Q^{L,C} + Q^{L,L} \qquad (B.7)$$

These four terms are defined as;

(1) the energy emitted and absorbed by the continuum;

---

* Throughout this appendix the parenthesis symbol ( ) is principly used to denote functional dependencies.

$$Q^{C,C} = 2\pi \int_0^\infty \alpha_\nu^C \left[\int_0^{E_\nu(0,y)} B_\nu(y') dE_\nu(y,y') + \int_0^{E_\nu(y,\delta)} B_\nu(y') dE_\nu(y',y) \right.$$

$$\left. - 2B_\nu(y) \right] d\nu \qquad \text{(B.8)}$$

(2) the energy emitted by the continuum and absorbed by the lines;

$$Q^{C,L} = 2\pi \sum_{\substack{\text{all lines} \\ \ell}} \int_0^{E_\nu(0,y)} B_i(y') \left[S_i(y) - A_i(y',y) \right] dE_\nu(y',y)$$

$$+ \int_0^{E_\nu(y,\delta)} B_i(y') \left[S_i(y) - A_i(y,y') \right] dE_\nu(y,y') \qquad \text{(B.9)}$$

(3) the energy emitted by lines and absorbed by the continuum;

$$Q^{L,C} = 2\pi \sum_{\substack{\text{all lines} \\ i}} \alpha_\nu^C(y) \int_0^{w_i(0,y)} B_i(y') dw_i(y,y')$$

$$+ \int_0^{w_i(y,\delta)} B_i(y') dw_i(y,y') \qquad \text{(B.10)}$$

(4) the energy absorbed and emitted by lines:

$$Q^{L,L} = 2\pi \sum_{\substack{\text{all lines} \\ i}} \int_0^{A_i(0,y)} B_i(y') e^{-\frac{1}{f}\int_{y'}^{y} \alpha_{\nu_i}^C(\hat{y})dy} dA_i(y,y')$$

$$+ \int_0^{A_i(y,\delta)} B_i(y') e^{-\frac{1}{f}\int_{y}^{y'} \alpha_{\nu_i}^C(\hat{y})d\hat{y}} dA_i(y,y')$$

$$- 2B_i(y)S_i(y) \qquad \text{(B.11)}$$

In Eqs. (B.9) and (B.11) the frequency integration is performed in terms of an absorption equivalent width variable $A_i(y',y)$ defined as

$$A_i(y',y) = A_i[-(y,y')] = \int_{\Delta\nu} \alpha_i^L(y)\left[1 - e^{-\frac{1}{f}\sum_i \int_y^{y'} \alpha_i^L(\hat{y})d\hat{y}}\right]d\nu \qquad (B.12)$$

The line strength variable, S_i, is defined in section on transport by a single line.

TRANSPORT BY THE CONTINUUM PROCESS

Since the continuum absorption coefficient varies slowly as a function of frequency, except at photoionization edges, a monochromatic evaluation of the flux and flux divergence at selected frequencies followed by numerical quadrature over frequencies is realistic.

Four atomic species are considered, H, C, O, N. For these species and shock layer conditions of interest, the shock layer is optically thin below the first major photoionization edge. Furthermore, at frequencies above the first photoionization edge the absorption coefficient is essentially constant. Consequently the frequency dependent absorption coefficient can be represented by a series of grey absorption coefficients. For the optically thin groups the grey absorption coefficient is the Planck mean coefficient.

$$\alpha_P = \frac{\int_{\Delta\nu} \alpha_\nu B_\nu d\nu}{\int_{\Delta\nu} B_\nu d\nu} \qquad (B.13)$$

where

$$\alpha_\nu = \sum_j \alpha_{\nu j}^C = \sum_j N_j \sigma_j \left[1 - e^{-h\nu/kT}\right] \qquad (B.14)$$

and

$$\sigma_j = \sigma_j(\nu,T) \quad \text{for} \quad j = \text{species H, C, O, N}$$

The absorption cross section has the same form for the atomic species considered (all cross sections are given in cm^2/particle).

$0 \leq h\nu \leq h\nu_T^j$

$$\sigma_j = 7.26 \times 10^{-16} \Gamma_j \, kT \, e^{-[\epsilon_j - h\nu - \Delta]/kT} \frac{\xi_j}{[h\nu]^3} \tag{B.15}$$

$h\nu > h\nu_T^j$

$$\sigma_j = 7.26 \times 10^{-16} \Gamma_j \, kT \, e^{-[\epsilon_j - h\nu_T^j]/kT} \frac{\xi_j}{[h\nu]^3} \tag{B.16}$$

where

Γ_j = species statistical weight factor

ϵ_j = species ionization energy

Δ = photoionization edge shift

$h\nu_T^j$ = species merged energy level limit

ξ_j = species nonhydrogenic correction factor

Reference B.1 did not include molecular absorption or emission. However, continuum cross section for the molecules N_2, O_2, C_2, C_3, and CO were more recently included by Wilson in his Fortran subroutine TRANS which was obtained from Wilson and forms the basis of the radiative calculation method of the present work (Ref. B.2). In the present work the cross sections for H_2 and C_2H were added. The addition of

molecules to the radiative calculators dictated several changes in the continuum calculation procedure described in Ref. B.1. The following development includes these changes.

The continuum transport is calculated using a 12-band model (7-bands were used in Ref. B.1). In each group the absorption coefficient

$$\alpha = \sum_{j} N_j \sigma_j \qquad j = N, O, C, H, CO, C_3, C_2, O_2, N_2, H_2, C_2H \tag{B.17}$$

is calculated. The equations for the band averaged absorption cross sections for each band group is listed below.

Group 1: $0 \le h\nu \le 5.0$ ev

Atomic cross sections

In one band the partial Planck mean is used in which σ_j for each element has the form

$$\sigma_j = \frac{5.04 \times 10^3 kT\, \Gamma_j K_o}{B_P} e^{-\epsilon_j/kT} e^{\Delta/kT} h\nu_T{}^j \left[\theta_j + \frac{\beta_j}{3}\left[h\nu_T{}^j\right]^2\right]$$

$$+ kT\left\{\theta_j + 2\beta_j[kT]^2\right\} - kT\, e^{-\left[h\nu_B - h\nu_T{}^j\right]/kT}\left\{\theta_j + \beta_j(h\nu_B\right.$$

$$\left. - h\nu_T{}^j)^2\right\} - kTe^{-\left\{h\nu_B - h\nu_T{}^j\right\}\left\{2\beta_j[h\nu_B - h\nu_T{}^j]kT + 2\beta_j[kT]^2\right\}} \tag{B.18}$$

where

$$K_0 = 7.26 \times 10^{-16} cm^2 ev^2$$

$$h\nu_B = 5.0 \text{ ev}$$

and

$$P \quad .04 \times 10^{3}[kT]^{4} \left\{\frac{\pi^4}{15} - e^{-h\nu_B/kT}\left[\left(\frac{h\nu_B}{kT}\right)^3 + 3\left(\frac{h\nu_B}{kT}\right)^2 + 6\left(\frac{h\nu_B}{kT}\right) + 6\right]\right\} \tag{B.19}$$

For each atomic species the required parameters are:

	$h\nu_T{}^j$(ev)	ϵ_j(ev)	θ_j	β_j
H:	2.40	13.56	1.00	0.0
C:	3.78	11.26	0.30	0.0488
N:	4.22	14.54	0.24	0.0426
O:	4.22	13.51	0.24	0.0426

Molecular cross sections

$$\sigma_{O_2} = \sigma_{N_2} = \sigma_{H_2} = \sigma_{C_2} = \sigma_{C_3} = \sigma_{CO} = \sigma_{C_2H} = 0.0$$

Group 2: $5.0 \leq h\nu \leq 6.0$ ev

Atomic cross sections

σ_j = Eq. (B.16) $\quad j = N, O, H, C$

Molecular cross sections

$$\sigma_{C_2} = 3. \times 10^{-18} + 8. \times 10^{-18} e^{-.5/kT}$$

$$\sigma_{C_3} = 4. \times 10^{-18}$$

$$\sigma_{O_2} = \sigma_{N_2} = \sigma_{H_2} = \sigma_{CO} = \sigma_{C_2H} = 0.0$$

Group 3: $6.0 \leq h\nu \leq 7.0$ ev

Atomic cross sections

σ_j = Eq. (B.16) j = N, O, C, H

Molecular cross sections

$$\sigma_{C_2} = 1. \times 10^{-18}$$

$$\sigma_{CO} = 3. \times 10^{-18} e^{-.7/kT}$$

$$\sigma_{O_2} = \sigma_{N_2} = \sigma_{H_2} = \sigma_{C_3} = \sigma_{C_2H} = 0.0$$

Group 4: $7.0 \leq h\nu \leq 8.0$ ev

Atomic cross sections

σ_j = Eq. (B.16) j = N, O, H

$$\sigma_C = \text{Eq. (B.16)} + 5. \times 10^{-17} e^{-4.18/kT}/\Sigma_C$$

Molecular cross sections

$$\sigma_{CO} = 1.9 \times 10^{-17} e^{-.5/kT}$$

$$\sigma_{O_2} = 6.0 \times 10^{-19}$$

$$\sigma_{C_2H} = 1.3 \times 10^{-18}$$

$$\sigma_{C_2} = \sigma_{N_2} = \sigma_{H_2} = \sigma_{C_3} = 0.0$$

Group 5: $8.0 \leq h\nu \leq 9.0$ ev

Atomic cross sections

$$\sigma_j = \text{Eq. (B.16)} \qquad j = N, O, H$$

$$\sigma_C = \text{Eq. (B.16)} + 5. \times 10^{-17} e^{-4.18/kT}/\Sigma_C + 2.2 \times 10^{-17} e^{-2.68/kT}/\Sigma_C$$

Molecular cross sections

$$\sigma_{CO} = 2.5 \times 10^{-17}$$

$$\sigma_{O_2} = 2.0 \times 10^{-19}$$

$$\sigma_{C_2H} = 8.5 \times 10^{-19}$$

$$\sigma_{N_2} = \sigma_{H_2} = \sigma_{C_3} = \sigma_{C_2} = 0.0$$

Group 6: $9.0 \leq h\nu \leq 10.0$ ev

Atomic cross sections

$$\sigma_j = \text{Eq. (B.16)} \qquad j = N, O, H$$

$$\sigma_C = \text{Eq. (B.16)} + 5. \times 10^{-17} e^{-4.18/kT}/\Sigma_C + 2.2 \times 10^{-17} e^{-2.68/kT}/\Sigma_C$$

Molecular cross sections

$$\sigma_{CO} = 5.0 \times 10^{-18}$$

$$\sigma_{O_2} = 1.0 \times 10^{-18}$$

$$\sigma_{C_2} = \sigma_{N_2} = \sigma_{H_2} = \sigma_{C_3} = \sigma_{C_2H} = 0.0$$

Group [illegible] $10.0 \leq h\nu \leq 10.8$ ev

Atomic cross sections

$$\sigma_j = \text{Eq. (B.16)} \qquad j = O, N$$

$$\sigma_N = 3.2 \times 10^{-18} T \, e^{-10.2/kT} / \Sigma_N$$

$$\sigma_C = \left[8.5 \times 10^{-17} e^{-1.26/kT} + 2.2 \times 10^{-17} e^{-2.75/kT} + 5.0 \times 10^{-17} e^{-4.18/kT} \right] / \Sigma_C$$

Molecular cross sections

$$\sigma_{O_2} = 6.0 \times 10^{-19}$$

$$\sigma_{C_2} = \sigma_{N_2} = \sigma_{H_2} = \sigma_{C_3} = \sigma_{CO} = \sigma_{C_2H} = 0.0$$

Group 8: $10.8 \leq h\nu \leq 11.1$ ev

Atomic cross sections

$$\sigma_j = \text{Eq. (B.16)} \qquad j = O, N$$

$$\sigma_N = 5.16 \times 10^{-17} e^{-3.5/kT} / \Sigma_N$$

$$\sigma_C = \left[8.5 \times 10^{-17} e^{-1.26/kT} + 2.2 \times 10^{-17} e^{-2.75/kT} + 5.0 \times 10^{-17} e^{-4.18/kT} \right] / \Sigma_C$$

Molecular cross sections

$$\sigma_{O_2} = \sigma_{N_2} = \sigma_{H_2} = \sigma_{C_2} = \sigma_{C_3} = \sigma_{CO} = \sigma_{C_2H} = 0.0$$

Group 9: $11.1 \leq h\nu \leq 12.0$ ev

Atomic cross sections

$$\sigma_j = \text{Eq. (B.16)} \qquad j = O, H$$

$$\sigma_N = 5.16 \times 10^{-17} e^{-3.5/kT}/\Sigma_N$$

$$\sigma_C = \left[8.5 \times 10^{-17} e^{-1.26/kT} + 2.2 \times 10^{-17} e^{-2.75/kT} + 5.0 \times 10^{-17} e^{-4.18/kT}\right]/\Sigma_C$$

Molecular cross sections

$$\sigma_{N_2} = 1.0 \times 10^{-18}$$

$$\sigma_{O_2} = \sigma_{H_2} = \sigma_{C_2} = \sigma_{C_3} = \sigma_{CO} = \sigma_{C_2H} = 0.0$$

Group 10: $12.0 \leq h\nu \leq 13.4$ ev

Atomic cross sections

$$\sigma_j = \text{Eq. (B.16)} \qquad j = O, H$$

$$\sigma_N = \left[6.4 \times 10^{-17} e^{-2.3/kT} + 5.16 \times 10^{-17} e^{-3.5/kT}\right]/\Sigma_N$$

$$\sigma_C = \left[9.9 \times 10^{-17} + 8.5 \times 10^{-17} e^{-1.26/kT} + 2.2 \times 10^{-17} e^{-2.75/kT} + 5.0 \times 10^{-17} e^{-4.18/kT}\right]/\Sigma_C$$

Molecular cross sections

$$\sigma_{N_2} = 1.0 \times 10^{-17}$$

$$\sigma_{H_2} = 2.7 \times 10^{-17}$$

$$\sigma_{O_2} = \sigma_{C_2} = \sigma_{C_3} = \sigma_{CO} = \sigma_{C_2H} = 0.0$$

Group 11: $13.4 \leq h\nu \leq 14.3$ ev

Atomic cross sections

$$\sigma_H = 1.18 \times 10^{-17}/\Sigma_H$$

$$\sigma_O = 3.6 \times 10^{-17}/\Sigma_O$$

$$\sigma_N = \left[6.4 \times 10^{-17}\, e^{-\,2.3/kT} + 5.15 \times 10^{-17}\, e^{-\,3.5/kT}\right]/\Sigma_N$$

$$\sigma_C = \left[9.9 \times 10^{-17} + 8.5 \times 10^{-17}\, e^{-\,1.26/kT} + 2.2 \times 10^{-17}\, e^{-\,2.75/kT} + 5.0 \times 10^{-17}\, e^{-\,4.18/kT}\right]/\Sigma_C$$

Molecular cross sections

$$\sigma_{N_2} = 1. \times 10^{-17}$$

$$\sigma_{H_2} = 2.7 \times 10^{-17}$$

$$\sigma_{O_2} = \sigma_{C_2} = \sigma_{C_3} = \sigma_{CO} = \sigma_{C_2H} = 0.0$$

Group 12: $14.3 \leq h\nu \leq 20.0$

Atomic cross sections

$$\sigma_H = \sigma_O = 0.0$$

$$\sigma_N = \left[1.0 \times 10^{-18} + 6.4 \times 10^{-17}\, e^{-\,2.3/kT} + 5.16 \times 10^{-17} e^{-3.5/kT}\right]/\Sigma_N$$

$$\sigma_C = \left[9.9 \times 10^{-17} + 8.5 \times 10^{-17}\, e^{-\,1.26/kT} + 2.2 \times 10^{-17} e^{-\,2.5/kT} + 5.0 \times 10^{-17} e^{-\,4.18/kT}\right]/\Sigma_C$$

Molecular cross sections

$$\sigma_{N_2} = 1.0 \times 10^{-18}$$

$$\sigma_{O_2} = \sigma_{C_2} = \sigma_{C_3} = \sigma_{H_2} = \sigma_{CO} = \sigma_{C_2H} = 0.0$$

In the above expressions Σ_j is the partition function of the j-th species.

The flux and flux divergence equations in terms of the grey absorption coefficients for each group k are:

$$q^C_{R,k} = \pi \int_0^{E_k(0,y)} \bar{B}_k(y')dE_k(y',y) - \int_0^{E_k(y,\delta)} \bar{B}_k(y')dE_k(y,y') \qquad (B.20)$$

$$Q^{C,C}_k = 2\pi\alpha_k{}^C \Big[\int_0^{E_k(0,y)} \bar{B}_k(y')dE_k(y', y)$$

$$+ \int_0^{E_k(y,\delta)} \bar{B}_k(y')dE_k(y,y') - 2\,\bar{B}_k \Big] \qquad (B.21)$$

where

$$\bar{B}_k = \int_{\Delta\nu_k} B_\nu(T)d\nu \qquad (B.22)$$

and E_k is determined using Eq. B.4 and the grey absorption coefficient $\alpha_k{}^C$.

TRANSPORT BY A SINGLE LINE

Consider the transport by system of nonoverlapping, electron-impact broaden lines. An isolated line has a Lorentzian shape characterized by a strength S and (half) half-width γ, neglecting line shifts,

$$\alpha_\nu^L = \frac{S\gamma}{\pi}\left[\frac{1}{(\nu - \nu_0) + \gamma^2}\right] \tag{B.23}$$

where

$$S = \int_0^\infty \alpha_\nu^L d\nu = \frac{\pi e^2}{mc} N_n f_{nn'}\left[1 - e^{-h\nu_0/kT}\right] \tag{B.24}$$

and where N_n is the lower state number density and $f_{nn'}$, the f-number. The f-number represents the transition probability strength and is the number appropriate for a single line, or multiplet, or whatever collection of line transitions is represented by the lower state number density, N_n.

The spatial dependence of the half-width γ in the denominator of Eq. (B.23) precludes a closed-form evaluation of the frequency integration required by the equivalent width variables W and A. For computational expediency, the actual half-width in the denominator of Eq. B.23 is replaced with a spatial average $\bar{\gamma}$. When the line center is optically thick in near constant temperature regions the effect of the half-width γ in the denominator of Eq. B. 23 is negligible. Thus, the spatially averaged value for γ is defined such that in the optically thin limit the correct flux is obtained. To this end, consider the spatial integral appearing in $W(y,y')$ and $A(y,y')$ of Eqs. B.6 and B.12.

$$Z = \frac{1}{f}\int_{y'}^{y} \alpha_\nu^L(\hat{y})d\hat{y} \tag{B.25}$$

Define a transport variable

$$z = \frac{1}{f\pi}\int_{y'}^{y} S(\hat{y})\ \gamma(\hat{y})d\hat{y} \tag{B.26}$$

then using Eq. B.23 and approximating $\gamma(\hat{y})$ in the denominator by $\bar{\gamma}(z)$, Eq. B.25 is rewritten as

$$Z = z\left[\frac{1}{[\nu - \nu_0]^2 + \bar{\gamma}^2(z)}\right] \tag{B.27}$$

where $\bar{\gamma}^2(z)$ is yet to be determined. Note $\bar{\gamma}(z)$ is constant over the interval y to y′ but not over the entire shock layer. Using this half-width approximation the following expressions for W(z) and A(z) are obtained.

$$W(z) = 2\pi\,\bar{\gamma}\; t\; e^{-t}[I_0(t) - I_1(t)][\text{continuum attenuation}] \tag{B.28}$$

$$A(z) = S(y)[1 - e^{-t}I_0(t)] \tag{B.29}$$

where $t = z/2\,\bar{\gamma}^2$

and I_0 and I_1 are modified Bessel functions of the first kind. For the optically thin limit $t \ll 1$

$$W = \int_{y'}^{y} S(\hat{y})d\hat{y} \tag{B.30}$$

requires

$$\bar{\gamma}(z) = \frac{\int_{y'}^{y} S(\hat{y})\gamma(\hat{y})d\hat{y}}{\int_{y'}^{y} S(\hat{y})dy} \tag{B.31}$$

For the flux divergence equivalent width calculation the appropriate value for $\bar{\gamma}$ is the value at the local point at which Q(y) is being calculated, i.e. $\bar{\gamma} = \gamma(y)$.

TRANSPORT BY A COLLECTION OF ISOLATED LINES

To calculate the flux and flux divergence, line groups are used where a "group" of lines is defined as a collection of adjacent lines within a spectral interval across which both the Planck function and continuum absorption coefficient can be approximated as being independent of frequency. The contribution from only neutral atom; H, O, N and C; transitions are considered since the contribution of ionic lines are negligible. All lines are considered non-overlapping. The overlapping corrections are developed in the next section.

Eq. B.5 yields the total flux from all lines in a group if $W(y, y')$ is interperted as the sum of the equivalent width from each individual line,

$$W(y,y') = \sum_{m=1}^{n} W_m(y,y') \tag{B.32}$$

where n is the total number of lines in the group. The right hand side of Eq. B.32 is approximated with a single expression of the form

$$\sum_{m=1}^{n} W_m(y,y') = nW(S^*,\gamma^*) \tag{B.33}$$

where S^* and γ^* are line parameters averaged over all lines in a group. Assuming that <u>all</u> lines in a group are either optically thin or optically thick expressions for S^* and γ^* are derived.

For the optically thin limit Eq. B.33 reduces to

$$\sum_{m} \int_{y'}^{y} S_m(\hat{y})d\hat{y} = n \int_{y'}^{y} S^*(\hat{y})d\hat{y} \tag{B.34}$$

which requires

$$S^* = \frac{1}{n} \sum_m S_m \tag{B.35}$$

For the optically thick limit the two sides of Eq. B.33 reduce to

$$\sum_m 2\left[\int_{y'}^{y} S_m(\hat{y})\gamma(\hat{y})d\hat{y} \right]^{\frac{1}{2}} = n\left[\int_{y'}^{y} S^*(\hat{y})\gamma^*(\hat{y})d\hat{y} \right]^{\frac{1}{2}} \tag{B.36}$$

Due to the square root operator a further approximation is made.

$$\left\{ \sum_m \left[\int_{y'}^{y} S_m(\hat{y})\gamma(\hat{y})d\hat{y} \right]^{\frac{1}{2}} \right\}^2 \approx \int_{y'}^{y} \left\{ \sum_m \left[S_m(\hat{y})\gamma_m(\hat{y}) \right]^{\frac{1}{2}} \right\}^2 d\hat{y} \tag{B.37}$$

This approximation is exact if the spatial variation of $S_m\gamma_m$ is the same for all lines or differs by a constant factor only.

The half-width γ_m is proportional to the electron number density

$$\gamma_m(\hat{y}) = \beta_m N_e(\hat{y}) \tag{B.38}$$

where β_m is a normalized half-width and is constant. The line strength is proportional to the lower state number density and the induced emission factor,

$$S_m(\hat{y}) = 1. \times 10^{-16} f_m N_m(\hat{y})[1 - e^{-h\nu/kT}] \tag{B.39}$$

When all lines within a group have a common lower state Eq. B.37 is exact. Using this as a basis Eqs. B.36 and B.37 yield

$$\gamma^* = \frac{1}{n^2 S^*} \left\{ \sum_m [S_m\gamma_m]^{\frac{1}{2}} \right\}^2 \tag{B.40}$$

which requires

$$S^* = \frac{1}{n} \sum_m S_m \tag{B.35}$$

For the optically thick limit the two sides of Eq. B.33 reduce to

$$\sum_m 2\left[\int_{y'}^{y} S_m(\hat{y})\gamma(\hat{y})d\hat{y} \right]^{\frac{1}{2}} = n\left[\int_{y'}^{y} S^*(\hat{y})\gamma^*(\hat{y})d\hat{y} \right]^{\frac{1}{2}} \tag{B.36}$$

Due to the square root operator a further approximation is made.

$$\left\{ \sum_m \left[\int_{y'}^{y} S_m(\hat{y})\gamma(\hat{y})d\hat{y} \right]^{\frac{1}{2}} \right\}^2 \approx \int_{y'}^{y} \left\{ \sum_m \left[S_m(\hat{y})\gamma_m(\hat{y}) \right]^{\frac{1}{2}} \right\}^2 d\hat{y} \tag{B.37}$$

This approximation is exact if the spatial variation of $S_m\gamma_m$ is the same for all lines or differs by a constant factor only.

The half-width γ_m is proportional to the electron number density

$$\gamma_m(\hat{y}) = \beta_m N_e(\hat{y}) \tag{B.38}$$

where β_m is a normalized half-width and is constant. The line strength is proportional to the lower state number density and the induced emission factor,

$$S_m(\hat{y}) = 1. \times 10^{-16} f_m N_m(\hat{y})[1 - e^{-h\nu/kT}] \tag{B.39}$$

When all lines within a group have a common lower state Eq. B.37 is exact. Using this as a basis Eqs. B.36 and B.37 yield

$$\gamma^* = \frac{1}{n^2 S^*} \left\{ \sum_m [S_m\gamma_m]^{\frac{1}{2}} \right\}^2 \tag{B.40}$$

A similar treatment of the flux equivalent width function A yields an identical expression for γ^*.

For each atomic specie individually Eq. B. 37 is reasonable. Thus for each line group the equivalent width for all lines of a given atom are computed. The total equivalent width for all lines of the group becomes

$$\sum_{m=1}^{n} W_m(y,y') = \sum_{j} n_j W_j(S_j^*, \gamma_j^*) \tag{B.41}$$

where W_j is the lumped equivalent width for each atom and where n_j, S_j^* and γ_j^* refer to the effective line parameters for that atom. The parameters S_j^* and γ_j^* are calculated from Eqs. B.35 and B.40 where the summation includes only those lines for a given atomic species. Using Eqs. B.38 and B.39 the line width and line strength can be expressed as

$$S_j^* = 1. \times 10^{-16} N_j f_j^* [1 - e^{-h\nu/kT}] \tag{B.42}$$

$$\gamma_j^* = N_e \beta_j^* \tag{B.43}$$

The f_j^* and β_j^* terms are

$$f_j^* = \sum_{m}^{n_j} \frac{f_m g_m e^{-\epsilon_m/kT}}{\Sigma_j} \tag{B.44}$$

$$\beta_j^* = \frac{1}{n_j f_j^*} \sum_{m}^{n_j} \left[\frac{f_m \beta_m g_m e^{-\epsilon_m/kT}}{\Sigma_j} \right]^{\frac{1}{2}} \tag{B.45}$$

The line spectrum for H, C, N, O, atoms was collected into nine groups. Within each group four "effective lines" were considered, one for each

atomic species. The f-number and half-width f_j^*, γ_j^* are calculated by rewritting Eqs. B.44 and B.45.

$$f_j^* = \frac{1}{n_j} \sum_{\ell} f_\ell{}^j P_\ell{}^j \tag{B.46}$$

$$\beta_j^* = \frac{1}{n_j{}^2 f_j^*} \sum_{\ell} [f\beta_\ell{}^j]^{\frac{1}{2}} [P_\ell{}^j]^{\frac{1}{2}} \tag{B.47}$$

where all transitions energies are calculated with respect to a common lower state ℓ and where $P_\ell{}^j$ is the fractional population of state ℓ in species j.

$$P_\ell{}^j = \frac{g_\ell e^{-\epsilon_\ell/kT}}{\Sigma_j} \tag{B.48}$$

$$f_\ell{}^j = \sum_{m \text{ in } \ell} f_m \tag{B.49}$$

$$[f\beta_\ell{}^j]^{\frac{1}{2}} = \sum_{m \text{ in } \ell} [f_m \beta_m]^{\frac{1}{2}} \tag{B.50}$$

The states ℓ considered for the H, C, N, and O species are listed in Tab. B.1.

The data for the spectral lines considered is given in Tab. B.2. For each line group, its spectral location and interval is listed. For each element the number of lines n_j in the group and for each state ℓ of that element the parameters $f_\ell{}^j$ and $(f\beta_\ell{}^j)^{\frac{1}{2}}$ are listed.

TRANSPORT BY OVERLAPPING LINES

This section considers the correction to the group equivalent width which accounts for overlapping lines.

The correct expression for the equivalent width for a collection of m lines within a group is (omitting the continuum attenunation factor for simplicity)

$$W_{group} = \int_D \left[1 - \exp\left(- \sum_m \int_{y'}^{y} \alpha_m^L(\hat{y})\, d\hat{y}\right)\right] d\nu \tag{B.51}$$

where the summation is over all lines and D is the spectral interval covered by the group. For the case of no lines overlapping in a group.

$$W_{group} = W_I = \sum_m W_m \tag{B.52}$$

However, when lines do overlap, an analytical result for the frequency integration in Eq. B.51 is not available. To avoid prohibitive calculation time required by a frequency integration an empirical correlation for the line group equivalent width for overlapping lines is used.

The spectral interval D defining a particular line group is a fixed interval. When the lines are optically thick and strongly overlapping within the interval, the line group equivalent width approaches the value of D. Thus a means of measuring the amount of overlapping within a group is to compare the isolated line value W_I with D. By comparison with exact calculations Wilson showed that the group equivalent width was correlated quite well by

$$\frac{W_{group}}{D} = \frac{2}{\pi} \tan^{-1}\left[\frac{\pi}{2}\frac{W_I}{D}\right] \tag{B.53}$$

For the flux divergence calculation, the parameter effected by overlapping is

$$\Gamma(y,y') = S(y) - A(y,y') = \int \alpha_\nu^L(y) e^{-\int_{y'}^{y} \alpha_\nu^L(\hat{y})d\hat{y}} d\nu \tag{B.54}$$

which, for a group, is

$$\Gamma_{group} = \int_D \left\{ \sum_m \alpha_m^L(y) \exp\left[- \int_{y'}^{y} \alpha_m^L(\hat{y})d\hat{y} \right] \right\} d\nu \tag{B.55}$$

For non-overlapping lines this parameter becomes

$$\Gamma_{group} = \Gamma_I = \sum_m \Gamma_m \tag{B.56}$$

Numerical results indicated that this parameter also could be correlated with the ratio W_I/D by the expression

$$\frac{\Gamma_{group}}{\Gamma_I} = e^{-W_I/D} \tag{B.57}$$

The two correlations, Eqs. B.53 and B.57, were found sufficient to account for line overlapping in the transport process.

LOCAL SOLUTIONS FOR THE FLUX DIVERGENCE

The numerical evaluation of the line flux term, Eq. B.5, and the flux divergence terms, Eqs. B.8, B.9 and B.10, present no particular problems. However, as noted by Wilson the numerical evaluation of $Q^{L,L}$ of Eq. B.11 presents difficulties for the case of optically thick lines. To eliminate this problem Eq. B.11 is written as (omitting the continuum attenuation for convenience)

$$Q^{L,L} = 2\pi \int_{A(\Delta y^-)}^{A(0,y)} B(y')dA(y,y') + 2\pi \int_{A(\Delta y^+)}^{A(y,\delta)} B(y)dA(y',y)$$

$$+ Q^{L,L,-}_{local} + Q^{L,L,+}_{local} \qquad \text{(B.58)}$$

where

$$Q^{L,L,-}_{local} = 2\pi \left[\int_0^{A(\Delta y-)} B(y')dA(y,y') - S(y)B(y) \right] \qquad \text{(B.59)}$$

$$Q^{L,L,+}_{local} = 2\pi \left[\int_0^{A(\Delta y+)} B(y')dA(y',y) - S(y)B(y) \right] \qquad \text{(B.60)}$$

Difficulties occur when, for a line which is very optically thick, $\Delta A^- \to S(y)$. The solution is found by evaluating the integral in B.59 or B.60 by parts. For example,

$$Q^{L,L,-}_{local} = B(\Delta t^-)A(\Delta t^-) - \int_0^{\Delta t^-} A(t) \frac{dB}{dt} dt \qquad \text{(B.61)}$$

where $t = z/2\bar{\gamma}^2$. Replacing dB/dt by constant

$$\frac{dB}{dt} = \frac{B(\Delta t^-) - B(0)}{\Delta t^-} \qquad \text{(B.62)}$$

Eq. B.61 becomes

$$Q^{L,L,-}_{local} = - B(\Delta t^-)\Gamma(\Delta t^-) + [B(\Delta t^-) - B(0)]\, \Lambda(\Delta t^-) \qquad \text{(B.63)}$$

where

$$\Gamma(\Delta t^-) = S(0) - A(\Delta t^-) = e^{-\Delta t^-/2} I_0(\Delta t^-/2) \qquad \text{(B.64)}$$

$$\Lambda(\Delta t^-) = \int_0^{\Delta t^-} A(t)dt = e^{-\Delta t^-/2}[I_0(\Delta t^-/2) + I_1(\Delta t^-/2)] \qquad (B.65)$$

Equation B.65 provides the correct limiting form for the flux divergence for the case of very large optical depth, $\Delta t^- \gg 1$. An analogous equation for $Q^{L,L,+}_{local}$ is used.

TABLE B.1 (from Ref. B.1)

FRACTIONAL POPULATION DATA

Element j	State ℓ	g_ℓ	ϵ_ℓ
H	1 2	2 8	0 10.20
C	1 2 3 4 5 6 7	9 5 1 5 12 36 60	0 1.264 2.684 4.183 7.532 8.722 9.724
N	1 2 3 4 5 6	4 10 6 18 54 90	0 2.384 3.576 10.452 11.877 13.002
O	1 2 3 4 5 6	9 5 1 8 24 40	0 1.967 3.188 9.283 10.830 12.077

TABLE B.2 (from Ref. B.1)

LINE GROUP DATA

Group No. i	Center Frequency $h\nu^i$(eV)	Spectral Interval D^i(eV)	Element j	Number of lines n_j	State ℓ	f_ℓ^j	$(f\beta_\ell^j)^{1/2}$
1	1.30 eV	.600 eV	C	28	5	1.16	7.42(-11)*
					6	1.12	1.91(-10)
					7	9.97(-1)	4.89(- 9)
			N	30	4	2.08(-1)	1.48(-11)
					5	1.52	2.26(-10)
					6	1.12	4.79(-10)
			O	10	5	1.04	1.22(-10)
					6	1.14	2.87(-10)
2	2.70 eV	2.20 eV	H	3	2	8.05(-1)	2.37(-10)
			C	7	5	4.06(-2)	9.40(-12)
					6	6.98(-2)	7.94(-11)
			N	16	4	9.08(-1)	1.64(-10)
					5	3.15(-2)	7.01(-11)
			O	11	4	1.02	6.13(-11)
					5	8.25(-2)	7.19(-11)
3	5.75 eV	1.50 eV	C	2	2	7.29(-2)	9.18(-12)
					3	6.76(-2)	8.75(-12)
4	7.57 eV	1.65 eV	C	8	1	1.05(-1)	9.57(-12)
					2	1.10(-2)	4.86(-12)
					3	1.50(-1)	5.93(-10)
			N	2	2	7.40(-2)	8.22(-12)
					3	6.34(-2)	7.60(-12)
5	9.10 eV	1.40 eV	C	14	1	3.29(-1)	3.65(-11)
					2	1.18(-1)	5.77(-10)
					4	2.36(-1)	6.56(-11)
			N	4	3	1.08(-1)	3.09(-11)
			O	1	1	4.71(-2)	5.08(-12)

Note: $7.42(-11) = 7.42 \times 10^{-11}$

TABLE B.2 (Ref. B.1)

(Continued)

Group No. i	Frequency $h\nu^i$(eV)	Spectral Interval D^i(eV)	Element j	Number of lines n_j	State ℓ	f_ℓ^j	$(f\beta_\ell^j)^{1/2}$
6	10.40 eV	1.00 eV	H	1	1	4.16(-1)	3.02(-11)
			C	4	1	8.65(-2)	2.35(-10)
			N	16	1	1.84(-1)	1.07(-11)
					2	2.90(-1)	4.41(-11)
					3	8.64(-2)	2.28(-10)
			O	2	3	1.51(-1)	9.93(-12)
					2	1.20(-1)	8.85(-12)
7	11.40 eV	1.20 eV	C	6	1	4.51(-2)	6.07(-10)
					2	7.05(-1)	2.10(-10)
			N	14	1	4.54(-1)	2.71(-12)
					2	9.63(-2)	2.34(-10)
					3	1.78(-1)	2.46(-11)
			O	3	3	4.23(-2)	2.52(-11)
8	12.70 eV	1.40 eV	H	2	1	1.08(-1)	1.32(-10)
			C	2	1	3.79(-1)	1.95(-11)
					3	1.05	1.27(-11)
			N	11	1	1.55(-1)	2.98(-11)
					2	1.42(-1)	7.08(-11)
					3	3.75(-2)	1.33(-10)
			O	15	1	1.46(-1)	1.97(-10)
					2	8.61(-2)	1.80(-11)
					3	9.33(-2)	8.13(-11)
9	13.90 eV	1.00 eV	C	1	2	2.95(-1)	5.85(-12)
			N	11	1	2.24(-1)	3.41(-10)
					2	2.92(-2)	1.48(-10)
			O	10	1	5.24(-2)	5.76(-12)
					2	7.22(-2)	7.20(-11)
					3	6.04(-2)	8.05(-11)

APPENDIX B

References

B.1 Wilson, K. H., "Stagnation Point Analysis of Coupled Viscous-Radiative Flow with Massive Blowing," NASA CR-1548, June 1970.

B.2 Wilson, K. H., Personal communication, August 1970.